

Radio Interferometric Studies of Cool Evolved Stellar Outflows

A dissertation submitted to the University of Dublin
for the degree of Doctor of Philosophy

Eamon O'Gorman

Supervisor: Dr. Graham M. Harper
Trinity College Dublin, September 2013

SCHOOL OF PHYSICS
UNIVERSITY OF DUBLIN
TRINITY COLLEGE



Declaration

I declare that this thesis has not been submitted as an exercise for a degree at this or any other university and it is entirely my own work.

I agree to deposit this thesis in the University's open access institutional repository or allow the library to do so on my behalf, subject to Irish Copyright Legislation and Trinity College Library conditions of use and acknowledgement.

Name: Your Name

Signature: **Date:**

Summary

You should write a nice summary here...

A dedication if you wish...

Acknowledgements

Some sincere acknowledgements...

List of Publications

Refereed

1. Richards, A. M. S., Davis, R. J., Decin, L., Etoka, S., Harper, G. M., Lim, J. J., Garrington, S. T., Gray, M. D., McDonald, I., **O'Gorman, E.**, Wittkowski, M.
“e-MERLIN resolves Betelgeuse at wavelength 5 cm”
Monthly Notices of the Royal Astronomical Society Letters, 432, L61 (2013)
2. **O'Gorman, E.**, Harper, G. M., Brown, J. M., Brown, A., Redfield, S., Richter, M. J., and Requena-Torres, M. A.
“CARMA CO($J = 2 - 1$) Observations of the Circumstellar Envelope of Betelgeuse”
The Astronomical Journal, 144, 36 (2012)
3. Sada, P. V., Deming, D., Jennings, D. E., Jackson, B. K., Hamilton, C. M., Fraine, J., Peterson, S. W., Haase, F., Bays, K., Lunsford, A., and **O'Gorman, E.**
“Extrasolar Planet Transits Observed at Kitt Peak National Observatory”
Publications of the Astronomical Society of the Pacific, 124, 212 (2012)
4. Sada, P. V., Deming, D., Jackson, B. K., Jennings, D. E., Peterson, S. W., Haase, F., Bays, K., **O'Gorman, E.**, and Lundsford, A.
“Recent Transits of the Super-Earth Exoplanet GJ 1214b”
The Astrophysical Journal Letters, 720, L215 (2010)

Non-Refereed

-
1. **O'Gorman, E., & Harper, G. M.**
“What is Heating Arcturus’ Wind?”,
Proceedings of the 16th Cambridge Workshop on Cool Stars, Stellar Systems and the Sun. Astronomical Society of the Pacific Conference Series, 448, 691 (2011)

Contents

List of Publications	vi
List of Figures	xi
List of Tables	xiv
1 Introduction	1
1.1 First Section	1
1.2 Second Section	1
1.3 Second Section	2
2 Introduction to Radio Interferometry	3
2.1 Radio Antenna Fundamentals	3
2.1.1 Properties of a Radio Antenna	4
2.1.2 Antenna Structural Design	7
2.1.3 Antenna Performance Parameters	9
2.2 Receiving System for an Interferometer	11
2.3 Fundamentals of Radio Interferometry	13
2.3.1 Young's Slits	13
2.3.2 The Two-element Interferometer	15
2.3.3 Complex Visibility	19
2.3.4 Coordinate Systems for Imaging	20
2.4 Synthesis Imaging	21
2.4.1 Visibility Sampling	22
2.4.2 Imaging (Making a Dirty Map)	23
2.4.3 Deconvolution (Making a CLEAN map)	25

CONTENTS

3 Targets, Instrumentation, and Observations	28
3.1 Betelgeuse	29
3.2 CARMA	33
3.3 CARMA Observations of Betelgeuse	37
3.4 Arcturus and Aldebaran	40
3.5 The Karl G. Jansky Very Large Array	45
3.6 VLA Observations of Arcturus and Aldebaran	49
3.7 VLA-Pie Town Observations of Betelgeuse	55
4 Radio Interferometric Data Analysis	58
4.1 Data Examination and Flagging	59
4.2 Calibration	62
4.2.1 Prior Calibration	64
4.2.2 Bandpass Calibration	66
4.2.3 Gain Calibration	68
4.2.4 Flux Scale Calibration and Application of Solutions	68
4.3 Imaging	70
4.3.1 Imaging the VLA Data	70
4.3.2 Imaging the CARMA Data	71
5 Multi-wavelength Study of Betelgeuse’s Extended Atmosphere	76
5.1 CO molecules in the CSE of Betelgeuse	77
5.2 Adopted Radial Velocity	80
5.3 CARMA CO($J = 2 - 1$) Spectra	81
5.4 Individual Configuration Image Cubes	86
5.5 Multi-configuration Image Cube Inspection	88
5.6 Spatial Extent of S2	90
5.7 Intensity distribution of CO	92
5.8 Spatial Extent of S1	95
5.9 Continuum Flux Densities	96
5.10 Higher CO rotational lines	98
5.11 CARMA CO observations in Context	101
5.12 e-Merlin 6 cm Results	103
5.13 VLA-Pie Town Maps vs e-MERLIN	108

CONTENTS

5.14	Long Term Radio Variability	110
5.15	0.7 cm VLA-Pie Town Maps	111
6	Multi-wavelength Radio Continuum Emission Studies of Dust-free Red Giants	115
6.1	Why Study Red Giants with the VLA?	116
6.2	Radio Maps	117
6.2.1	α Boo Maps	117
6.2.2	α Tau Maps	120
6.3	Results vs Previous Observations	121
6.4	Results vs Existing Models	125
6.5	Spectral Indices	129
6.6	Analytical Advection Model for α Boo's Wind	135
6.6.1	H II recombination in a stellar outflow	136
6.6.2	Application to α Boo's Wind	139
6.7	Constraining α Tau's Molsphere	141
6.8	Ionized Mass Loss Rates	143
A	List of Abbreviations	146
	References	148

List of Figures

1.1	Red Giant and Asymptotic Giant Branch Stars	2
2.1	Radiation and power pattern of a uniformly illuminated antenna.	6
2.2	Common optical systems used for radio antennas.	9
2.3	Block diagram of a superheterodyne receiver.	12
2.4	Fringe pattern produced by Young’s slits under various situations.	14
2.5	Visibilities for various source sizes.	16
2.6	Simplified schematic diagram of a two-element interferometer. .	17
2.7	The instantaneous point source responses of an interferometer. .	18
2.8	The (u, v, w) interferometric coordinate system.	22
2.9	VLA antenna layout and two examples of $u - v$ coverage for different track lengths.	23
2.10	The Fourier transform pairs in synthesis imaging.	25
3.1	VLA spatially resolved analysis of Betelgeuse.	31
3.2	The three CARMA array configurations used.	34
3.3	The layout of antenna pads for CARMA.	34
3.4	Major components in the signal path for CARMA.	35
3.5	Main features of a VLA antenna.	48
3.6	Importance of offsetting source from phase center.	52
3.7	Overview of a low and high frequency VLA observation.	53
4.1	Radio interferometry work flow chart.	59
4.2	Data examination of a VLA data set.	61
4.3	Eliminating RFI from the L band data set.	63
4.4	Calibration workflow diagram.	65

LIST OF FIGURES

4.5	Atmospheric opacity at the VLA site.	66
4.6	Gain variation as a function of frequency.	67
4.7	Example of a well calibrated source.	69
4.8	Wide field view of the VLA 20 cm image.	72
4.9	Comparing CLEAN to Multi-scale CLEAN.	74
5.1	Bernat (1979) CO line profile showing two sharp line cores.	78
5.2	Previous CO $J = 2 - 1$ rotational emission line profiles	79
5.3	Radial velocity data and model for α Ori.	81
5.4	Spectra integrated over a radius of 5'' for each array configuration image cube. The red and blue lines correspond to the high and low spectral resolution data respectively. The blueshifted emission component between -16.0 km s^{-1} and -10.0 km s^{-1} is almost resolved out in the C configuration image cube spectrum along with material with low absolute velocities.	82
5.5	Spectral profiles of the low spectral resolution multi-configuration image cube for circular extraction areas of radius 1'', 2'', 4'', 6'', 8'', and 10''. The S/N of the line profile reduces at larger extraction areas as more noise is included from the outer more noisy regions of the channel maps.	85
5.6	Discrete sources in individual configuration image cubes	87
5.7	Channel maps from the multi-configuration image cube	89
5.8	Geometry of a spherical symmetric flow.	91
5.9	S2 radius as a function of channel velocity	92

LIST OF FIGURES

5.10 <i>Left Column:</i> Surface Brightness as a function of projected radius on sky, R (red line). The emission has been extracted from the low spectral resolution multi-configuration image cube and is integrated over the channels where S1 is present (bottom) and over the channels where only S2 is present (top). Intensity proportional to R^{-1} and R^{-2} is also shown for comparison. <i>Right Column:</i> The corresponding visibility amplitude as a function of $u - v$ distance (q) of both outflows can be modeled well by a R^{-1} fall off in intensity. The error bars in all plots represent the standard error of the mean.	94
5.11 CARMA maps of the inner S1 flow.	96
5.12 CO and SiO rotational emission lines from the CSE of Betelgeuse.	100
5.13 First e-MERLIN results for Betelgeuse.	104
5.14 Predicted position of Betelgeuse on 2012 July using the astrometric solutions of Harper <i>et al.</i> (2008)	106
5.16 Radio flux density variation of Betelgeuse between 1996 and 2004.	112
5.17 High resolution Q band images spanning six years.	113
6.1 Final VLA multi-wavelength radio maps of α Boo and α Tau.	118
6.4 1-D semi-empirical model atmospheres for α Boo and α Tau.	126
6.5 Power law fits to the spectra of α Boo and α Tau.	131
6.6 Variation of density and temperature coefficients for α Boo and α Tau.	132
6.7 Predicted effective radius as a function of wavelength for α Boo and α Tau.	134
6.8 Illustration of how the ionization fraction <i>freezes-in</i> in a stellar wind.	138
6.9 The temperature dependent recombination rates for hydrogen.	140
6.10 Hybrid Drake model which undergoes rapid wind cooling beyond $\sim 2.3 R_\star$	142

List of Tables

3.1	Physical Properties of α Ori.	30
3.2	Properties of the 5 CARMA configurations.	35
3.3	CARMA Observations of α Ori.	39
3.4	Basic Properties of α Boo and α Tau.	42
3.5	Improved Performance Parameters of the VLA.	46
3.6	Frequency coverage, primary beam, and spatial resolution of the VLA.	49
3.7	VLA Observations of α Boo and α Tau.	50
3.8	Multi-wavelength VLA + Pie Town Observations of Betelgeuse .	56
5.1	CARMA Continuum Fluxes at 230 GHz	97
5.2	Summary of the S1 and S2 Flow Properties.	102
6.1	VLA Flux Densities of α Boo and α Tau.	119
6.2	Compilation of Previous Radio Observations ($\nu \leq 250$ GHz).	122
6.3	Ionized mass loss rates for α Boo and α Tau.	144
A.1	List of Abbreviations	147

1

Introduction

Here is the introduction of the thesis, complete with a few references ([Prothero & Buell, 2007](#); [Sagan, 1997](#)). Section 1.1 contains Equation 1.1, Section 1.2 has Figure 1.1 and Section 2.3 has Table ???. Chapter 2 has pretty much nothing in it.

1.1 First Section

This section has an equation. Here it is:

$$L_{\odot} = 4\pi R_{\odot}^2 \sigma T_e^4 \quad (1.1)$$

which is a nice way of describing the luminosity.

1.2 Second Section

So this section has a figure in it¹. That figure depicts the basic structure of a red giant.

¹And also a footnote.

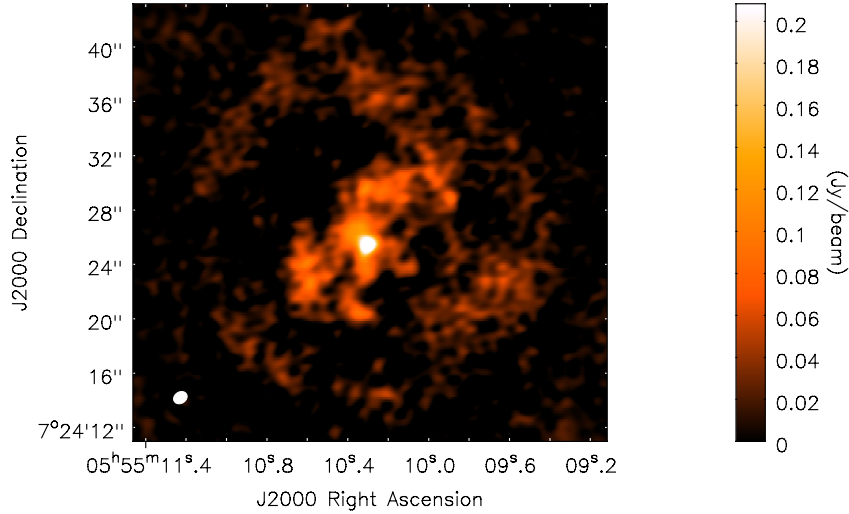


Figure 1.1: Red Giant and Asymptotic Giant Branch Stars. The left side of the figure shows the basic structure of a star on the giant branch of the HR diagram, while the right side shows a similar star after it has evolved to ascend the asymptotic giant branch. *Image Credit: Australian Telescope National Facility.*

1.3 Second Section

2

Introduction to Radio Interferometry

The poor spatial resolution provided by a single dish radio antenna can cause difficulties in obtaining accurate flux density measurements of radio astronomical sources, especially at long wavelengths. A single dish radio antenna is unable to distinguish against background radio emitters located in the primary beam, and therefore the observed flux density can contain emission from unrelated sources. This limitation can be overcome through interferometry. An interferometer acts as a spatial filter, and can discriminate against smooth backgrounds, while its higher resolution allows separation of the target from nearby confusing sources. This chapter describes the basic elements of a radio interferometer, what happens to the radio signal before it is sent for correlation, introduces the general concept of interferometry, and explains the process of synthesis imaging.

2.1 Radio Antenna Fundamentals

The quality and properties of the final radio image produced from a synthesis array are partially dependent on the properties of the individual antennas in the array. The most important such properties are discussed in the following sections and include aperture size, aperture efficiency, pointing accuracy and sidelobe

level. We define the radio antenna as the piece of equipment which converts the electromagnetic waves emitted from the observed source into an electric current ready to be input into to the first low noise amplifier where the signal is at the radio/sky frequency, ν_{RF} . What happens to the signal after this will be discussed in Section 2.2.

2.1.1 Properties of a Radio Antenna

The power gain of a transmitting antenna is a measure of the antenna's capability of converting power into radio waves in a specific direction. In radio astronomy, the receiving counterpart of transmitting power gain is the effective collecting area of an antenna, $A(\nu, \theta, \phi)$, where ν is frequency and θ and ϕ are direction coordinates. An ideal radio antenna would collect all incident radiation from a distant point source and convert it to electrical power. The total spectral power P_ν collected by it would then be a product of its geometric area and the incident spectral power per area, or flux density F_ν . By analogy then, the effective area of a real radio antenna is defined

$$A(\nu, \theta, \phi) = \frac{P_\nu}{F_\nu} = \frac{P}{I(\nu, \theta, \phi)\Delta\nu\Delta\Omega} \quad (2.1)$$

where $I(\nu, \theta, \phi)$ is the source brightness in units $\text{W m}^{-2} \text{ Hz}^{-1} \text{ sr}^{-1}$ that the antenna is pointing at and P is the power (in Watts) received by the antenna in bandwidth $\Delta\nu$ from element $\Delta\Omega$ of solid angle. The normalized antenna reception pattern \mathcal{A} , often referred to as the power pattern due to the duality between receiving and transmitting, is defined as

$$\mathcal{A}(\nu, \theta, \phi) = \frac{A(\nu, \theta, \phi)}{A_0} \quad (2.2)$$

where A_0 (m^2) is often referred to as the effective area of the antenna and is the response at the center of the main lobe of $A(\nu, \theta, \phi)$ [i.e., $A(\nu, 0, 0)$]. Then the beam solid angle, Ω_A , of the primary beam is

$$\Omega_A = \iint_{\text{all sky}} \mathcal{A}(\theta, \phi) d\Omega \quad (2.3)$$

and is a measure of the field of view of the antenna.

2.1 Radio Antenna Fundamentals

In the case of an isotropic antenna [i.e., $\mathcal{A}(\nu, \theta, \phi) = 1$], it can be shown that the product of the effective area and the primary beam solid angle is equal to the square of the wavelength ([Kraus et al., 1986](#))

$$A_0 \Omega_A = \lambda^2. \quad (2.4)$$

Ω_A has its maximum possible value of 4π if \mathcal{A} is everywhere equal to 1. This means that the primary antenna can see the whole sky with equal sensitivity. Even though a large field of view is usually desirable in radio astronomy, [Equation 2.4](#) ensures that for any given wavelength, when Ω_A is a maximum, the power received is a minimum and therefore the sensitivity is also at a minimum. To improve sensitivity, one could increase the collecting area of the antenna, but [Equation 2.4](#) then ensures that the field of view must decrease. Thus, when deciding on the primary antenna size in a synthesis array, there is always a trade-off between field of view and sensitivity.

In reality, an antenna cannot radiate isotropically and will radiate preferentially in one or more directions. A Fourier transform relationship exists between the complex voltage distribution of the field, $f(u, v)$, in the aperture of the antenna and the complex far-field voltage radiation pattern, $F(l, m)$, of the antenna ([Kraus et al., 1986](#))

$$F(l, m) = \iint_{\text{aperture}} f(u, v) e^{2\pi i(ul+vm)} dudv \quad (2.5)$$

and

$$f(u, v) = \int_{-\infty}^{\infty} \int_{-\infty}^{\infty} F(l, m) e^{-2\pi i(ul+vm)} dl dm \quad (2.6)$$

where

$$u = \sin\theta \cos\phi \quad \text{and} \quad v = \sin\theta \sin\phi \quad (2.7)$$

2.1 Radio Antenna Fundamentals

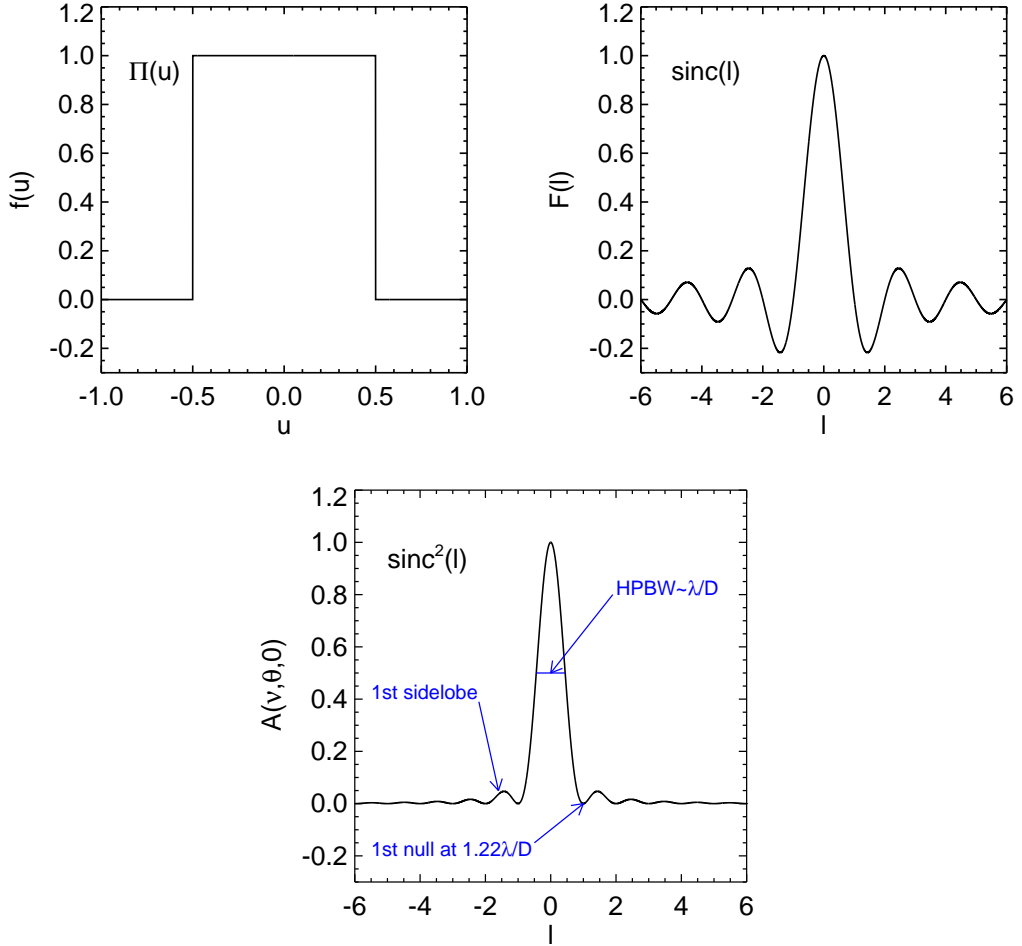


Figure 2.1: *Top Left:* A uniformly illuminated 1-D aperture $f(u)$. *Top Right:* The Fourier transform of $f(u)$ gives the antenna radiation pattern in the far-field, $F(l)$. *Bottom:* The power pattern of the antenna is given by $\mathcal{A} = |F(l)|^2$.

are the antenna coordinates and l and m are their Fourier counterparts. The from of $f(u, v)$ is determined by the manner in which the antenna feed illuminates the aperture. Therefore Equations 2.6 and 2.7 tell us that the radiation pattern in the far-field of a two-dimensional aperture is the two-dimensional Fourier trans-form of the aperture field illumination. For a uniformly illuminated 1-D aperture shown in Figure 2.1, the radiation pattern in the far-field is the *sinc* function. The radiation pattern in the far-field, $F(l, m)$, of such an antenna is related to the antenna power pattern by $\mathcal{A} = |F(l, m)|^2$. This power pattern is known as the Airy pattern if the antenna is uniformly illuminated and is also shown in Figure

[2.1](#). The central peak of this power pattern is called the main beam while the smaller secondary peaks are called sidelobes. The antenna is maximally sensitive to radiation from the direction of the peak of the beam, but is also slightly sensitive to radiation in the direction of the side lobes. The half-power beamwidth (HPBW) of the main beam θ_{HPBW} is a term commonly used in the literature to describe the field of view of an antenna/interferometer and satisfies

$$\theta_{\text{HPBW}} \propto \frac{\lambda}{D} \quad (2.8)$$

where D is the diameter of the antenna. The constant of proportionality varies slightly with the illumination taper and can be shown to be equal to ~ 0.89 for a uniformly illuminated 1-D aperture and ~ 1.2 for most single dish radio antennas. When the sky is scanned with a single dish antenna, then this HPBW is the resolution of the resulting map.

2.1.2 Antenna Structural Design

The design of the primary antenna element of an interferometric array will depend on the wavelength range to be observed. In general, dipoles are used for wavelengths longer than ~ 1 m, while reflector antennas are typically used at shorter wavelengths. The reason why the more simple and less expensive dipoles are not used at all wavelengths is given by Equation [2.4](#). For an isotropic antenna, this equation tells us that the effective area is just

$$A_0 = \frac{\lambda^2}{4\pi}. \quad (2.9)$$

Therefore, at short wavelengths a non-directional antenna such as a dipole, will have a small effective collecting area, giving it poor sensitivity for reception. Thus, dipoles can be used at long wavelengths as they have sufficient collecting area, but cannot be used at shorter wavelengths as an impractical amount would be needed to produce useful collecting areas. Since the interferometric arrays used in this thesis use reflector antennas, the rest of this section will focus on them.

2.1 Radio Antenna Fundamentals

Choice of Antenna Mount. Nearly all interferometric arrays consist of antennas which have altitude over azimuth (alt-azimuth) mounts. These antennas lie on a horizontal azimuth track on which the antenna can turn in azimuth, and on a horizontal elevation axle about which the antenna can change in zenith angle. The main advantage of such a design is simplicity and thus lower cost. Gravity always acts on the reflector in the same plan thus reducing the problem of keeping the reflector profile accurate during the duration an observation. However, sources close to the zenith can usually not be observed due to the high rate of azimuth rotation required. Also, the beam rotates with respect to the source for long duration observations which can affect the dynamic range of total intensity images of very large sources. The other type of mount occasionally used is the equatorial mount. Its polar axis is aligned parallel to the axis of rotation of the Earth and therefore only needs to rotate about the declination axis to observe a source. Its beam also doesn't have the beam rotation problem encountered by the alt-azimuth design and can track sources close to the zenith. Its major disadvantage and the reason for its scarce usage is the complexity of its design and resulting increased cost.

Choice of Antenna Optics. In Figure 2.2 we show the main optical systems which can be used to feed a large radio reflector. The prime focus system (e.g. used in the Giant Meter Radio Telescope) has the advantage that it can be used at long wavelengths where the use of secondary focus feeds (i.e., sub-reflectors) become impractical. However, access to and space for the feeds and receivers are limited, and sensitivity can be lost due to spillover noise from the ground. The other designs have the advantage of easier access to the feeds and receivers and less spillover noise from the ground. The off-axis Cassegrain (e.g. used in the Very Large Array) also has the advantage of increased frequency capability as many feeds can be located in a circle around the center of the reflector and a slight rotation of the sub-reflector is all that is required to change observing frequency. The receivers and feeds in the Naysmith geometry (e.g. used in the Combined Array for Research in Millimeter wave Astronomy) are located externally to the antenna structure. Finally, the offset Cassegrain (e.g. used in the Green Bank Telescope)

has no blockage and will have a circularly symmetric beam with low sidelobes although the increase complexity of its structure leads to increased costs.

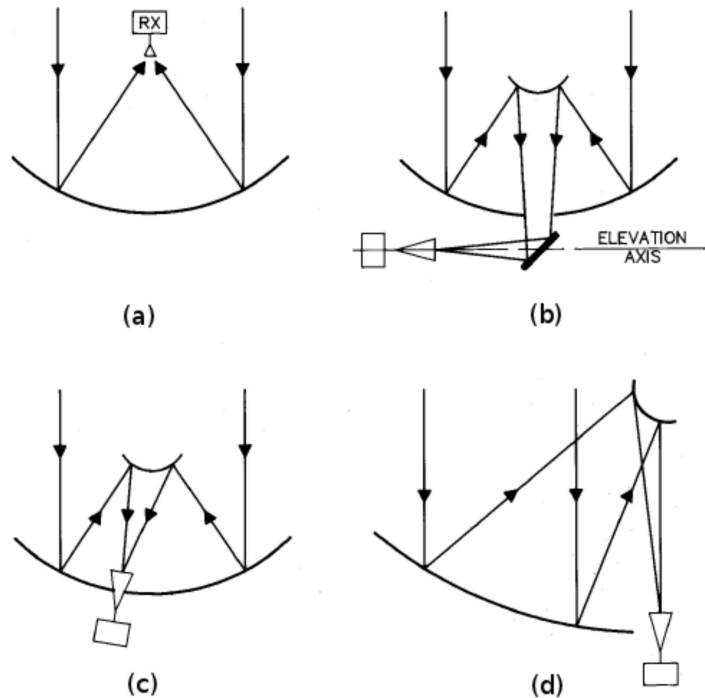


Figure 2.2: Common optical systems used for radio antennas. (a) Prime focus, (b) Naysmith, (c) Off-axis Cassegrain, (d) Offset Cassegrain [Figure adapted from Taylor *et al.* (1999)].

2.1.3 Antenna Performance Parameters

Aperture Efficiency. The geometric collecting area of a parabolic antenna A_{geo} ($= \pi D^2/4$) is related to the effective area (i.e., the collecting area when pointing directly at a source) via the dimensionless quantity η ($\eta < 1$) known as the aperture efficiency where

$$\eta = \frac{A_0}{A_{\text{geo}}}. \quad (2.10)$$

The aperture efficiency directly impacts on the sensitivity of the interferometric array and can be defined as the product of a number of different efficiency loss

2.1 Radio Antenna Fundamentals

factors,

$$\eta = \eta_{\text{sf}} \eta_{\text{bl}} \eta_s \eta_t \eta_{\text{misc}}. \quad (2.11)$$

The surface efficiency η_{sf} accounts for the aperture efficiency loss as a result of reflector profile inaccuracies. Such inaccuracies result in the electric field from various parts of the aperture not adding together in phase at the feed leading to a decrease in power. The aperture blockage efficiency η_{bl} accounts for the fact that the sub-reflector (or feed) and its support structure result in a reduction in the incident radiation on the antenna. The feed spillover efficiency η_{bl} is best understood if the antenna is considered in transmission rather than in reception mode, and is defined as the fraction of power radiated by the feed that is intercepted by the reflector for a prime focus system, or by the sub-reflector for a Cassegrain system. The illumination taper efficiency η_t accounts for the fact that the feed pattern does not illuminate the primary reflector uniformly but illuminates the outer part of the reflector at a lower level than the inner part. Finally, the miscellaneous efficiency losses such as reflector diffraction and feed position phase errors are accounted for in η_{misc} . As an example, the total aperture efficiency of the VLA antennas can vary between 0.65 and 0.2 at 6 and 0.7 cm, respectively.

Pointing Accuracy. The main lobe of an antenna's power pattern will usually not point exactly in the desired direction due to gravity deformations, wind pressure deformations, and mechanical inaccuracy. The angular offset, $\Delta\theta$, between the actual and desired pointing direction is called the pointing error. Usually, the desirable pointing error of an antenna at the highest operational frequency is $\Delta\theta < \theta_{\text{HPBW}}/20$ ([Taylor et al., 1999](#)). With this specification reached, an antenna pointing at a compact source will suffer negligible intensity variations as $\mathcal{A}(\theta_{\text{HPBW}}/20) > 0.99$. However, this pointing error of only $\theta_{\text{HPBW}}/20$ will still have a substantial effect on the accuracy of the outer image. For example, a source located at the half power point will suffer a substantial fractional intensity variation of $2\mathcal{A}(\theta_{\text{HPBW}}/2 + \theta_{\text{HPBW}}/20) \simeq 0.86$. The blind pointing of a VLA antenna is only about $10''$ and can be much worst in daytime, occasionally exceeding $1'$. This means that at Q-band (45 GHz; 0.7 cm), which is the highest observing frequency on the VLA, the pointing error is only at best $\theta_{\text{HPBW}}/6$, and

2.2 Receiving System for an Interferometer

at worst $> \theta_{\text{HPBW}}$, meaning that the target may lie outside of the primary beam. To overcome this problem of large antenna pointing errors at high frequencies with the VLA, a technique known as referenced pointing is implemented. This technique will be discussed further in Chapter 3.

2.2 Receiving System for an Interferometer

A radiometer (a radio receiver) is a device used to measure the timed-averaged power of the noise coming from a radio telescope within a well-defined radio frequency (RF) range, $\nu_{\text{RF}} - \Delta\nu_{\text{RF}}/2 \rightarrow \nu_{\text{RF}} + \Delta\nu_{\text{RF}}/2$, where $\Delta\nu_{\text{RF}}$ is the bandwidth of the receiver and $\Delta\nu_{\text{RF}} < \nu_{\text{RF}}$. The simplest radiometer carries out the following tasks:

1. Filters the broadband noise coming from the antenna via a bandpass filter.
2. Multiplies the filtered voltage by itself (i.e., its output voltage is proportional to its input power).
3. Smooths out the rapidly fluctuating output of the detected voltage via a signal averager or integrator.
4. Measures the smoothed voltage.

In practice, radiometers are never as simple as those described above and nearly all practical radiometers are *superheterodyne* receivers which incorporate a number of additional steps to produce an output voltage.

The RF front end is the term used to describe all the circuitry between the feed horn and the lower intermediate frequency (IF) stage. The first task of the front end is to amplify the received signal. The radio signals we want to measure are generally very weak and therefore need to be initially amplified by many orders of magnitude so they are above the noise level in succeeding stages. However, the front end electronic components produce random electrical noise which will also get amplified by this large amount. Therefore the role of the pre-amplifier is to amplify the incoming signal from the antenna while adding as little noise as possible. For this reason, the pre-amplifier is often called a low noise amplifier

2.2 Receiving System for an Interferometer

(LNA) and are often cooled to very low temperatures to minimize the amount of noise contributed by the components.

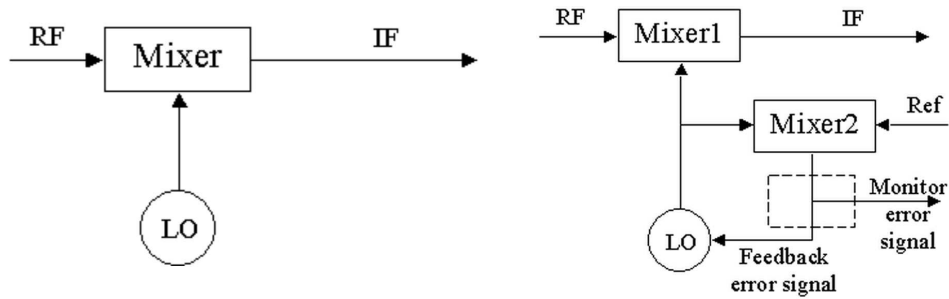


Figure 2.3: *Left:* Block diagram of a simple superheterodyne receiver. The amplified RF signal is mixed with a signal from a local oscillator to convert the signal to the more manageable intermediate frequency. *Right:* For interferometry, a phase lock loop is used to ensure all antennas are locked to the same frequency.

The amplified RF signal is then sent through a mixer which multiplies the RF signal by a sine wave of frequency ν_{LO} which is generated by a local oscillator (LO), as shown in Figure 2.3. The effect of this is that RF signal is changed to a lower frequency which can be easier handled by the IF amplifier and improves frequency selectivity. Mathematically, the mixer does the following

$$2\sin(2\pi\nu_{\text{LO}}t) \times \sin(2\pi\nu_{\text{RF}}t) = \cos[2\pi(\nu_{\text{LO}} - \nu_{\text{RF}})t] - \cos[2\pi(\nu_{\text{LO}} + \nu_{\text{RF}})t], \quad (2.12)$$

and produces two additional outputs, one at the input signal frequency minus the local oscillator frequency, and one at the sum of these frequencies. The lower of the two outputs called the intermediate frequency (IF) is taken by passing the mixer output through a filter in the IF amplifier. In interferometry, where the signals from two antennas are correlated, it is crucial that the receivers from both antennas are operating at the same frequency to control the phase difference between them. This is achieved by using a phase lock system, whose block diagram is laid out in Figure 2.3. In this system another mixer compares the LO to a reference frequency, which is the same for all antennas. Any existing phase error results in an error signal that is sent back to the oscillator so that its frequency can be adjusted to maintain exact frequency tuning. After this, the IF can finally be sent to the radiometer and recorded.

2.3 Fundamentals of Radio Interferometry

The angular resolution $\Delta\theta$ of a radio antenna is the minimum angular separation which two point sources can have in order to be recognized as separate objects. The *Rayleigh criterion* is the generally accepted criterion for defining the angular resolution of a filled circular aperture of diameter D , at the observational wavelength λ and is given as

$$\Delta\theta = 1.22 \frac{\lambda}{D} \text{ rad.} \quad (2.13)$$

The Rayleigh criterion states that two objects are resolved when the first null of the diffraction pattern of one object coincides with the maximum of the diffraction pattern of the other. An immediate consequence of Equation 2.13 is that at large wavelengths, the angular resolution becomes large unless the diameter of the aperture can be increased substantially. In order to achieve modest angular resolution at radio wavelengths with a single radio antenna then, the diameter becomes impractically large. For example, in order to achieve an angular resolution of $1''$ at 6 cm a 12 km aperture would be required. Radio interferometry is a technique used in radio astronomy to overcome this problem of poor angular resolution at long wavelengths.

2.3.1 Young's Slits

The basic principles of interferometry can be understood through Young's double-slit experiment. If coherent radiation emitted from a distant point source propagates through two slits, an illumination pattern composed of bright and dark fringes is observed. The phenomenon is a result of the constructive and destructive interference between the secondary waves produced by the slits. The fringe separation is λ/B , where B is the projected separation of the slits and is called the baseline. The fringe contrast which is historically known as the fringe visibility, V , can be written as

$$|V| = \frac{I_{\max} - I_{\min}}{I_{\max} + I_{\min}} \quad (2.14)$$

where I_{\max} and I_{\min} are the maximum and minimum intensity of the fringes, respectively. In other words, the fringe visibility is the fringe amplitude normalized

2.3 Fundamentals of Radio Interferometry

by the sum of the maximum and minimum intensity.

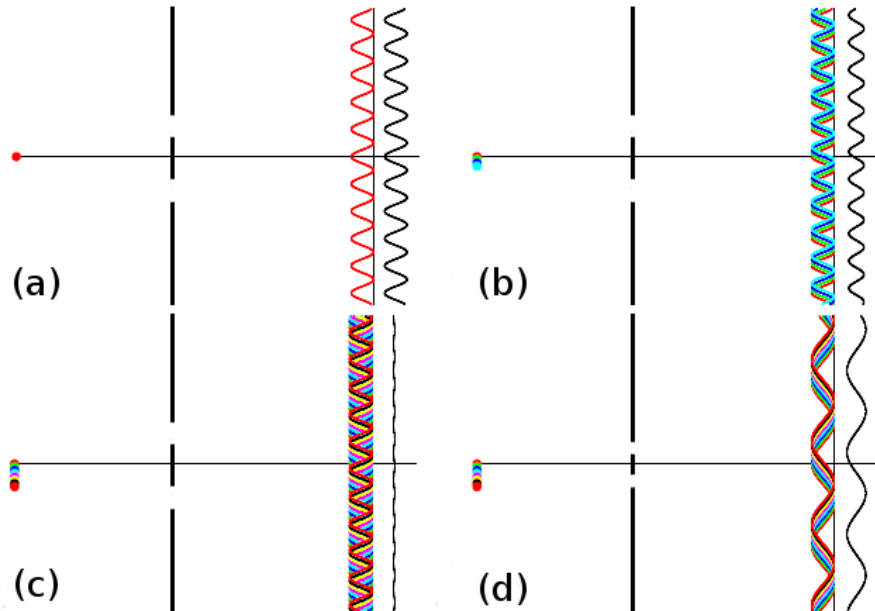


Figure 2.4: The resulting fringe pattern produced by Young's slits under various conditions. The source is shown on the left of the slits in each panel, while the separate fringe patterns (colors) along with the added fringe pattern (black) is shown on the right of the slits. (a) Point source at infinity, (Visibility = 1). Fringes are separated by an angular distance of λ/B . (b) An increase in source size results in a drop in visibility. (c) When the source size is equal to λ/B , the visibility is zero. (d) If the source size remains the same as in (c) and the slit spacing is reduced, then the fringes re-appear. Figure adapted from [Jackson \(2008\)](#).

In the simple case shown in Figure 2.4a, the angular size of the source is $\ll \lambda/B$ and the fringe visibility is 1. In interferometry, this equates to the situation in which the source size is smaller than the synthesized beam and only an upper limit of the source size can be obtained (i.e., the source is unresolved). In Figure 2.4b, the angular size of the source is now larger and can be thought of as a sequence of point sources each emitting radiation which is uncorrelated with emission from the others. An angular shift of ϕ , called phase, in the sources position results in a shift in the corresponding fringe pattern by the same angle the other way. The total interference intensity pattern is then just the sum of these individual patterns and the visibility is reduced. When the extension of the

2.3 Fundamentals of Radio Interferometry

source equals λ/B , the fringes disappear and give a constant illumination pattern. In this case the fringe visibility is zero and the source is completely resolved as shown in Figure 2.4c. Finally, if the source size is the same as that in Figure 2.4c but the slit separation is reduced, then the fringe separation λ/B will again increase as shown in Figure 2.4d. This is because the source now produces much less displacement of the fringe patterns as a fraction of the fringe separation. In interferometry, this result means that extended sources can only be probed with short baselines.

Visibility and phase are often expressed together as the complex visibility $V = |V|e^{i\phi}$, which completely defines a pattern of interference fringes. Young's double-slit experiment demonstrates a fundamental property of interferometry, namely that the contrast of fringes is a function of the geometry of the source. The results of the experiment are summarized in Figure 2.5. The top row shows that a large source (i.e., one whose intensity distribution extends out to a large angle on the sky) has a fringe visibility pattern which falls off quickly as projected baseline length increases. The bottom row shows that for compact sources the fringe visibility remains high out to large baselines. In the following section we will show that the relationship between the sky brightness distribution $I(\theta)$ and the visibility $V(B)$ is a Fourier transform.

2.3.2 The Two-element Interferometer

Interferometers with N antennas can be treated as $N(N - 1)/2$ independent interferometer pairs so it is worthwhile studying the simplest case of the two-element interferometer. A simplified block diagram of the components of such an interferometer is shown in Figure 2.6. The figure shows two identical antennas separated by a baseline vector \mathbf{b} pointing towards a distant radio source in a direction indicated by the unit vector \mathbf{s} . The plane waves from the distant radio source reach antenna 1 at a time τ_g later than they reach antenna 2. τ_g is called the geometric delay and is given by

$$\tau_g = \frac{\mathbf{b} \cdot \mathbf{s}}{c} = \frac{b \cos \theta}{c} \quad (2.15)$$

2.3 Fundamentals of Radio Interferometry

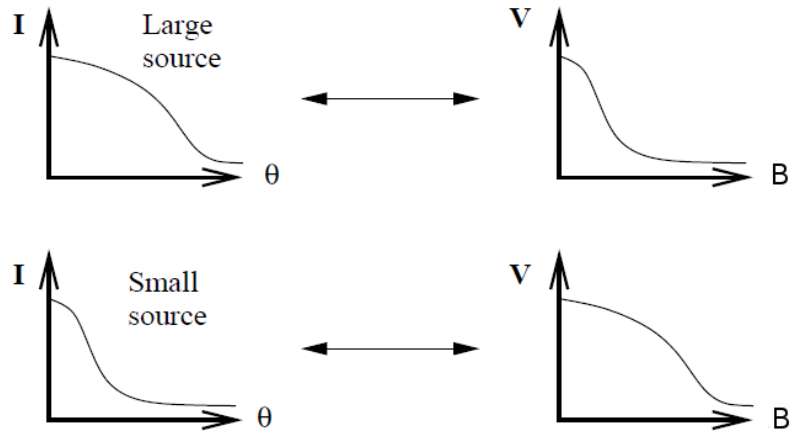


Figure 2.5: *Left column:* Intensity distribution as a function of sky angle for an extended source (top) and for a more compact source (bottom). *Right column:* The corresponding fringe visibility as a function of slit separation or baseline. Figure adapted from [Jackson \(2008\)](#).

where c is the speed of light. If we assume that the interferometer only responds to a very narrow band centered on frequency $\nu = \omega/2\pi$, then the output voltages of antennas 1 and 2 at time t can be written as

$$V_1(t) = V \cos[\omega(t - \tau_g)] \quad \text{and} \quad V_2(t) = V \cos(\omega t). \quad (2.16)$$

The signals are then passed through a correlator which first multiplies these voltages to give

$$V_1(t)V_2(t) = \frac{V^2}{2} [\cos(2\omega t - \omega\tau_g) + \cos(\omega\tau_g)] \quad (2.17)$$

and then averages them over a time interval Δt which is long enough such that $\Delta t \gg (2\omega)^{-1}$ to give the final output R :

$$R = \langle V_1(t)V_2(t) \rangle = \frac{V^2}{2} [\cos(\omega\tau_g)]. \quad (2.18)$$

As the Earth rotates, τ_g varies slowly with time and the resultant oscillations in the correlator output voltage represent the motion of the source. These

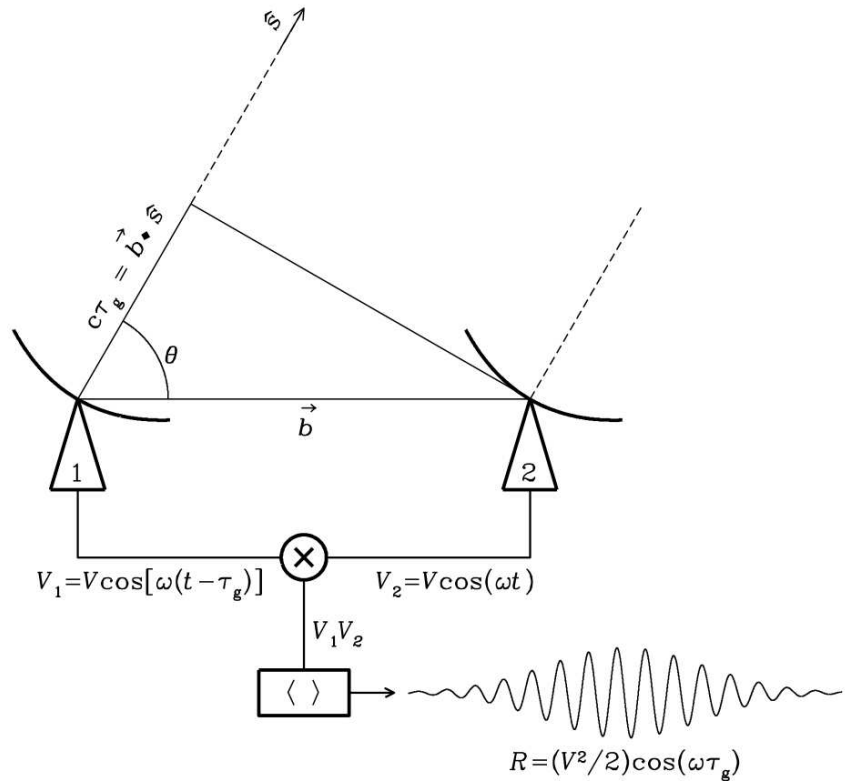


Figure 2.6: Simplified schematic diagram of a two-element interferometer. The correlator multiplies and averages the voltage outputs V_1 and V_2 of the two dishes and yields an output amplitude $V^2/2$ which is proportional to the point-source flux density F_ν . *Image Credit:* National Radio Astronomy Observatory.

sinusoidal oscillations are called fringes, and the fringe phase is

$$\phi = \omega\tau_g = \frac{\omega b \cos\theta}{c} \quad (2.19)$$

which changes with source direction as follows

$$\frac{d\phi}{d\theta} = \frac{\omega b \sin\theta}{c} = 2\pi \left(\frac{b \sin\theta}{\lambda} \right). \quad (2.20)$$

The fringe phase completes a full period (i.e., $\Delta\phi = 2\pi$) when an angular change $\Delta\theta = (\lambda/b \sin\theta)$ occurs. This tells us that the fringe phase is an extremely sensitive measure of source position if the projected baseline $b \sin\theta$ is many wavelengths long

2.3 Fundamentals of Radio Interferometry

and is the reason why interferometers can determine the positions of compact radio sources with exquisite accuracy.

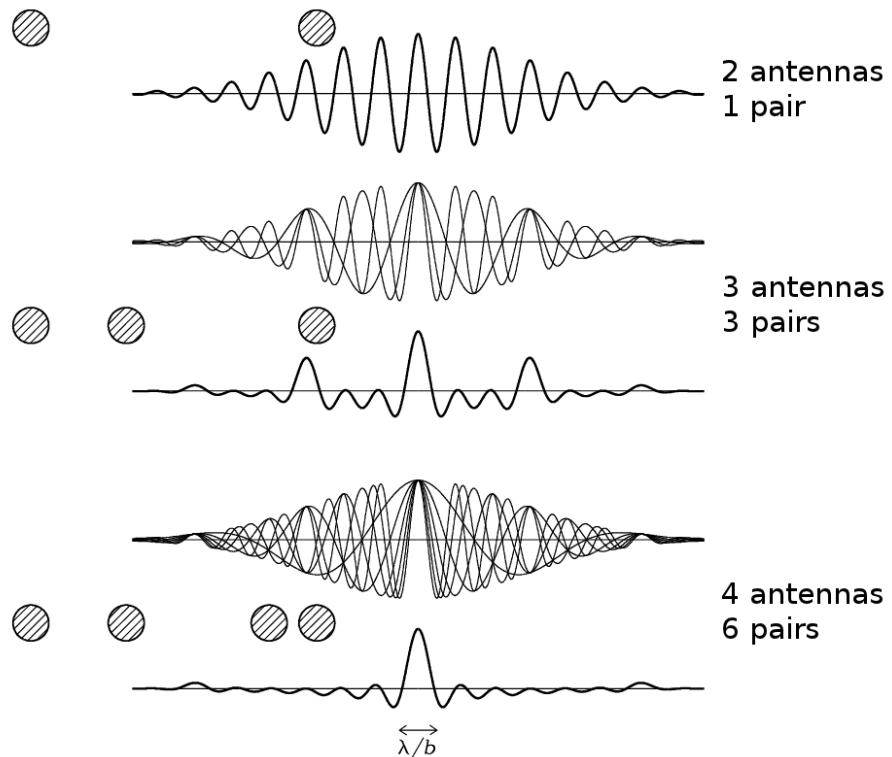


Figure 2.7: The instantaneous point source responses of an interferometer with two, three and four elements is indicated by the thick curves. The individual responses of the three pairs of two-element interferometers of the three-element interferometer and the six pairs of two-element interferometers of the four-element interferometer are plotted as thin curves. The main beam of the four-element interferometer is nearly Gaussian and has a width of $\sim \lambda/B$. This is known as the instantaneous synthesized beam of the interferometer. *Image Credit:* National Radio Astronomy Observatory.

If the antennas in an interferometric array are isotropic, then the point-source response of the interferometer would be a sinusoid spanning the entire sky and the interferometer would be only sensitive to one Fourier component of the sky brightness distribution having angular period $\lambda/b\sin\theta$. The response of a two-element interferometer R with non-isotropic antennas is this sinusoid multiplied by the product of the voltage patterns (i.e., defined as $f(u, v)$ in Section 2.1.1)

2.3 Fundamentals of Radio Interferometry

of the individual antennas. If the antennas are identical then this product is the power pattern of the individual antennas called the primary beam. The primary beam is usually a Gaussian that is much wider than the fringe period as $D \ll b\sin\theta$. The result is that an interferometer with directive antennas responds to a finite range of angular frequencies centered on $b\sin\theta/\lambda$. The instantaneous point source response of an interferometer is known as the synthesized beam and is the point source response obtained by averaging the outputs of all antenna pairs. The synthesized beam of an interferometer is an important quantity as it defines the maximum angular resolution of the instrument. The synthesized beams produced by an interferometer with a various number of antennas arranged in 1-D is shown in Figure 2.7. The figure shows that the synthesized beam can be improved by acquiring more Fourier components (i.e., baselines) and rapidly approaches a Gaussian as N increases. However, sidelobes are still significant and a broad negative “bowl” exists between the main beam and the first sidelobes due to the absence of short spacings.

2.3.3 Complex Visibility

The interferometer output can be expressed in terms of the radio brightness over the sky, which is sometimes also called specific intensity and has units $\text{W m}^{-2} \text{Hz}^{-1} \text{sr}^{-1}$. If the radio brightness of a spatially incoherent extended source in the direction of unit vector \mathbf{s} is $I(\mathbf{s})$, then the response of the two-element interferometer with “cosine” correlator output near frequency $\nu = \omega/2\pi$ is obtained by treating the extended source as the sum of independent point sources:

$$R_c = \int_{\Omega} \mathcal{A}(\mathbf{s}) I_{\nu}(\mathbf{s}) \cos\left(\frac{2\pi\mathbf{b}\cdot\mathbf{s}}{\lambda}\right) d\Omega \quad (2.21)$$

where \mathcal{A} is the normalized antenna reception pattern defined in Section 2.1.1 and we call $\mathcal{A}(\mathbf{s}) I_{\nu}(\mathbf{s})$ the modified brightness distribution. However, the cosine function in the “cosine” correlator output is only sensitive to the even part of the sky brightness distribution, which can be written as the sum of even and odd parts:

$$I(\mathbf{s}) = I_e(\mathbf{s}) + I_o(\mathbf{s}). \quad (2.22)$$

2.3 Fundamentals of Radio Interferometry

A “sine” correlator whose output is odd, is needed to detect the odd part of $I(\mathbf{s})$ and this is implemented by inserting a 90° phase delay into the signal of one of the antennas to give

$$R_s = \int_{\Omega} \mathcal{A}(\mathbf{s}) I_{\nu}(\mathbf{s}) \sin\left(\frac{2\pi\mathbf{b}\cdot\mathbf{s}}{\lambda}\right) d\Omega \quad (2.23)$$

It is convenient to write the cosines and sines as complex exponentials using the identity

$$e^{i\phi} = \cos(\phi) + i\sin(\phi) \quad (2.24)$$

and so the combination of “cosine” and “sine” correlators is called a “complex” correlator. The term *visibility* was first introduced by [Michelson \(1890\)](#) to describe the relative amplitudes of the optical fringes that he observed. The visibility is a complex quantity in radio astronomy and has dimensions of spectral power flux density ($\text{W m}^{-2} \text{ Hz}^{-1}$). The complex visibility is the response of a two-element interferometer with a complex correlator to an extended source with brightness distribution $I(\mathbf{s})$ and is defined as

$$V \equiv R_c - iR_s, \quad (2.25)$$

i.e.,

$$V_{\nu} = \int_{\Omega} \mathcal{A}(\mathbf{s}) I_{\nu}(\mathbf{s}) e^{-2\pi i \nu \mathbf{b} \cdot \mathbf{s} / c} d\Omega. \quad (2.26)$$

2.3.4 Coordinate Systems for Imaging

The baseline vector \mathbf{b} has coordinates (u, v, w) in three dimensions shown in Figure 2.8 where w points in the directions of interest, i.e., towards a direction s_0 that becomes the center of the synthesized image. u , v and w are measured in wavelengths (i.e., the components of \mathbf{b}/λ) and have directions towards the East, the North and the phase tracking center, respectively. An arbitrary unit vector \mathbf{s} has components (l, m, n) called direction cosines, where $n = \cos\theta =$

2.4 Synthesis Imaging

$(1 - l^2 - m^2)^{1/2}$. Using these coordinates the parameters in Equation 2.26 become

$$\begin{aligned}\frac{\nu \mathbf{b} \cdot \mathbf{s}}{c} &= ul + vm + wn, \\ d\Omega &= \frac{dl dm}{n} = \frac{dl dm}{\sqrt{1 - l^2 - m^2}}.\end{aligned}\quad (2.27)$$

Therefore Equation 2.26 can be defined in terms of the coordinate system laid out in Figure 2.8 as

$$V_\nu(u, v, w) = \int_{-\infty}^{\infty} \int_{-\infty}^{\infty} \mathcal{A}_\nu(l, m) I_\nu(l, m) e^{-2\pi i [ul + vm + w(\sqrt{1 - l^2 - m^2})]} \frac{dl dm}{\sqrt{1 - l^2 - m^2}} \quad (2.28)$$

which is not a three-dimensional Fourier transform. This equation becomes a two-dimensional Fourier transform if $w = 0$ which is a good approximation for small field imaging, i.e., when $|l|$ and $|m|$ are small. Thus, for an incoherent source in the far field observed with a small FOV and ignoring the response of the primary beam, the complex visibility is the 2-dimensional Fourier Transform of the sky brightness distribution

$$V_\nu(u, v) = \int_{-\infty}^{\infty} \int_{-\infty}^{\infty} I_\nu(l, m) e^{-2\pi i [ul + vm]} dl dm. \quad (2.29)$$

This Fourier transform relationship is the result of the van Cittert-Zernike theorem (van Cittert, 1934), upon which synthesis imaging is based. Since $I_\nu(l, m)$ is real, $V(u, v)$ is Hermitian [i.e., $V(-u, -v) = V^*(u, v)$] and so one measurement of the sky brightness gives two measurements of the complex visibility. Also, $V(u = 0, v = 0)$ is the integral of $I_\nu(l, m) dl dm$, which is the total flux. An interferometer cannot measure this value because it cannot take measurements at $(u = 0, v = 0)$.

2.4 Synthesis Imaging

A synthesis imaging telescope consists of a number radio antennas fixed on the ground and uses the Earth's rotation to vary the projected baseline coverage to increase the sampling of the $u - v$ plane. In this section we describe how Earth-

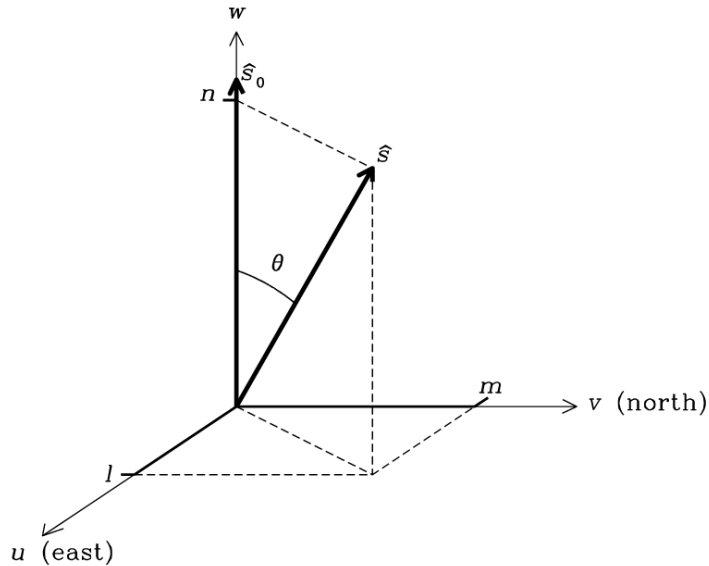


Figure 2.8: The (u, v, w) interferometric coordinate system. l , m , and n are the projections of the unit vector \mathbf{s} onto the u , v , and w axes, respectively.

rotation aperture synthesis is used to convert the complex visibilities outputted from the correlator to a final radio image of the observed sky.

2.4.1 Visibility Sampling

An example of how a radio interferometer samples the $u - v$ plane is shown in Figure 2.9. The left panel of this figure shows the overhead view of the VLA in its most extended configuration while the other two panels show the corresponding $u - v$ coverage for different periods of time. We define u and v as the east-west and north-south components of the projected baseline in wavelengths, respectively. As the Earth rotates, the projected baseline of every two-element pair in the array changes, thus sampling a different part of the $u - v$ plane. The middle panel shows that the total $u - v$ coverage of the VLA for a very short duration track (i.e., a snapshot) results in a ‘snowflake’ like pattern, with more dense coverage in the direction of the arms of the array due to the larger number of baselines. Most radio interferometers have their own unique array configuration layout and thus produce a different ‘snapshot’ $u - v$ coverage to that shown in Figure 2.9. Over many hours, the $u - v$ points trace out portions of ellipses and eventually

2.4 Synthesis Imaging

after a full Earth rotation the points can trace out full ellipses as shown in the right panel of Figure 2.9.

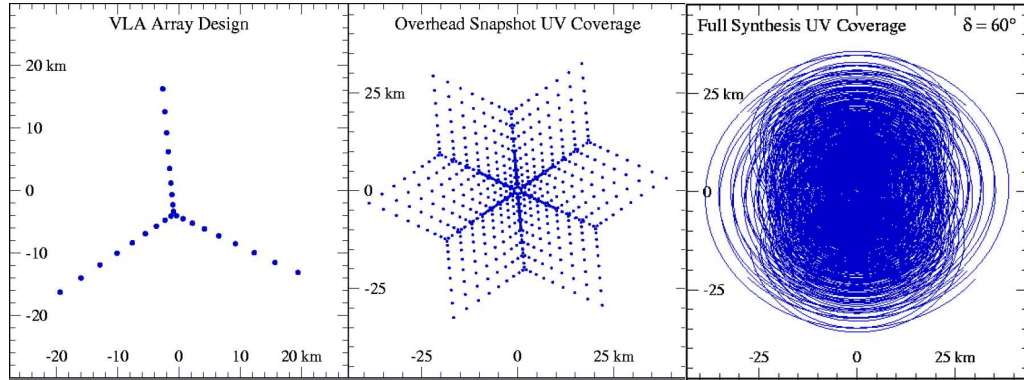


Figure 2.9: *Left:* The VLA in A-configuration is an example of an ‘Y’ shaped array design. *Middle:* The corresponding overhead snapshot $u - v$ coverage results in ‘snowflake’ pattern. *Right:* The corresponding $u - v$ coverage after a 12 hour track of a source at a declination of 60° . Note the more intense $u-v$ coverage in the direction of the three straight arms of the VLA for a snapshot track compared to the more uniform coverage over a longer duration track.

2.4.2 Imaging (Making a Dirty Map)

For every sky brightness distribution $I(l, m)$ there exists a continuous complex visibility function $V(u, v)$ that is its Fourier Transform. An array of antennas will only ever measure a certain set of values of this visibility function where the measured set is called the sampling function $S(u, v)$. This function is zero where no data have been taken. The actual data provided by the array is known as the sampled visibility function, $S(u, v)V(u, v)$. If we take the inverse Fourier transform of this function we get what is known as the *dirty image*:

$$I_\nu^D(l, m) = \int_{-\infty}^{\infty} \int_{-\infty}^{\infty} S(u, v)V_\nu(u, v)e^{2\pi i(ul+vm)} du dv. \quad (2.30)$$

where we have used $I_\nu(l, m)$ to denote the modified sky brightness $\mathcal{A}(l, m)I_\nu(l, m)$ as the correction for primary beam can be made at the final stage of data processing. Using the convolution theorem, the relationship between the dirty image

2.4 Synthesis Imaging

and the desired intensity distribution $I_\nu(u, v)$ is

$$I_\nu^D(u, v) = I_\nu(u, v) * B(l, m) \quad (2.31)$$

where the asterisk implies convolution and

$$B(l, m) = \int_{-\infty}^{\infty} \int_{-\infty}^{\infty} S(u, v) e^{2\pi i(u l + v m)} du dv \quad (2.32)$$

is the *point spread function* (PSF), or *synthesized beam*, or *dirty beam* (i.e., the inverse Fourier Transform of the sampling function S). Equation 2.31 says that the dirty image I^D is the true intensity distribution I , convolved with the synthesized beam B .

In Figure 2.10 we graphically summarize what has been said above. The panels in the upper row show the sky plane representations of the true image, the point spread function and the dirty image, while the panels in the lower row show the corresponding $u - v$ plane representations of the true visibility, the sampling function and the sampled visibility. In other words, Equation ?? is summarized graphically by the relationship between panels (a) and (d), Equation 2.32 by (b) and (e), and Equations 2.30 and 2.31 by (c) and (f).

Before the dirty image is computed, a weighting system is often applied to the visibilities to control the PSF. The two most common types of weighting system used are:

$$D_k = 1, \quad \text{natural weighting} \quad (2.33)$$

$$D_k = \frac{1}{N_s(k)}, \quad \text{uniform weighting} \quad (2.34)$$

where D_k is the weight to be applied to cell k , and $N_s(k)$ is the number of data samples falling into cell k of characteristic width s . Natural weighting treats all points alike and gives the best signal-to-noise ratio for detecting weak sources. However, it produces a beam with a broad low-level plateau which is undesirable when imaging sources with both large and small scale structure. Uniform gridding produces fewer artifacts in the final map, while keeping the full resolution of the array but gives poorer signal-to-noise than natural weighting.

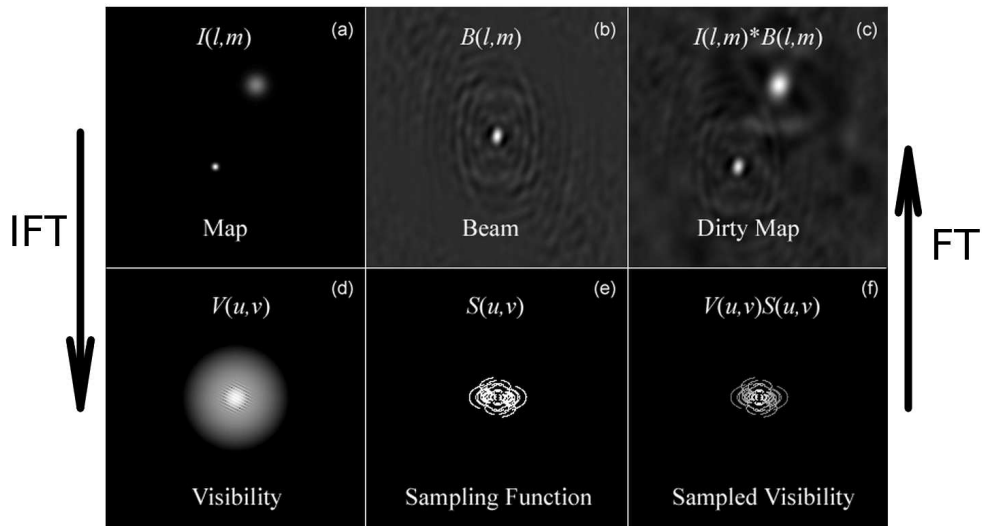


Figure 2.10: The Fourier transform pairs in synthesis imaging. (a) and (d): The true sky brightness and the visibility. (b) and (e): The dirty beam and the sampling function. (c) and (f): The dirty image and the sampled visibility. *Image Credit:* Prof. Dale E. Gary (New Jersey Institute of Technology).

The ‘direct Fourier transform’ method can then be used to solve for the dirty image Equation 2.30. However, if this method is evaluated at every point on a $N \times N$ grid, then the number of multiplications required goes as N^4 . The fast Fourier transform (FFT) algorithm can also be used to solve Equation 2.30 but requires interpolating the data onto a regular grid (i.e., a process known as *gridding*). This method is widely used for large data volumes as it requires only a few times $N^2 \log_2 N$ operations - not $\mathcal{O}(N^4)$, and the total time taken for gridding and FFT is usually a lot less than would take using the direct Fourier transform method.

2.4.3 Deconvolution (Making a CLEAN map)

The solution to the inverse Fourier transform given in Equation ?? is not unique, because the unmeasured points in the $u - v$ plane could have *any* value without violating the data constraints. The ‘principle solution’ is the one in which all missing $u - v$ measurements are set to zero and gives the dirty image discussed in the previous section. The dirty image is usually not a satisfactory representation

2.4 Synthesis Imaging

of the sky as one would expect a more continuous distribution of visibilities than that provided by the array. The goal of the deconvolution process is to find a method that determines more reasonable values for the unmeasured $u - v$ data. A priori information is the key to choosing ‘reasonable’ values. For example, we know that the Stokes parameter I must be positive and that radio sources generally do not have sidelobe patterns.

The CLEAN algorithm (Cornwell *et al.*, 1999; Högbom, 1974; Schwarz, 1978) is the most widely used technique in radio interferometry to deconvolve the true sky intensity from the dirty beam. It assumes that the radio source can be represented by a number of point sources in an otherwise empty field and a simple iterative process is used to find the strengths and positions of these point sources. The final CLEAN image (i.e., the deconvolved image) is the sum of these point sources convolved with a CLEAN beam, which is usually an elliptical Gaussian of the same size and shape as the inner part of the dirty beam. The CLEAN algorithm obeys the following steps:

1. Find the strength and position of the brightest point in the dirty image. It may also be desirable to search for peaks in specified areas of the image, called CLEAN windows or regions.
2. At this position in the dirty image, subtract the dirty beam multiplied by the peak strength and a damping factor g ($g \leq 1$, usually called the loop gain).
3. Record the position and the subtracted flux in a model.
4. Iterate between (1), (2), and (3) until the peak is below some user specified level. The remainder of the dirty image is now termed the residuals.
5. Convolve the accumulated point source model with an idealized CLEAN beam (usually an elliptical gaussian of the same size and shape as the central lobe of the dirty beam).
6. Add the residuals to the image in (5) to create the final CLEAN image.

2.4 Synthesis Imaging

A problem with CLEAN is that the final CLEANed image is somewhat dependent upon the various control parameters such as CLEAN boxes, the loop gain and the number of CLEAN subtractions. For example, using too high a gain tends to make extended, weak emission undetectable and noisy. This problem is unavoidable, and input values must be chosen on a case by case basis, depending on the source and data quality.

Another deconvolution algorithm used in radio synthesis imaging, albeit less often, is the Maximum Entropy Method (MEM) which operates by minimizing a smoothness function ('entropy') in an image. To conclude this section, we briefly discuss the practical differences between CLEAN and MEM:

1. CLEAN is nearly always faster than MEM, unless the image contains more than 1 million pixels.
2. MEM images are nearly always smoother than CLEAN images. This is because for CLEAN, what happens at one pixel is not coupled to what happens to its neighbours, while MEM couples pixels together by minimizing the spread in pixel values.
3. CLEAN sometimes makes extended emission look blotchy and may introduce artificial stripes into the image while MEM copes very poorly with point sources in extended emission. (Multi-scale CLEAN which is discussed in Chapter 3 is now becoming a popular choice in the radio community as an alternative deconvolution algorithm for images containing extended emission.)
4. For MEM, it is necessary to know the noise level quite well and it also helps to know the total flux density of the image. Knowledge of these are not required for CLEAN.

3

Targets, Instrumentation, and Observations

Two unique data sets were analyzed as part of this thesis. The first data set was a millimeter interferometric multi-configuration study of Betelgeuse’s circumstellar envelope at 1.3 mm. In the first half of this chapter we give a detailed introduction to Betelgeuse and discuss our current understanding of the star and its complex stellar atmosphere. We give a description of the millimeter interferometer CARMA, which we used to study its complex outflow region on a number of spatial scales and also describe our observations which spanned ~ 2.5 yr. The second data set consisted of a multi-wavelength centimeter study of two non-dusty red giants, Arcturus and Aldebaran. In the second half of this chapter we give a detailed introduction to both of these stars, including a description of their stellar properties, and their existing atmospheric models which we test against our data in Chapter 6. We give a short description of the VLA, which was the centimeter interferometer we used to study these stars, and finally describe our VLA observations.

3.1 Betelgeuse

Betelgeuse (α Ori: M2 Iab) is the second closet red supergiant [$D = 197$ pc (Harper *et al.*, 2008), barely losing that honor to Antares (α Sco: M1.5 Iab + B2.5 V)], and subtends the largest angular diameter of any star in the northern sky apart from the Sun. It is by far the best studied red supergiant and has been observed with various techniques from the radio to the UV. According to Harper *et al.* (2001), Betelgeuse probably was a runaway star from the star-formation region Ori OB1 (see, e.g., Hoogerwerf *et al.*, 2000), and was a spectral type O9 V star while on the main sequence where it had a mass of $\sim 20 M_{\odot}$. The evolutionary models of Meynet & Maeder (2003) suggest that its current mass is $18 M_{\odot}$ which corresponds to a surface gravity of 0.5 cm s^{-2} (i.e., $2 \times 10^{-5} g_{\odot}$). Its mass loss is characterized by a low velocity wind ($10 - 17 \text{ km s}^{-1}$) and a mass loss rate of $\sim 2 \times 10^{-6} M_{\odot} \text{ yr}^{-1}$ (Harper *et al.*, 2001). Like most late-type evolved stars, Betelgeuse's terminal wind velocity v_{∞} is smaller than the surface escape speed v_{esc} (values given in Table 3.1). This means that most of the energy and momentum are deposited into its flow within the first few stellar radii.

Betelgeuse has an extremely slow rotation period of about 17 yr (Uitenbroek *et al.*, 1998) which implies that it is probably experiencing very limited action of a solar-like dynamo. Its large radius ($950 R_{\odot}$) means that any possible remnant of a strong main sequence magnetic field is likely negligible due to a large dilution factor. In comparison to Sun like stars, its large radius also means that it has a large photospheric scale height ($H_{\star} \sim 0.01 R_{\star}$). The expected result of this is the presence of no more than a few giant and stable convection cells in the photosphere Schwarzschild (1975). Such features should enhance the detectability of the magnetic fields generated through a turbulent dynamo (Vögler & Schüssler, 2007). Bedecarrax *et al.* (2013) have recently monitored Betelgeuse over a three year period using high resolution spectropolarimetry, and find a longitudinal magnetic field strength which varies in values ranging from -3 G to $+2 \text{ G}$ with temporal changes in the field strength occurring over timescales as short as a few weeks.

Various studies have assumed that Betelgeuse has a warm ($T_e \sim 8000 \text{ K}$) extended atmosphere where ionized hydrogen dominates the electron density (e.g.,

3.1 Betelgeuse

Table 3.1: Physical Properties of α Ori.

Property	Value	Reference
HD Number	39801	...
Spectral Type	M2 Iab	Perryman <i>et al.</i> (1997)
App. Mag. (V)	0.45	Perryman <i>et al.</i> (1997)
RA (ICRS: ep=J2000)	05 ^h 55 ^m 10.305 ^s	van Leeuwen (2007)
dec (ICRS: ep=J2000)	+07°24'25.430"	van Leeuwen (2007)
Proper motion-RA (mas yr ⁻¹)	27.54	van Leeuwen (2007)
Proper motion-dec (mas yr ⁻¹)	11.30	van Leeuwen (2007)
π (mas)	5.07 ± 1.1	Harper <i>et al.</i> (2008)
d (pc)	197 ± 45	Harper <i>et al.</i> (2008)
Main Sequence M_* (M_\odot)	~ 20	Meynet & Maeder (2003)
Main Sequence Spectral Type	O9 V	Harper <i>et al.</i> (2008)
Current M_* (M_\odot)	~ 18	Meynet & Maeder (2003)
θ_{UD} (mas)	43.33 ± 0.04	Perrin <i>et al.</i> (2004)
R_* (R_\odot)	950	Harper <i>et al.</i> (2008)
T_{eff} (K)	3650	Levesque <i>et al.</i> (2005)
Log L_*/L_\odot	5.10 ± 0.22	Harper <i>et al.</i> (2008)
g_* (cm s ⁻²)	0.5	Meynet & Maeder (2003)
Heliocentric v_{rad} (km s ⁻¹)	20.7 ± 0.4	Harper <i>et al.</i> (2008)
v_{esc} (km s ⁻¹)	85	...
v_∞ (km s ⁻¹)	10, 17	Bernat <i>et al.</i> (1979)
T_{wind} (K)	< 4000	Lim <i>et al.</i> (1998)
\dot{M}_* (M_\odot yr ⁻¹)	3 × 10 ⁻⁶	Harper <i>et al.</i> (2001)
Photospheric H_* (R_*)	0.006	...
Fe/H	0.05 ± 0.14	Ramírez <i>et al.</i> (2000)
O/C	2.5	Lambert <i>et al.</i> (1984)
Rotational period (yr)	17	Uitenbroek <i>et al.</i> (1998)
B_* (G)	~ 1	Aurière <i>et al.</i> (2010)
Chromosphere Model	...	Harper <i>et al.</i> (2001)
Wind Model	...	Harper <i>et al.</i> (2001)
Outer CSE	...	Rodgers & Glassgold (1991)
$^{12}\text{C}/^{13}\text{C}$	6 ± 1	Harris & Lambert (1984)
$^{16}\text{O}/^{17}\text{O}$	525 ± 250	Harris & Lambert (1984)
$^{16}\text{O}/^{18}\text{O}$	700 ± 300	Harris & Lambert (1984)

3.1 Betelgeuse

Hartmann & Avrett, 1984; Newell & Hjellming, 1982). In fact, high resolution UV imaging with the HST partially resolved the *hot* chromosphere revealing $6000 - 8000$ K plasma extending to more than $2 R_\star$ (Gilliland & Dupree, 1996). However, Lim *et al.* (1998) spatially resolved Betelgeuse with the ‘old’ VLA at 5 different wavelengths and showed that the mean electron temperature is actually much cooler, i.e., $T_e = 2000 - 4000$ K and extends out to several stellar radii as shown in Figure 3.1. In fact, the mid-IR [Fe II] line studies of Harper *et al.* (2009) suggest that the temperature of the bulk of the plasma where the chromosphere has its largest filling factor is < 2500 K. Therefore, it appears that the hot chromospheric plasma has a small filling factor and co-exists with the much more abundant cool plasma within several stellar radii. Harper *et al.* (2001) constructed a detailed physical model for the inner atmosphere of Betelgeuse which reproduces the radio fluxes of Lim *et al.* (1998) and consists of electron temperature and gas densities as a function of radius.

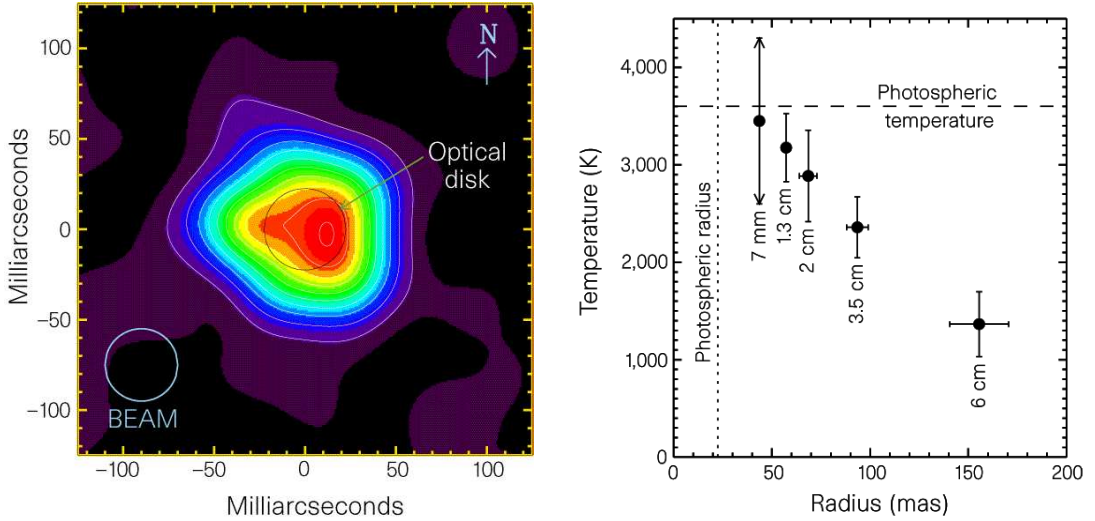


Figure 3.1: Left: The spatially resolved Q-band VLA image of Betelgeuse showing asymmetry in its atmosphere. Right: The multi-frequency spatially resolved radio maps revealed that the mean electron temperature profile was lower than expected (Lim *et al.*, 1998).

In comparison to other well studied red supergiants such as VY CMa, Betelgeuse has a modest mass loss rate, a low gas-to-dust mass ratio of $200 - 1700$, and low molecular abundances (Harper *et al.*, 2001). However, it is known to possess

3.1 Betelgeuse

a molecular shell known as a MOLsphere above its photosphere (Tsuji, 2000), and recently Verhoelst *et al.* (2006) and Perrin *et al.* (2007) have used the VLTI to establish some of its properties. They find the MOLsphere to have a geometrical thin extent ($\sim 0.1 R_\star$) with a temperature of ~ 1500 K at $\sim 1.4 R_\star$, and contains molecules such as H₂O, SiO, and Al₂O₃. Notably, they suggest that this molecular layer is where dust nucleation commences in support of a dust-driven wind scenario. However, the existence of Al₂O₃ is disputed by Kamiński *et al.* (2013) who argue that the absence of AlO (which is required to form Al₂O₃) in the photospheric spectrum is puzzling, and verification by independent studies is needed. In addition, Woitke (2006) finds that the average temperature between $1 - 3 R_\star$ is too high for silicates to form, and indeed recent studies suggest that silicates are not formed inside $\sim 23 R_\star$ (Skinner *et al.*, 1997; Tatebe *et al.*, 2007). For Betelgeuse, it therefore appears that radiation pressure on dust grains is not the main mechanism driving its mass loss (Harper, 2010).

In the past decade or so, a number of sensitive multi-wavelength studies of Betelgeuse have revealed a complex non-spherically symmetric circumstellar environment. Starting at its surface, a *H* band interferometric image was reconstructed using data from the Infrared Optical Telescope Array (IOTA) and showed a non-uniform brightness distribution across its surface (Haubois *et al.*, 2009). This data was modelled with 3-D hydrodynamical simulations by Chiavassa *et al.* (2010), resulting in the detection of a granulation pattern on the surface. They concluded that the surface contains a large (~ 30 mas) convective cell and a few small to medium scale (5 – 15 mas) convection-related surface structures. Adaptive optics images with the Very Large Telescope (VLT) at $1.04 - 2.17 \mu m$ revealed an irregular circumstellar envelope at a few R_\star with a few bright plumes extending out to $6 R_\star$ (Kervella *et al.*, 2009). These plumes have been attributed to the action of giant convection cells. Thermal infrared VLT ($\lambda = 8 - 20 \mu m$) imaging revealed oxygen-rich dust out to $100 R_\star$ (2.5'') (Kervella *et al.*, 2011), while Herschel images show a chaotic dust distribution far out in the circumstellar envelope, i.e., beyond $600 R_\star$ (i.e. $> 15''$) (Decin *et al.*, 2012). A conclusion that can be drawn from these studies is the constant presence of inhomogeneities in the circumstellar environment which probably play a role in

the formation of dust and molecular species. We defer a discussion on previous observations of CO in Betelgeuse's circumstellar environment until Chapter 5.

3.2 CARMA

The Combined Array for Research in Millimeter-wave Astronomy (CARMA) (Bock, 2006) is a millimeter interferometer located at Cedar Flat in eastern California at an elevation of 2200 m. The array consists of nine 6.1 m antennas and six 10.4 m antennas formerly from the Berkeley Illinois Maryland Association (BIMA) and the Owens Valley Radio Observatory (OVRO) arrays respectively, and operates at 85-115 GHz (3 mm) and 215-270 GHz (1.3 mm). Eight additional 3.5 m antennas known as the Sunyaev-Zel'dovich Array (SZA) can also be added to CARMA for continuum observations at 26-36 GHz (1 cm) and 85-115 GHz (3 mm). The different sizes of the CARMA antennas makes it a heterogeneous array with a total collecting area equivalent to a single 32 m dish antenna. Despite some technical difficulties associated with image restoration for a heterogeneous array (e.g., the 15-element CARMA array has 3 different primary beams), there are a number of advantages. Such an array samples shorter $u-v$ spacings directly when the smallest antennas are in a compact configuration. This results in more of the total flux density being recovered and also recovers more of the large scale structure and is the reason why the smaller diameter antennas are usually left in the center of the array as shown in Figure 3.2. In fact, it has been shown that a heterogeneous CARMA array produces better image fidelity than a homogeneous array with the same number of antennas and collecting area (Wright, 1999).

CARMA is a reconfigurable array and has 5 different configurations providing baselines ranging between 8 m and 2 km; A configuration being the most extended and E configuration being the most compact. Figure 3.3 gives an overview of how these configurations are achieved at Cedar Flat. As the resolution is set by the array configuration and frequency of observation, we list the various achievable resolutions (i.e. the HPBW of the synthesized beam) for each of CARMA's 5 configurations at 230 GHz, in Table 3.2. We also list the largest angular scale that can be imaged at 230 GHz as this is an important property of each configuration, especially when imaging extended emission (i.e., Chapter 5). This limitation

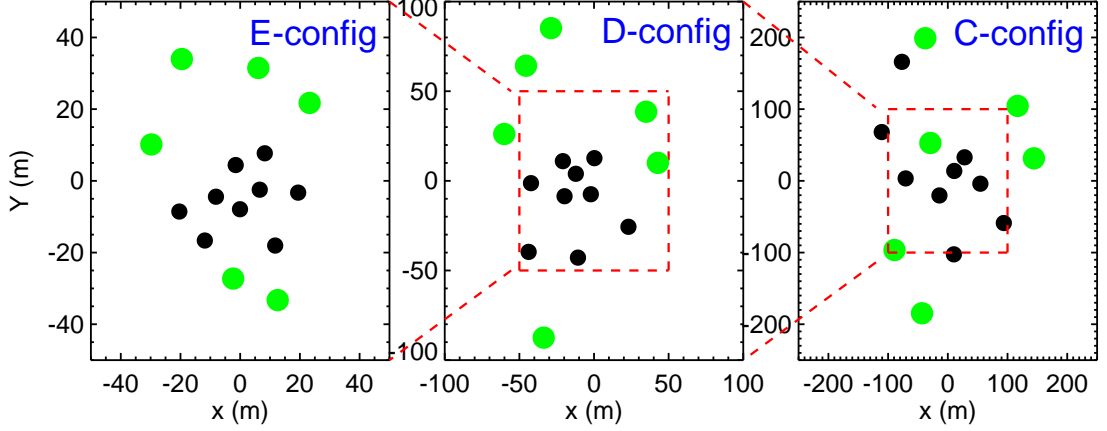


Figure 3.2: The three CARMA array configurations used to study the CSE of Betelgeuse. The most compact CARMA configuration is E configuration (*left*) which has $B_{\max} = 66$ m, D configuration (*middle*) has $B_{\max} = 148$ m, while C configuration (*right*) has $B_{\min} = 370$ m and was the most extended configuration used in our study. The 10.4 m antennas are marked green while the 6.1 m antennas are marked black.

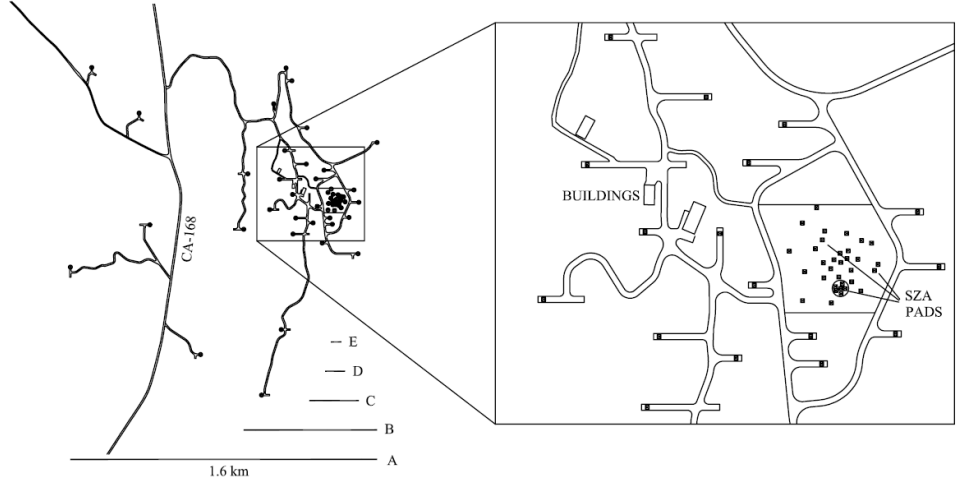


Figure 3.3: The layout of antenna pads for CARMA and a visual of the extent of each configuration (Bock, 2006).

is unique to interferometers and means that structures on angular scales significantly larger than the fringe spacing formed by the shortest baseline are not measured. This information can only be obtained by observing in a smaller array configuration or by using the mosaicing method. The half-power beamwidth of

3.2 CARMA

the primary beam (i.e., the FOV) at a frequency ν is $50'' \times (230 \text{ GHz}/\nu)$ for the 6.1 m antennas, while is $30'' \times (230 \text{ GHz}/\nu)$ for the 10.4 m antennas.

Table 3.2: Properties of the 5 CARMA configurations.

	A	B	C	D	E
B_{\max} (m)	1883	946	370	148	66
B_{\min} (m)	150	82	26	11	8.5
Synthesized Beam θ_{HPBW} ('')	0.15	0.38	0.86	2.1	4.4
Largest Angular Scale θ_{LAS} ('')	1.1	2.0	6.2	14.6	18.9
6.1 m Primary Beam θ_{HPBW} ('')			$50'' \times (230 \text{ GHz}/\nu)$		
10.4 m Primary Beam θ_{HPBW} ('')			$30'' \times (230 \text{ GHz}/\nu)$		

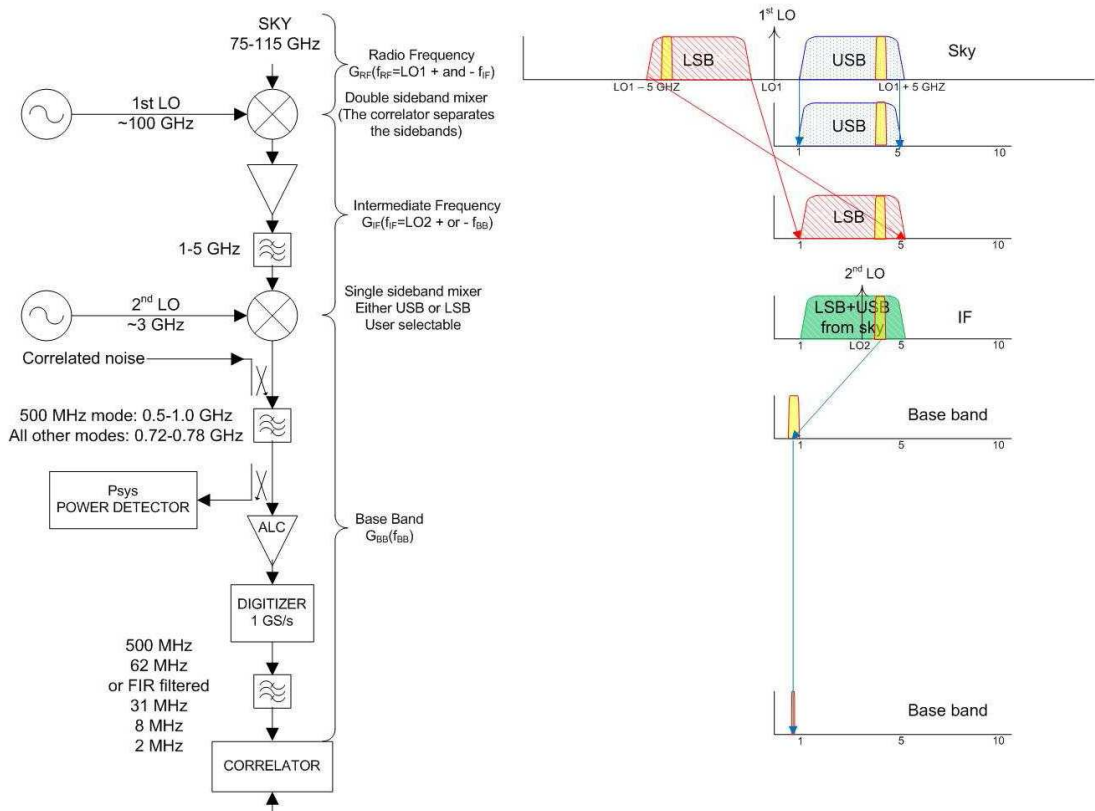


Figure 3.4: Major components in the signal path through the CARMA system (Wei *et al.*, 2008).

The 10.4 meter and 6.1 meter antennas are equipped with circular polarization SIS receivers for the 1mm band, and single-polarization SIS receivers for the 3 mm band. The tuning ranges of the 1mm and 3mm receivers are 215-265 GHz and 85-116 GHz, respectively. Figure 3.4 shows the main components in the signal path through the CARMA system. Upon passing through the atmosphere and antenna Naysmith optics, the RF signal is sent through the cooled low noise double sideband mixer where it is combined with a local oscillator $\nu_{\text{LO}1}$ to produce the intermediate frequency ν_{IF} . The $\nu_{\text{LO}1}$ can be either below or above the ν_{RF} ; known as the upper and lower sidebands, respectively, giving:

$$\nu_{\text{IF}} = \nu_{\text{RF}} \pm \nu_{\text{LO}1}. \quad (3.1)$$

The radio frequency gain $G_{\text{RF}}(\nu_{\text{RF}})$, results from components before this mixer (i.e., the sky and antenna optics) and depends only on the sky frequency. The IF signals then pass through amplifiers and attenuators in the antenna, are converted to light and sent along fibers to the control building, where they are then converted back to microwaves, amplified and attenuated some more before reaching the second mixer. Even though many of the components in the IF path are common across all bands, the IF gain $G_{\text{IF}}(\nu_{\text{IF}})$, will vary per band as there are components in the second mixer which are separate for each band. The second mixer is a single sideband mixer and its baseband output contains either the upper sideband signals above the second LO or the lower sideband:

$$\nu_{\text{BB}} = \nu_{\text{IF}} \pm \nu_{\text{LO}2}. \quad (3.2)$$

A noise signal is passed through all of the remaining correlator configuration dependent components and the selectable analog filters are measured by this noise source. The power measurement P_{sys} , used for the system noise temperature measurement is calculated after the analog filters and before the automatic level control (ALC) amplifier which ensures that the digitizers operate at a constant level.

3.3 CARMA Observations of Betelgeuse

We used CARMA to obtain on-source profiles of the rotational transition line $^{12}\text{C}^{16}\text{O}(J = 2\text{-}1)$ which has a rest frequency of 230.538 GHz (1.3 mm). Table 3.3 summarizes our complete set of multi-configuration observations which span the period 2007 May - 2009 November. Our first set of observations took place in June 2007 when CARMA was in D configuration providing a spatial resolution of 2.1''. A total of 5 D configuration tracks were carried out and one which took place in 18 May 2007 was excluded from the final analysis due to large levels of noise in the final map as a result of poor weather conditions. We obtained five E configuration (the most compact configuration available) tracks during the summer of 2009 which provided a relatively low spatial resolution of 4.4'' but gave the best sensitivity to extended emission. However, only one track was found to be of sufficient quality to be included in the final analysis. Our C configuration observations which provide sub-arcsecond resolution at 230 GHz (i.e., 0.9'') were due to take place in December 2008 but were postponed for a full year due to very poor weather conditions at Cedar Flat. We obtained a total of 4 usable tracks in C configuration amounting to 8.4 hours on source. The FOV of the individual 10.4 m antennas is $\sim 32''$ at the observed frequency.

CARMA can now take measurements in eight bands yielding a maximum bandwidth of 4 GHz per sideband. However, back when our data was obtained, the CARMA correlator took measurements in just three separate bands, each having an upper and lower sideband. One band was set to the low resolution 468 MHz bandwidth mode (15 channels of 31.25 MHz each) to observe continuum emission and was centered on the line. The other two bands were configured with 62 MHz and 31 MHz bandwidth across 63 channels (with a resolution of 1.3 km s^{-1} and 0.65 km s^{-1} respectively) and were also centered on the line. The line was measured in the upper sideband in the C and E array and in the lower sideband in the D array.

Bandpass and phase calibration were performed using 3C120 and 0530+135. 0532+075 was used as a secondary phase calibrator to determine the quality of the phase transfer from the primary phase calibrator. The observing sequence was to integrate on the primary phase calibrator for ~ 2.5 minutes, the target

3.3 CARMA Observations of Betelgeuse

for \sim 18 minutes, and the secondary phase calibrator for \sim 2.5 minutes. The cycle was repeated for each track which lasted between 1.5 hours and 5 hours. Absolute flux calibration was carried out with 0530+135 and 3C120 using the continuously updated CARMA flux catalog to obtain their flux values at each observation.

Table 3.3: CARMA Observations of α Ori between June 2007 and November 2009.

Date	Configuration	Time on Source (hr)	Flux Calibrator	Phase Calibrator	Image Cube Dynamic Range
2007 Jun 18	D	0.9	0530+135	0530+135, 0532+075	22.8
2007 Jun 21	D	3.0	0530+135	0530+135, 0532+075	22.7
2007 Jun 24	D	2.1	0530+135	0530+135, 0532+075	26.1
2007 Jun 25	D	2.4	0530+135	0530+135, 0532+075	30.2
2009 Jul 07	E	3.2	3C120	3C120, 0532+075	30.1
2009 Nov 05	C	1.2	3C120	3C120, 0532+075	17.3
2009 Nov 09	C	3.0	3C120	3C120, 0532+075	27.2
2009 Nov 15	C	1.0	3C120	3C120, 0532+075	17.8
2009 Nov 16	C	3.2	3C120	3C120, 0532+075	32.0
All	C	8.4	43.8
All	D	8.4	31.9
All	Multi-configuration	20.0	52.3

3.4 Arcturus and Aldebaran

Currently the most detailed spatial information about the atmospheres of K and early M spectral type evolved stars is obtained from eclipsing binaries such as the ζ Aurigae and symbiotic systems (e.g., Wright 1970; Baade *et al.* 1996; Eaton 2008; Crowley *et al.* 2008). Even though these systems offer us the best opportunity to obtain information on the dynamics and thermodynamics at various heights in the evolved star's atmosphere, the very nature of the binary system may introduce further complexities. For example, the orbital separation is often within the wind acceleration region and one could expect flow perturbations to be present (e.g., Chapman 1981). Using the old VLA, Harper *et al.* (2005) find a slow wind acceleration for ζ Aurigae and confirm that its velocity structure is not typical of single stars with similar spectral types, such as λ Velorum (Carpenter *et al.*, 1999). In order to avoid the assumed additional complexities of a companion, we have selected two single luminosity class III red giants: Arcturus (α Boo: K2 III) and Aldebaran (α Tau: K5 III). These nearby red giants have been extensively studied at other wavelengths and their stellar parameters, which are summarized in Table 3.4, are accurately known. These stars are predicted to be point sources at all frequencies between 1 and 50 GHz in all VLA configurations so our radio observations measure their total flux density, F_ν . For example, our observations of these stars which are discussed in Section 3.6, were taken in B configuration providing a maximum spatial resolution of $\sim 0.14''$ at 45 GHz which is equivalent to $\sim 7 R_*$ for both stars. The radio emission from these stars at 45 GHz is expected to be chromospheric in origin (Harper *et al.*, 2013), and as the spatial extent of red giant chromospheres is expected to be less than $1.5 R_*$ (Berio *et al.*, 2011), then we can be assured that these targets will be unresolved even at the highest VLA frequencies. Moreover, both stars have existing semi-empirical 1-D chromospheric and wind models which we can directly compare our data against.

Arcturus (α Boo: K2 III)

Arcturus (α Boo: K2 III) is the nearest ($d = 11.3$ pc) and brightest ($V = -0.04$ mag) noncoronal red giant and is probably the best example of a red giant whose

atmosphere can be studied in detail with the VLA. It is the leader of a group of stars that share a similar V space velocity (the component of stellar motion relative to the LSR in the direction of rotation), age (≥ 10 Gyr), and metallicity ($[\text{Fe}/\text{H}] \sim -0.5$), known as the Arcturus moving group (Eggen, 1971). The group has traditionally been regarded as the remains of a dissolved open cluster (e.g., Eggen, 1971, 1996) but it has also been suggested to be the debris of a metal-poor accreted satellite some billions of years ago (Navarro *et al.*, 2004). Recent analysis of chemical abundances are consistent with the former hypothesis but do not entirely rule out a merger one (Williams *et al.*, 2009). Arcturus is ascending the red giant branch and being a single star, its mass is relatively poorly constrained but is similar to that of the Sun ($0.8 \pm 0.2 M_{\odot}$ by Kallinger *et al.*, 2010). During the last decade there has been a large dispersion in the reported values of Arcturus' effective temperature (a nice graph summarizing this is presented in Griffin, 1996) but nowadays it is generally accepted to be about 4300 K (di Benedetto, 1993). A number of interferometric measurements of the limb-darkened angular diameter of the star are available in the literature with most values agreeing within their uncertainties. The weighted mean value of these values is $\theta_{\text{LD}} = 21.06 \pm 0.17$ mas (Ramírez & Allende Prieto, 2011) giving the star a radius of $25.4 \pm 0.3 R_{\odot}$.

Arcturus is an important target for high spatial and spectral resolution calibration. Thus when the Hipparcos catalog flagged Arcturus as a two component object (Perryman *et al.*, 1997) it caused quite a stir in the community. However, the uncertainties in the Hipparcos data (Soderhjelm & Mignard, 1998) along with a non-detection in adaptive optics observations (Turner *et al.*, 1999) and sensitive interferometric techniques (Lacour *et al.*, 2008) suggest that Arcturus is single and can still be used as a calibrator. Nevertheless, Lacour *et al.* (2008) still do not rule out the possibility of a planetary companion of a few Jovian masses as suggested by its long period radial velocity variations of ~ 233 days (Brown, 2007; Hatzes & Cochran, 1993). Variations in the order of a few days period are also seen in its radial velocity (Merline, 1999) as well as photometry (Retter *et al.*, 2003). The photometric amplitude oscillations can vary by up to a percent and may be the manifestation of convection such as large-scale granulation, or solar-like oscillations (Dziembowski *et al.*, 2001).

3.4 Arcturus and Aldebaran

The first detailed model of the atmosphere of Arcturus was the 1-D time-independent semi-empirical model of Ayres & Linsky (1975) which was based on diagnostics observable from the ground (i.e. Ca II h and k and the Ca II IR triplet) and early satellite observations of the Mg II h and k emission lines from *Copernicus*. They were able to calculate temperature and mass column densities

Table 3.4: Basic Properties of α Boo and α Tau.

Property	α Boo	α Tau	Reference
HD Number	124897	29139	...
Spectral Type	K2 III	K5 III	1
App. Mag. (V)	-0.5	0.86v	1
RA (ICRS: ep=J2000)	14 ^h 15 ^m 39.672 ^s	04 ^h 35 ^m 55.239 ^s	2
dec (ICRS: ep=J2000)	+19°10'56.673"	+16°30'33.489"	2
Proper motion-RA (mas yr ⁻¹)	-1093.39 ± 0.44	63.45 ± 0.84	2
Proper motion-dec (mas yr ⁻¹)	-2000.06 ± 0.39	-188.94 ± 0.65	2
π (mas)	88.83 ± 0.54	48.94 ± 0.77	2
d (pc)	11.3 ± 0.1	20.4 ± 0.3	2
M_\star (M_\odot)	0.8 ± 0.2	1.3 ± 0.3	3, 4
θ_{LD} (mas)	21.06 ± 0.17	20.58 ± 0.03	5, 6
R_\star (R_\odot)	25.4 ± 0.3	44.2 ± 0.9	...
T_{eff} (K)	4294 ± 30	3970 ± 49	7
L_\star/L_\odot	198 ± 3	442 ± 11	...
g_\star (cm s ⁻²)	34	18	...
Heliocentric v_{rad} (km s ⁻¹)	+5.19 ± 0.04	+54.11 ± 0.04	8
v_{esc} (km s ⁻¹)	110	106	...
v_∞ (km s ⁻¹)	35 – 40	30	9, 10
T_{wind} (K)	~10,000	~10,000	9, 10
\dot{M}_\star (M_\odot yr ⁻¹)	2×10^{-10}	1.6×10^{-11}	9, 10
Photospheric H_\star (R_\star)	0.005	0.005	...
Fe/H	-0.5 ± 0.2	-0.15 ± 0.2	11
Rotational period (yr)	2.0 ± 0.2	1.8	12, 13
B_\star (G)	0.65 ± 0.26	unknown	14
Chromosphere Model	Drake (1985)	McMurtry (1999)	...
Wind Model	Drake (1985)	Robinson <i>et al.</i> (1998)	...

References.-(1) Perryman *et al.* (1997); (2) van Leeuwen (2007); (3) Kallinger *et al.* (2010); (4) Lebzelter *et al.* (2012) (5) Ramírez & Allende Prieto (2011) (6) Richichi & Roccatagliata (2005); (7) di Benedetto (1993); (8) Massarotti *et al.* (2008); (9) Drake (1985); (10) Robinson *et al.* (1998); (11) Decin *et al.* (2003); (12) Gray *et al.* (2006); (13) Hatzes & Cochran (1993); (14) Sennhauser & Berdyugina (2011)

for the upper photosphere and chromosphere and estimated the temperature at the top of the chromosphere to be ~ 8000 K. They also found that $T_{\min}/T_{\text{eff}} \sim 0.77$ which is similar to that of the Sun. The important IUE cool star survey by Linsky & Haisch (1979) placed Arcturus on the right of the dividing line. This meant that its atmosphere showed lines formed at temperatures no hotter than $10,000 - 20,000$ K, suggestive of a chromosphere only. However, they also developed a hot coronal wind model for the star and found it to be consistent with the absence of transition region material in the IUE data; that is, the high temperature transition region emission line fluxes could be below the detection limit. Drake (1985) developed a semi-empirical chromosphere and wind model for Arcturus based on the Mg II k emission line from the IUE and showed that its wind is very extended and estimated a mass loss rate of $2 \times 10^{-10} M_{\odot} \text{ yr}^{-1}$.

Evidence began to emerge that Arcturus actually falls into the class of late type stars known as hybrids when deeply exposed IUE echelle spectrograms showed the weak presence of the Si III] $\lambda 1892.0$ feature, indicating the existence of a small amount of plasma at temperatures as hot as 6×10^4 K. Its hybrid status was confirmed when C IV and N V (indicative of temperatures $\sim 1 \times 10^5$ K) were detected with the HST STIS, and also with a tentative 3σ X-ray detection made with the Chandra X-Ray Observatory (Ayres *et al.*, 2003). It appears that Arcturus has been able to sustain a modest level of magnetic activity. In fact, three possible values for the mean longitudinal magnetic field (albeit weak: $B = 0.65 \pm 0.26$, 0.43 ± 0.16 , and -0.23 ± 0.20 G) have reportedly been detected on the star via the Zeeman effect (Sennhauser & Berdyugina, 2011), and a magnetic cycle with a period of ≥ 14 years has also been reported (Brown *et al.*, 2008).

Arcturus appears to have a thermally bifurcated chromosphere which consists of material within the chromosphere that is cooler than the surrounding chromospheric temperature minimum [i.e a CO-mosphere, Wiedemann *et al.* (1994)]. This suggests that the assumption in current semi-empirical chromospheric models of the *hot* UV emitting material having a filling factor of unity may not be correct. The more recent spectroscopic analysis of CO and H₂O transitions have confirmed the existence of cooler molecular *clouds* in the outer atmosphere of Arcturus (Ryde *et al.*, 2002; Tsuji, 2009).

Aldebaran (α Tau: K5 III)

At a distance of 20.4 pc, Aldebaran (α Tau: K5 III) is a nearby red giant and is one of the most easily recognizable stars from the northern and most of the southern hemisphere. Even though it is almost twice as far away as Arcturus, its large stellar radius ($R_\star = 44.2 \pm 0.9 R_\odot$) gives it a comparable angular diameter ($\theta_{\text{LD}} = 20.58 \pm 0.03$), and is therefore another excellent candidate for multi-frequency studies with the VLA. Its effective temperature ($T_{\text{eff}} = 3970 \pm 49$ K) is slightly lower than Arcturus', and it also has a slightly higher mass ($M = 1.3 \pm 0.3 M_\odot$). Using these values for its radius and mass gives a surface gravity of $g_\star = 18$ (in units of cm s^{-2}), about 1500 times lower than the Sun's. The metallicity of Aldebaran is marginally subsolar with $[\text{Fe}/\text{H}] = -0.15 \pm 0.2$ (Decin *et al.*, 2003). Using high spectral resolution in the H, K, and L bands, Tsuji (2008) derived the carbon, nitrogen, and oxygen abundances in Aldebaran which suggests the mixing of the CN-cycled material in the first dredge-up. A 643 day period in the radial velocity for Aldebaran was reported by Hatzes & Cochran (1993), and Hatzes & Cochran (1998) find evidence to support the hypothesis that this variability comes from the reflex motion of the central star due to a planetary companion having a mass of $11 M_{\text{Jup}}$ although this has not been confirmed to date.

Aldebaran has been extensively studied at UV wavelengths. Early IUE observations placed the star well to the noncoronal side of the Linsky-Haisch dividing line (Linsky & Haisch, 1979). The first chromospheric model of the star was developed in the late 1970s (Kelch *et al.*, 1978) and was based on both optical (mainly Ca II H and K) and UV (Mg II *h* and *k*) emission line fluxes. Later, GHRS spectra revealed the presence of significant flux in the C IV resonance lines around 1550 Å (Carpenter & Robinson, 1996), indicating the presence of some *hot* transition region plasma. In light of the new GHRS findings, a new model of the chromosphere and transition region of Aldebaran was developed, with temperatures reaching up to $T_e \sim 1 \times 10^5$ K. Modelling the GHRS optically thick Mg II and O I resonance lines (which show typical stellar wind absorption features), Robinson *et al.* (1998) found evidence for the acceleration of a slow wind and derived a mass-loss rate of $1.6 \times 10^{-11} M_\odot \text{ yr}^{-1}$ and a terminal wind velocity of 30 km s^{-1} . Unexpectedly, FUSE spectra revealed the presence (albeit weak)

3.5 The Karl G. Jansky Very Large Array

of the coronal proxy O VI 1032 and 1038 Å emission lines (Dupree *et al.*, 2005) although Ayres *et al.* (2003) failed to detect any X-ray emission from the star. Like Arcturus, Aldebaran appears to harbour small levels of magnetic activity.

Wiedemann *et al.* (1994) observed Aldebaran's infrared ro-vibration absorption lines ($v = 2 - 1$) and matched them with synthetic spectra based on a model containing the semi-empirical photosphere of Kelch *et al.* (1978) and the best fitting temperature and column density profiles. Like Arcturus, they found a steady decrease in temperature with height, with the chromospheric temperature being constantly below the temperature minimum ($T_e^{\min} \sim 2800$ K) of the Kelch model. Again, they explained their results by suggesting the existence of an extra *cool* component with a large (> 99%) filling factor in the outer atmosphere (i.e. a thermally bifurcated CO-mosphere). Recently, Ohnaka observed the CO first overtone lines ($v = 2 - 0$) of Arcturus near 2.3 μm with the Very Large Telescope Interferometer (VLTI) and discovered a CO layer extending out to $2.5 R_\star \pm 0.3 R_\star$. They were unable to constrain the geometrical thickness of this CO layer from their data but we will show how our VLA radio data can constrain this value in Chapter 6. H₂O was also confirmed in its MOLsphere when Tsuji (2001) detected a H₂O absorption feature at ∼ 6.6 μm. A narrow absorbtion feature in the midst of the wind absorption of the GHRS Mg II h and k lines has been interpreted and modelled as a feature of α Tau's wind-ISM interaction region also known as its astrosphere (Wood *et al.*, 2007).

3.5 The Karl G. Jansky Very Large Array

The NRAO¹ Karl G. Jansky Very Large Array (VLA) is an aperture synthesis radio telescope located on the Plains of San Agustin, New Mexico, USA and is capable of producing radio images with a spatial resolution greater than that of the HST. It is the product of a program to modernize the electronics of the old VLA which had been in operation at the same site since the late 1970's. One of the main upgrades to the VLA is the addition of the Wideband Interferometric Digital Architecture (WIDAR) correlator which allows the digital correlation of

¹The National Radio Astronomy Observatory is a facility of the National Science Foundation operated under cooperative agreement by Associated Universities, Inc.

3.5 The Karl G. Jansky Very Large Array

Table 3.5: Improved Performance Parameters of the VLA.

Parameter	old VLA	VLA	Improvement Factor
Continuum sensitivity (1σ , 9 hr)	$10 \mu\text{Jy}$	$1 \mu\text{Jy}$	10
Bandwidth per polarization	0.1 GHz	8 GHz	80
Coarsest frequency resolution	50 MHz	2 MHz	25
Finest frequency resolution	381 Hz	0.12 Hz	3180
Channels at max. bandwidth	16	16,384	1024
Maximum number of channels	512	4,194,304	8192

very wideband signals. WIDAR digitally filters and splits the data into sub-bands which are then separately cross correlated and integrated before being stitched together again to yield the final wideband spectrum. The new WIDAR correlator and its superior bandwidth capability provides the VLA with greater sensitivity, allowing the detection of lower flux density sources than was previously possible with the old VLA. A comparison of the performance parameters of the VLA with those of the old VLA is shown in Table 3.5. The three major new observational abilities of the VLA are:

1. Complete frequency coverage between 1 and 50 GHz opening up new regions of the electromagnetic spectrum to astronomy.
2. An increase in continuum sensitivity by an order of magnitude at some frequencies, by increasing the bandwidth to 8 GHz per polarization.
3. Process the large bandwidth with a minimum of 16,384 spectral channels per baseline.

Apart from the addition of more feeds at the center of the reflector, the structural design of the VLA has not changed during its recent upgrade. As before it consists of 27 fully steerable alt-azimuth antennas arranged along the arms of an upside-down ‘Y’ as shown in Figure 2.9. The array is re-configurable and can vary its resolution by over a factor of ~ 50 through movement of its component antennas along twin railroad tracks. Four standard configurations of antennas along the arms of the array are possible whose scales vary by the ratios 1 : 3.28

3.5 The Karl G. Jansky Very Large Array

: 10.8 : 35.5 from smallest to largest. These are called D, C, B, and A configurations, with A having the longest baselines (~ 36 km) giving the best spatial resolution, but lacking short baselines needed for imaging extended structure. In each configuration, the distance of each antenna from the center of the ‘Y’ is equal to $m^{\ln 2}$ where m is the antenna location number, counting outwards from the center of each arm. With this design, the m ’th station in any configuration coincides with the $2m$ ’th station in the next smaller configuration. This means that only 72 stations are needed to handle all four configurations. Additionally, there are 3 hybrid configurations called DnC, CnB, and BnA, which are well suited for sources with low declination. In these configurations, the North arm antennas are deployed in the next larger configuration than the SE and SW arm antennas resulting in a more circular synthesized beam for these sources.

Each antenna is 25 m in diameter giving the array a total collecting area equivalent to a single dish of 130 m in diameter. Each antenna has an off-axis Cassegrain design with a rotatable sub-reflector at the prime focus of the main reflector and is supported by four feed legs as shown in Figure 3.5. All feeds are located on a feed ring at the Cassegrain focus and the observing feed is changed by rotating the asymmetric sub-reflector about the main reflector axis so that the secondary focal point moves to the desired feed. The standard observing mode for all feeds is circular polarization. RF signals from each feed are sent via a waveguide to the antenna vortex room located directly underneath the main reflector where they are feed into low noise front ends. The vortex room is temperature controlled and also contains cryogenic cooling systems for the front end, portions of the LO, and IF equipment. IF signals from each antenna are sent by cable to a shielded room where the signals are cross correlated.

All VLA antennas are outfitted with eight receivers providing continuous frequency coverage between 1 and 50 GHz. As shown in Table 3.6, the frequency ranges of 1-2 GHz, 2-4 GHz, 4-8 GHz, 8-12 GHz, 12-18 GHz, 18-26.5 GHz, 26.5-40 GHz, and 40-50 GHz, are commonly referred to as L, S, C, X, Ku, K, Ka, and Q bands, respectively. Additionally, the VLA is currently being outfitted with even lower frequency receivers, P-band (230-470 MHz) and 4-band (54-86 MHz). The VLA’s spatial resolution is set by the maximum baseline B_{\max} and frequency of observation. This means that structures smaller than the diffraction

3.5 The Karl G. Jansky Very Large Array

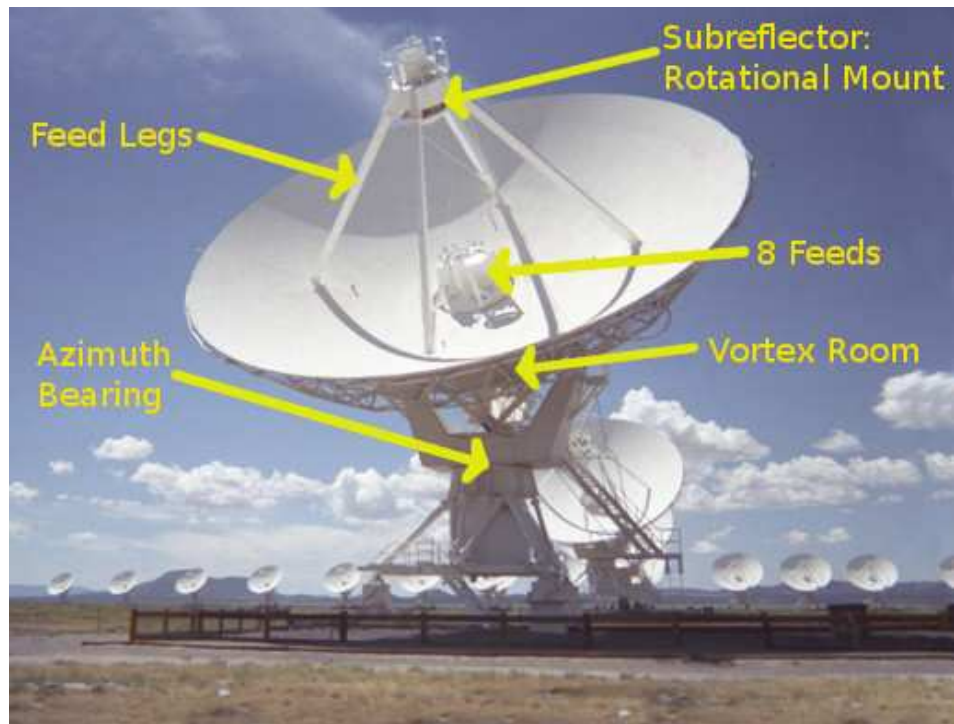


Figure 3.5: Main features of a VLA antenna. The sub-reflector is located at prime focus on a rotational mount is supported by four feed legs. The 8 feeds are located in a ring at the secondary focus. The feeds send the RF signal to the front end located in the vortex room directly beneath the main reflector.

limit ($\theta_{\text{HPBW}} \sim \lambda/B_{\max}$) will be smoothed to the resolution of the array. Table 3.6 also summarizes the maximum resolution for each of the four main configurations at each wavelength. The resolution is defined here as the HPBW of the synthesized beam, using uniform weighting, over a full 12 hour synthesis observation of a source which passes near the zenith. For completeness, we also give the field of view (FOV) at each observing frequency in Table 3.6, defined as the HPBW of the primary beam, which for the VLA antennas can be approximated using the formula: $\text{FOV}(') = 45/\nu_{\text{GHz}}$.

3.6 VLA Observations of Arcturus and Aldebaran

Table 3.6: Frequency coverage, primary beam, and spatial resolution of the VLA.

	L	S	C	X	Ku	K	Ka	Q
ν (GHz)	1.5	3.0	6.0	10	15	22	33	45
λ (cm)	20	13	6.0	3.0	2.0	1.3	1.0	0.7
ν Range (GHz)	1-2	2-4	4-8	8-12	12-18	18-26.5	26.5-40	40-50
A config: θ_{HPBW} ('")	1.3	0.65	0.33	0.20	0.13	0.089	0.059	0.043
B config: θ_{HPBW} ('")	4.3	2.1	1.0	0.6	0.42	0.28	0.19	0.14
C config: θ_{HPBW} ('")	14	7.0	3.5	2.1	1.4	0.95	0.63	0.47
D config: θ_{HPBW} ('")	46	23	12	7.2	4.6	3.1	2.1	1.5
FOV(')	30	15	7.5	4.5	3.0	2.0	1.4	1.0

3.6 VLA Observations of Arcturus and Aldebaran

The Open Shared Risk Observing (OSRO) program at the VLA existed during its commissioning phase to provide observers with early access to a number of VLA correlator capabilities and observing modes. This represented a considerable improvement over the capabilities of the old VLA correlator as observes were provided with increased bandwidth capability at existing VLA bands, increased spectral resolution capabilities, and access to new spectral bands. In September 2010 our proposal (PI: G. M. Harper, Program ID: 10C-105) to observe two archetypical red giants at multiple frequencies was allocated the requested 15.5 hours of observing time with the VLA as part of NRAO’s OSRO Science Program 2010C. A number of observing scripts called scheduling blocks (SBs) were prepared during December 2010 and their duration were kept to ≤ 2.5 hours to increase their likelihood of being scheduled. The VLA now uses dynamic scheduling for deciding which SBs are executed at any time. This takes into account many factors like the scheduling priority assigned by the time allocation committee, weather constraints, and SB duration. Dynamic scheduling means that the observer does not know when their observations will occur but in general, the chances of observations being scheduled are increased if the duration of the SB is kept short.

Table 3.7: VLA Observations of α Boo and α Tau obtained in February 2011 and July 2012.

Star	Date	Band	ν (GHz)	λ (cm)	Time on Star (hr)	Restoring Beam ("×")	Bandwidth (GHz)	Number of Antennas	Phase Calibrator
α Boo	2011 Feb 22	Q	43.3	0.7	0.3	0.19×0.15	0.256	22	J1357+1919
	2011 Feb 22	Ka	33.6	0.9	0.2	0.25×0.20	0.256	23	J1357+1919
	2011 Feb 22	K	22.5	1.3	0.4	0.35×0.28	0.256	24	J1357+1919
	2011 Feb 11	X	8.5	3.5	0.3	1.14×0.70	0.256	18	J1415+1320
	2011 Feb 11	C	5.0	6.0	0.5	2.02×1.30	0.256	21	J1415+1320
	2011 Feb 13	S	3.1	9.5	1.8	2.57×2.08	0.256	12	J1415+1320
	2012 Jul 19	S	3.0	10.0	0.7	2.82×2.30	2.0	23	J1415+1320
	2012 Jul 20	L	1.5	20.0	1.6	4.46×3.94	1.0	23	J1415+1320
α Tau	2011 Feb 11	Q	43.3	0.7	0.3	0.18×0.16	0.256	22	J0431+1731
	2011 Feb 11	Ka	33.6	0.9	0.2	0.22×0.20	0.256	19	J0449+1121
	2011 Feb 11	K	22.5	1.3	0.4	0.35×0.31	0.256	21	J0449+1121
	2011 Feb 13	X	8.5	3.5	0.5	0.85×0.78	0.256	25	J0449+1121
	2011 Feb 13	C	5.0	6.0	1.2	1.48×1.32	0.256	21	J0449+1121
	2011 Feb 12	S	3.1	9.5	1.8	2.74×2.02	0.256	11	J0431+2037

3.6 VLA Observations of Arcturus and Aldebaran

Our main set of observations took place in February 2011 while the VLA was in B configuration. All observations were taken in continuum mode and the correlator was set up with two 128 MHz sub-bands centered on the frequencies listed in Table 3.7. Each sub-band had sixty-four channels of width 2 MHz and four polarization products (RR, LL, RL, LR). We obtained all our requested observations of α Tau in just two days between the 11th and 13th of February 2011 which consisted of Q, Ka, K, X, C, and S band observations of the star. We did not request L band (i.e. 1.5 GHz) observations of α Tau as it was believed that the star would be too faint to be observable at this frequency. There was also insufficient Ku band receivers available at the time to carry out observations at 15 GHz. We obtained Q, Ka, K, X, C, and S band observations of α Boo in eleven days between the 11th and 22nd of February 2011. We also had prepared a 2.5 hour SB for α Boo at L-band but this SB was never executed.

For this reason we applied for (and were awarded) 3 additional hours of directors discretionary time (DDT) in early 2012 (PI: E. O’Gorman, Program ID: 12A-472) to observe α Boo at S and L band. We decided to include a short observation at S band even though we already had an observation at this band to make sure that the stars flux density had not significantly changed over that period and so any possible L band detection could be included in the analysis of the main set of data from the previous year. Our DDT observations took place in July 2012 when the VLA was again in B configuration with details given in Table 3.7. The capabilities of the VLA had greatly increased in the ~ 1.5 years since the main set of observations and we now could utilize the full 1 and 2 GHz of bandwidth at L and S band, respectively. The 1-2 GHz and 2-4 GHz frequency ranges were both divided into 16 sub-bands, each with sixty-four channels. The channel width was 2 and 1 MHz for S and L-band, respectively, and each sub-band had four polarization products (RR, LL, RL, LR).

In radio interferometry, baseline-dependent additive errors in the visibilities can occasionally lead to artifacts occurring at phase center of the final image. Such errors may be caused by unflagged low level interference picked up by some antennas baselines. An example of this is demonstrated in Figure 3.6 in which two radio images of Betelgeuse at 15 GHz are shown (A. Brown, priv. comm.). The left panel was taken on 2nd February 2002 and shows a 30σ detection of Betelgeuse

3.6 VLA Observations of Arcturus and Aldebaran

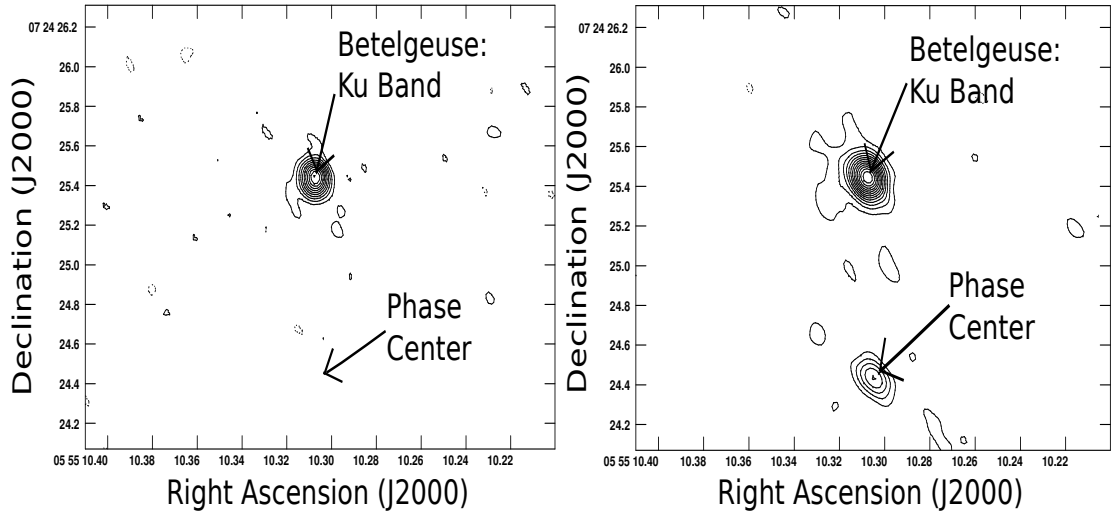


Figure 3.6: An example to highlight the importance of offsetting the source from phase center. *Left:* Old VLA image of Betelgeuse at 15 GHz taken on showing no source at the phase center of the image. Contour levels at $\sigma(-6,-3,3,\dots,30)$ where $\sigma = 84 \mu\text{Jy}$. *Right:* Two months later Betelgeuse was again imaged at 15 GHz but now shows a strong artifact at phase center. Contour levels at $\sigma(-6,-3,3,\dots,45)$ where $\sigma = 90 \mu\text{Jy}$ (A. Brown, priv. comm.).

with low level background noise. The right panel which was taken two months later on 2nd April 2002 shows a 45σ detection of the star but also now shows a 15σ artifact at phase center. If the target had been observed at phase center in this case, then this artifact would lead to an incorrect flux density measurement for the star. For our VLA observations, both α Boo and α Tau were slightly offset from the phase-center by ~ 5 synthesized beam widths in order to avoid source contamination by these rare but possible phase center artifacts and therefore avoiding spurious detections.

The main problem at low VLA frequencies (L and S bands) is disturbances in the ionosphere caused by solar activity. At L-band, solar flares can be as strong as 1×10^6 Jy and are a major source of interference, with their effects sometimes being impossible to remove from the data. To avoid such problems the S and L band SBs were scheduled for night time observing only. The low to intermediate frequency observations (L - X bands) were composed of repeatedly interleaved observations of the target and a nearby phase calibrator with cycle times of 12 minutes; 10 minutes on the target and 2 minutes on the phase calibrator. For α

3.6 VLA Observations of Arcturus and Aldebaran

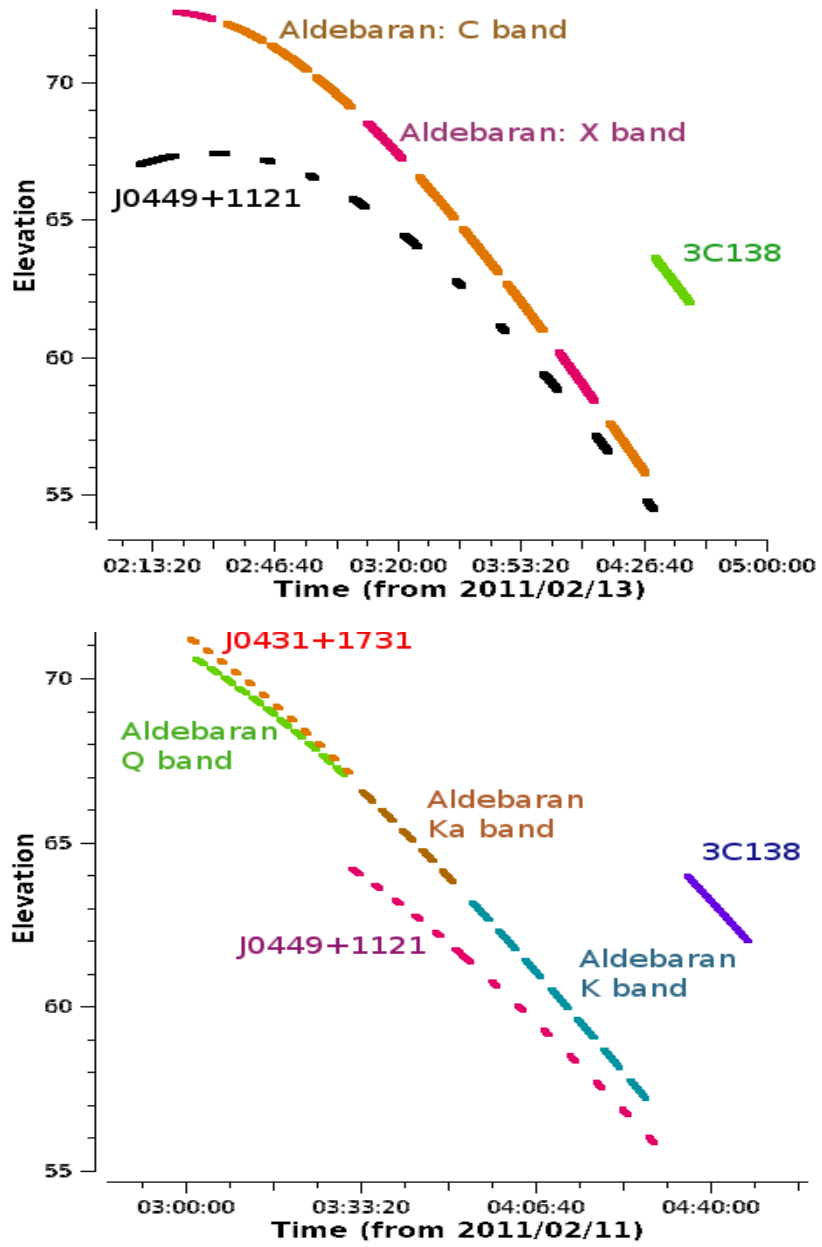


Figure 3.7: Overview of a low and high frequency VLA SB for α Tau. *Top Panel:* The low frequency observations consisted of interleaved observations of the target and a nearby phase calibrator with cycle times of 12 minutes. The X band observations were interspersed between C band observations to obtain a good spread in $u-v$ coverage. *Bottom Panel:* The high frequency observations had short cycle times to compensate for tropospheric effects. Q band observations were taken first to ensure the best pointing solutions were applied to them.

3.6 VLA Observations of Arcturus and Aldebaran

Boo, the point source J1415+1320 which is located 6° away was used as the phase calibrator at these frequencies. For α Tau, the point source J0449+1121 located 6° away was used at C and X band, while the brighter J0431+2037 located 4° away was used at S band due to it being unresolved at this frequency (but is resolved at C and X band). The primary calibration sources 3C286 and 3C138 were observed at the end of all low and intermediate frequency SBs and were used to measure the bandpass and set the absolute flux for α Boo and α Tau, respectively. The top panel in Figure 3.7 shows a plot of elevation against time for all the sources observed in the SB of the C and X band observations of α Tau. In this SB, observations of α Tau at X band were interspersed between C band observations throughout the track to obtain a good spread in $u - v$ coverage.

At high VLA frequencies (i.e. K, Ka, and Q band) the troposphere can cause major phase variations to incoming radio waves. To reduce this problem, the old VLA used a technique called *fast switching* which reduced the setup overhead and slewing compared to traditional iterating between source and calibrator scans. This overhead is sufficiently reduced with the new VLA and no special fast switching mode is necessary. Instead regular but short duration source-calibrator loops are implemented. As a result, the calibration overheads for high frequency observing are typically considerably larger than for lower frequency observations. For both stars, the total cycle times for the Q, Ka, and K-band observations were 160, 230, and 290 s, respectively. These high frequency observations were combined into a single 2 hour SB for each star and commenced with X-band reference pointing with solutions being applied on-line. As mentioned in Section 2.1.3, the blind pointing errors of the VLA antennas can occasionally be as large as the HPBW of the primary beam at high frequencies. Thankfully, the pointing can be calibrated for using a technique known as *reference pointing* whereby a nearby known calibrator is observed in interferometer pointing mode every hour or so. The measured local pointing corrections are then be applied to subsequent target observations. Reference pointing can reduce the rms pointing errors to as little as $2''$ if the reference source is with 10° of the target source. After X-band pointing the target source was observed at Q-band to ensure the best pointing solutions were used as shown in the lower panel of Figure 3.7 for α Tau.

3.7 VLA-Pie Town Observations of Betelgeuse

As part of our study into Betelgeuse’s extended atmosphere we decided to re-visit some archival high spatial resolution VLA data from the early 2000’s. This was motivated by the recent findings of [Richards *et al.* \(2013\)](#) who detected two hot chromospheric features with the very long baseline interferometer e-MERLIN. The two features, also referred to as ‘hot spots’, were found to have brightness temperatures well above the mean brightness temperature measured at the same radio wavelength, and were separated from each other by 90 mas. We wanted to see if these features were present at other wavelengths and if so, how they varied over time.

Asymmetries in Betelgeuse’s atmosphere were first detected in the radio in old VLA-MERLIN combined images at 6 cm (Dr. Rhys Morris, personal communication, 2012 Dec 23) and at then confirmed by [Lim *et al.* \(1998\)](#) at 0.7cm. To see how these asymmetries evolved with time, a multi-wavelength study into the temporal evolution of Betelgeuse’s atmosphere was carried out with the old VLA over a number of years in the early 2000’s in its most extended A configuration plus the Pie Town link¹. This study focused on fitting various models to the visibility data as was done by [Lim *et al.* \(1998\)](#), i.e., the analysis was mainly carried out in the visibility plane. The detection of the two unique hot spots in the e-MERLIN radio maps by [Richards *et al.* \(2013\)](#) inspired us to revisit this data which, because of the addition of the Pie Town link to the VLA, gave spatial resolution comparable to or exceeding that of e-MERLIN at some wavelengths. Our goal was to carry out the analysis in the image plane to make a direct comparison with the findings of [Richards *et al.* \(2013\)](#). In Table 3.8 we summarize this unique data set which consists of almost four years of high resolution multi-wavelength observations of Betelgeuse. To increase our observational time period we also include the short wavelength high resolution (i.e., A configuration) observations of the star from 1998. Betelgeuse was resolved at all wavelengths listed in Table 3.8 except at L band.

The VLA-Pie Town Link

¹This data was carefully calibrated by Dr. Alexander Brown.

3.7 VLA-Pie Town Observations of Betelgeuse

Table 3.8: Multi-wavelength VLA + Pie Town Observations of Betelgeuse

Date	Band	λ (cm)	Time on Star (hr)	Restoring Beam (mas)	rms noise (mJy/beam)
2004 Oct 21,30	Q	0.7	1.2	39×26	0.37
	K	1.3	2.6	80×41	0.09
	U	2.0	3.3	121×91	0.08
	X	3.5	3.8	208×126	0.02
	C	6.2	2.9	377×265	0.02
	L	16.7	2.4	1262×889	0.03
2003 Aug 10,12	Q	0.7	0.9	40×27	0.46
	K	1.3	2.6	80×42	0.18
	U	2.0	3.3	119×96	0.10
	X	3.5	3.0	204×139	0.03
	C	6.2	2.8	378×297	0.03
	L	16.7	2.6	1247×931	0.04
2002 Feb 17,18	K	1.3	2.0	82×47	0.14
	U	2.0	2.0	128×90	0.11
	X	3.5	2.1	200×135	0.03
	C	6.2	1.6	372×273	0.3
	L	16.7	1.1	1312×951	0.05
2002 Apr 12,13	K	1.3	2.0	91×59	0.18
	U ^a	2.0	2.0	130×98	0.39
	X	3.5	2.1	224×154	0.03
	C ^b	6.2	1.6	406×295	0.3
	L	16.7	0.9	1397×1146	0.07
2001 Jan 02	K	1.3	6.0	78×42	0.08
2000 Dec 23	Q	0.7	6.0	44×20	0.18
1998 Mar 29,30	Q ^c	0.7	5.3	39×36	0.38
	K ^c	1.3	6.3	114×89	0.25

^a Spurious source seen at phase center of image.

^b The star was not detected in this data set.

^c No Pie Town link was used in this data.

The 25 m antenna located at Pie Town, New Mexico is one of 10 antennas spread across the United States of America which together make up the Very Long Baseline Array (VLBA). It was successfully connected in real time via a 104 km long

3.7 VLA-Pie Town Observations of Betelgeuse

fiber optic line to the VLA in 1999 and was operational at all old VLA frequencies prior to its upgrade to the Karl G. Jansky VLA. The Pie Town antenna is located approximately 52 km west of the center of the VLA, effectively doubling its resolution while in A configuration when connected. It is worth noting that the Pie Town link was only functional when the VLA was in A configuration. The extra collecting area together with 27 additional baselines also increases the sensitivity of the array. The Pie Town antenna generates IF signals in VLBA format and these are converted, at Pie Town, to a 50 MHz wide VLA signal where they are multiplexed and then modulated onto a single laser before being sent over 104 km of fiber to the VLA. When the signal arrives at the VLA site it is received and converted back into an RF signal. The received RF signal is then amplified and filtered before its is sent on to the backend receiver.

4

Radio Interferometric Data Analysis

The complex visibilities outputted from the correlator of a radio interferometer are far from ideal and many additional steps of processing are required before they can be of scientific use. The imperfection of the synthesis radio telescopes (e.g., surface accuracy, receiver noise, gain stability, etc.), the adjustments to the signal (e.g., filter bandpass, etc.), hardware or software failures, poor atmospheric conditions, and the presence of RFI are some of the many sources of visibility corruption that must be accounted for before they can be Fourier transformed to get the sky brightness distribution. This chapter describes the three main steps involved in reducing any standard radio interferometric data set, namely: data examination and flagging, data calibration, and imaging. In each step we give relevant examples of the data reduction techniques used in O’Gorman *et al.* (2012) and O’Gorman *et al.* (2013). A general work flow chart is given in Figure 4.1 which highlights the standard procedure required to go from raw visibilities to image analysis and summarizes what will be discussed in this chapter.

4.1 Data Examination and Flagging

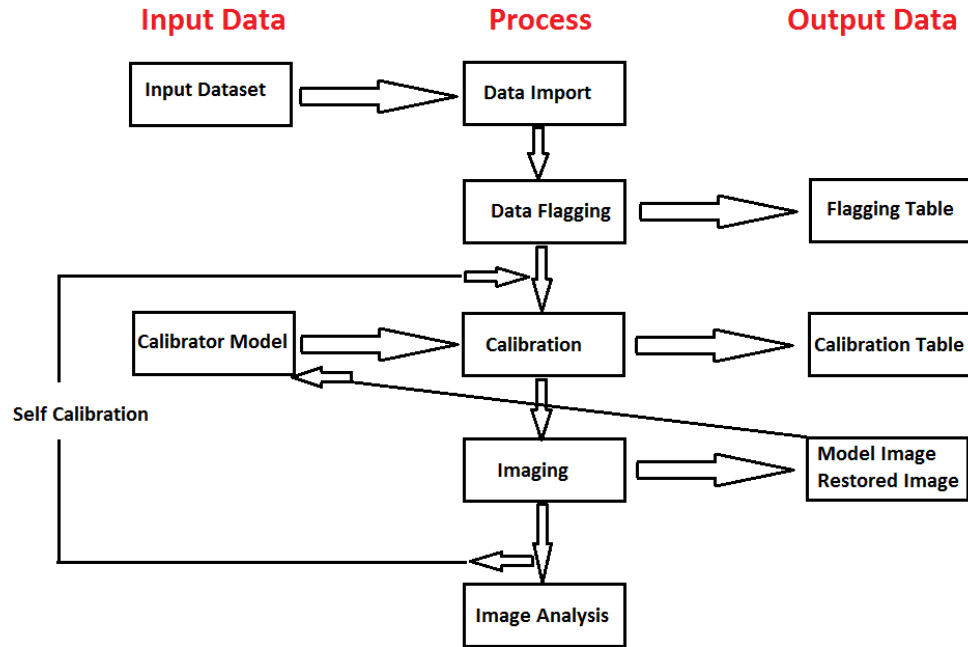


Figure 4.1: Work flow chart highlighting the general procedure required to go from the raw visibilities outputted by the correlator to a final radio image that can be used for scientific analysis. (Image adapted from the CASA cookbook, NRAO)

4.1 Data Examination and Flagging

The Common Astronomy Software Application (CASA; McMullin *et al.*, 2007) package was used to flag, calibrate, and image the main data sets used in this thesis. CASA is operated through a Python interface and uses a suite of astronomical data reduction tools which have been developed to meet the processing requirements of the large data sets from the Karl G. Jansky VLA and ALMA. It can also be used to process data from practically all other modern radio synthesis arrays. For synthesis data to be processed in CASA, it must be in a “measurement set” format. VLA data is easily transferable into this format using the *importevla* task within CASA. CARMA data files however come in *Miriad* format and need to be first converted into Flexible Image Transport System (i.e., FITS) format within the *Miriad* (Sault *et al.*, 1995) data reduction package. During this process the raw data are smoothed by a Hanning filter (combining adjacent frequency chan-

4.1 Data Examination and Flagging

nels with weights 0.25, 0.5, and 0.25) to dampen ringing in the bandpass. Once in FITS format, the data can then be imported into CASA using the *importuvfits* task.

Once the data has successfully been imported into CASA the *listobs* task can be used to get a summary of the data set allowing the user to make sure the observing track contains the requested sources observed at the correct times. At this point it is also a good idea to check any observing logs which are created on site during the observation by the array operators. These logs contain important information about the specific track such as non-operational antennas, unavailable receivers, weather conditions etc., and such data will either need to be treated appropriately during calibration or flagged at this stage. The *plotms* task, which is a GUI-style plotter, can then be used to obtain X-Y plots of the visibility data. A good visual overview of the observation track is obtained by plotting all the source visibility amplitudes as a function of time. Averaging the data over channels or baselines often alerts the user of obvious bad data, which can be manually flagged through the *plotms* interface or through the *flagdata* task. An example of such a plot is shown in Figure 4.2 where the visibility amplitudes of three sources in a 1.3 cm VLA observing track for Aldebaran are displayed against time. The relatively weak target is shown between interleaving scans of the stronger phase calibrator, while the flux calibrator is the scan at the end of the observing track and is the strongest source in this observation. The data has been averaged over channels or baselines to speed up the plotting process. Some relatively low visibility amplitudes can clearly be seen for all scans of the phase calibrator which can be traced to a single poor performing antenna.

Another important way to represent the data at this stage of the flagging process is to plot the visibility amplitude of each of the sources as a function of $u-v$ distance or baseline length (i.e., $\sqrt{u^2 + v^2}$). The amplitude distribution should be relatively constant as a function of $u-v$ distance for the phase calibrator (i.e., a point source) and will fall off with increasing baseline length if the flux calibrator is resolved. Plotting the data in this format often results in extreme points at certain baselines which can then often be traced back to poorly behaving antennas or corrupt baselines. There is also some flagging which can be carried out based in part on a priori information. Antennas in very compact configurations can

4.1 Data Examination and Flagging

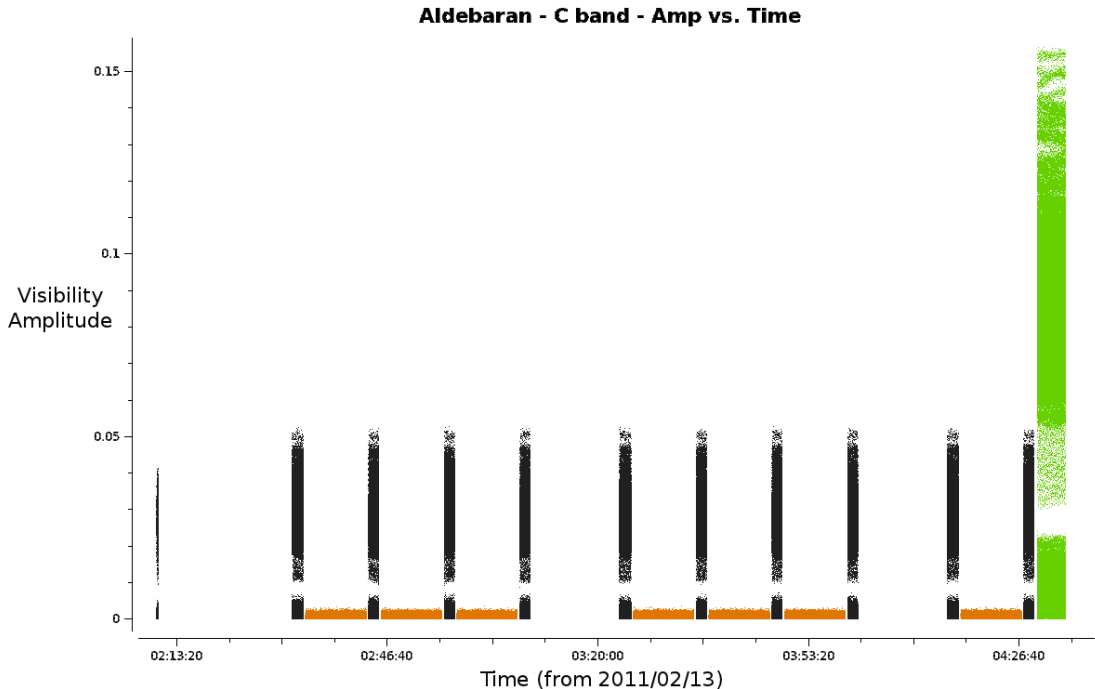


Figure 4.2: Data examination of a 6 cm VLA data set for Aldebaran. A good visual overview of the observation track is obtained by plotting all the source visibility amplitudes as a function of time. Averaging the data over channels or baselines sometimes allow rogue data to stand out. Here the black, orange, and green data points represent the phase calibrator, the science source, and the flux calibrator, respectively. The left most black data points are part of the dummy scan which has to be flagged. The low data points of the phase calibrator are data which needs further investigation. The absence of data at certain times is just when observations at 3 cm where being taken.

partially block the incoming RF signal to other antennas which is often referred to as antenna shadowing. This was not a problem in our VLA B configuration observations but some data obtained in the more compact CARMA configurations had to be flagged as a result of this shadowing. At the time when our VLA observations took place, every observing track (i.e., scheduling block) needed to commence with at least a one minute *dummy scan* to facilitate the correlator setup. We subsequently flagged these scans as they contained no useful scientific data. Other a priori flagging was to remove any visibilities with zero amplitudes and to flag the edge channels in the CARMA data sets. Finally, visual inspection

of each scan was carried out to determine if data at the beginning or end of these scans needed to be flagged. This processes is often referred to as quacking in radio interferometry analysis.

No RFI was present in any of the CARMA data sets and in any of the VLA data sets at wavelengths $\lesssim 3\text{ cm}$ (i.e., X, K, Ka, and Q bands). For the 2011 long wavelength ($> 3\text{ cm}$) data, the two sub-bands were centered at relatively RFI free regions of the bandpass and only a very small amount of RFI had to be manually flagged. The 2012 wide-band data were taken at 10 cm (i.e., S band) and 20 cm (i.e., L band) and many of the sub-bands were severely contained with RFI, especially at 20 cm. In Figure 4.4 we plot the visibility amplitude of the flux calibrator 3C286 against frequency for the 2012 wide-band data set at 20 cm. The upper panel shows the raw data before any RFI has been removed. Some of the sub-bands were badly contaminated with RFI ($> 90\%$) and had to be completely flagged. The remaining sub-bands were initially Hanning smoothed to suppress Gibbs ringing. This action spreads the single-channel RFI into three channels, but importantly removes the effects of some of the worst RFI from a number of channels and allows as much good data to be retained as possible. The *testautoflag* task was then used to conservatively flag RFI from all sources and any remaining RFI was manually flagged. The final result for the flux calibrator is shown in the bottom panel of Figure 4.4 with only some residual RFI still remaining, particularly between 1 and 1.2 GHz.

4.2 Calibration

The role of calibration is to correct the measured visibilities $V'(u, v)$ to approximate as closely as possible the true visibilities $V(u, v)$. As discussed in Chapter 2, the true visibilities are related to the sky brightness via the Fourier transform:

$$V_{ij}[u_{ij}(t), v_{ij}(t)] = \int A(l, m) I(l, m) \exp[-i2\pi(u_{ij}(t)l + v_{ij}(t)m)] dl dm \quad (4.1)$$

where i, j represent the discrete sampling of the antennas i and j at time t . The term $u_{ij}(t)l + v_{ij}(t)m$ is the geometric phase difference produced by the geometric path length difference between antenna i and antenna j from the source (or part

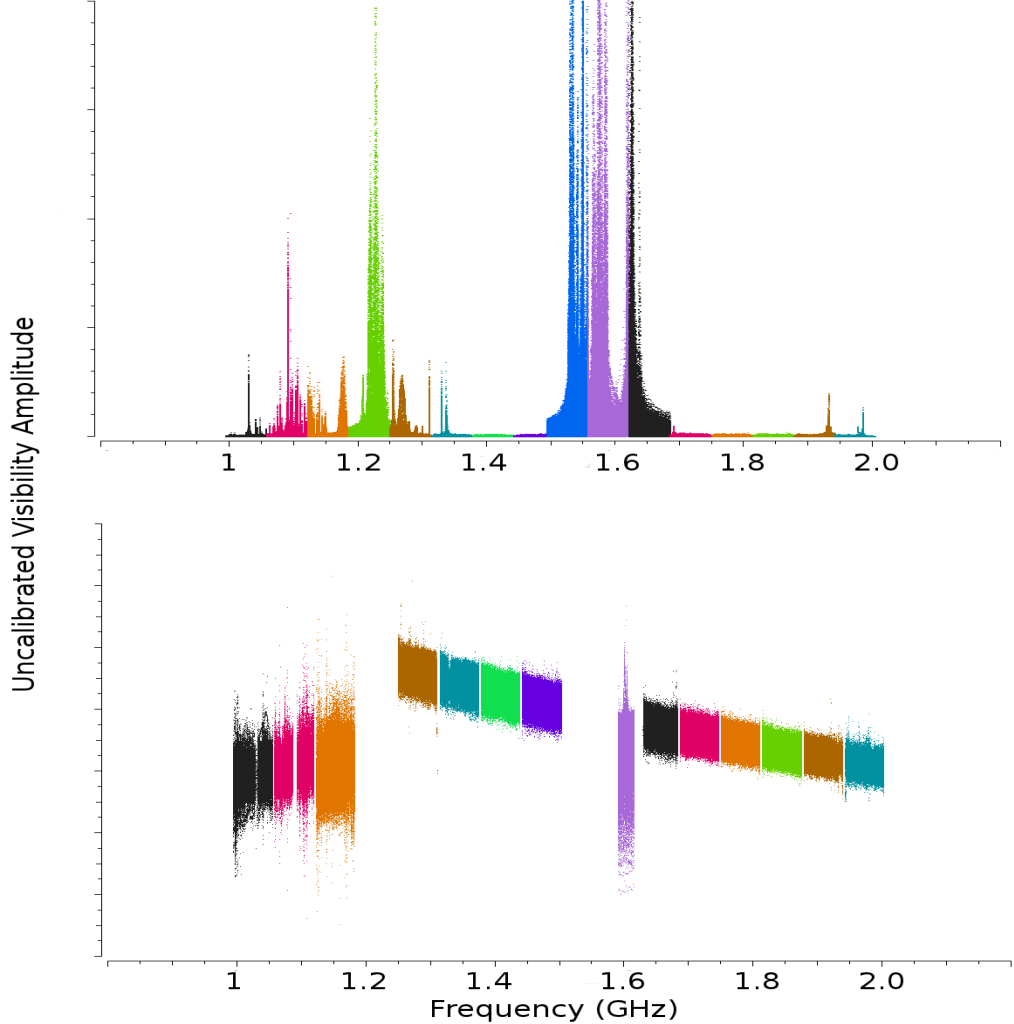


Figure 4.3: Eliminating RFI from the 20 cm wide-band data set. *Top panel:* Raw visibility amplitudes showing the presence of high levels of RFI in many sub-bands. *Bottom panel:* Post flagging visibility amplitudes. Some of the sub-bands were so severely contaminated with RFI that they had to be completely flagged. The data is still uncalibrated at this stage and the gain as a function of frequency is clearly present.

of) at location (l, m) relative to the phase center. The relationship between the measured visibility and the true visibility on a baseline between antennas i and j may be expressed as

$$V'_{ij} = J_{ij} V_{ij} \quad (4.2)$$

where J_{ij} represents the accumulation of all corruptions affecting baseline ij . This equation is known as the Hamaker-Bregman-Sault Measurement Equation ([Hamaker *et al.*, 1996](#)). The most important of the effects contained in J_{ij} are antenna-based and arise from the measurable physical properties of individual antenna elements or the measurable physical conditions in the atmosphere above them. Thus, an array of N antennas forming $N(N - 1)/2$ baselines can usually be adequately calibrated through the determination of only N factors.

For the purpose of the work presented in this thesis, the Measurement Equation can be written as

$$V'_{ij}(u, v, \nu) = b_{ij}(t)[B_i(\nu, t)B_j^*(\nu, t)](t)g_i(t)g_j(t)V_{ij}(u, v, \nu)e^{i[\theta_i(t) - \theta_j(t)]} \quad (4.3)$$

where

- g_i and θ_i are the amplitude and phase portions of the complex gain. These are usually determined separately in the calibration process and may change over the observation period with temperature, atmospheric conditions, etc.
- B_i is the complex bandpass, the instrumental response as a function of frequency, ν , and may also vary over time.
- $b_{ij}(t)$ is the baseline term and is important shortly after a configuration change when antenna positions may not be known well.

The general calibration strategy is then to derive a series of scaling factors from both the phase and flux calibrators, which are then collectively applied to the science target in the final stage of calibration. A general workflow diagram describing the main steps involved in calibration process are summarized in Figure [4.4](#). We now discuss each of these steps while placing emphases on our CARMA and VLA data.

4.2.1 Prior Calibration

Our 2011 VLA data were acquired just after an array re-configuration which meant that the positions of some of the antennas were not accurately known at the time of observations. This resulted in some data points having inaccurate

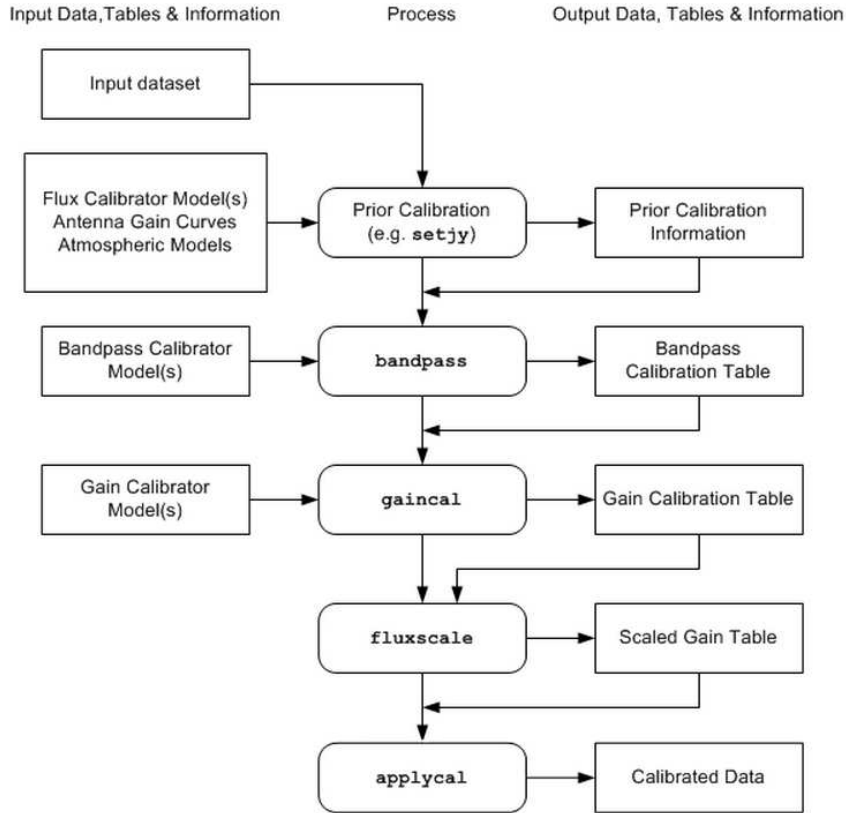


Figure 4.4: A workflow diagram outlining the main steps involved in calibrating radio interferometric data. Each of these steps are discussed in the text in relation to our CARMA and VLA observations (CASA cookbook, NRAO).

$u - v$ coordinates. During the course of observations in each configuration, the exact position of all antennas become known and so the $u - v$ data could be calibrated to account for the discrepancies in the $u - v$ coordinates. At the VLA site, atmospheric opacities become significant at frequencies $\gtrsim 20$ GHz as shown in Figure 4.4 and so opacity corrections were applied to the high frequency data sets. The adjustment values were based on the average of a seasonal model (based on many years of measurements) and information from the weather station obtained during the observations. For the CARMA data, the opacity at 1.3 mm is measured by a tipper (White, 2009). The tipper reflects radiation from the blank sky at different inclinations onto a radiometer. The voltage from the radiometer can then be plotted against inclination to allow the opacity to be calculated.

The final a priori calibration step is to provide a flux density value to the flux calibrator via CASA’s *setjy* task. The VLA flux calibrators were assigned values using the “Perley-Butler 2010” flux density standard models and with assumed systematic uncertainties of 3% at all frequencies (Perley & Butler, 2013). At the time, no Ka or S-band flux density standard models were available so instead for these we used the K and L-band models, respectively, which were scaled according to their spectral indices. The absolute flux scale for CARMA observations is often determined by observing a planet and using a model of its flux as a function of baseline length. However, no such models were available in the earlier versions of CASA which we used at the time and so the flux calibration was carried out with the quasars, 0530+135 and 3C120. The continuously updated CARMA flux catalog was accessed via the *xplore* GUI to obtain their flux values at each observation. The flux of these objects are more unpredictable and the systematic uncertainties are about 20%.

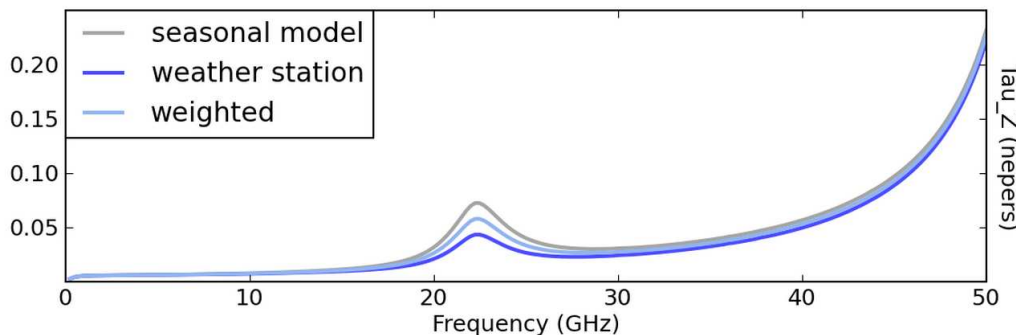


Figure 4.5: Calculation of the atmospheric opacity at the VLA site between 1 – 50 GHz on 2011 February 11. The adjustment values applied to the data were based on the average of a seasonal model and information from the weather station obtained during the observations.

4.2.2 Bandpass Calibration

The bandpass is the relative gain as a function of frequency and solving for it is the first part of the calibration process. Variation in frequency arises from frequency dependent effects in signal transmission. Such variation is shown in

4.2 Calibration

Figure 4.6 for both phase and amplitude for a single antenna. For the VLA data, the flux calibrators were also used as the bandpass calibrators. Their phases were found to vary significantly over the 5 – 10 minutes of observation especially at high frequencies; in most cases by a few 10s of degrees. Before a solution to the bandpass could be found, these phase variations needed to be corrected for to prevent decorrelation of the vector averaged bandpass solution. The complex bandpass, B_i , could then be solved using the *bandpass* task and applying the antenna positions and phase solutions. The bandpass solutions were then applied to the bandpass calibrator to check that both the amplitude and phase were then almost constant across channels/frequency.

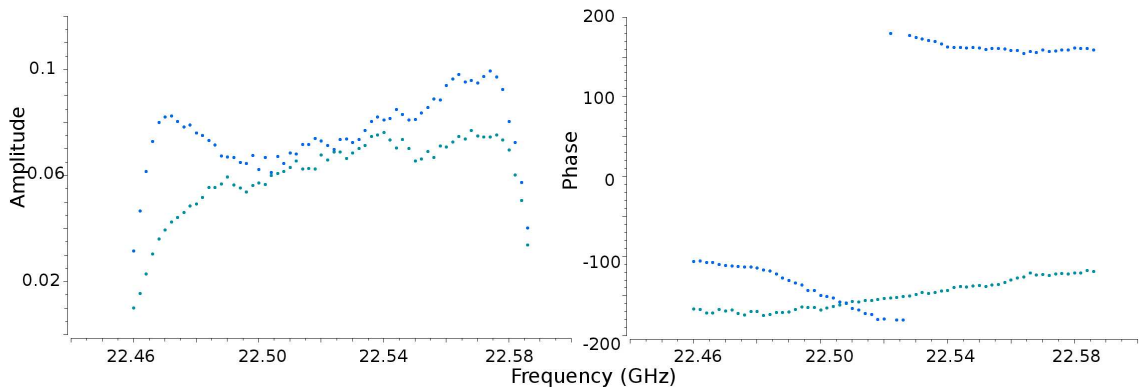


Figure 4.6: One antenna’s gain variation as a function of frequency for the flux calibrator 3C138 at 1.3 cm. Bandpass calibration corrects for this variation.

The CARMA data contained three spectral windows (i.e., 468, 62, and 31 MHz in width), each having independent bandpass shapes in both amplitude and phase. For each of these spectral windows, the gain calibrations are typically the same after the full bandpass dependence has been removed. The strategy to calibrate the CARMA data was to initially carry out the bandpass calibration on the wideband data (i.e., 468 MHz) using the same strategy outlined in the previous paragraph, and then carry out the gain calibration on this wideband data. Once this had been done, these bandpass independent gain solutions were applied to the narrow band data (i.e., 62, and 31 MHz) while solving for their bandpass.

This narrow band bandpass solution could then be applied to the target and phase calibrator.

4.2.3 Gain Calibration

Once a bandpass solution has been applied, the next step is to derive corrections for the antenna amplitude and phase gains, g_i and θ_i , as a function of time. The amplitude changes on a much longer timescale than the phase and so they are solved separately. The general procedure then is to solve for these antenna-based gain factors for each scan on all calibrators. In order to determine the appropriate antenna-based complex gains for the science target, a phase calibrator which is always a point source and located much closer to the target than the flux calibrator, is regularly observed to minimize differences through the atmosphere. If there is a substantial change in phase over a scan and the uncorrected phases were averaged over this timescale, then the amplitude would be decorrelated. It is therefore important to correctly determine appropriate scan lengths when preparing the observations, especially at high frequencies, where time-dependent gain errors are introduced by the troposphere.

During gain calibration, the relative gain amplitudes and phases for different antennas are determined using the phase calibrator. The *gaincal* task is used to do this. The absolute flux density scale of the phase calibrator is later determined by comparison against the gain amplitudes g_i derived for the flux calibrator. To find the relative phases, a zero phase is determined by selecting a reference antenna for which the phase is defined to be zero. In the first step new solutions of complex gains g_i and θ_i are derived for the flux density calibrator which are corrected for the bandpass shape (here we assume the flux density calibrator has been used as the bandpass calibrator as was the case for our observations). The second and final step requires the determination of the appropriate complex gains from the phase calibrator.

4.2.4 Flux Scale Calibration and Application of Solutions

The penultimate stage of the calibration process is to use the known flux density of our flux calibrator (whose flux density was set using *setjy*) to derive the flux

4.2 Calibration

density of the phase calibrator, which was previously assumed to be a point source of 1 Jy located at the phase center. This is achieved using the *fluxscale* task. The final step of the calibration process is to apply the calibration solutions to all the targets, using the task *applycal*. During this process, the calibration solutions are applied to the DATA column in the measurement set, and the results are written in the CORRECTED_DATA column of the measurement set. For the calibrators, the phase and amplitude calibration solutions come from their own solutions and the bandpass solutions come from the bandpass calibrator. For the science target we again apply the bandpass solution of the bandpass calibrator but the gain solutions come from the close by phase calibrator.

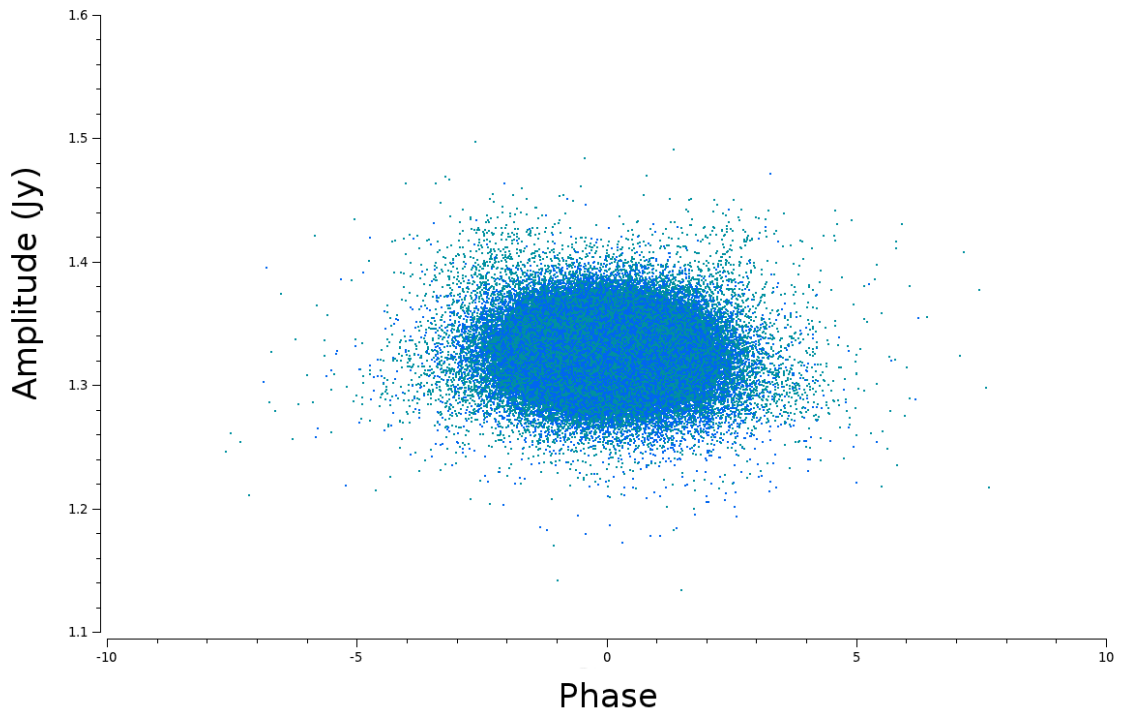


Figure 4.7: A well calibrated source will produce a compact ball of visibilities centered at zero phase and at the amplitude found for that source. Here we plot the calibrated visibilities at 3cm for J0449+1121; the phase calibrator in the 3cm data set for Aldebaran.

Once calibration of the data is complete, it is worth spending time inspecting the corrected data to make sure there are no obvious errors in the data. If such

errors are indeed found at this stage, then their cause will need to be flagged and the data must be re-calibrated. Some insightful plots to investigate how successful the calibration was, are: amplitude vs time, amplitude vs $u - v$ distance, and amplitude vs phase. If a point source has been successfully calibrated then it will have an appearance similar to that in Figure 4.7, i.e., a compact ball of visibilities centered at zero phase and at the amplitude found for that source. Once the data has been successfully calibrated, the science data is split off into a separate measurement set using the *split* task. The calibrated visibilities can then be either directly analyzed by fitting simple models (e.g. point sources, disks, etc.,) to them or, as is more common, Fourier transformed and CLEANed to create an image of the source.

4.3 Imaging

We have shown in Chapter 2 that the visibility as a function of baseline coordinates (u, v) is the Fourier transform of the sky brightness distribution as a function of the sky coordinates (l, m) , i.e.,

$$I(l, m) = \int \int V(u, v) e^{2\pi i(ul+vm)} dudv. \quad (4.4)$$

Taking the inverse Fourier transform of the calibrated visibilities results in a dirty image which can then be deconvolved to produce a good estimate of the true sky brightness distribution. CASA has a single task called *clean* which carries out both of these operations on the data. In the following two sections we describe how both the VLA and the CRAMA visibility data sets were imaged using this task.

4.3.1 Imaging the VLA Data

The calibrated visibilities were both inverse Fourier transformed and deconvolved using the CASA *clean* task in multi-frequency synthesis imaging mode. This imaging mode separately grids the multiple spectral channels onto the $u-v$ plane and therefore improves the overall $u-v$ coverage. As all science targets were expected to be point sources at all wavelengths, resolution was not paramount

and so we used natural weighting for maximum sensitivity. The cell size was chosen so that the synthesized beam was about five pixels across. The FOV of the VLA at short wavelengths is small (see Table 3.6) and at these wavelengths there are less serendipitous background objects. This meant that the science targets were the only objects within a few primary beams of the phase center and so it was sufficient to place just one CLEAN circle around the target source. The general procedure was to first use *clean* to create a dirty image (i.e., by setting $niter = 0$) allowing the root mean square noise of this dirty image, σ_{rms} , to be determined. The final CLEAN image was then created by setting $niter$ to a very large number and setting the CLEANing threshold to be $\sim 3\sigma_{rms}$. Setting $niter$ to a very large number ensures that this CLEANing threshold is reached.

At long VLA wavelengths the primary beam becomes larger and the background sky sources become brighter. The new wide bandwidth capabilities of the VLA means that it is quite sensitive to emission far from phase center. For example, at ~ 20 cm (L-band), the HPBW of the primary beam is $\sim 30'$ and yet the primary beam gain is as much as 10% around 1° away. In Figure 4.9 we show a wide field view of our VLA 20 cm image clearly showing many serendipitous sources out to and beyond the HPBW of the primary beam, all of which needed to be individually CLEANed to reduce their sidelobe contamination of the final image. For this reason the image sizes were usually set to a few times the size of the primary beam (if not too computationally expensive) so that any nearby strong serendipitous sources could be CLEANed. These images were again CLEANed interactively while taking sky curvature into account. CLEANing was carried out interactively with CLEAN circles first placed around the strongest sources in the image and then placing them around weaker sources as they appeared in the residual image.

4.3.2 Imaging the CARMA Data

The CO emission around Betelgeuse is extended and has many different spatial scales. Traditional deconvolution techniques such as the CLEAN and MEM algorithms are scale-free and have no concept of source size. Both algorithms treat each pixel as an independent degree of freedom. However, adjacent pixels in an

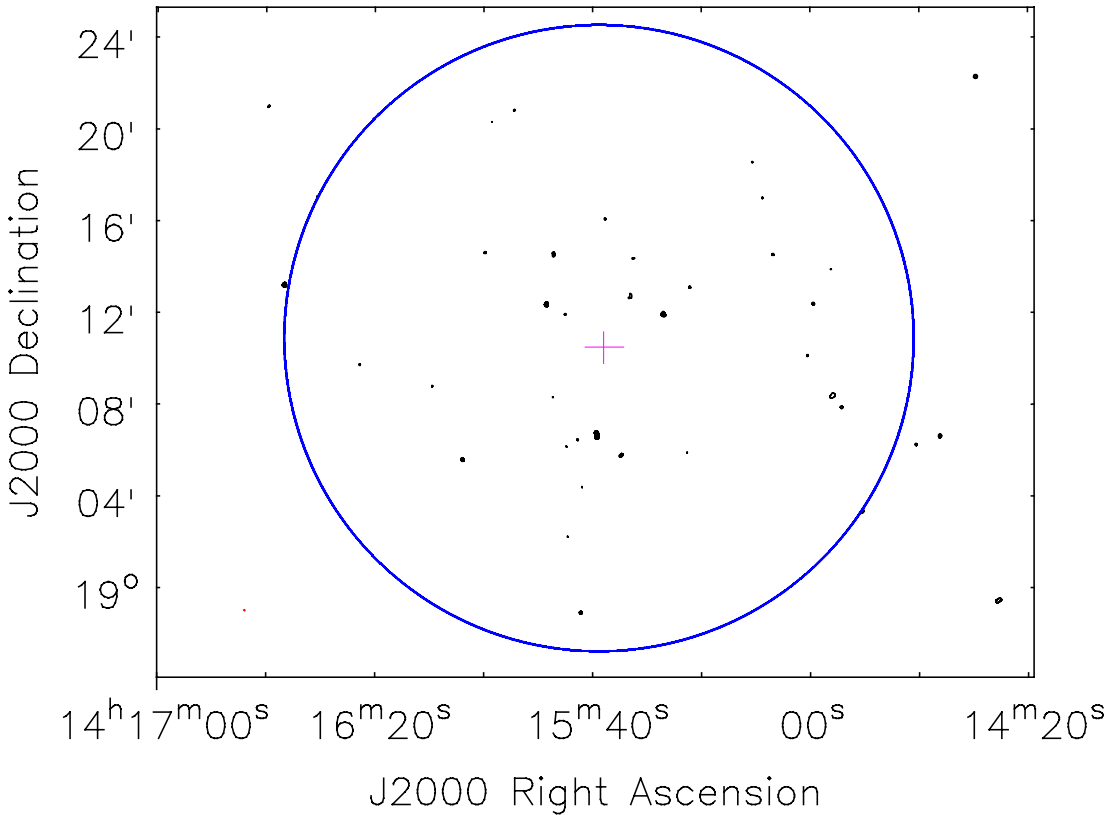


Figure 4.8: Wide field view of the VLA 20 cm CLEANed image showing the many serendipitous background sources close to Arcturus (pink cross). Many of these sources were a few orders of magnitude brighter than Arcturus at 20 cm. CLEAN circles were placed around all these sources during interactive CLEANing. The blue circle marks the FOV (i.e., the HPBW of the primary beam) of the VLA at 20 cm while the pink cross in the center marks the position of Arcturus. The contour levels are set at $(0.005, 0.01, 0.05, 0.1, 0.2, 0.4, 0.6, 0.8) \times 80.3 \text{ mJy}$, where 80.3 mJy is the flux of the brightest source in the image.

image are not independent due to the limiting resolution set by the dirty beam and the intrinsic source size. For example a Gaussian source covering 50 pixels can be characterized by only 5 parameters, not 50. The CASA multi-scale algorithm uses “Multi-scale CLEAN” (Cornwell, 2008) which is a scale sensitive algorithm that employs fewer degrees of freedom to model plausible sky brightness distributions. Instead of deconvolving using just delta-functions (or pixels)

as in other clean algorithms, Multi-scale CLEAN carries out the deconvolution using delta-functions and circular Gaussians of various scales. It has been shown to produce more realistic representations of the sky brightness distribution for extended complex emission than the traditional CLEAN algorithm does ([Rich et al., 2008](#)).

Multi-Scale CLEAN is really just a modification of the classical CLEAN algorithm. It assumes that sources in the sky are actually extended structures of different scales (which can include point sources), unlike the traditional CLEAN algorithm which assumes the sky is empty apart from a limited number of point sources. The function used to define the shape of the different spatial scales (usually a truncated circular Gaussian) has a finite extent and becomes a delta-function in the limit of zero scale-size. The Multi-scale CLEANing process is then as follows:

1. The dirty map is convolved with each scale size to create n convolved images, where n is the number of defined scale sizes.
2. The global scale among these images that contains the maximum total flux has its position, flux, and scale size recorded.
3. The pre-computed scale in which the peak was found, is convolved by the dirty beam, multiplied by some gain factor, and the subtracted from all the images made in the first step.
4. The subtracted component and its scale size is stored in a table.
5. Steps 1 – 4 are repeated until a flux threshold is reached in one of the residual images.

The new model is then convolved with a CLEAN beam and the residuals are added to it to get the restored image.

The combined CARMA configuration image cubes were Multi-scale CLEANed down to the $3\sigma_{\text{rms}}$ threshold. Natural weighting was applied to the $u - v$ data to maximize sensitivity and the CLEAN region was set to be about the size of the HPBW of the primary beam. The Multi-scale algorithm within CASA was set to four unique scales; the largest corresponding to the largest structures visible

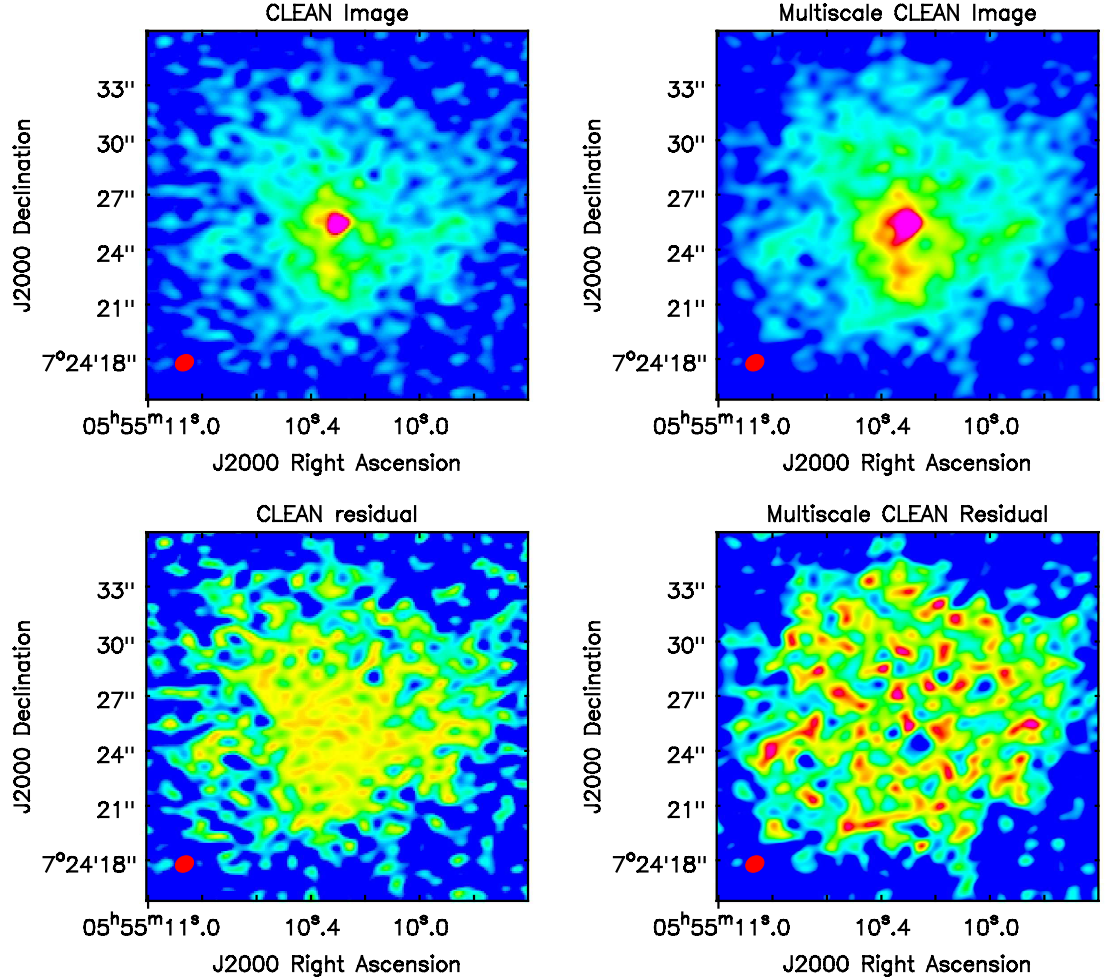


Figure 4.9: Comparing CLEAN to Multi-scale CLEAN using one of the combined configuration CARMA channel maps at -14.1 km s^{-1} . The top panel shows the final deconvolved images using CLEAN (left) and Multi-scale CLEAN (right) with the emission in both maps truncated between 0 and 0.2 Jy beam^{-1} to enhance weak emission. Multi-scale CLEAN is more successful at recovering large-scale structure. The bottom panel shows the residual images after using CLEAN (left) and Multi-scale CLEAN (right) where the emission in both images have been truncated between 0 and $0.06 \text{ Jy beam}^{-1}$. The emission appears more noise-like in the Multi-scale residual image while the CLEAN residual image contains some uncleaned flux.

in individual channel maps. Each scale was approximately set to three times smaller than the preceding scale and a zero-scale was included to account for point sources. In Figure 4.9 we plot one channel from the final restored image cube

4.3 Imaging

and compare this to the same channel from an image cube that was deconvolved using the traditional CLEAN algorithm. It can clearly be seen that Multi-scale CLEAN produces more extended emission around the star. This is because Multi-scale CLEAN removes large-scale structure before finer details while the CLEAN algorithm cannot distinguish noise peaks from faint real signals ([Rich *et al.*, 2008](#)). We also include the resultant residual images from both algorithms in the bottom panel of Figure [4.9](#). The CLEAN residual image still contains some uncleared flux while the emission appears more noise-like in the Multi-scale residual image.

5

Multi-wavelength Study of Betelgeuse's Extended Atmosphere

In this chapter we present the results from our multi-wavelength high resolution study of Betelgeuse's extended atmosphere. The majority of this chapter is based on the findings of O'Gorman *et al.* (2012) and detail the results of our sub-arcsecond resolution study into the distribution and kinematics of CO¹ around Betelgeuse using the CO($J = 2 - 1$) rotational line as the main probe. The variation of the emission line profile with different CARMA array configurations provides us with a unique insight into the distribution and kinematics of the two previously known flows, S1 and S2, around Betelgeuse. We successfully image the star on spatial scales as small as $0''.9$ ($\sim 20 R_\star$) over a $32''$ ($\sim 750 R_\star$) field of view and we discuss these radio maps in detail. We then compare these results to higher CO rotational lines obtained with other instruments. We also present the recent findings of Richards *et al.* (2013) who image two distinct chromospheric features at centimeter wavelengths. These surprising findings motivated us to re-analyze old VLA-Pie Town data to search for these features at shorter wavelengths

¹Throughout this chapter the usage of the term CO refers to the molecular isotope $^{12}\text{C}^{16}\text{O}$.

5.1 CO molecules in the CSE of Betelgeuse

with comparable resolution, the results of which are presented at the end of this chapter.

5.1 CO molecules in the CSE of Betelgeuse

The CSE of Betelgeuse (α Ori) is a proving ground for ideas and theories of mass loss from oxygen-rich M-type supergiants. Currently it is losing mass at a respectable rate $\sim 2 \times 10^{-6} M_{\odot} \text{ yr}^{-1}$ (Harper *et al.*, 2001), as it has been over the past ~ 1000 years. Most of the optically thin silicate dust lies beyond $\sim 46 R_{\star}$ (Danchi *et al.*, 1994) and therefore dust is unlikely to be responsible for the bulk mass loss. This raises the important point that if the mass loss from Betelgeuse is not a result of dust then perhaps the same mechanisms that are responsible might also be active in the more dusty later M-type supergiants. Radiation pressure on atoms and molecules is another potential contributing candidate as a mass loss mechanism and so spatial and dynamical studies of molecules are a fruitful line of investigation, especially in relation to eventual formation of dust. Such studies also allow us to calculate the time scales on which certain mass loss episodes have occurred, and these can then be compared to the time scales of potential mass-loss initiators such as convection or magnetic dynamo cycles.

Despite the initial reports of an enhancement of C abundance in its atmosphere (Spinrad & Vardya, 1966), Betelgeuse is now known to be an oxygen-rich star. The comprehensive study of CO and OH ro-vibrational bands by Lambert *et al.* (1984) found $\log \epsilon(\text{C}) = 8.4$ and $\log \epsilon(\text{O}) = 8.8$. For any species X

$$\log \epsilon(\text{X}) = \log (\text{X/H}) + 12, \quad (5.1)$$

which can be used to show $\text{O/C} = 2.5$. Lambert *et al.* (1984) also found $\log \epsilon(\text{N}) = 8.6$ which indicates a contamination of the atmosphere with C-N processed material. This is in agreement with the theoretical work of Lamb *et al.* (1976) who predict the dredging up of processed material by the deep convective envelope which a supergiant like Betelgeuse is expected to possess. Betelgeuse is unlikely to have undergone a second dredge-up of material that would cause small changes in the CNO abundances due to its mass being greater than the upper mass limit for a second dredge-up to occur. This second dredge-up is predicted to occur after

5.1 CO molecules in the CSE of Betelgeuse

He core exhaustion for stars below $8 - 10 M_{\odot}$ (Kaler *et al.*, 1978). The observed $^{12}\text{C}/^{13}\text{C}$ ratio, which is an indication of the history of nuclear processing and mixing in the interior of stars (Eggleton *et al.*, 2007; Pavlenko *et al.*, 2003) has consistently found to be between 6 and 7 (Bernat *et al.*, 1979; Harris & Lambert, 1984; Hinkle *et al.*, 1976; Lambert *et al.*, 1974), well below the predicted value of 20 (Charbonnel, 1995; Pavlenko *et al.*, 2003), which is the case for most red giant stars (e.g., Boothroyd & Sackmann, 1999).

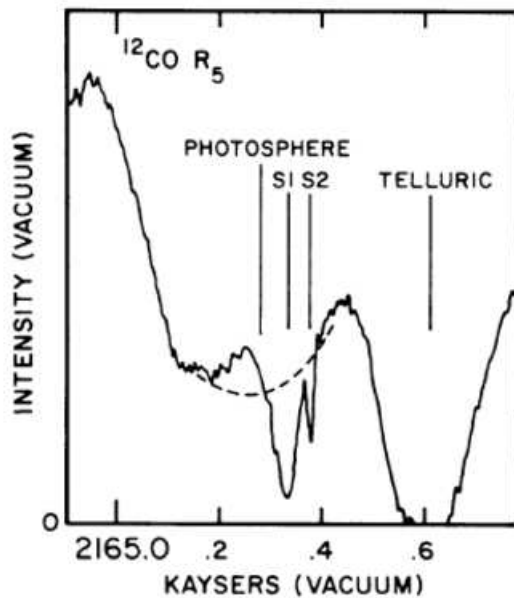


Figure 5.1: CO ro-vibrational fundamental line showing two sharp blueshifted absorption features originating from the expanding envelope (Bernat *et al.*, 1979). These two features became known as the S1 and S2 components of Betelgeuse's outflow having outflow velocities of ~ 9 and $\sim 16 \text{ km s}^{-1}$, respectively. The units of the x-axis are cm^{-1} .

The study of CO molecules in the CSE of Betelgeuse began with the detection of $4.6 \mu\text{m}$ ro-vibrational absorption lines of $^{12}\text{C}^{16}\text{O}$ and $^{13}\text{C}^{16}\text{O}$ by Bernat *et al.* (1979) who identified two absorption features shown in Figure 5.1, implying two distinct components within the overall outflow. One component, known as S1, has a Doppler shift of 9 km s^{-1} towards us with $T_{\text{exc}} \simeq 200 \text{ K}$, $v_{\text{turb}} \simeq 4 \text{ km s}^{-1}$, and $N_{\text{CO}} = 4.7 \times 10^{17} \text{ cm}^{-2}$. The second faster component, known as S2, has a

5.1 CO molecules in the CSE of Betelgeuse

Doppler shift of 16 km s^{-1} towards us with $T_{\text{exc}} \simeq 70 \text{ K}$, $v_{\text{turb}} \simeq 1 \text{ km s}^{-1}$, and $N_{\text{CO}} = 1.2 \times 10^{16} \text{ cm}^{-2}$. [Bernat et al. \(1979\)](#) noted that a simple assumption of the dust and gas being in thermal equilibrium would infer that the S1 and S2 components have a spatial extent of 4 and $55''$ respectively, using the dust model of [Tsuji \(1979\)](#). The S1 feature with its higher column density was well known from atomic absorption line studies (e.g. [Weymann, 1962](#)) and both features had been detected in high spectral resolution atomic Na and K absorption profiles ([Goldberg et al., 1975](#)).

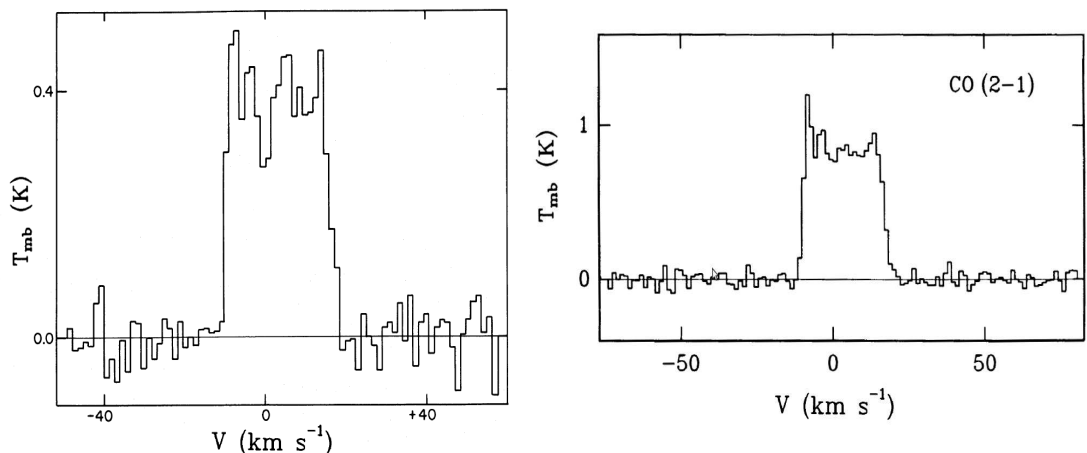


Figure 5.2: Previous single dish CO($J = 2 - 1$) rotational emission line profiles of Betelgeuse. *Left:* [Huggins \(1987\)](#) line profile using a HPBW of $32''$. They found some evidence for an S2 radius of about $16''$. *Right:* The line of [Huggins et al. \(1994\)](#) looks very similar even using a smaller HPBW in conflict with the findings of [Huggins \(1987\)](#). Velocities are plotted in the local standard of rest (LSR) frame.

CO was first detected at radio wavelengths by [Knapp et al. \(1980\)](#) who presented a low S/N ratio spectrum of the $J = 2 - 1$ rotational emission line at 230 GHz. They used a single dish antenna with a HPBW of $\sim 30''$ and detected one component expanding at 15 km s^{-1} . They assumed this component to be the S2 component detected by [Bernat et al. \(1979\)](#) and by assuming that they had resolved a flat top profile, predicted that its spatial extent did not exceed $10''$. The weaker CO($J = 1 - 0$) line was tentatively detected by [Knapp & Morris \(1985\)](#) with a 7 m dish which had a HPBW of $100''$. [Huggins \(1987\)](#) presented a higher S/N CO($J = 2 - 1$) profile that was obtained with a HPBW of $32''$ and

is shown in Figure 5.2. By comparing the $(2 - 1)/(1 - 0)$ line intensities they found some evidence for an S2 radius of $\sim 16''$. However, a 30 m IRAM $J = 2 - 1$ line profile was later presented by Huggins *et al.* (1994) and as can be seen in Figure 5.2 looks remarkably similar, even though it was observed with a smaller $12''$ HPBW. The profile did not show the horned wing signature expected if it had been resolved as discussed in Chapter 1, apparently in conflict with the previous S2 radius estimate. These single dish line profiles also showed no signature of the slower S1 shell and so questions remained about the spatial extent of these two distinct outflow components in the CSE of Betelgeuse. A sensitive high spatial resolution study of its atmosphere was needed to untangle this puzzling evidence.

5.2 Adopted Radial Velocity

Before we discuss the CO($J = 2 - 1$) spectra obtained from our multi-configuration CARMA observations, which are summarized in Chapter 3, we begin by explaining which radial velocity value v_{rad} , for Betelgeuse was adopted. An accurate value of v_{rad} is necessary when plotting the spectra of any star with respect to its center of mass rest frame, as we do for all spectra in this chapter. Plotting spectra in this frame of reference is intuitive as it allows the reader to immediately see the gas expansion velocity relative to the photosphere. A positive v_{rad} denotes recession (i.e., redshifted lines) while a negative v_{rad} denotes advancement (i.e., blueshifted lines).

Betelgeuse is a semi-regular variable and its radial velocity exhibits variability on time scales ranging from short 1.5 year periods as suggested by Stebbins & Huffer (1931) to longer 5.8 year periods (Smith *et al.*, 1989; Spencer Jones, 1928). Stothers & Leung (1971) interpreted the long period as being the convective turnover time of giant convection cells on the stellar surface while Dupree *et al.* (1990) attribute the shorter period with pulsation. Betelgeuse's radial velocity amplitudes are also known to vary by at least $\pm 3 \text{ km s}^{-1}$ (Smith *et al.*, 1989) making it difficult to determine a precise value for the stellar center of mass radial velocity. In Figure 5.3 we plot the radial velocity data and the corresponding model derived in the classical paper by Sanford (1933) which is based on observations spanning 1923 to 1931. We have also extrapolated the model back

5.3 CARMA CO($J = 2 - 1$) Spectra

to show that it matches the earlier data of Bottlinger (1911) and Spencer Jones (1928) quite well, as shown in Figure 5.3. Goldberg (1984) has also shown that the model of Sanford (1933) can be extrapolated forward to give a reasonable fit to his measurements. In this study we adopt a heliocentric radial velocity of $+20.7 \text{ km s}^{-1}$; a value used by Weymann (1962) and Harper *et al.* (2008) and is based on the mean values of Spencer Jones (1928) and Sanford (1933) radial velocity models.

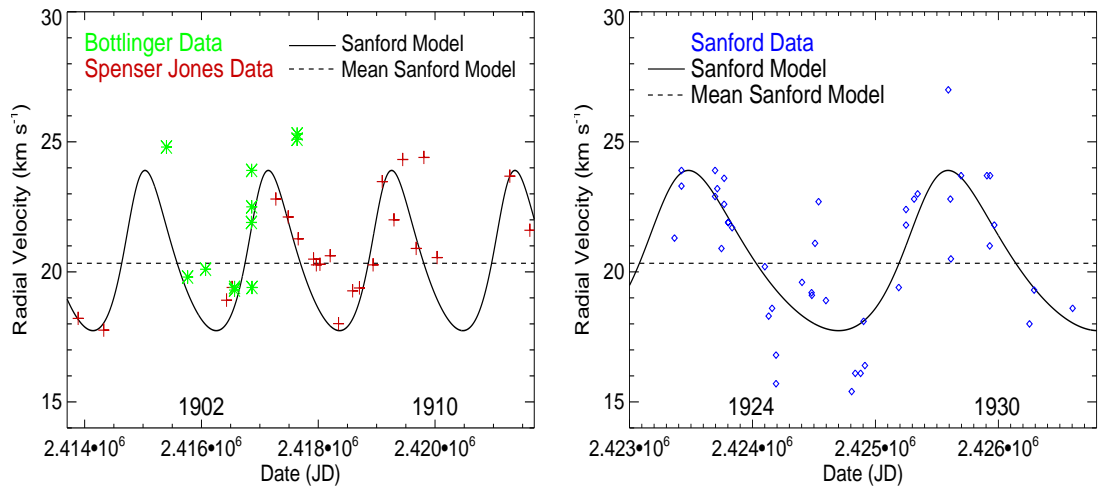


Figure 5.3: The radial velocity model of Sanford (1933) along with measurements from Bottlinger (1911), Spencer Jones (1928), and Sanford (1933) spanning from 1897 – 1931. In this study we use $+20.7 \text{ km s}^{-1}$ which is the mean value from the models of Spencer Jones (1928) and Sanford (1933). The radial velocity amplitude variations of $\sim \pm 3 \text{ km s}^{-1}$ is clearly evident in these data.

5.3 CARMA CO($J = 2 - 1$) Spectra

The spectrum for each individual CARMA configuration image cube (which are composed of all the appropriate configuration tracks listed in Table 3.3) along with the multi-configuration image cube (which is composed of the entire data set spanning $\sim 2.5 \text{ yr}$) can be used to obtain information on the kinematics of the S1 and S2 flows. In particular, it is of interest to see how the CO($J = 2 - 1$) line profile changes when observed with different array configurations as each of these

5.3 CARMA CO($J = 2 - 1$) Spectra

will be sensitive to emission on different spatial scales. The spectra corresponding to the C, D, and E configuration image cubes are plotted in Figure 5.4 for both the high ($0.65 \text{ km s}^{-1} \text{ bin}^{-1}$) and low ($1.3 \text{ km s}^{-1} \text{ bin}^{-1}$) spectral resolution data and were obtained by integrating all emission within a circular area of radius $5''$ centered on the source. The high and low spectral resolution modes allow two independent sets of spectra to be measured for each observation and thus provide a good check on the data quality. The high resolution spectra (channel width = 0.65 km s^{-1}) give the best measure of the S1 and S2 flow kinematics and therefore all outflow velocities are derived from these spectra.

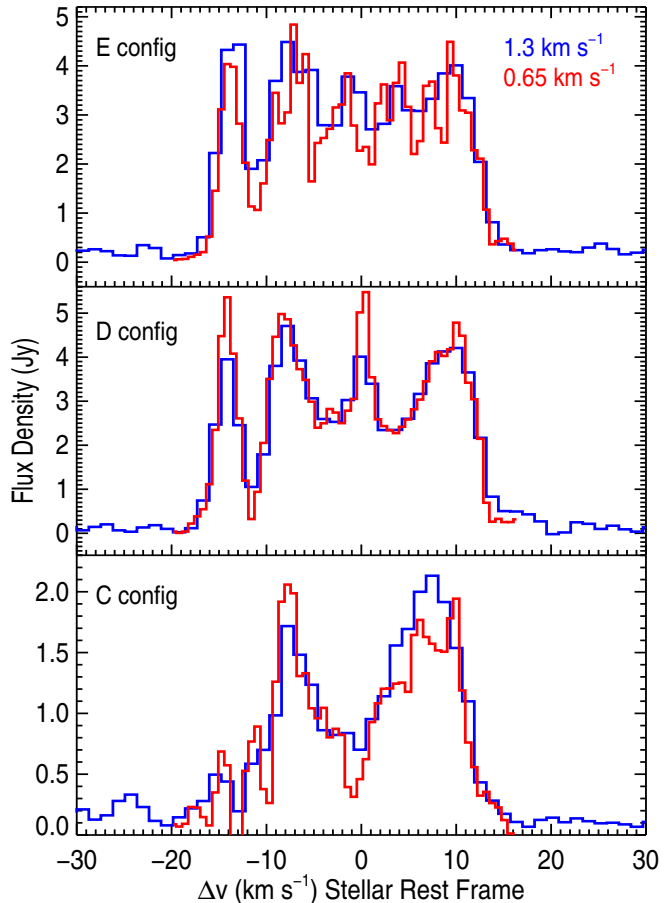


Figure 5.4: Spectra integrated over a radius of $5''$ for each array configuration image cube. The red and blue lines correspond to the high and low spectral resolution data respectively. The blueshifted emission component between -16.0 km s^{-1} and -10.0 km s^{-1} is almost resolved out in the C configuration image cube spectrum along with material with low absolute velocities.

5.3 CARMA CO($J = 2 - 1$) Spectra

The E configuration image cube spectrum has a total line width of 29.2 km s^{-1} and the low spectral resolution profile contains a steep blue wing emission feature between -16.0 km s^{-1} and -11 km s^{-1} and a more flat-topped feature between -10.3 km s^{-1} and $+13.2 \text{ km s}^{-1}$. This steep emission wing shows that the turbulence in the flow is less than or equal to the velocity bin size. The blue wing in the high resolution profile matches the lower resolution profile well but the remainder of the profile looks more complex than the flat-topped feature seen in the lower resolution profile. The line profile shape has been well documented by previous single dish observations (e.g., Figure 5.2) and, out of our three individual configuration spectra, we expect the most compact E configuration spectra to resemble these single dish measurements the closest due to its better sampling of the inner $u - v$ plane and consequent sensitivity to extended structures. This indeed turns out to be the case when we compare our three individual configuration spectra to those previous single dish profiles. The blue wing emission feature appears again in the D configuration spectrum at the same velocities as those in the E configuration spectrum but the remainder of the profile appears quite different. Between -10.3 km s^{-1} and $+13.2 \text{ km s}^{-1}$ the D configuration spectrum is dominated by a blue wing at $\sim -10.0 \text{ km s}^{-1}$, a red wing at $\sim +13.0 \text{ km s}^{-1}$ and an emission feature at $\sim 0 \text{ km s}^{-1}$. The large drop in emission at certain velocities in the D configuration spectrum is probably a result of the lower sensitivity to large scale structure in comparison to the E configuration as described in Table 3.2.

The line profile has a lower flux ($\sim 50\%$) in the high spatial resolution C configuration spectrum due to its lack of sensitivity to extended structure. Notably, the blueshifted emission feature located between -16.0 km s^{-1} and -11.0 km s^{-1} in the E and D configuration spectra is almost completely spatially filtered by the extended C configuration. This component of the line has previously been associated with the outer S2 flow (Huggins, 1987) and as the majority of it has been spatially filtered by our C configuration we expect even less contribution from the S2 flow at even lower absolute velocities. For the redshifted line emission we again expect the majority of the S2 contribution to be spatially filtered, so we conclude that most, if not all of the emission in the C configuration spectrum emanates from the inner S1 flow. The spectrum is double peaked with the blue and redshifted wings extending to $-9.0 \pm 0.7 \text{ km s}^{-1}$ and $+10.6 \pm 0.7 \text{ km s}^{-1}$

5.3 CARMA CO($J = 2 - 1$) Spectra

respectively, and we define these as the outflow velocities of S1. As discussed in Chapter 3 the C configuration has a resolving out scale of $\sim 6''$ at 1.3 mm and so is not sensitive to angular scales larger than this. If the emission between -9.0 km s^{-1} and $+10.6 \text{ km s}^{-1}$ in the C configuration spectrum appeared as a flat topped profile then we could conclude that the S1 flow lies within a radius of $3''$ from the star. Clearly however, the profile has a more *horned* shaped appearance and so the lower absolute velocity components of this profile have been spatially filtered. We can therefore conclude that the radial extent of the S1 from the star is greater than $3''$. If we assume that the S1 flow would produce a 19.6 km s^{-1} wide top-hat line profile of 2 mJy were it not for the resolving out effects of the interferometer, its minimum integrated line flux is then

$$F_{\text{tot S1}} = F_\nu \times \left(\frac{\Delta v}{\lambda} \right) = 3.1 \times 10^{-19} \text{ W m}^{-2}. \quad (5.2)$$

To obtain the most robust value for the S2 outflow velocities we examine the high spectral resolution multi-configuration image cube spectrum which is composed of all tracks from all three configurations. It is worth stressing that by analyzing the multi-configuration image cube we make the assumption that the physical properties of all three components (i.e. α Ori, S1 and S2) have not changed over the total observation period (i.e. ~ 2.5 yr). The profile is found to have a total linewidth of $28.6 \pm 0.7 \text{ km s}^{-1}$, which is in good agreement with previous single dish observations of the line where values of $30.6 \pm 2.5 \text{ km s}^{-1}$ and 28.6 km s^{-1} were reported by Knapp *et al.* (1980) and Huggins (1987), respectively. The centroid velocity of the spectrum is $-1.1 \pm 0.7 \text{ km s}^{-1}$ ($v_{\text{lsr}} = 3.7 \pm 0.7 \text{ km s}^{-1}$) which again is in good agreement with Knapp *et al.* (1980) and Huggins (1987) values of $v_{\text{lsr}} = 3.0 \pm 2.5 \text{ km s}^{-1}$ and $v_{\text{lsr}} = 3.7 \pm 0.4 \text{ km s}^{-1}$, respectively. We use Equation 5.2 to find the integrated total line flux to be $1.5 \times 10^{-18} \text{ W m}^{-2}$, of which at least 20% emanates from the S1 flow.

The outflow velocities of S2 are $-15.4 \pm 0.7 \text{ km s}^{-1}$ and $+13.2 \pm 0.7 \text{ km s}^{-1}$ which, like the S1 flow, are slightly asymmetric but in the opposite sense. Note that the S1 and S2 outflow velocities are dependent on the adopted radial velocity of Betelgeuse. If for instance, we instead adopt a radial velocity of 21.9 km

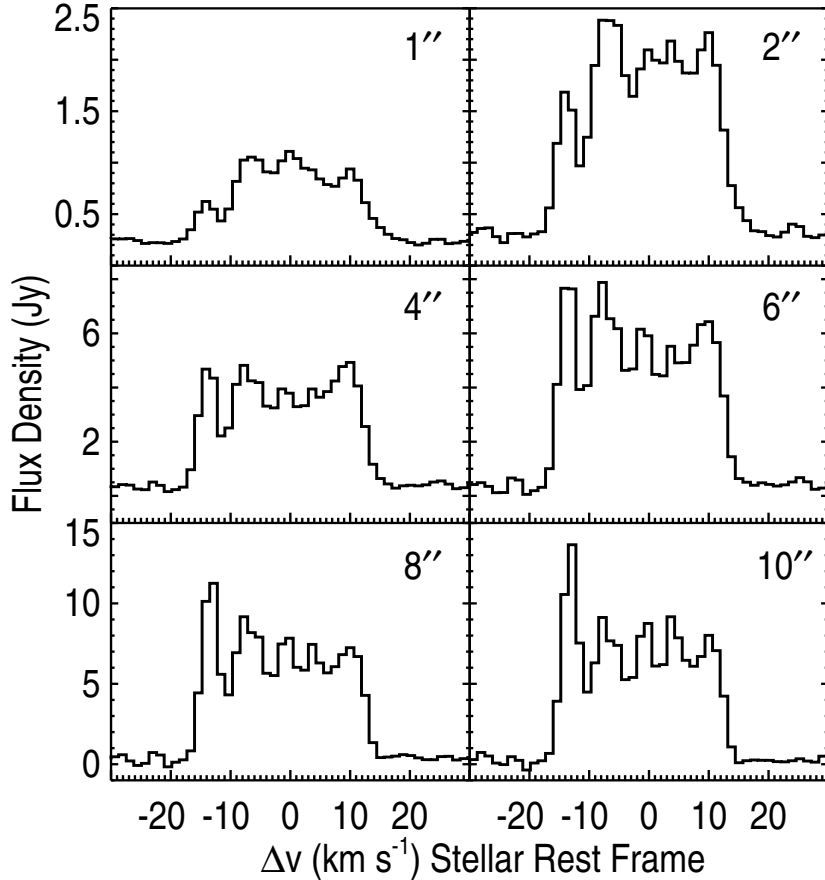


Figure 5.5: Spectral profiles of the low spectral resolution multi-configuration image cube for circular extraction areas of radius 1'', 2'', 4'', 6'', 8'', and 10''. The S/N of the line profile reduces at larger extraction areas as more noise is included from the outer more noisy regions of the channel maps.

s^{-1} ([Famaey et al., 2005](#)) then the S2 outflow velocities become even more asymmetric (-16.6 and +12.0 km s^{-1}) while the S1 outflow becomes less so (-10.2 and +9.4 km s^{-1}). Both S1 and S2 therefore cannot have spherically symmetric outflow velocities regardless of the adopted stellar radial velocity. Adopting a mass of $18 M_{\odot}$ ([Meynet & Maeder, 2003](#)) and a radius of $950 R_{\odot}$ ([Harper et al., 2008](#)) then the escape velocity for Betelgeuse is 85 km s^{-1} which is much greater than the S1 and S2 outflow velocities. This indicates that the majority of the stellar mass loss mechanism's energy goes into lifting the CO molecules out of the gravitational potential and not into their outflow velocities. These outflow velocities

5.4 Individual Configuration Image Cubes

are greater than the adiabatic hydrogen sound speed (i.e., $11.7\sqrt{10^{-4}T_e}$), which, if we assume that the gas temperature is the same as the excitation temperature, are 1.7 km s^{-1} and 1 km s^{-1} for S1 and S2 respectively.

The spectra in Figure 5.5 are taken from the low resolution multi-configuration image cube using circular extraction areas ranging in radius from $1''$ to $10''$ and demonstrates how the line profile changes over these different extraction areas. The most striking change in the line profile is the change in appearance of the extreme blue wing. At small extraction radii where we sample the most compact emission, the feature is weak in comparison to the rest of the line but becomes more dominant as we begin to sample more of the extended emission. This indicates that even the high absolute velocity components of the S2 flow have extended emission and this is why they are almost completely spatially filtered by CARMA's C configuration. The large reduction of flux at -11 km s^{-1} suggests that there is more material moving towards the observer than at other lower absolute velocities indicating a non-isotropic (or non-spherical) S2 flow. This suggests a more sheet like (flatter) structure rather than a spherical cap.

5.4 Individual Configuration Image Cubes

We created three image cubes for each configuration by concatenating all good tracks together per configuration. The gradual formation of a ring type structure as one goes from high absolute velocities to lower absolute velocities indicative of a shell was not seen in any of these three image cubes. However, an additional spatially unresolved source was clearly detected in a number of the D configuration image cube maps (both high and low spectral resolution). The component is present in five continuous channel maps between $\sim -4.0 \text{ km s}^{-1}$ and $+2.4 \text{ km s}^{-1}$ and is located $\sim 5''$ S-W of α Ori. Its peak emission lies at $\sim 0 \text{ km s}^{-1}$ and has a flux density of 1.8 mJy which is approximately 60% of the total source flux density at this velocity. The middle row in Figure 5.6 are two of these D configuration channel maps which clearly show this discrete source. The contour levels are set at the $4\sigma_{\text{rms}}$ level so the detection of the second source in the D configuration is significant. The corresponding channel maps in the E configuration image cube show extended emission out to $8''$ in the same S-W direction as can be seen in

5.4 Individual Configuration Image Cubes

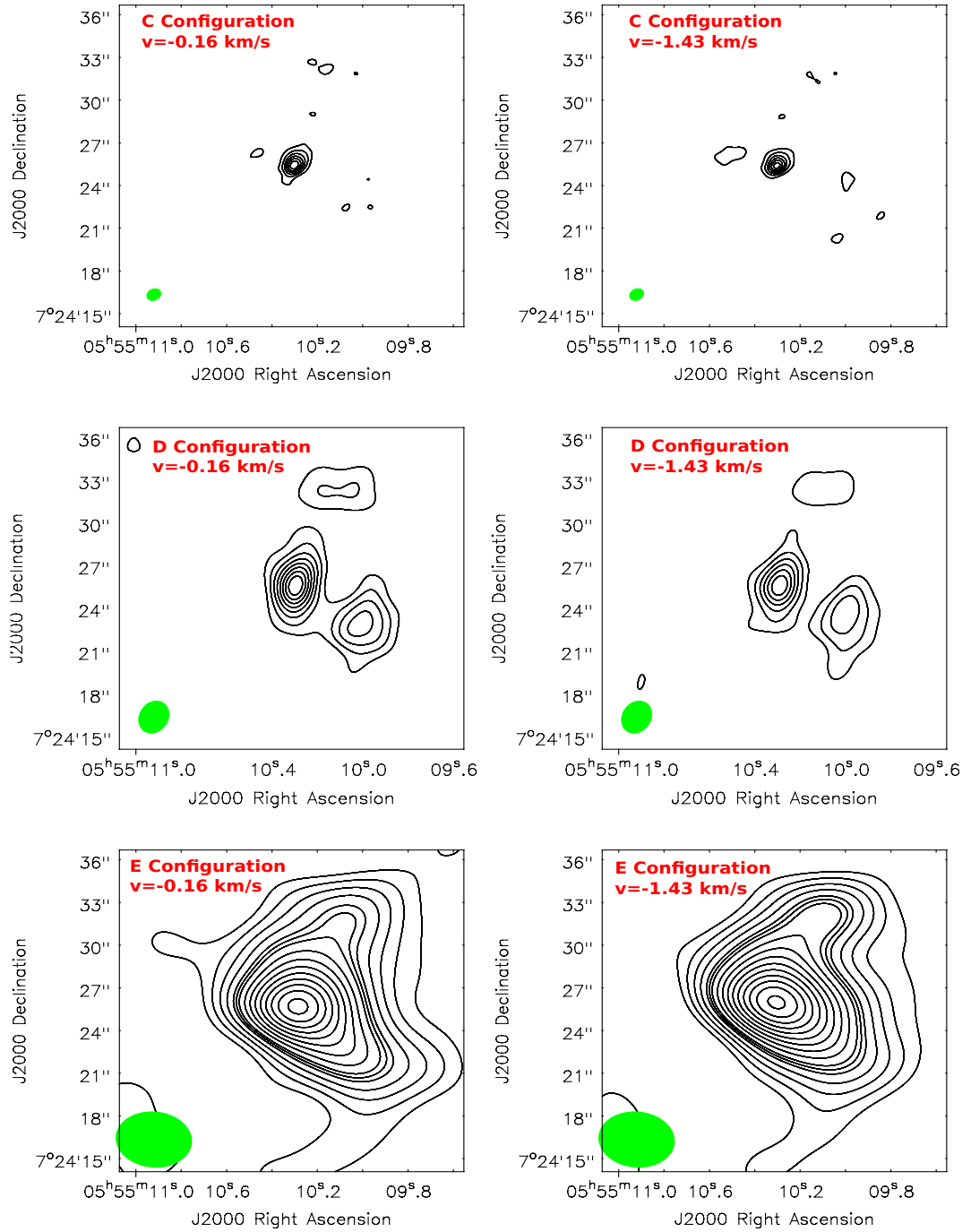


Figure 5.6: Two channel maps from each of the three individual configuration image cubes. A spatially unresolved source is present in five continuous channel maps between $\sim -4.0 \text{ km s}^{-1}$ and $+2.4 \text{ km s}^{-1}$ and is located $\sim 5''$ S-W of α Ori. Contour levels begin at $4\sigma_{\text{rms}}$ where $1\sigma_{\text{rms}}$ is the rms channel noise. The restoring beam is shown in green in the lower left corner of each map.

5.5 Multi-configuration Image Cube Inspection

the lower panel of Figure 5.6. There is only weak emission detected in the same position in the corresponding C configuration channel maps, probably due to the lower sensitivity resulting from the smaller HPBW (i.e., the flux is diluted). This discrete second source thus has the effect of adding extra emission to the corresponding multi-configuration image cube spectrum at the low absolute velocities where it is present. The presence of this addition source at these low absolute velocities is probably one of the reasons why Huggins *et al.* (1994) did not detect a horned shaped spectrum with his 12'' HPBW. We also note that there is a weaker emission feature 7'' north north-west of α Ori in these maps also which too can be seen in Figure 5.6. Finally, the Submillimeter Array CO($J = 3 - 2$) line profile will be discussed in Section 5.10 but here we confirm that its image cube also contains this spatially unresolved source $\sim 5''$ S-W of α Ori at the same velocities.

5.5 Multi-configuration Image Cube Inspection

A subset of the blueshifted velocity channel maps of the low spectral resolution multi-configuration image cube is presented in Figure 5.7. The first channel map at -17.9 km s^{-1} shows just the compact unresolved continuum emission with no extended emission present. Between -16.7 km s^{-1} and -9.0 km s^{-1} we see evidence for the development of a classical shell signature for the S2 flow. We first sample the highest velocity components where the emission is relatively compact (i.e. between -16.7 km s^{-1} and -12.9 km s^{-1}) and then sample lower absolute velocity components where S2 becomes a faint ring (i.e. between -11.6 km s^{-1} and -9.0 km s^{-1}). At lower velocities again, these rings disappear into the noise of the maps and possibly extend out beyond the primary beam at zero velocity where S2 should have maximum spatial extent. The emission from the channel maps between -15.3 km s^{-1} and -11.6 km s^{-1} correspond to all the emission in the extreme blue wing component of the multi-configuration image cube line profile discussed in Section 5.3. We can see in Figure 5.7 that all of this emission is greater than the C configuration resolving out scale of $\sim 6''$, therefore confirming that our C configuration line profile is mainly composed of S1 emission. The shell formation signature of S2 is also apparent in the redshifted velocity channel maps

5.5 Multi-configuration Image Cube Inspection

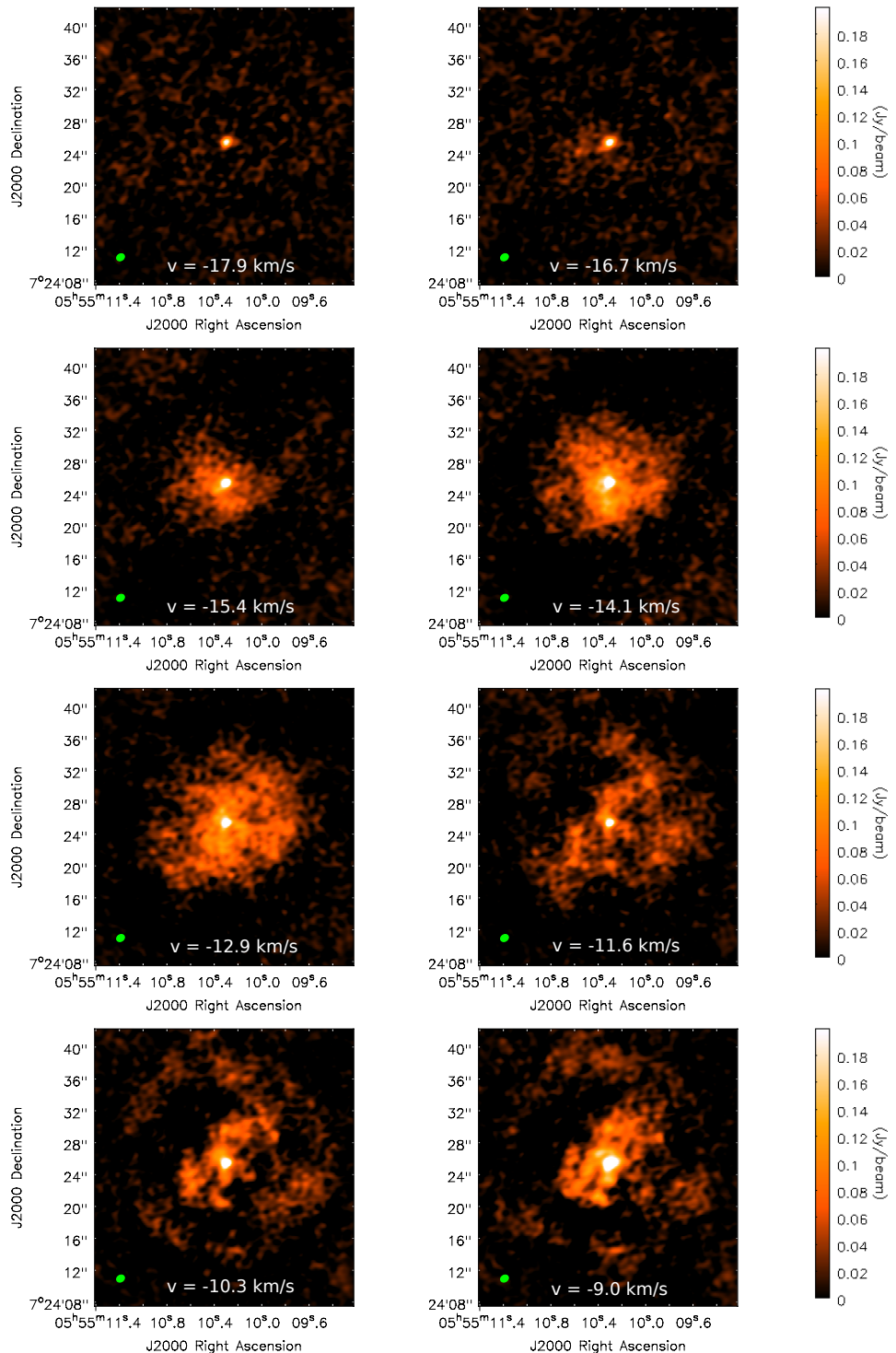


Figure 5.7: 8 channel maps from the multi-configuration image cube ($\Delta v = 1.3 \text{ km s}^{-1}$). The peak emission has been cut at 0.2 Jy beam^{-1} to emphasize the fainter emission. The map at -17.9 km s^{-1} is the star in the continuum while the blue wing of the line starts at -16.7 km s^{-1} . The formation of a weak ring-like structure is seen as one goes from high absolute velocities to lower ones.

5.6 Spatial Extent of S2

between $+7.5 \text{ km s}^{-1}$ and $+13.8 \text{ km s}^{-1}$ but the emission appears weaker and the rings fainter confirming that S2 is inhomogeneous. The multi-configuration maps also show the central compact emission from the S1 flow at velocities between -10.3 km s^{-1} and $+11.3 \text{ km s}^{-1}$. This S1 emission can be seen in the final two maps of Figure 5.7 as a central slightly elongated emission feature surrounded by the fainter rings of the S2 flow.

5.6 Spatial Extent of S2

The spatial extent of the S2 flow around Betelgeuse was not directly determined from either the CO infrared absorption spectra of Bernat *et al.* (1979) or previous CO single dish radio observations (Huggins, 1987; Huggins *et al.*, 1994; Knapp *et al.*, 1980). Our low spectral resolution multi-configuration image cube has sufficient spatial resolution and S/N to make direct estimates of its maximum radius. We find that little or no signature of the S2 flow is present in the low absolute velocity channel maps where its spatial extent is maximum and either lies outside of the primary beam or is lost into the noise near the edge of the maps. Therefore we cannot make a simple direct measurement of its maximum size. However, by measuring how its size varies in the higher absolute velocity maps where it is clearly present allows us to derive its maximum spatial extent.

If we assume that S2 is spherically symmetric with an outer radius R_{S2} , and is undergoing steady expansion with velocity V_{S2} , then its geometry is described by Figure 5.8. As we sample the line at different velocities, the spatial extent of S2 changes and gets progressively larger at lower absolute velocities as can be seen in Figure 5.7. The spatial extent of S2 in each map is

$$r_{\text{chan}} = R_{S2} \times \sin\theta \quad (5.3)$$

which can be directly measured in many of the channel maps. Each of these channel maps have an associated velocity V_{chan} , which we know, and is related to the actual velocity of the S2 flow by

$$V_{\text{chan}} = V_{S2} \times \cos\theta. \quad (5.4)$$

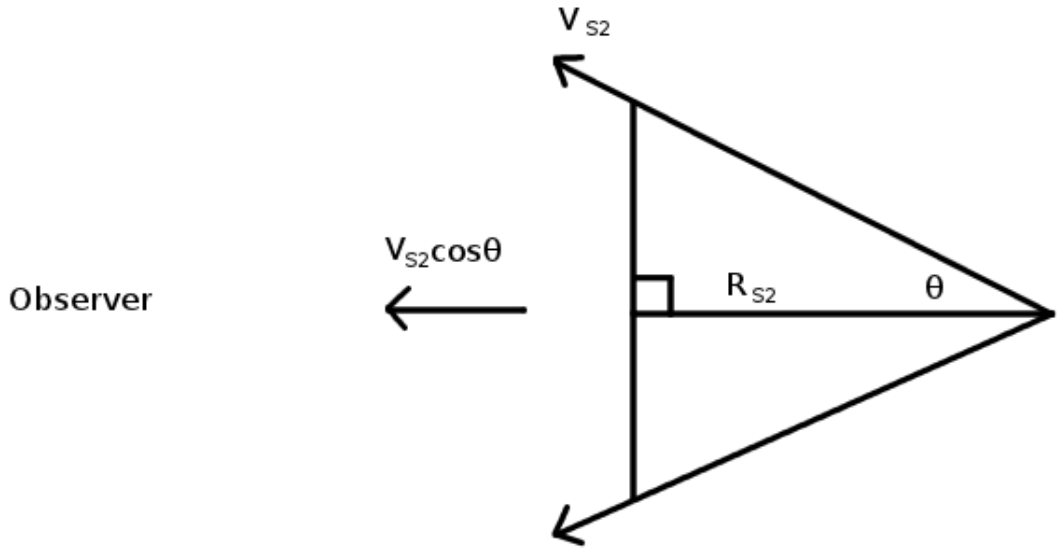


Figure 5.8: Geometry of a spherical symmetric flow used to derive the spatial extent of the S2 flow. By measuring the spatial extent of S2 (i.e., $R_{S2}\sin\theta$) as a function of channel/velocity (i.e., $V_{S2}\cos\theta$) the maximum spatial extent of the S2 flow can be derived.

Combining Equations 5.3 and 5.4 via the angle dependence, gives the following equation which contains R_{S2} as the only unknown parameter,

$$r_{\text{chan}} = R_{S2} \times \sin \left[\cos^{-1} \left(\frac{V_{\text{chan}}}{V_{S2}} \right) \right]. \quad (5.5)$$

An estimate of the S2 radius per channel (r_{chan}) was found by creating annuli of increasing radius around the central emission in each relevant line channel map of the multi-configuration image cube, extracting all flux within each annulus and then plotting the integrated flux against distance from the star for each channel map. The maximum of these resultant curves were then deemed to be the maximum radius of S2 per channel map. Figure 5.9 shows these data overplotted with two model outflows which were created using Equation 5.5. The blueshifted data points were best fitted by a model outflow having a maximum radius 17'' and outflow velocity 16.7 km s^{-1} , while the redshifted data points were best fitted by a model outflow with a maximum radius 16'' and outflow velocity 13.8 km s^{-1} . It is worth mentioning that this estimate for the spatial extent of

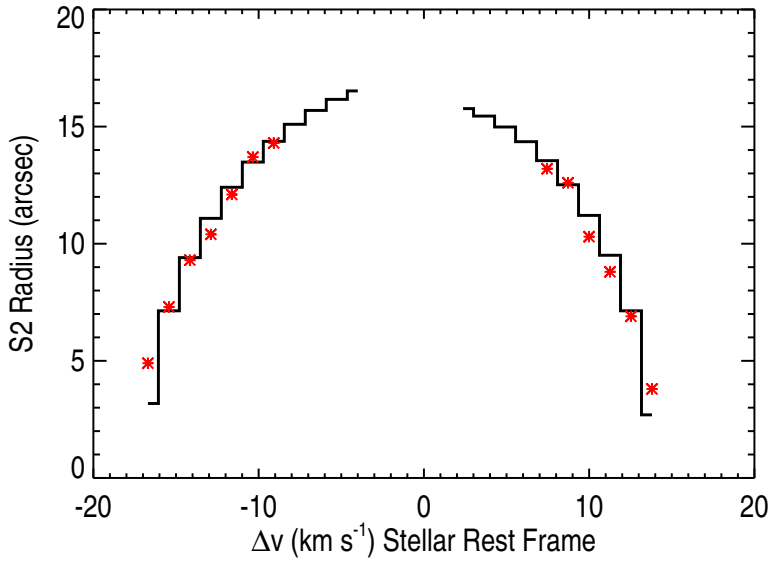


Figure 5.9: The derived S2 radius as a function of velocity (red points) overplotted with two model outflows. The blueshifted model (left) corresponds to an outflow with a maximum radius of 17'' and a velocity of 16.7 km s⁻¹ while the redshifted model (right) corresponds to an outflow with a maximum radius of 16'' and a velocity of 13.8 km s⁻¹. Note: The line profile is 1.9 km s⁻¹ wider in the low resolution image cube ($\Delta v = 1.3$ km s⁻¹) than in the high resolution image cube.

S2 is only weakly dependent on our adopted radial velocity value for Betelgeuse and adopting a slightly different value would simply alter the outflow velocities.

5.7 Intensity distribution of CO

We first investigate how one would expect the intensity of CO to vary as a function of distance from the star for a spherically symmetric optically thin outflow. The CO($J = 2 - 1$) emission line is formed over an extended region around Betelgeuse so a constant outflow velocity can be assumed when investigating the intensity distribution of the S1 and S2 outflow. This allows us to use the equation of mass continuity to find the number density of the molecules in the lower level of the transition, n_l , i.e., $n_l \propto r^{-2}$. The Boltzmann formula can then be used to find

5.7 Intensity distribution of CO

the number density of CO molecules in the upper level, n_u ,

$$n_u(r) = n_l(r) \frac{g_u}{g_l} e^{-(E_u - E_l)/kT_{\text{exc}}(r)} \quad (5.6)$$

where g_u and g_l are the statistical weights of the two rotational levels, and E_u and E_l are their respective energies. Here, T_{exc} is the excitation temperature and equals to the gas temperature if collisions dominate the redistribution of the populations over the rotational ladder. To find the intensity we first need to know the emissivity, j_l , of the line photons which is just $n_u(r)$ times the probability for spontaneous de-excitation per second, A_{ul} , times the energy of the emitted photons, $h\nu$, i.e.,

$$\begin{aligned} j_l(r) &= n_u(r) A_{ul} h\nu \\ &\propto r^{-2} e^{-(E_u - E_l)/kT_{\text{exc}}(r)}. \end{aligned} \quad (5.7)$$

If T_{exc} is constant then the line intensity, I_{CO} , can be written as

$$\begin{aligned} I_{\text{CO}} &= \int j_l(r) dr \\ &\propto r^{-1}. \end{aligned} \quad (5.8)$$

Therefore, the intensity distribution for an optically thin spherically symmetric constant velocity outflow should vary as r^{-1} .

In the left column of Figure 5.10 we investigate the intensity distribution of CO emission as a function of projected radius, R , for both the S1 and S2 flows. From our discussions in Section 5.3 we can assume that all line emission between $-15.4 \rightarrow -10.3 \text{ km s}^{-1}$ and $+12.4 \rightarrow +13.8 \text{ km s}^{-1}$ emanates solely from the S2 flow. Using the low spectral resolution multi-configuration image cube we integrate the surface brightness over these channels and find that the intensity fall-off is close to being proportional to R^{-1} (Figure 5.10: *top left*). To investigate the S1 flow intensity distribution around α Ori we integrate the surface brightness over the channels between $-9 \rightarrow +10.6 \text{ km s}^{-1}$. Although these channels contain emission from both S1 and S2, most of the S2 emission here will have larger projected radii and thus the majority of the inner emission should emanate from the S1 flow. Between $0.5''$ and $4''$ from the star the intensity is again found to be close

5.7 Intensity distribution of CO

to proportional to R^{-1} (Figure 5.10: bottom left). We have just showed that such an intensity distribution is expected for an optically thin spherically symmetric constant velocity outflow with $\rho \propto 1/R^2$. Beyond $\sim 6''$ the intensity fall off is more rapid and is steeper than a R^{-2} distribution and may be caused by factors such as a variation in the thermal or velocity profile, or even the absence of emitting material altogether. This region may mark the initiation of the current epoch of mass loss.

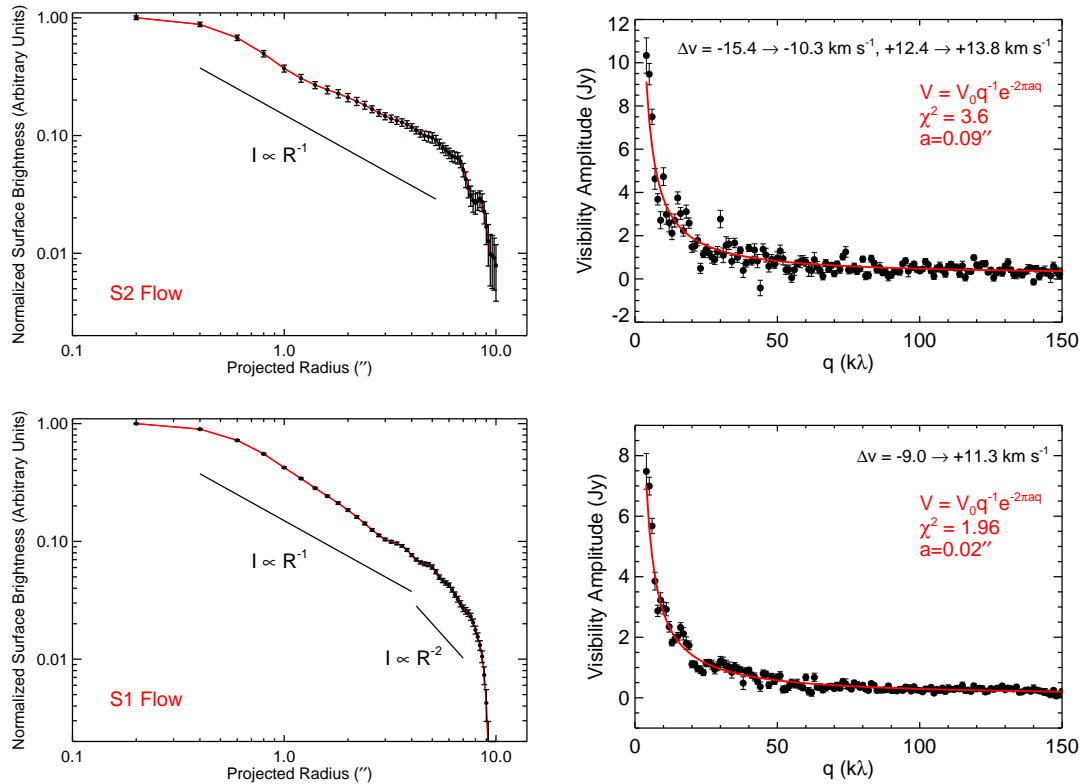


Figure 5.10: *Left Column:* Surface Brightness as a function of projected radius on sky, R (red line). The emission has been extracted from the low spectral resolution multi-configuration image cube and is integrated over the channels where S1 is present (bottom) and over the channels where only S2 is present (top). Intensity proportional to R^{-1} and R^{-2} is also shown for comparison. *Right Column:* The corresponding visibility amplitude as a function of $u-v$ distance (q) of both outflows can be modeled well by a R^{-1} fall off in intensity. The error bars in all plots represent the standard error of the mean.

Insight can also be gained into how the intensity varies on different size scales by conducting analysis in the $u - v$ plane and plotting the visibility amplitude of our CO data against $u - v$ distance. The result of this is shown in the right column of Figure 5.10 where the same channels corresponding to the S1 and S2 flows defined in the last paragraph have been used. The data are azimuthally averaged, and have been binned to produce one data point per $k\lambda$. The result for both the S1 and S2 data is a steep drop-off in visibility amplitude over a relatively short $u - v$ distance, signaling that the sources are well resolved, as expected. Both sets of visibility data are consistent with an intensity proportional to $(a^2 + R^2)^{-1/2}$, where a is an inner spatial limit. This is because the Hankel transform of this function is $q^{-1}e^{-2\pi aq}$ (Bracewell, 2000), where q is the $u - v$ distance, and a vertically scaled version of this function is shown to match the visibility data very well in Figure 5.10. As analysis in both the sky and $u - v$ plane indicate the intensity of both flows is proportional to R^{-1} we conclude that both outflows are consistent with an optically thin and quasi-steady flow which is in agreement with Smith *et al.* (2009) (i.e., S1) and Plez & Lambert (2002) (i.e., S2).

5.8 Spatial Extent of S1

It is difficult to exactly determine of the maximum spatial extent of the S1 flow as we do not see the classical shell formation signature as we sample across velocities, like we do for the S2 flow. Its spatial extent varies in different channel maps and, as can be seen in Figure 5.11, the emission is very inhomogeneous/clumpy. This clumpy nature of the S1 flow has been previously reported in other studies (Kervella *et al.*, 2011; Smith *et al.*, 2009) and Smith *et al.* (2009), who studied photospheric scattered emission, estimated its spatial extent to lie within $3''$ from the star. At 20% of maximum emission in the integrated intensity S1 map (i.e. composed of all channels between $-9 \rightarrow +10.6 \text{ km s}^{-1}$) the S1 flow extends out to a mean distance of $\sim 4''$ and is even more extended in the S-W direction due to the presence of the second emission feature in the compact configuration data sets. Even though the emission is inhomogeneous, the intensity when averaged on the sky is consistent with a $\sim R^{-2}$ density distribution out to $\sim 6''$, as discussed

in Section 5.7, and may mark the end of the S1 flow. The HPBW of $0.9''$ is not sufficient to determine whether the S1 flow is discrete or an extension of the current wind phase seen in ultraviolet spectra (e.g., Carpenter & Robinson, 1997) and cm-radio continuum interferometry (Lim *et al.*, 1998).

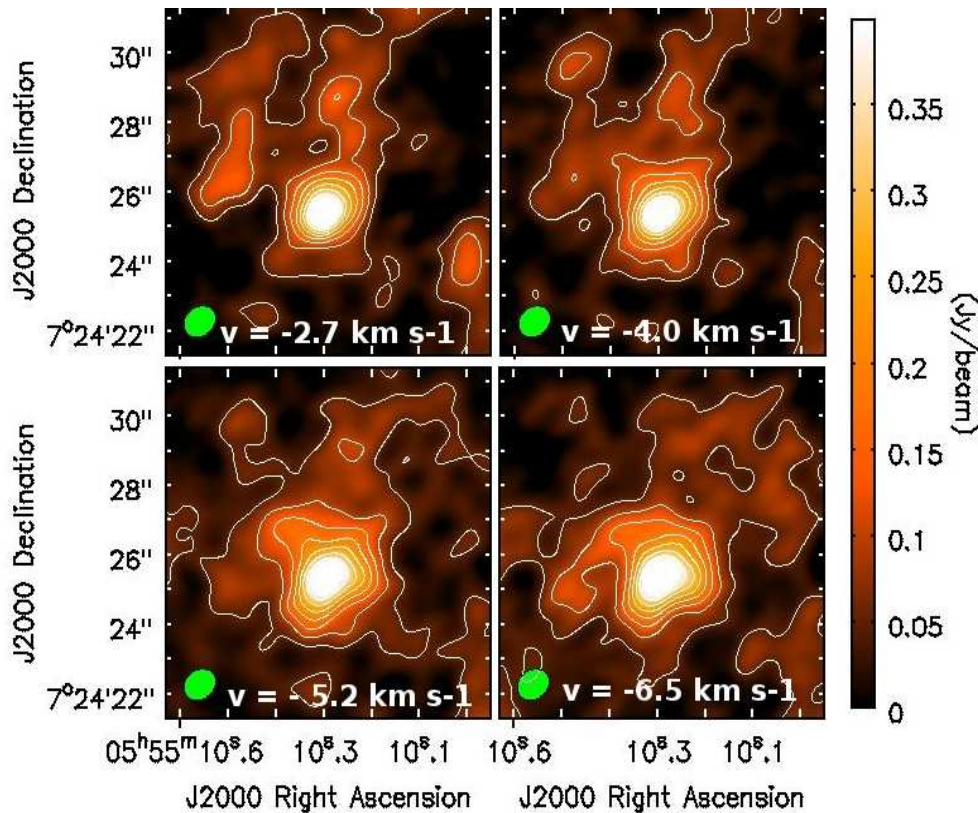


Figure 5.11: CARMA combined image cube low spectral resolution, 1.3 km s^{-1} , maps of the inner S1 flow. These maps are $10'' \times 10''$ in size and show the irregular nature of the S1 emission around the star. Going clockwise from the top left panel, the channel map velocities are -2.7 , -4.0 , -5.2 , and -6.5 km s^{-1} . The restoring beam is shown in green in the bottom left of each map. Contour levels are at $(3, 6, 9\dots) \times \sigma_{\text{rms}}$ where $\sigma_{\text{rms}} = 16 \text{ mJy beam}^{-1}$.

5.9 Continuum Flux Densities

Betelgeuse is known to show brightness variations at many continuum wavelengths. Goldberg (1984) reports a decrease of half a magnitude in visual bright-

5.9 Continuum Flux Densities

ness over a period of six years. [Bookbinder *et al.* \(1987\)](#) found stochastic 30%-40% variations in flux density at 6 cm over timescales as short as 10 days to as long as 8 months (i.e. the observational period). A more comprehensive study was carried out by [Drake *et al.* \(1992\)](#) who observed Betelgeuse with the VLA at centimeter wavelengths from 1986 to 1990 and found stochastic variability of 22%, 15%, and 21% at 6 cm, 3.6 cm, and 2 cm respectively, at a variety of different timescales down to less than one month (a possible source for this variability will be described in Section 5.11). The mm-continuum emission that we measure arises mainly from electron-ion and electron-atom bremsstrahlung (also the source of the longer wavelength continuum emission) and possibly dust emission, so it is not unreasonable to also expect variability at mm-wavelengths too.

Table 5.1: CARMA Continuum Fluxes at 230 GHz between 2007 → 2009.

Configuration	Date ("×")	Restoring Beam	Flux (mJy)	Uncertainty (mJy)
C	2007 Jun	0.96×0.76	234	18
D	2009 Jul	2.33×1.87	389	72
E	2009 Nov	4.93×3.84	278	40
Multi-configuration	2007 → 2009	1.05×0.84	289	21

In Table 5.1 we list the derived continuum flux densities for each of the three configuration image cubes and also the multi-configuration image cube. The high spectral resolution ($\Delta v = 0.65 \text{ km s}^{-1}$) image cubes were just wide enough to image the CO line but were too narrow to make accurate estimates of the continuum flux density. Therefore, all continuum flux density estimates are derived from the lower spectral resolution ($\Delta v = 1.3 \text{ km s}^{-1}$) image cubes from which we were able to take accurate measurements at both sides of the line. We fitted elliptical Gaussians to ~ 20 continuum channels using CASA's *imfit* routine allowing the flux and corresponding uncertainties to be calculated. The source was unresolved in most of these continuum channels. The D configuration data were acquired under adverse weather conditions and these data have the highest noise levels out of the three configurations. Its continuum emission measurement is approximately 50%

5.10 Higher CO rotational lines

greater than the C and E configuration continuum measurements which were also acquired approximately two years after the D configuration data. We believe the continuum emission value of 289 ± 21 mJy derived from the multi-configuration image cube is a reasonable estimation of the mean mm-continuum flux density over the 2.5 yr period, 2007 → 2009. It is in reasonably good agreement with the 250 GHz flux density of [Altenhoff *et al.* \(1994\)](#) who report a mean value of 351 ± 25 mJy for 1986 → 1989.

5.10 Higher CO rotational lines

As part of our larger multi-wavelength study of the CO surrounding Betelgeuse we were also able to obtain emission line profiles of higher rotational CO lines. First we observed the star (PI Harper: ID 81-0005-1) with the German Receiver for Astronomy at Terahertz Frequencies (GREAT; [Guesten *et al.*, 2000](#)) instrument on NASA and DLR's Stratospheric Observatory for Infrared Astronomy (SOFIA; [Becklin & Gehrz, 2009](#)) 2.5 m airborne observatory. Observations of the CO($J = 12 - 11$; 1.382 THz) line were made during Flight 86 on 2011 November 10 at 13,100 m ($\sim 43,000$ ft) when the star had an elevation of 45° . The HPBW was $\sim 19''$ and the effective on source exposure time was 12 minutes which was considerably lower than the requested on source time of 70 minutes due to technical difficulties during the flight. We also obtained 4.1 hours on source at 345 GHz with the Submillimeter Array (SMA; [Blundell, 2007](#)) on 2012 January 12 (PI J. Brown: ID 2011B-S051). The SMA is a submillimeter interferometer located atop Mauna Kea in Hawaii and consists of eight antennas each 6 m in diameter. Our data were acquired in the compact configuration ($B_{\max} = 70$ m) which at the observing frequency of ~ 345 GHz gave a synthesized beam of 5×4.5 arcsec 2 (similar to the CARMA E configuration at 230 GHz). We obtained very high spectral resolution ($\Delta v = 0.088$ km s $^{-1}$) of the CO($J = 3 - 2$; 345.796 GHz) line which is more than a factor of 7 better than the highest spectral resolution CARMA CO($J = 2 - 1$) line, and also a weak detection of the SiO($J = 8 - 7$; 347.331 GHz) line at a spectral resolution of 0.55 km s $^{-1}$. Finally we obtained archival data of the CO($J = 6 - 5$; 691.473 GHz), CO($J = 10 - 9$; 1.15198 THz), and CO($J = 16 - 15$; 1.84135 THz) rotational lines which were obtained with

5.10 Higher CO rotational lines

the Heterodyne Instrument for the Far Infrared (HIFI; [de Graauw *et al.*, 2010](#)), on board the Herschel Space Observatory ([Pilbratt *et al.*, 2010](#)). The HPBW for these lines were 31'', 18'', and 11.5'' respectively.

We plot all these line profiles in order of decreasing excitation energy in the stellar rest frame in Figure 5.12 to allow easy comparison. The profiles have been binned to 1.3 km s^{-1} spectral resolution to match the CARMA low resolution profiles described in Section 5.3, except for the SMA profiles which have exquisite resolution. In this figure the dashed vertical red lines mark the derived outflow velocities of the S1 flow from Section 5.3. This figure clearly demonstrates that the CO rotational lines get narrower as one goes from lower rotational levels to higher ones, i.e., as the excitation temperature increases. A noticeable consequence of this is the evolution of the contribution of the S2 blueshifted component which is the dominant feature in the CO($J = 2 - 1$) combined configuration CARMA profile; its relative strength in relation to the rest of the line dramatically reduces at higher excitation temperatures. This indicates that the higher lines are predominately formed in the S1 flow region. The SOFIA CO($J = 12 - 11$) profile is found to have a line width of $\sim \pm 7.5 \text{ km s}^{-1}$ when centered on the stellar rest frame but because the higher S/N ratio CO($J = 16 - 15$) HIFI profile is slightly wider, the narrowness of the SOFIA line is probably due to its low S/N ratio. The weak SiO($J = 8 - 7$) line profile is unfortunately contaminated with an atmospheric absorption feature but its linewidth is comparable to the CO($J = 3 - 2$) line profile meaning that SiO is also present in the S2 flow. Previous searches for SiO in the CSE of Betelgeuse have been unsuccessful (e.g., [Lambert & Vanden Bout, 1978](#)) and this may be the first, albeit weak, detection of the molecule.

For the lower rotational line profiles it is difficult to infer the level of flux contribution from each of the S1 and S2 components making the analysis of integrated line flux ratios difficult. Also, some of these profiles shown in Figure 5.12 were obtained over many years with different instruments and techniques. It appears likely however, that the majority of the emission in the higher rotational profiles [i.e., the CO($J = 16 - 15$), CO($J = 12 - 11$), and CO($J = 10 - 9$) line profiles] emanates from the S1 flow, while the other lower level lines contain various amounts of emission from both flows. However, the CO($J = 12 - 11$) line profile has a low S/N ratio and its flux scale is rather uncertain due to the poor

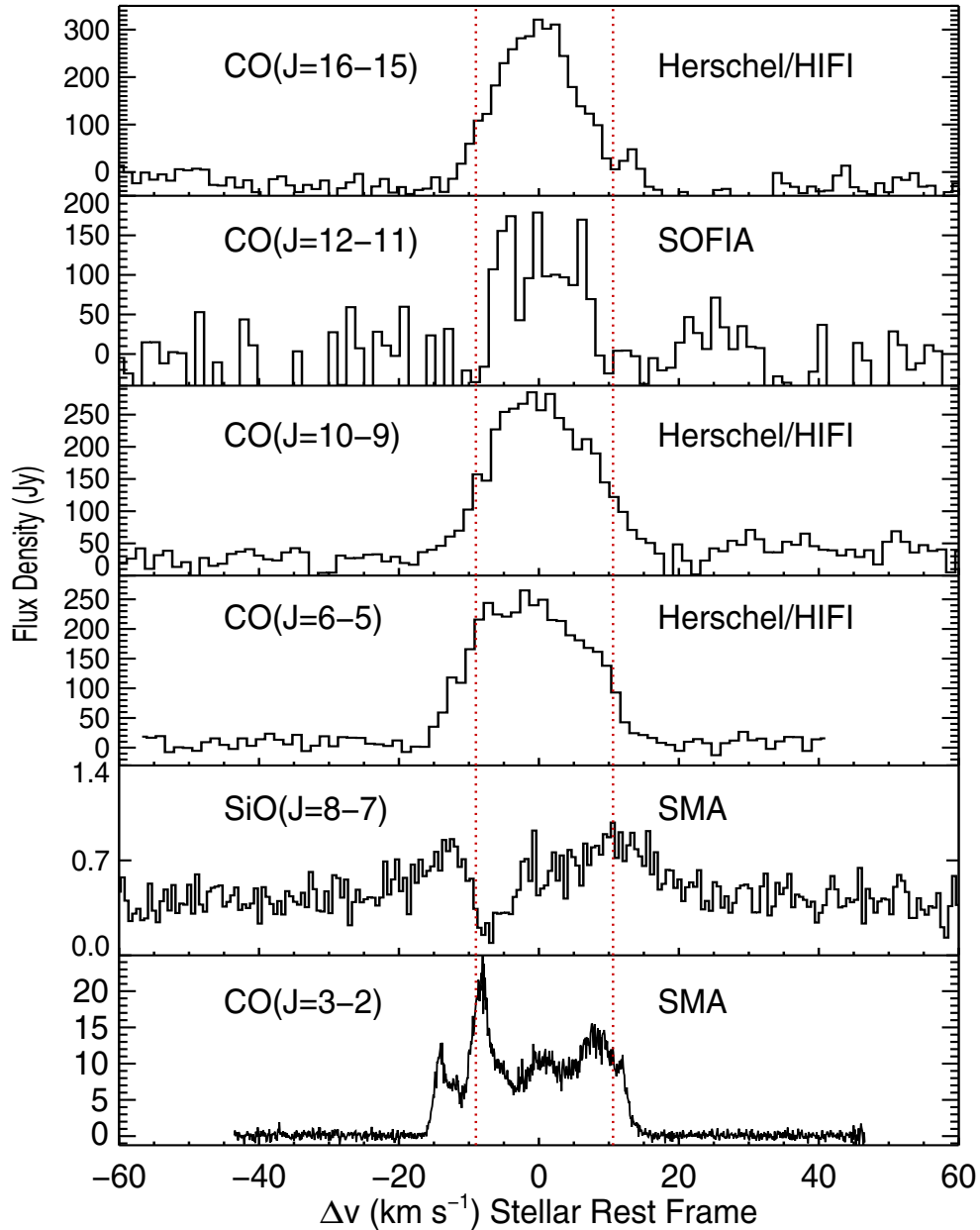


Figure 5.12: CO and SiO rotational emission lines from the CSE of Betelgeuse. The lines are listed in order of decreasing excitation energy from top to bottom and are plotted in the stellar rest frame. The vertical dashed red lines mark the outflow velocities of the S1 flow. At higher excitation energies the relative strength of the blueshifted S2 feature in relation to the rest of the line decreases dramatically and the lines get narrower overall indicating that the higher excitation lines are formed mainly in the S1 flow.

5.11 CARMA CO observations in Context

pointing accuracy during our SOFIA-GREAT observation. For this reason only the Herschel/HIFI CO($J = 16 - 15$) and the CO($J = 10 - 9$) line profiles are suited for probing the thermodynamics of one of the flows, i.e., the S1 flow. The ratio of the integrated flux from these two rotational emission lines in a linear molecule like CO can be written as

$$\frac{F_{10-9}}{F_{16-15}} = \left(\frac{J_{10-9}}{J_{16-15}} \right)^5 \exp \left(\frac{B[J_{16-15}(J_{16-15} + 1) - J_{10-9}(J_{10-9} + 1)]}{kT_{\text{exc}}} \right) \quad (5.9)$$

where F , J , and B are the integrated line flux, the rotational quantum number, and the rotational constant respectively. For the CO molecule $B/k = 2.77$. The integrated line fluxes for the CO($J = 16 - 15$) and the CO($J = 10 - 9$) profiles are 2.4×10^{-16} and 1.8×10^{-16} W m² respectively. Equation 5.9 can then be used to show $T_{\text{exc}} = 220$ K which is in excellent agreement with Bernat *et al.*'s 1979 value of 200^{+50}_{-10} K for the S1 flow.

5.11 CARMA CO observations in Context

We have found the spatial extent of the S2 flow to be greater than the HPBWs of some of the previous single dish antenna observations of the CO($J = 2 - 1$) line. So why was did these line profiles not show the classical resolved signature of high emission at large absolute velocities and low emission at low absolute velocities? First, the S1 flow was still unresolved in these single dish observations and thus contributes emission and at the lower absolute velocities. As well as this, the multi-configuration CARMA maps show that the S2 emission is brighter at higher absolute velocities than at lower absolute velocities and so when the emission from the fainter rings is neglected (i.e. when observed with a small HPBW), the overall line profile does not change significantly. Finally, our maps have revealed that some discrete strong emission features are present at low absolute velocities which would also have been present in the HPBW of previous single dish observations, thus contributing the line profile flux at these velocities.

The main properties of the S1 and S2 flows which have been derived in the previous sections of this chapter are summarized in Table 5.2. Assuming a mean outflow velocity of 14.3 km s⁻¹ and 9.8 km s⁻¹ for the S2 and S1 flows respectively

5.11 CARMA CO observations in Context

then their ages are ~ 1100 yr and $\sim 400 - 600$ yr. Since [Plez & Lambert \(2002\)](#) have detected K I out to $55''$ at a similar velocity (18 ± 2) to the CO S2 flow, then, assuming the CO and K I are coupled, there appears to be little further acceleration in Betelgeuse's outflow once the S2 flow begins (which is somewhere greater than $6''$).

Table 5.2: Summary of the S1 and S2 Flow Properties.

	S1	S2
Outflow Velocities (km s^{-1})	$-9.0 \pm +10.6$	$-15.4 \pm +13.2$
Maximum Spatial Extent ('')	$\sim 4 \rightarrow 6$	~ 17
Age (yr)	$\sim 400 \rightarrow 600$	1100

Despite decades of research, it is also unknown if Betelgeuse's loses mass through episodic ejections or through more of a constant and global process. We have shown that when averaged across the sky, the variation in mean density is consistent with a spherically symmetric and constant velocity outflow. However, the presence of clumping is also evident in our radio maps and emission from the S2 flow appears weaker at redshifted stellar rest frame velocities indicating an inhomogeneous flow. Higher spatial resolution studies like those described in the following sections, are needed to determine if clumping is a result of growing instabilities in a global outflow or as a product of the mass loss mechanism. The reason for two unique velocities in the outflow are also a puzzle. One possibility is that the dust properties change at $\sim 6''$ and lead to a sudden increase in speed. However, the S2 component has a small velocity component along the line of sight ([Bernat et al., 1979](#)) and appears as a shell like structure in our CARMA data so this scenario is unlikely. Another possibility is that the mass loss mechanism is magnetic in origin and that these components represent phases in the order of ~ 600 yr of a stellar dynamo cycle. In this scenario, then one would expect more tenuous flows further out still. Such flows could be detectable with ALMA by mosaicing many images together to overcome the limited field of view of the antennas.

5.12 e-Merlin 6 cm Results

The first detailed study of Betelgeuse at centimeter wavelengths was carried out by [Newell & Hjellming \(1982\)](#) who observed the star at multiple wavelengths (20, 6, 2, and 1.3 cm) in a compact VLA configuration. The star was unresolved but a radio spectral index of 1.32 was derived and the radio emission was interpreted as emanating from a spherically symmetric, partially ionized chromosphere with an temperature of $\sim 10,000$ K extending from 1 to $4 R_\star$, in agreement with the Alfvén wave models of the time ([Hartmann & Avrett, 1984](#)). The star was first spatially resolved at radio wavelengths by [Skinner *et al.* \(1997\)](#) with both the old VLA in its most extended configuration, and MERLIN (the predecessor to e-MERLIN). The data were taken ~ 2.5 yr apart and it was found that the 6 cm radio emitting region was up to three time larger than the optical photosphere. The spatially resolved multi-wavelength study of [Lim *et al.* \(1998\)](#) revealed a cool, low hydrogen ionization inner atmosphere. To reconcile these observations with spatially resolved UV observations [Gilliland & Dupree \(1996\)](#) which showed a much warmer inner atmosphere, [Lim *et al.* \(1998\)](#) concluded that there must be at least 3 orders of magnitude more cooler plasma than hot chromospheric plasma. This is because the radio opacity of the warm gas is much greater than that of the cooler gas and yet the radio observations preferentially detect the cooler gas. We now discuss the recent findings of [Richards *et al.* \(2013\)](#) who observed Betelgeuse at 6 cm with the very long baseline interferometer, e-MERLIN.

e-MERLIN ([Muxlow, 2003](#)) consists of seven radio antennas spread out across the United Kingdom that are connected via a fiber optic network to a central correlator at Jodrell Bank Observatory. It will eventually be able to observe in three frequency bands at 1.3–1.8 GHz, 4–8 GHz, 22–24 GHz, and its maximum baseline of 220 km will provide resolution up to 10 mas at the μ Jy sensitivity level. Betelgeuse was observed at 5.76 GHz (5.2 cm) in 2012 July with e-MERLIN as part of Cycle-0 observations, with a total bandwidth of 0.512 GHz. The final high resolution image which is shown in Figure 5.13 had a $\sigma_{\text{rms}} = 9 \mu\text{Jy}$ and was produced using uniform weighting with a restoring beam of 80×60 mas². The first thing to notice about the radio map is the presence of three clumps of radio emission in the south-west quadrant approximately 250 mas ($11.5 R_\star$)

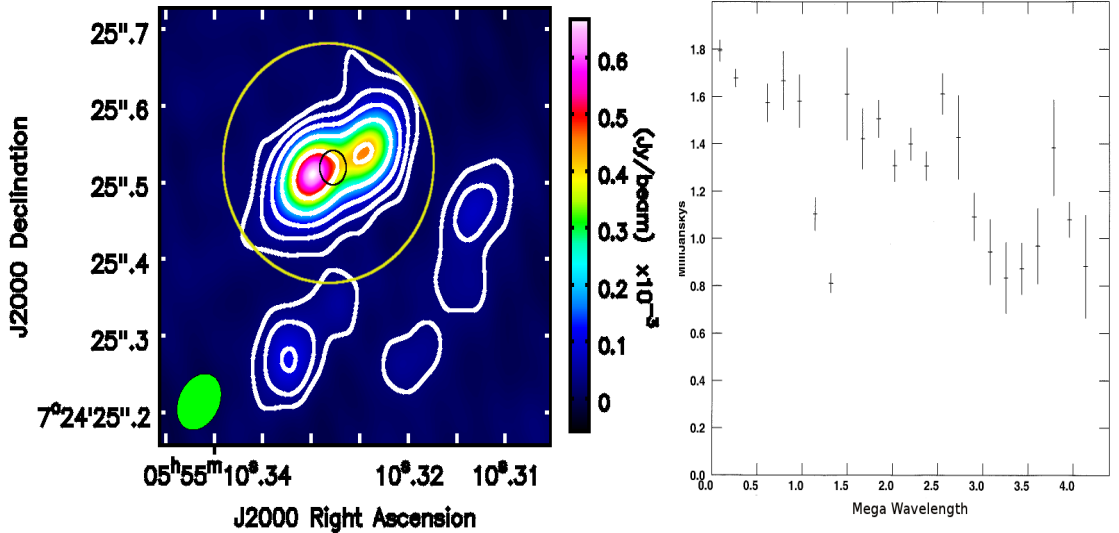


Figure 5.13: First e-MERLIN results for Betelgeuse. *Left:* 5.2 cm e-MERLIN image of Betelgeuse taken in July 2012 showing two unresolved emission features separated by 90 ± 10 mas. The image was restored with a 80×60 mas 2 beam marked in green in the lower left corner and using uniform weighting. Contour levels are at $(-3, 3, 6, 12, 24, 48) \times \sigma_{\text{rms}}$ where $\sigma_{\text{rms}} = 9 \mu\text{Jy}$. The photospheric radius is the small black circle while the large yellow circle defines the 6 cm radio disk of Lim *et al.* (1998). *Right:* The calibrated visibility amplitudes (in mJy) versus $u - v$ distance measured in mega-wavelengths with the possible signature of two unresolved components with a brightness ratio differing from unity.

from the star, with detections ranging from 4 to $12\sigma_{\text{rms}}$. These clumps of radio emitting plasma are probably the remnants of past localized episodic mass loss events from the star, which as they escaped the gravitational potential of the star, expanded, cooled allowing hydrogen to recombine and thus in the process becoming fainter radio continuum emitters than they initially were. Assuming a mean constant flow velocity of 10 km s^{-1} (assuming the velocity of the S1 flow), then this plasma was ejected from the star ~ 22 yr prior to these observations. The time since ejection could in fact be much larger than this (~ 90 yr) if the slow wind acceleration profile given in Harper *et al.* (2001) is assumed.

The second and more remarkable feature of the image is that the star at

6 cm appears as two unresolved peaks separated by ~ 90 mas. To make sure this unexpected result was not an artifact of the imaging process we plotted the visibility amplitude as a function of baseline (i.e., $\sqrt{u^2 + v^2}$) as shown also in Figure 5.13. If we had fully resolved a standard uniform disk, which should be a good first order approximation for any *standard* star, then we would expect the visibility amplitude to drop to zero at some baseline, which clearly does not happen. On the other hand, the visibility amplitude for a double source would depict two peaks with the minimum visibility amplitude being a function of the component brightness ratio. For equal brightness (i.e., the ratio is 1) the first visibility amplitude minimum drops to zero but does not for sources of different brightness (Saha, 2011). Therefore, the visibility amplitudes of our calibrated data appear to be in agreement with what is seen in the final image, i.e., two sources of different brightness producing a sinusoidal visibility pattern which does not drop to zero.

The brighter feature was found to have a brightness temperature of $T_b = 5,400 \pm 600$ K while the weaker feature had $T_b = 3,800 \pm 500$ K. To find the position of the optical photosphere, Richards *et al.* (2013) took the peak flux position from a low resolution radio map which was optimized for sensitivity to extended structure. In this scenario the two features, referred to as *hotspots* by Richards *et al.* (2013) are located 1.0 ($T_b = 5,400$ K) and $1.5 R_\star$ ($T_b = 3,800$ K) from the optical photosphere. A more rigorous approach to finding the position of the optical photosphere is to use the astrometric solutions derived in a study to find the distance to Betelgeuse (solution 5 in Harper *et al.*, 2008) and propagate these forward to find its expected position in 2012 July. Doing this we get RA = 05:55:10.3250 and dec = +07:24:25.536 which includes the correction for parallax. We plot this expected position on top of the e-MERLIN map in Figure 5.14. Interestingly, this puts the expected optical photospheric position almost directly on top of the weaker emission feature. The effective temperature of Betelgeuse is 3,650 K (Levesque *et al.*, 2005) which is slightly below the brightness temperature derived for this feature but well within its errors (i.e., $T_b = 3,800 \pm 500$ K). If this weaker source is indeed the optical photosphere, then the brighter source with $T_b = 5,400 \pm 600$ K is located at least $3.5 R_\star$ from the

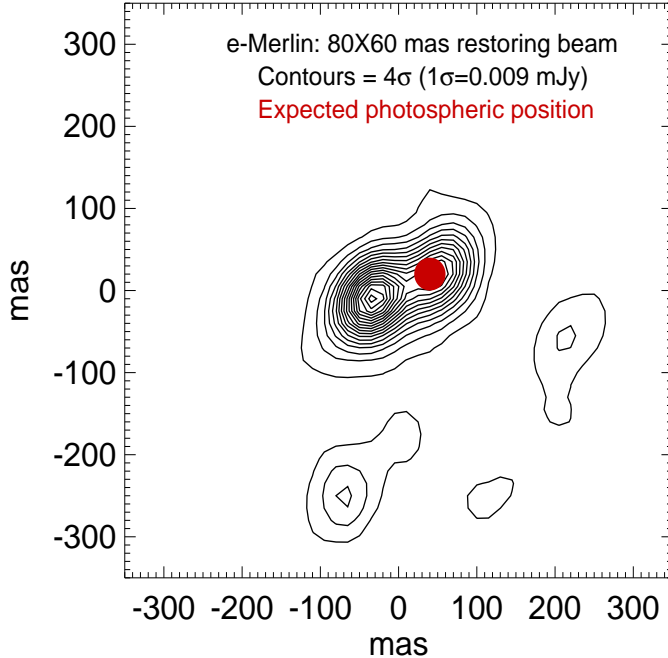


Figure 5.14: The red filled circle marks the predicted position of the optical photosphere of Betelgeuse on 2012 July using the astrometric solutions of [Harper et al. \(2001\)](#). The black contours represent the high spatial resolution 6 cm image of the star from [Richards et al. \(2013\)](#) and are at the $4\sigma_{\text{rms}}$ level. This solution puts the optical photospheric position almost at the position of the weaker unresolved peak.

surface of the optical photosphere. Its value is significantly higher than that predicted in the spherically symmetric semi-empirical model of [Harper et al. \(2001\)](#) who predict a value of 2,300 K at a projected radius of 95 mas (i.e., $3.5 R_\star$ from the photosphere).

The semi-empirical model of [Harper et al. \(2001\)](#) is the current *state of the art* inner (i.e., $1 \rightarrow 10 R_\star$) atmospheric model for Betelgeuse. It consists of a detailed mean density and temperature one-dimensional model and is based on the spatially resolved VLA data of [Lim et al. \(1998\)](#). In this model the temperature distribution peaks at $1.45 R_\star$ where it reaches ~ 3800 K and decreases to ~ 1200 K at $10 R_\star$. The dominant source of electrons is from photoionized metals while hydrogen has a low level of ionization. We use this model to create

5.12 e-Merlin 6 cm Results

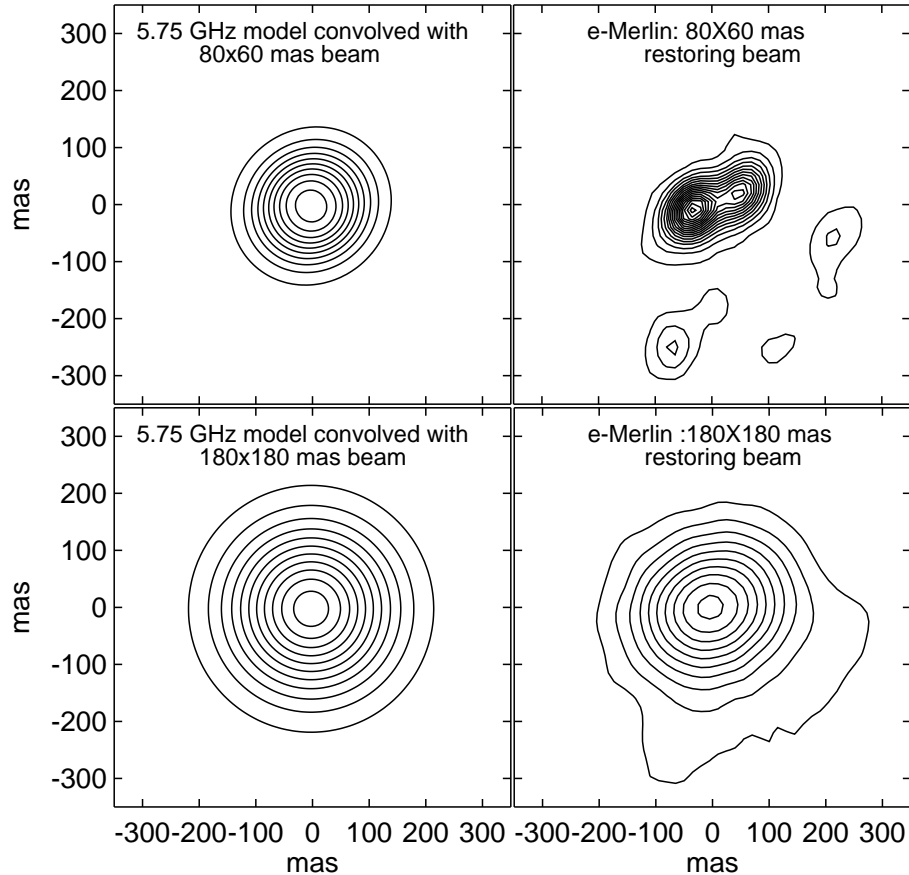


Figure 5.15: *Left column:* Two-dimensional specific intensity contour maps at 5.2 cm (5.75 GHz) created using the one-dimensional inner atmospheric model of Betelgeuse by [Harper *et al.* \(2001\)](#) described in the text. The maps have been convolved with a beam having dimensions $80 \times 60 \text{ mas}^2$ (top) and $180 \times 180 \text{ mas}^2$ (bottom). *Right column:* The observed high (top) and low (bottom) resolution e-MERLIN images. The high resolution image is a poorly described by the model of [Harper *et al.* \(2001\)](#) highlighting the inadequacies of one-dimensional spherically symmetric models in describing the inner atmosphere of Betelgeuse. Contour levels are $(4, 8, 12, \dots) \times \sigma_{\text{rms}}$ where $\sigma_{\text{rms}} = 6 \mu \text{Jy}$ in the top row and $\sigma_{\text{rms}} = 27 \mu \text{Jy}$ in the bottom row.

a two-dimensional spherically symmetric specific intensity map to examine how it compares with the new e-MERLIN high resolution data at 5.2 cm (5.75 GHz). As shown in Figure 5.15, we convolved this map with a restoring beam, first with dimensions $180 \times 180 \text{ mas}^2$ to match the low resolution e-MERLIN image and then with dimensions $80 \times 60 \text{ mas}^2$ to match the high resolution e-MERLIN

5.13 VLA-Pie Town Maps vs e-MERLIN

image. As can be seen from Figure 5.15, the atmospheric model of [Harper *et al.* \(2001\)](#) does a good job in reproducing the low resolution e-MERLIN image but, as would be expected from a spherically symmetric 1-D model, fails to reproduce the more complex structure which is seen in the higher resolution e-MERLIN image. The advent of the new e-MERLIN interferometer with its superior spatial resolution to that of the VLA has revealed that 1-D spherically symmetric atmospheric models are probably inadequate to describe the inner atmospheric conditions of Betelgeuse. Time dependent models which radically diverge from spherical symmetry will ultimately be needed to accurately describe the inner atmospheric conditions of Betelgeuse.

5.13 VLA-Pie Town Maps vs e-MERLIN

At the end of Chapter 3 we describe the VLA-Pie Town observations of Betelgeuse from the early 2000's along with the motivation for analyzing it. In summary, we wanted to see if there were some signatures of the e-MERLIN asymmetries in the data set. This is because the Pie-Town link, when connected to the VLA, provides spatial resolution comparable to or exceeding that of the high resolution e-MERLIN image at the shortest wavelengths. The two main features present in the e-MERLIN map were separated by ~ 90 mas and so the most interesting VLA-Pie Town data sets were the 0.7, 1.3, and 2.0 cm maps which had restoring beams of $\sim 40 \times 25$, $\sim 80 \times 40$, and $\sim 120 \times 90$ mas² when imaged with uniform weighting.

All the data sets listed in Table 3.8 were CLEANed using uniform weighting and using a conservative, slow CLEAN to accommodate the frequent elliptical shape of the beam caused by the Pie Town link. The images were subsequently investigated for signs of asymmetries. The 6 cm VLA-Pie Town data sets had synthesized beams typically of size $\sim 380 \times 270$ mas² which was far too large to be capable of resolving the structures seen with e-MERLIN at similar wavelengths. As expected, the VLA-Pie Town 6 cm images show no signs of asymmetries. In fact, all data sets at wavelengths at or longer than 1.3 cm show no obvious asymmetries apart from that caused by the asymmetric nature of the restoring beam. This is surprising because the north-west location of the Pie Town antenna

5.13 VLA-Pie Town Maps vs e-MERLIN

relative to the VLA array results in an elliptical beam with a semi-minor axis lying in the same direction as that of the two peaks seen with e-MERLIN, i.e., the beam shape should be well suited to resolving these peaks. There are two possible reasons why the shorter wavelength VLA-Pie Town maps do not contain the asymmetries which are present in the longer wavelength e-MERLIN map:

1. In an ionized or partially ionized outflow, the radio opacity, $\kappa_\lambda \propto \lambda^{2.1}$. This means that the longer wavelengths probe further out in the atmosphere than the shorter wavelengths. It may be possible that at the short wavelengths (where the VLA-Pie Town data have the expected resolution to image these features) the outer atmosphere where the features are located is optically thin and therefore the features are not present in the short wavelength VLA-Pie Town maps. However, the e-MERLIN data has shown that the outflow is clearly not spherically symmetric. In fact, the radio opacity also varies as, $\kappa_\lambda \propto n_e n_{\text{ion}}^2$ and because the e-MERLIN features should be more ionized than the surround plasma, they could be present even at the shortest wavelengths.
2. The VLA-Pie Town data were taken ~ 10 yr prior to the e-MERLIN data when the separation of the two peaks was probably less. This reduction in separation may be significant and may make them unresolvable even at the shortest wavelengths. Let us now consider this possibility and estimate their separation 10 yr prior to the e-MERLIN observations. First, as highlighted in the Section 5.12, the astrometric solutions of [Harper et al. \(2008\)](#) indicate that the star is located on the weaker emission peak. If we then assume that the stronger emission peak has been moving away from the star at the velocity of the S1 flow (i.e, 10 km s^{-1}) then the distance traversed in 10 yr would be $\sim 4.8 R_\star$ which means that these features would not have been resolvable. However, the outflow is still expected to be accelerating with velocities only between $1 - 7 \text{ km s}^{-1}$ within these spatial scales ([Carpenter & Robinson, 1997](#)) and so the actual distance traversed is probably less.

Nevertheless, at these spatial scales the structural changes over a few years is probably important and may be the reason for not seeing the expected asymmetries in the VLA-Pie Town data. In fact, if the star is close to the center of

these two peaks as was assumed by Richards *et al.* (2013), then the two features are presumably moving away from each other which would strengthen the idea that time variability is the reason why they are not seen in the VLA-Pie Town data. The discovery of these bright radio peaks by Richards *et al.* (2013) along with their notable absence in data with superior resolution less than 10 yrs before is a compelling case for consistent monitoring with e-MERLIN over a number of years.

5.14 Long Term Radio Variability

Betelgeuse's atmosphere is optically thick at radio wavelengths allowing its radio flux to be characterized as resulting from an opaque disk with $F_\nu \propto T_e \phi_\nu^2$. This relationship tells us that variations in radio flux are caused by changes in size or changes in the gas temperature distribution. The size of the radio emitting region is controlled mainly by the distribution in ionized material. Betelgeuse has been observed at radio wavelengths since the mid 1970's (e.g. Newell & Hjellming, 1982). Bookbinder *et al.* (1987) found that the 6 cm flux can vary by as much as $\sim 40\%$ on a 20 day timescale while Drake *et al.* (1992) monitored the star over a four year period and reported stochastic flux variability at 2.0 and 3.6 cm of $\lesssim 25\%$ and possibly at 6 cm on a timescale $\lesssim 1$ month. Here we report on how the radio flux has varied during the period 1996 – 2004 using the measurements of Lim *et al.* (1998) and the archival VLA-Pie Town data.

To obtain a value for the total flux at each wavelength and epoch, we fitted 2-D elliptical Gaussians to the source to obtain the integrated flux. To get a better fit to the 0.7 cm data, (where the source size was found to be asymmetric as outlined in the next section) we re-imaged the visibilities using natural weighting and then carried out the fit. We plot the resulting flux densities against time in Figure 5.16 and also include the measurements of Lim *et al.* (1998). We find significant variability at all at all wavelengths and at all epochs apart from the 2002 data sets which were only obtained two months apart from each other. Over the 10 yr period, the maximum variability is found to be 53, 72, 78, 42, and 90% at 0.7, 1.3, 2.0, 3.5, and 6.2 cm respectively which are well above those reported by Drake *et al.* (1992) and Bookbinder *et al.* (1987). Between 2003 and

2004 all wavelengths show an increase in flux. This may be a coincidence since the radio emission comes from different layers of the stars atmosphere and the timescale for a change to propagate from the shortest wavelength layer to the longest wavelength layer would be a couple of years. The shortest wavelengths (i.e., 0.7 and 1.3 cm) are at the most sampled and although there are only five data points at these wavelengths to compare, there does appear to be a correlation in their flux variability. The contribution functions given in [Harper *et al.* \(2001\)](#) show that the peak flux contribution at both 0.7 and 1.3 cm come from a similar region of the atmosphere (i.e., $\sim 1.2 R_\star$) and so at these wavelengths a correlation is not surprising.

The red dot-dash line and the blue dotted line in Figure 5.16 represent the mean of the two 1.3 and 2.0 cm flux density values between 1978 – 1981 ([Newell & Hjellming, 1982](#)) which are not significantly different from our maximum measurements at the same wavelengths. This would indicate that there has been no significant long term change in atmospheric or thermal structure over ~ 3 decades. However, our data indicates that large structural changes or thermal changes occur over the order of only a few years. The dashed red line represents the 6 cm flux of [Richards *et al.* \(2013\)](#) which lies within the range of 6 cm values observed between 1996 and 2004. This is surprising because most of the 6 cm flux in the e-MERLIN map is contained in the two bright features and as we see no evidence for these features in our VLA-Pie Town data, we would expect the 6 cm flux in the e-MERLIN map to be larger. This adds weight to the idea discussed in Section 5.13 that the e-MERLIN feature(s) are optically thin at the shorter VLA wavelengths and therefore are not detectable in our highest resolution data sets. Nevertheless, the large variations at 6 cm could still indicate that these features undergo large structural changes on timescales of only a few years or perhaps even shorter.

5.15 0.7 cm VLA-Pie Town Maps

All the VLA-Pie Town data were imaged using uniform weighting where each unit of area in the $u - v$ plane is given the same weight irrespective of the number of visibility measurements it contains. The 0.7 cm (i.e., Q band) maps which are

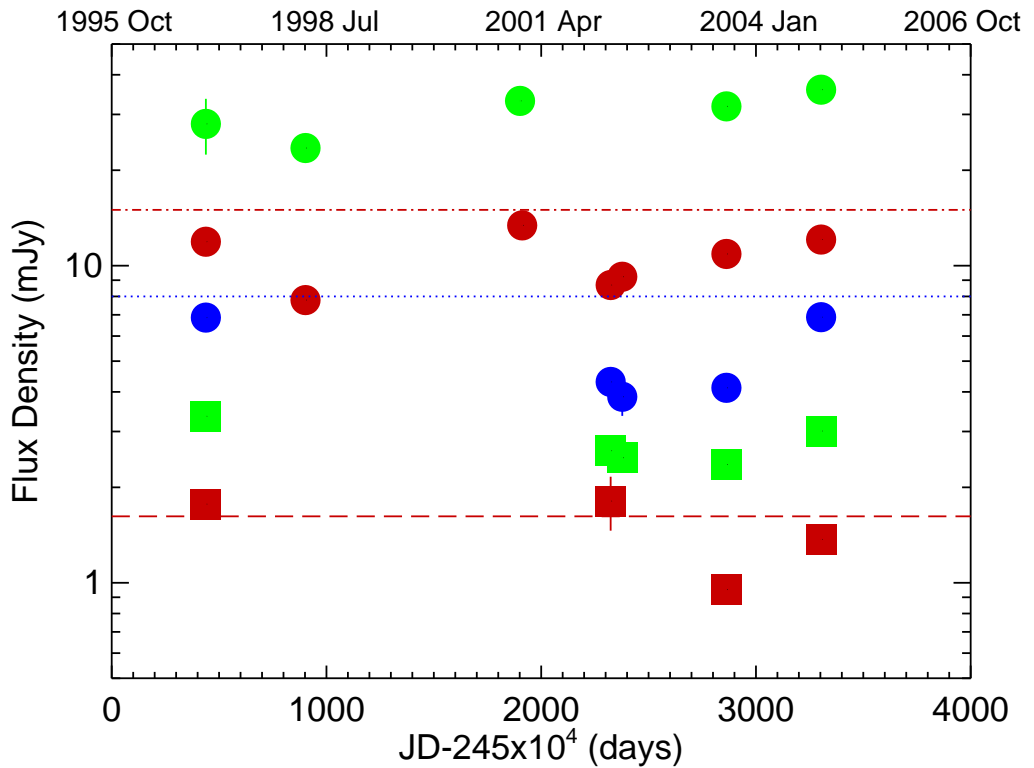


Figure 5.16: Radio flux density variation of Betelgeuse between 1996 and 2004. The green, red, and blue filled circles are the 0.7, 1.3, and 2.0 cm measurements respectively, while the green and red filled squares are the 3.5 and 6.2 measurements, respectively. The red dot-dash line and the blue dotted line represent the mean of two 1.3 and 2.0 cm flux density values taken between 1978-1981 and are not significantly different from the data plotted. The dashed red line represents the e-MERLIN 6 cm flux from 2012 and lies within the range of 6 cm values observed between 1996 and 2004.

presented in Figure 5.17 were the only ones to show significant asymmetric structure in them. The 2004 and 2003 data contain two and three distinct unresolved features respectively, all separated from each other by only ~ 40 mas. The elongated restoring beam in the 2000 data set makes it difficult to detect any distinct features in the north south direction although asymmetries are clearly present at a high level of significance. Finally the 1998 data set which does not contain the Pie Town link but has a very circular restoring beam once again looks highly asymmetric but in a different direction to the other epochs.

5.15 0.7 cm VLA-Pie Town Maps

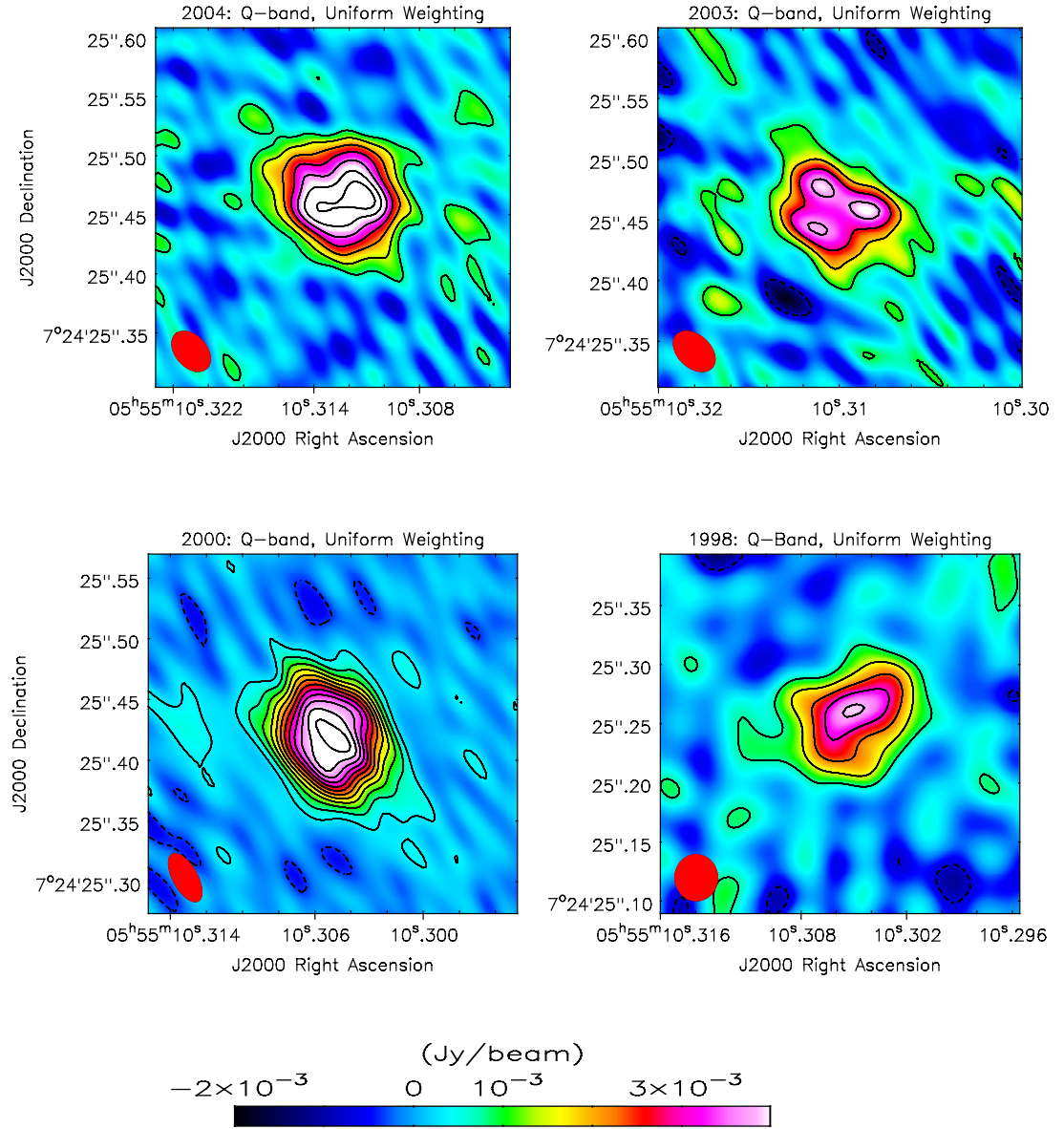


Figure 5.17: High resolution Q band images of Betelgeuse spanning six years. Asymmetries in the inner atmosphere are clearly present in all images. Image contours are set at $(2, 4, 6, \dots, 24) \times \sigma_{rms}$ where $\sigma_{rms} = 0.35, 0.46, 0.18$, and 0.38 mJy for the 2004, 2003, 2000, and 1998 data respectively. The restoring beam is shown in red at the bottom left corner of each image. The 1998 data does not contain the Pie Town link and thus has a more circular restoring beam. The color scheme in all images have the same scaling, i.e., between -2 and $+4$ mJy. Each image represents 300×300 mas 2 in area.

5.15 0.7 cm VLA-Pie Town Maps

These high resolution data sets appear to indicate dramatic changes in the radio emitting topology over a time period of only one to two years. The relatively small separation of the distinct unresolved features indicate that they are probably located in the lower chromosphere and may be formed by the large scale convective features believed to exist on the photospheric surface of all red supergiants ([Schwarzschild, 1975](#)). In fact, using optical interferometry, such features have been confirmed to exist on the surface of Betelgeuse (e.g., [Buscher *et al.*, 1990](#); [Tuthill *et al.*, 1997](#); [Wilson *et al.*, 1992](#)). [Stothers & Leung \(1971\)](#) believed that the long period brightness variation of 2100 days present in Betelgeuse's optical continuum emission were related to the giant convection cell turnover time. However, [Schwarzschild \(1975\)](#) claimed that their evolution may be as short as 200 days and optical observations appear to agree with this ([Tuthill *et al.*, 1997](#)). These timescales would then be consistent with our findings. What we may actually be observing at 0.7 cm is the convective overshoot of these convection cells into an overall weakly ionized atmosphere ([Gray, 2008](#); [Josselin & Plez, 2007](#)) releasing the hotter more ionized plasma which radio observations are sensitive to. The changes in the radio emitting topology evident in Figure [5.17](#) caused by this convection cell overshoot may then be the source of the radio flux variability discussed in Section [5.15](#).

6

Multi-wavelength Radio Continuum Emission Studies of Dust-free Red Giants

The vast increase in bandwidth coverage of the new VLA now allows possible detections of historically weak or undetectable red giants at multiple radio wavelengths. In this chapter we present and analyze the most comprehensive set of multi-wavelength thermal radio continuum observations of two standard luminosity class III red giants, Arcturus (α Boo: K2 III) and Aldebaran (α Tau: K5 III), to date. We report the first detections at several wavelengths for each star including a detection at 10 cm (3.0 GHz: S-band) for both stars and a 20 cm (1.5 GHz: L-band) detection for α Boo. This is the first time single luminosity class III red giants have been detected at these continuum wavelengths. We compare our data with published semi-empirical atmospheric models based on UV data, and spectral indices are used to discuss the possible properties of the stellar atmospheres. Finally, we develop a simple analytical wind model for α Boo based on our new long wavelength flux measurements. This chapter is based on the main findings of O’Gorman *et al.* (2013).

6.1 Why Study Red Giants with the VLA?

Although studies of wind-scattered UV and optical line profiles have provided clues to the mass loss rates and radial distribution of the mean and turbulent velocity fields, the thermal structure remains poorly constrained. In the UV, the source function S_ν , of electron collisionally excited emission lines is sensitive to electron temperature T_e , (i.e., $S_\nu \propto e^{-h\nu/kT_e}/\sqrt{T_e}$). Therefore, a localized hot plasma component in a dynamic atmosphere can completely dominate the temporally and spatially averaged emission and hence not reflect the mean radial electron temperature distribution. At radio wavelengths however, the source function is thermal and is just the Rayleigh-Jeans tail of the Planck function, which is linear in electron temperature (i.e., $S_\nu = 2kT_e\nu^2/c^2$). This should give a more appropriate estimate of the mean radial electron temperature. It is this value that controls the atomic level populations and ionization of the mean plasma which is needed to quantify the implied thermal heating supplied to the wind by the unknown driving source/sources, allowing constraints on potential mass loss mechanisms to be derived.

In the cm-radio regime the radio opacity κ_λ , strongly increases with wavelength (i.e., $\kappa_\lambda \propto \lambda^{2.1}$) and so the longer wavelengths sample the extended layers of a stars atmosphere, thus providing us with spatial information about the star's mass outflow region. The VLA is sensitive to over three orders of magnitude in continuum optical depth τ_λ , ($\tau_{20 \text{ cm}}/\tau_{0.7 \text{ cm}} \approx 10^3$) and provides an area-averaged sweep through the wind acceleration zone of evolved late-type stars. The thermodynamic properties in this spatial region control the ionization in the far wind because the ionization balance, which also controls the cooling rates, becomes *frozen-in* at large radii due to advection. Furthermore, it is these outer extended regions of the star's atmosphere that contribute to the commonly seen P Cygni line profiles in the UV. In these profiles the line-of-sight absorption caused by the star's wind is superimposed on the blueshifted scattered emission. Thus, centimeter radio continuum observations can provide a test of models based on these UV profiles.

Despite the importance of radio continuum emission as a tool for studying cool evolved stellar outflows, red giants are feeble emitters at these wavelengths

however, and previous observations have provided only a small number of modest signal-to-noise measurements slowly accumulated over three decades. As most of our VLA observations were carried out over just a few days, we have obtained a unique snapshot of the different stellar atmospheric layers sampled at different wavelengths, independent of any long-term variability.

6.2 Radio Maps

Apart from α Boo at C-band and α Tau at S-band, detections were made in every sub-band for the 2011 data. For all other bands, the flux densities of the targets in both sub-bands were found to be the same within their uncertainties so we do not present separate values here. Instead we give the values from the radio maps produced by concatenating the two sub-bands. We present in Table 6.1 the target flux densities extracted from these concatenated radio maps. In each of these maps the flux density from the unresolved target source was calculated by, 1) taking the peak pixel value from the source, 2) manually integrating the flux density around the source, and 3) fitting an elliptical Gaussian model to the source and deriving the integrated flux density using the CASA *imfit* task. Each of these values along with the image rms noise measured from adjacent background regions and fitting error produced by *imfit* are given in Table 6.1 to indicate the quality of each radio map. Both sources are point sources at all frequencies so the peak flux value given in Table 6.1 will also be its total flux density value. For weak detections (i.e., $F_\nu \lesssim 5\sigma$) we avoid using the *imfit* task to obtain a flux density estimate, as this may produce biased parameter estimates (Taylor *et al.*, 1999). The flux density values used in the following Sections are the peak values listed in Table 6.1. We assume absolute flux density scale systematic uncertainties of 3% at all frequencies (Perley & Butler, 2013). In the following two sections we briefly discuss the properties of these maps for both targets which are shown in Figure 6.1.

6.2.1 α Boo Maps

High S/N detections ($>19\sigma$) of α Boo were made at 22.5, 33.6, and 43.3 GHz. Some residuals of the dirty beam remained in the CLEANed maps due to the

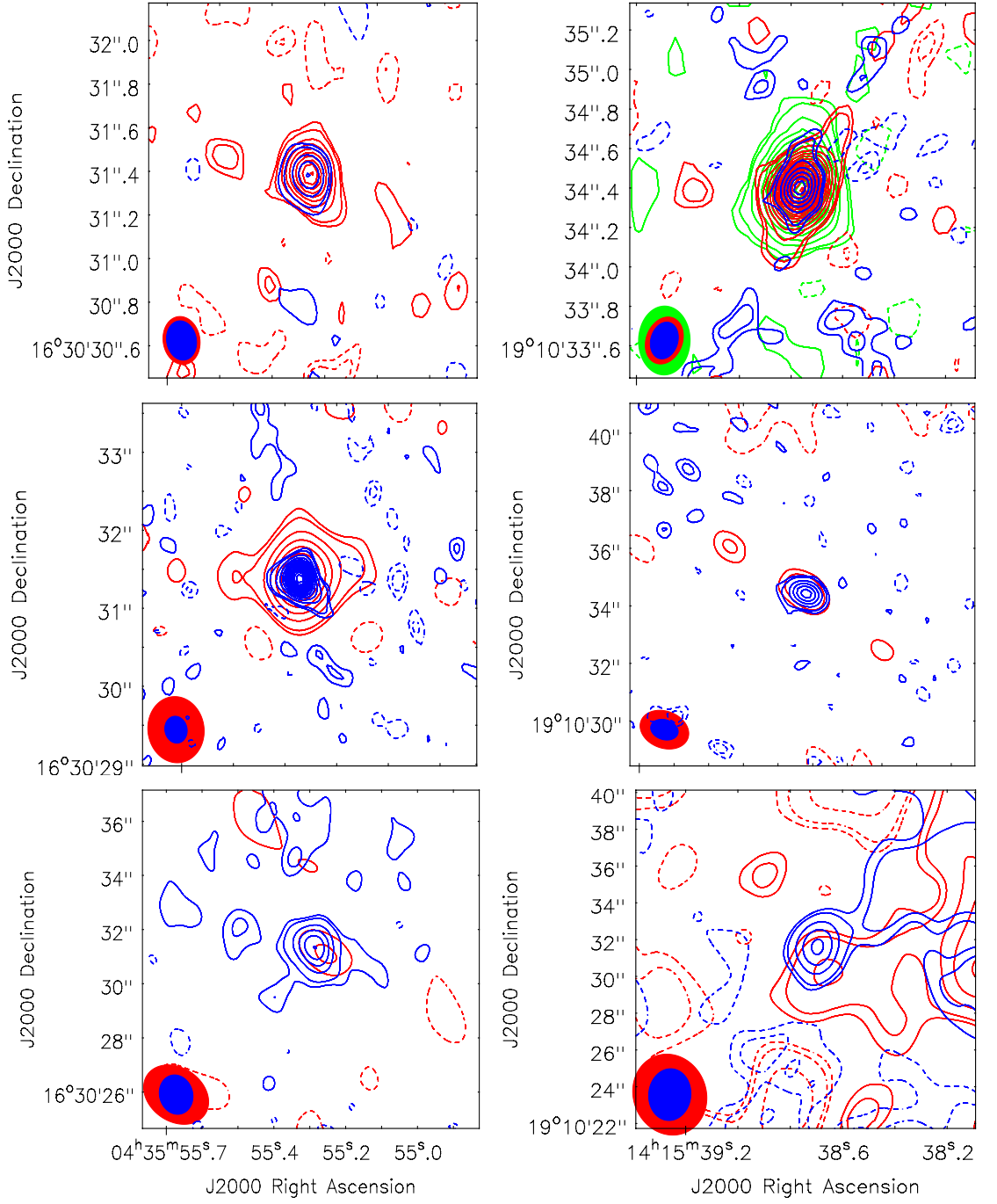


Figure 6.1: Final VLA multi-wavelength radio maps of α Tau and α Boo. *Left column:* Q and Ka-band (top), K and X-band (middle), C and S-band (bottom) maps of α Tau. *Right column:* Q, Ka, and K-band (top), X and C-band (middle), S and L-band (bottom) maps of α Boo. Contour levels are set at $(-6, -3, -2, +2, +3, +6, +9, \dots) \times \sigma$ where σ is the rms noise of each radio map. For α Boo, artifacts from the dirty beam can be seen in the Q-band map, while artifacts caused by the serendipitous strong source in the S and L-band maps are also present.

Table 6.1: VLA Flux Densities of α Boo and α Tau.

Star	Band	ν^a (GHz)	λ (cm)	Peak F_ν (mJy beam $^{-1}$)	Integrated F_ν (mJy)	<i>Imfit</i> Integrated F_ν (mJy)	Image rms (mJy beam $^{-1}$)	<i>Imfit</i> Fitting Error (mJy)
α Boo	Q	43.28	0.7	5.94	6.09	6.42	0.30	0.26
	Ka	33.56	0.9	4.16	4.32	4.49	0.08	0.09
	K	22.46	1.3	1.83	1.78	1.81	0.04	0.05
	X	8.46	3.5	0.51	0.51	0.53	0.03	0.02
	C	4.90	6.1	0.21	0.14	0.16	0.04	0.01
	S	3.15	9.5	0.15	0.14	-	0.03	-
	S	2.87	10.4	0.13	0.12	0.12	0.01	0.02
	L	1.63	18.4	0.07	0.07	-	0.01	-
α Tau	Q	43.28	0.7	3.67	3.73	4.08	0.26	0.18
	Ka	33.56	0.9	2.19	1.96	2.13	0.09	0.07
	K	22.46	1.3	1.86	1.88	2.07	0.04	0.08
	X	8.46	3.5	0.30	0.29	0.28	0.01	0.02
	C	4.96	6.0	0.15	0.17	0.18	0.01	0.01
	S	3.15	9.5	0.06	0.04	-	0.02	-

^aFrequency of the final image produced using the multi-frequency synthesis imaging mode within CASA's *clean* task.

paucity of uv-coverage in these short high frequency observations (see Figure 6.1, top right panel). At the lower frequencies, it was necessary to image confusing sources, notably a strong radio source located 186'' north-west of α Boo. This non-thermal source was reported by [Drake & Linsky \(1983a\)](#) and their flux density of 25 mJy at 4.9 GHz is in close agreement with our measurement of 23.2 mJy at the same frequency. We find the source to have a spectral index α ($F_\nu \propto \nu^\alpha$) of -1.4 between 8.5 and 1.6 GHz; its flux density reaches 80.3 mJy at 1.6 GHz.

We detected α Boo at 6σ in the lower frequency sub-band of C-band, at 4.9 GHz. The noise was slightly higher and the images were poorer quality in the C-band higher frequency sub-band, with artifacts exceeding $\pm 200 \mu\text{Jy}$, and we cannot report a detection in this sub-band, so values given in Table 6.1 are taken from the lower frequency sub-band only. We obtain good detections ($>5\sigma$) of the star for both epochs at ~ 3 GHz (S-band) and the peak flux densities agree within their uncertainties. We can therefore safely assume that the 1.5 GHz (L-band) flux density has not changed significantly over that period either, and so can safely be included in any analysis. The map at L-band was highly contaminated by the sidelobes of the strong source north-west of α Boo but the star is still detected at the 5σ level. There is a slight positional offset of 1'' between the position of the peak flux density at 1.5 and at 3.0 GHz for the 2012 data, which were taken within 1 day of each other. However, the position uncertainties due to noise and phase uncertainties between the directions of the phase reference source and the target are at least 1'', and so we feel that it is highly likely that both detections are of α Boo.

6.2.2 α Tau Maps

The final deconvolved radio maps of α Tau were of excellent quality with the rms noise reaching the predicted noise levels in many cases. The target field at all frequencies was free from strong serendipitous radio sources and thus the final images were free of the sidelobe contamination that were present in the low frequency α Boo images. α Tau was the only source in the high frequency maps while the brightest source in the low frequency maps was located 106'' north north-east of α Tau and had flux densities of 0.85, 1.35, and 1.7 mJy at 8.5, 5.0,

6.3 Results vs Previous Observations

and 3.5 GHz, respectively. Strong detections ($>14\sigma$) of α Tau were made at all frequencies between 5.0 and 43.3 GHz. Due to the limited number of S-band receivers available at the time, a full 2.5 hr track was dedicated to α Tau at 3.1 GHz in order to achieve the required sensitivity to give a possible detection. We report a tentative 3σ detection of α Tau at 3.1 GHz when we take its peak pixel value as its total flux density.

6.3 Results vs Previous Observations

Prior to and during the early operation of the ‘old’ VLA, a small number of single dish radio observations reported the detection of flares from single red giants (e.g., [Slee *et al.* 1989](#)). These transient radio events have never been re-observed however, even with more sensitive interferometers, suggesting that such detections were spurious (e.g., [Beasley *et al.* 1992](#)). The first definitive detection of thermal free-free emission from a luminosity class III single red giant at centimeter wavelengths was of α Boo at 6 cm ([Drake & Linsky, 1986, 1983a](#)). Since then there has been a modest number of centimeter and millimeter observations of this star. In Table A.1 we list the majority of these observations and plot their flux densities as a function of frequency in Figure 6.2 (red diamonds). In comparison to other single red giants, α Boo had been relatively well observed at radio continuum wavelengths before this study, including detections in four VLA bands (i.e., Q, K, Ku, and C). No Ku band receivers were available during the commissioning phase of the VLA in early 2011 so we can compare three of our detections with previous ones.

Previous detections of α Boo at 6 cm ranged from a 3σ upper limit of 0.18 mJy to a 3σ detection at 0.39 mJy. Our 6 cm value agrees to within $\sim 10\%$ of the highest S/N (5σ) value of [Drake & Linsky \(1986\)](#). There is no significant difference between our 1.3 cm value and that of [Dehaes *et al.* \(2011\)](#). There is however a notable difference in flux density values at 0.7 cm where [Dehaes *et al.* \(2011\)](#) report values that are lower than ours by over 40%. Although we do not rule out such a level of chromospheric radio variability, it is not expected based on the small level of UV variability observed from such supposedly inactive stars ([Harper *et al.*, 2013](#)). Another possibility for the difference in values is that the

6.3 Results vs Previous Observations

Table 6.2: Compilation of Previous Radio Observations ($\nu \leq 250$ GHz).

Source	ν (GHz)	Date	F_ν (mJy)	S/N	Reference
α Boo	4.9	1983 Jan 21	0.39	3.0	1
	4.9	1983 May 20	0.26	3.3	1
	4.9	1983 Dec 26	$\leq 0.18(3\sigma)$	-	1
	4.9	1984 Mar 17	0.24	4.8	1
	15.0	1984 Nov 6	0.68	7.6	1
	22.5	1999 Jan 06	1.7	8.5	2
	43.3	1999 Jan 06	3.3	8.3	2
	43.3	2004 Jan 25	3.34	41.8	2
	86.0	1985 Nov	21.4	3.0	3
	108.4	1997 Nov - 2000 Jun	20.1	29.1	4
α Tau	217.8	1997 Nov - 2000 Jun	83.5	48.8	4
	250.0	1986 Dec - 1989 Mar	78.0	9.8	5
	4.9	1983 Jan 21	$\leq 0.27(3\sigma)$	-	1
α Tau	4.9	1984 Nov 6	$\leq 0.22(3\sigma)$	-	1
	5.0	1997 Sep 27	$\leq 0.07(3\sigma)$	-	6
	8.5	1997 Sep 27	0.28	9.3	6
	14.9	1997 Sep 27	0.95	11.9	6
	15.0	1984 Nov 6	0.60	6.0	1
	108.4	1997 Nov - 2000 Dec	14.0	9.6	4
	217.8	1999 Sep - 2000 Dec	25.8	4.6	4
	250.0	1986 Dec - 1987 Jan	51.0	8.5	5

References.-(1) [Drake & Linsky \(1986\)](#); (2) [Dehaes *et al.* \(2011\)](#); (3) [Altenhoff *et al.* \(1986\)](#); (4) [Cohen *et al.* \(2005\)](#); (5) [Altenhoff *et al.* \(1994\)](#); (6) [Wood *et al.* \(2007\)](#);

longer cycle time used by [Dehaes *et al.* \(2011\)](#), which was over double our value, may lead to larger phase errors and thus lower final flux density values. Future high frequency VLA observations of α Boo will clarify this discrepancy at 0.7 cm but past detections at longer wavelengths appear to be in good agreement with our data.

In Figure 6.3 we plot the previous radio measurements of α Tau at all frequencies below 250 GHz (i.e. > 0.12 cm). Prior to this study, α Tau had only been detected at two VLA bands (i.e., X and Ku) and had never been detected at wavelengths longer than 3 cm due to its relatively low mass-loss rate. Our

6.3 Results vs Previous Observations

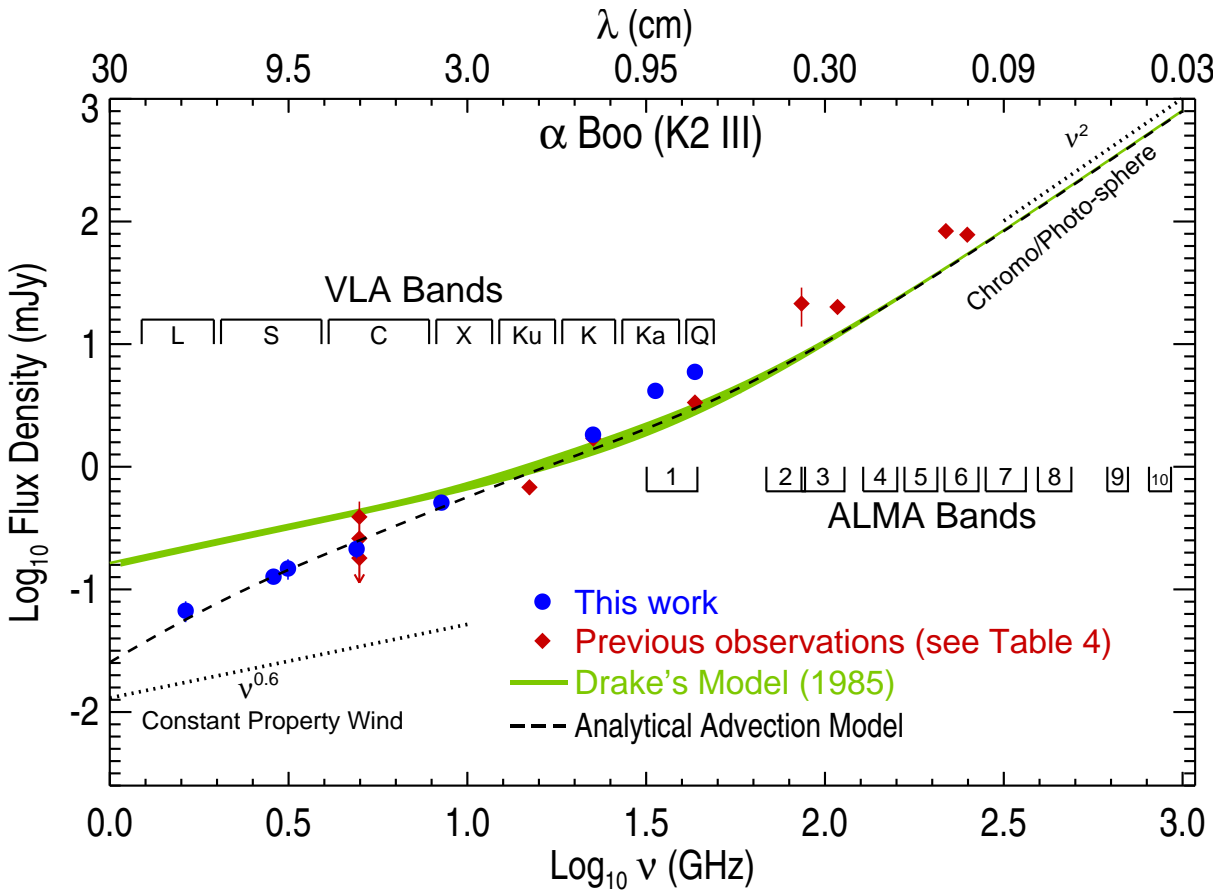


Figure 6.2: Spectral energy distribution of α Boo for $1 \text{ GHz} \leq \nu \leq 1 \text{ THz}$. Our new multi-frequency VLA observations which were mainly acquired over a few days in February 2011 are the blue circles and disagree with the existing chromospheric and wind models of Drake (1985). The overlap between the two models is represented by the green shaded area. The red diamonds are previous observations which were acquired sporadically over the last three decades with the ‘old’ VLA, IRAM and BIMA. The black dashed line is the expected radio emission from the Drake model which undergoes rapid wind cooling beyond $\sim 2.3 R_\star$ (see Section 6.5 and 6.6).

6.3 Results vs Previous Observations

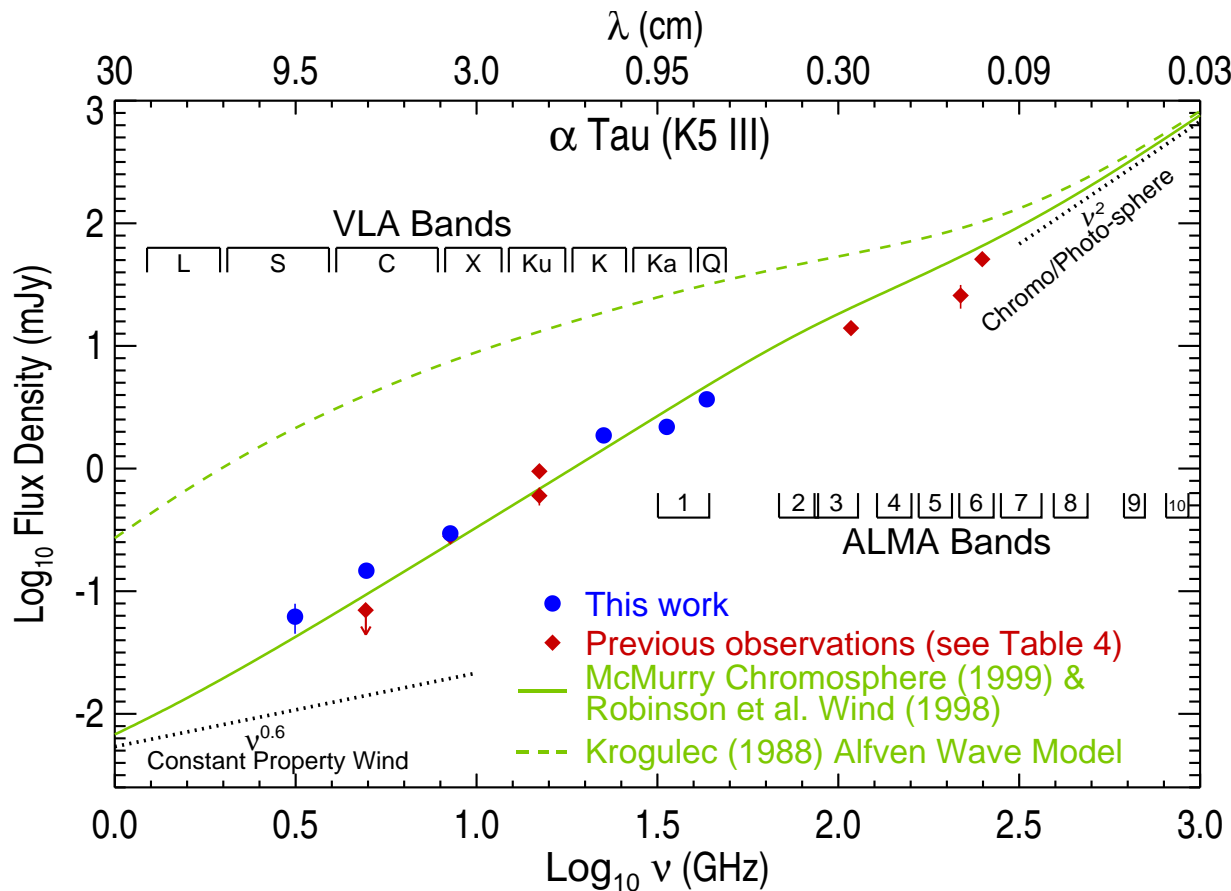


Figure 6.3: Spectral energy distribution of α Tau for $1 \text{ GHz} \leq \nu \leq 1 \text{ THz}$. Our new multi-frequency VLA observations of α Tau (blue circles) were acquired in just two days in February 2011. The red diamonds are the previous radio observations of the star which were acquired over many years (see Table 6.1). The green line is the expected radio emission from the existing hybrid chromosphere and wind model, while the dashed green line is the expected radio emission from a theoretical Alfvén wave driven model atmosphere.

6.4 Results vs Existing Models

lack of a Ku-band measurement means that we can only compare the previous 3 cm detection reported in [Wood *et al.* \(2007\)](#) to ours. We find that there is no significant difference between the two. Interestingly, [Wood *et al.* \(2007\)](#) report a non-detection of α Tau at 6 cm and placed a 3σ upper limit of 0.07 mJy on its emission. In stark contrast to this, we were able to detect the star at 6 cm with a flux density over two times greater than this value. This hint of variability at long wavelengths would be consistent with the predictions of the broadband nonlinear Alfvén wave model of [Airapetian *et al.* \(2010\)](#) but can again only be confirmed with future high S/N observations.

6.4 Results vs Existing Models

One of the most important diagnostic features indicating mass outflows in late-type evolved stars are the blue shifted absorption components present in the Ca II H and K and Mg II h and k resonance lines. Figure 6.4 shows one of the two chromosphere and wind models of α Boo ([Drake, 1985](#), ‘model A’) which is based on the Mg II k 2796 Å emission line observed with the International Ultraviolet Explorer. The line was modeled by solving the radiative transfer equation in a spherical co-moving frame and the effects of partial redistribution (e.g., [Drake & Linsky, 1983b](#)) were taken into account. Both of Drakes atmospheric models are semi-empirical and contain no assumptions about the wind driving mechanism. They contain the photospheric model of [Ayres & Linsky \(1975\)](#), predict the wind to reach a terminal velocity of 35 - 40 km s⁻¹ by $2 R_\star$, and reach a maximum microturbulence of 5 km s⁻¹. They contain a broad temperature plateau with $T_e \approx 8,000$ K between 1.2 and $\sim 20 R_\star$ with a cooler region further out, and hydrogen is 50% ionized throughout. We compute the radio spectrum from these models assuming spherical 1-D geometry ([Harper, 1994](#)) with the free-free Gaunt factors from [Hummer \(1988\)](#). The radiative transfer equation is solved using the Feautrier technique ([Mihalas, 1978](#)) and the boundary condition is determined by ensuring the atmosphere is optically thick at the deepest layers. [Drake \(1985\)](#) predicts that their atmospheric model would produce a flux density value of 0.4 mJy at 6 cm and encouragingly, our radio spectrum reproduces this value. Departures from spherical symmetry are to be expected in magnetic stellar atmospheres. For

6.4 Results vs Existing Models

example, α Boo has an inclination axis of $58^\circ \pm 25^\circ$ (Gray *et al.*, 2006) and a global magnetic dipole could cause density variations between the equator and the polar regions. Despite this fact, the study of a spherically symmetric atmosphere forms the basis of understanding the more complex environments in real stellar atmospheres.

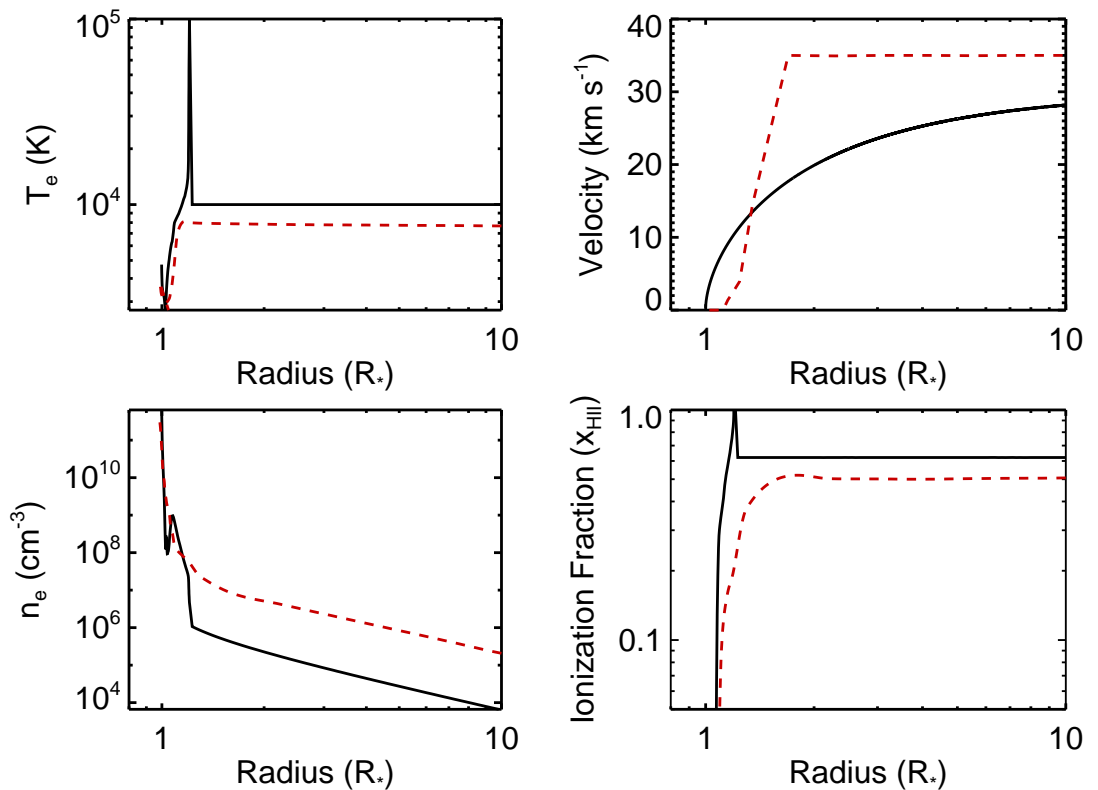


Figure 6.4: 1-D semi-empirical model atmospheres for α Boo and α Tau. The dashed red line is the model atmosphere for α Boo (Drake, 1985) while the solid black line is the model atmosphere of α Tau which consists of the chromosphere and transition region model of McMurry (1999) and the wind model of Robinson *et al.* (1998).

Figure 6.2 shows the resulting predicted radio spectrum between 1 GHz and 1 THz for α Boo from these chromosphere and wind models (green line). At high frequencies the radio spectra produced by these models have a blackbody-like slope (i.e., $\sim \nu^2$) as a result of the small ion density scale heights close to the star where the temperature is changing slowly. At low frequencies however,

6.4 Results vs Existing Models

where the Drake models predict the wind to have constant velocity, ionization fraction, and temperature, the slopes approaches the well known $\sim \nu^{0.6}$ limit (Olnon, 1975; Panagia & Felli, 1975; Wright & Barlow, 1975). The paucity and, in some cases low S/N, of previous observations made it difficult to discern the validity of this model prior to our multi-frequency study of α Boo. Our new data reveal significant deviations from the semi-empirical model at both low and high frequencies (in this case below ~ 8 GHz and above ~ 25 GHz). At high frequencies our VLA data indicates a flux excess which is in agreement with previous mm-observations. This may be due to larger chromospheric ion densities or to the possible presence of transition region plasma not accounted for in the Drake model. The discrepancy at low frequencies may be due to a lower ionization fraction in the wind, or a lower mass loss rate than that used in the Drake model and this will be discussed further in Section 6.6.

In Figure 6.3 we plot the expected radio spectrum of α Tau based on the semi-empirical 1-D chromosphere and transition region model of McMurry (1999) embedded in the 1-D wind model of Robinson *et al.* (1998). The semi-empirical McMurry model was created by using the radiative transfer code MULTI (Carlssson, 1986) to reproduce the fluxes of collisionally excited C I, C II, Si III, Mg II, and C IV lines in a plane-parallel, hydrostatic, one-component atmosphere. It contains the photospheric model of Johnson (1973) and reaches a maximum temperature of 10^5 K at $1.2 R_\star$. As it does not contain a wind outflow, we use Robinson et al.'s wind characteristics beyond $1.2 R_\star$ to describe the outflow velocity. In this wind model, the wind reaches $\sim 80\%$ of its terminal value of 30 km s^{-1} by $3 R_\star$. The Robinson et al. wind characteristics are based on matching the Fe II 2755 Å line and the O I triplet near 1304 Å with a simplified wind model using the SEI computer code (Lamers *et al.*, 1987). We assume the wind to have a constant temperature of 10,000 K and have a constant ionization fraction of $x_e = 0.6$ throughout, based on the ionization fraction at the corresponding temperature in the McMurry model. This idealized *hybrid* model atmosphere for α Tau is plotted in Figure 6.4.

The radio flux densities at high frequencies (i.e., $\nu > 30$ GHz) are overestimated by the combination of both atmospheric models, although this approach

6.4 Results vs Existing Models

does well in reproducing the VLA flux densities below 30 GHz. The VLA, Institut de Radioastronomie Millimétrique (IRAM) 30 m-telescope and Berkeley Illinois Maryland Association (BIMA) continuum flux densities confirm that this model predicts a flux excess at even higher frequencies. One possible explanation for this is that the inner atmosphere contains extensive amounts of cooler gas than that predicted by the 1-D static chromospheric model of McMurry. This scenario agrees with the findings of [Wiedemann *et al.* \(1994\)](#) who conclude that cool regions exist close to the stellar surface with large ($> 99\%$) filling factors i.e., a thermally bifurcated CO-mosphere ([Ayres, 1996](#)). The wind which we have overlain on top of the McMurry chromosphere and transition region is found to be optically thin at nearly all VLA wavelengths, and only contributes a very small flux density at the longest wavelengths. As our model matches the data reasonably well below 30 GHz we conclude that α Tau's wind is optically thin and the VLA radio emission at all wavelengths emanates from the inner atmosphere.

We also include the predicted radio spectrum from the theoretical Alfvén wave-driven outflow model for α Tau ([Krogulec, 1989](#)) in Figure 6.3 to demonstrate how radio observations can empirically challenge theoretical models. This model has a fully-ionized outflow inside $10 R_\star$, and has a mass loss rate of $6.3 \times 10^{-9} M_\odot \text{ yr}^{-1}$, more than two orders of magnitude higher than the more recent estimate given in Table 6.1. As the radio opacity is proportional to $n_e n_{\text{ion}}$, where n_e and n_{ion} are the electron and ion number densities respectively, this model greatly overestimates the actual radio flux density at all VLA wavelengths. The linear Alfvén wave models for α Boo ([Krogulec, 1988](#)) also assume full ionization and have higher mass loss rates than the value given in Table 6.1, predicting higher flux densities than observed. The lack of agreement between the Alfvén wave-driven wind models of [Krogulec \(1988, 1989\)](#) and our observed radio fluxes may not necessarily be due to an incorrect wind driving mechanism and instead may be due to the simplifications and uncertainties in these models, such as wind densities, magnetic field strengths, damping lengths, and flow geometries close to the star. For example, the mass loss rate is very sensitive to the radial surface magnetic field strength (i.e., $\dot{M} \propto B^4$) in these Alfvén wave models ([Holzer *et al.*, 1983](#)) so a small uncertainty in the mass loss rate can lead to a large uncertainty in the magnetic field strength. Relaxing some of these simplifications such as

purely radial flows or non-assumption of the WKB approximation ([Charbonneau & MacGregor, 1995](#)) may also also lead to better agreement with our radio data.

6.5 Spectral Indices

Long wavelength radio emission from non-dusty K spectral-type red giants is due to thermal free-free emission in their partially ionized winds while shorter wavelength radio emission emanates from the near static and more ionized lower atmospheric layers. The radio flux density-frequency relationship for these stars is usually found to be intermediate between that expected from the isothermal stellar disk emission, where α follows the Rayleigh-Jeans tail of the Planck function (i.e., $\alpha = +2$), and that from an optically thin plasma (i.e., $\alpha = -0.1$). We have shown in Chapter 1 that the expected radio spectrum from a spherically symmetric isothermal outflow with a constant velocity and ionization fraction varies as $\nu^{0.6}$ ([Olonon, 1975](#); [Panagia & Felli, 1975](#); [Wright & Barlow, 1975](#)). In reality however, thermal gradients will exist in the wind when the heating mechanisms become insufficient to counteract adiabatic and line cooling, so one would expect a temperature decrease in the wind at some point. Also, if the radio emission emanates from the wind acceleration zone then the electron density will not follow $n_e \propto r^{-2}$.

We therefore relax some of the constant property wind model assumptions and assume that the electron density and temperature vary as a function of distance from the star r , and have the power-law form $n_e \propto r^{-p}$ and $T_e \propto r^{-n}$, respectively (e.g., [Seaquist & Taylor, 1987](#)). Finding the spectral index for an outflow with these conditions is non-trivial so we highlight the main steps required to do so here. We assume the same geometry and notation used for the constant property wind model in Chapter 1, and again start by calculating the total optical depth for a ray with an impact parameter b , through the atmosphere:

$$\tau_\nu = \frac{0.212Z^2 n_e^2(r_0) r_0^{2p}}{T^{1.35} \nu^{2.1} T_e^{1.35}(r_0) r_0^{1.35n}} \int_{-\infty}^{\infty} \frac{1}{(b^2 + z^2)^{(2p-1.35n)/2}} dz. \quad (6.1)$$

6.5 Spectral Indices

This integral can be solved using the relationship

$$\int_{-\infty}^{\infty} \frac{1}{(b^2 + z^2)^{t/2}} dz = b^{1-t} \sqrt{\pi} \left[\frac{\Gamma(0.5t - 0.5)}{\Gamma(0.5t)} \right] \quad (6.2)$$

and setting $t = (2p - 1.35n)$. Here Γ is the gamma function i.e., $\Gamma(y) = \int_0^\infty u^{y-1} e^{-u} du$. The total optical depth along a ray is then

$$\tau_\nu(b) = G b^{1-2p+1.35n} \quad (6.3)$$

where G is a constant that incorporates ν . As the total flux density is

$$F_\nu = \frac{2\pi}{D^2} \int_0^\infty B_\nu [1 - e^{-\tau_\nu(b)}] b db, \quad (6.4)$$

we can now substitute in the Rayleigh Jeans function for B_ν (remembering that T_e now depends on distance from the star) to get

$$F_\nu = \frac{4\pi k \nu^2 T_e(r_0) r_0^n}{D^2 c^2} \int_0^\infty (1 - e^{-\tau_\nu}) (b^2 + z^2)^{-\frac{n}{2}} b db. \quad (6.5)$$

Expansion of the second term inside the integral gives

$$F_\nu \simeq \frac{4\pi k \nu^2 T_e(r_0) r_0^n}{D^2 c^2} \int_0^\infty (1 - e^{-\tau_\nu}) b^{1-n} db. \quad (6.6)$$

To progress further, Equation 6.3 can be rearranged to find b and db in terms of τ_ν , and can then be inserted into Equation 6.6 to give

$$F_\nu \simeq \frac{4\pi k \nu^2 T_e(r_0) r_0^n}{D^2 c^2} \int_0^\infty (1 - e^{-\tau_\nu}) \left(\frac{\tau_\nu}{G} \right)^{\frac{1-2.35n+2p}{1-2p+1.35n}} \frac{d\tau_\nu}{G(1-2p+1.35n)}. \quad (6.7)$$

This allows ν to be separated out to give

$$F_\nu \propto \nu^2 G^{\frac{2.35n-2p-1}{1-2p+1.35n}} G^{-1} \quad (6.8)$$

and as $G \propto \nu^{-2.1}$ we get

$$F_\nu \propto \nu^2 \nu^{\frac{4.2-2.1n}{1-2p+1.35n}}, \quad (6.9)$$

i.e.,

$$\alpha = \frac{4p - 6.2 - 0.6n}{2p - 1 - 1.35n}. \quad (6.10)$$

Therefore, if the spectral index of a stellar outflow can be measured, and if we make an assumption about the property of either the thermal or electron density profile of the wind, then Equation 6.10 provides us with information on how the other value varies.

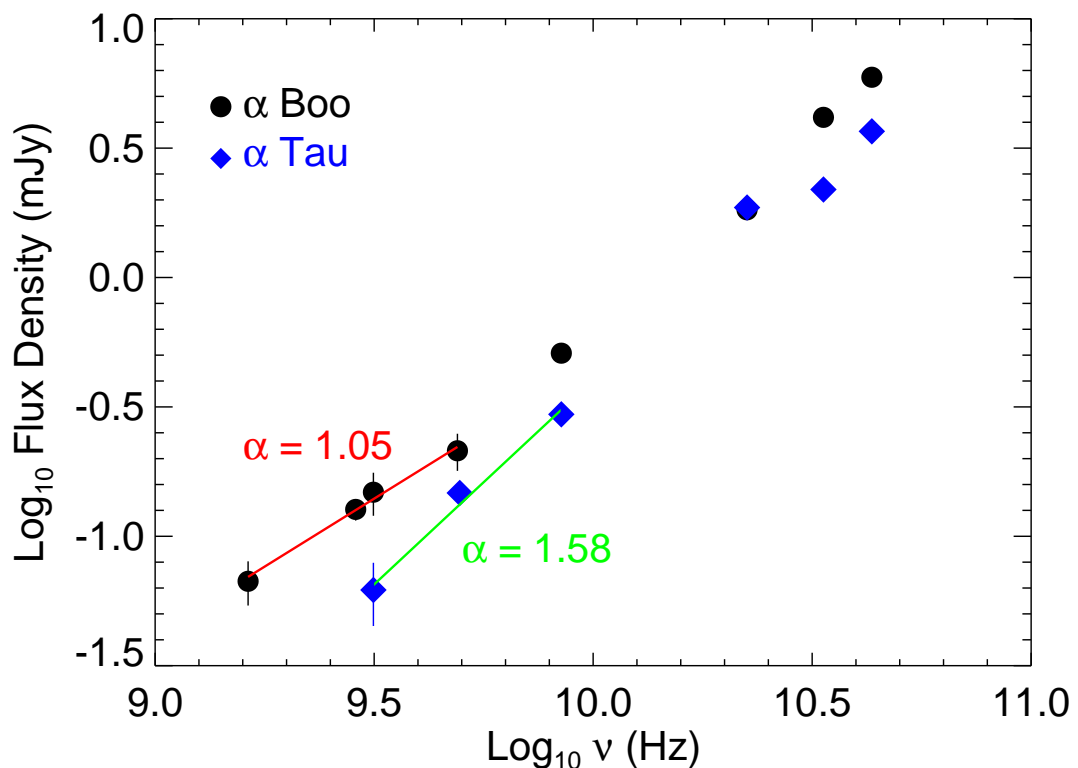


Figure 6.5: Radio spectra for α Boo and α Tau, together with the best fit power law to their long wavelength flux densities and the resulting spectral indices. The spectral indices for α Boo and α Tau are found to be 1.05 and 1.58, respectively, which are both larger than the 0.6 value expected for a constant property wind model.

The radio spectra for both stars are shown in Figure 6.5, together with the power laws that were fitted to the long wavelength flux densities by minimizing the chi-square error statistic. For α Boo, a power law with $F_\nu \propto \nu^{1.05 \pm 0.05}$ fits the four longest wavelength data points well. This spectral index is larger than the 0.8 value obtained by [Drake & Linsky \(1986\)](#) whose value was based on a shorter wavelength (2 cm) value and a mean value of four low S/N measurements

6.5 Spectral Indices

at 6 cm. α Tau was found to have a larger spectral index and a power law with $S_\nu \propto \nu^{1.58 \pm 0.25}$ best fitted the three longest wavelength data points. This value is in agreement with [Drake & Linsky \(1986\)](#) who report a value ≥ 0.84 and is lower than the value of 2.18 that can be derived from the shorter wavelength data given in [Wood *et al.* \(2007\)](#). It should be emphasized that the spectral index for both stars is a lot steeper than that expected from the idealized constant property wind model.

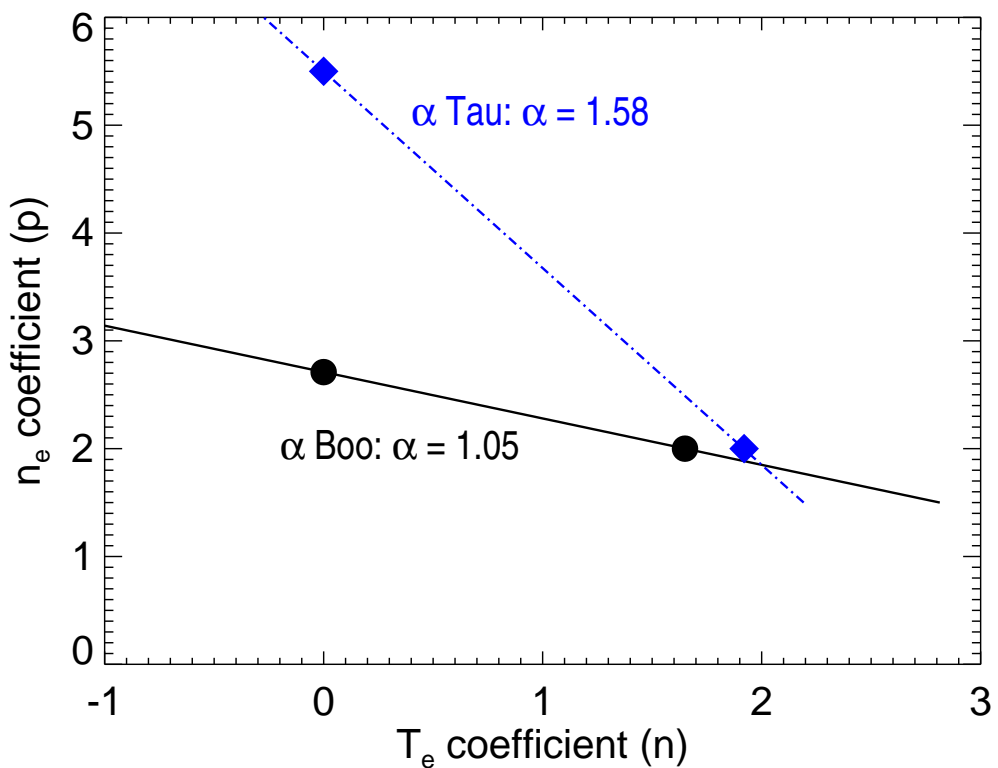


Figure 6.6: The variation of density and temperature coefficients for the empirically derived spectral indices. The density coefficients for an isothermal flow ($n=0$) along with the temperature coefficients for a constant outflow velocity ($p=2$) are also shown for both stars.

Equation 6.10 can be used in conjunction with our new spectral index for each star to calculate the density and temperature coefficients that may describe their outflows. The combinations of the electron temperature and density coefficients are shown for each star in Figure 6.6 (α Boo is represented by the solid line and

6.5 Spectral Indices

α Tau by the dash-dotted line) along with the coefficients obtained by assuming either an isothermal flow ($n = 0$) or a constant velocity flow ($p = 2$). One potential explanation for spectral indices of stellar outflows being larger than 0.6 is that the wind is still accelerating in the radio emitting region, if the thermal gradients are assumed to be small. For an isothermal flow, the density coefficients are $p = 2.7$ and 5.5 for α Boo and α Tau, respectively. From mass conservation and assuming a steady flow, the power law coefficients for the velocity profiles of each star can be found, ie., $v(r) \propto r^{p-2}$. For α Boo we find $v(r) \propto r^{0.7}$ while for α Tau we find $v(r) \propto r^{3.5}$. This suggests that our long VLA wavelengths may probe a steep acceleration region for α Tau's outflow but for α Boo, may probe a region where the wind is close to its terminal velocity.

The assumption of shallow thermal gradients in a stellar outflow is probably unreliable however. It is likely that some form of Alfvèn waves are required to lift the material out of the gravitational potential as suggested by Hartmann & MacGregor (1980). These waves need damping lengths which are much larger than the chromospheric density scale height H (where $H \sim 0.01 R_\star$ for our targets), in order to lift the material out of the gravitational potential but $\lesssim 1 R_\star$ in order to avoid wind terminal velocities greater than those observed (e.g. Holzer *et al.*, 1983). It has also been shown that these waves are expected to produce substantial heating near the base of the wind (e.g. Hartmann *et al.*, 1982). If the long wavelength radio emission from α Tau is indeed emanating from the wind acceleration region, then the dissipation of these Alfvèn waves may introduce thermal gradients in this region and its velocity profile will not be described by $v(r) \propto r^{3.5}$. Furthermore, diverging flow geometries have been invoked as a more realistic representation of stellar atmospheres (Hartmann *et al.*, 1982; Jatenco-Pereira & Opher, 1989; Vidotto *et al.*, 2006) and so one could write the area of a flux tube (normalized to its value at r_1) as $(r/r_1)^2 f(r)$ where $f(r)$ is a function describing the divergence from a purely radial flow [i.e., when $f(r) = 1$]. If the non-radial expansion term can be described by a power law $f(r) \propto r^s$, where $s > 1$ indicates super-radial expansion, then $v(r) \propto r^{3.5-s}$ would describe the velocity profile of α Tau (assuming an isothermal flow with a constant ionization fraction). Therefore, including diverging geometries reduces the magnitude of the acceleration. Further out in the wind, where it has reached its terminal

velocity, one would also expect a thermal gradient (but now of opposite sign) due to adiabatic expansion and line cooling. If the long wavelength radio emission emanates from this region of the wind then Equation ?? provides us with a direct estimate of the temperature coefficient as we can assume the density coefficient is $p = 2$. This may be the case for our long VLA wavelength measurements of α Boo in which case $T_e(r) \propto r^{-1.65}$.

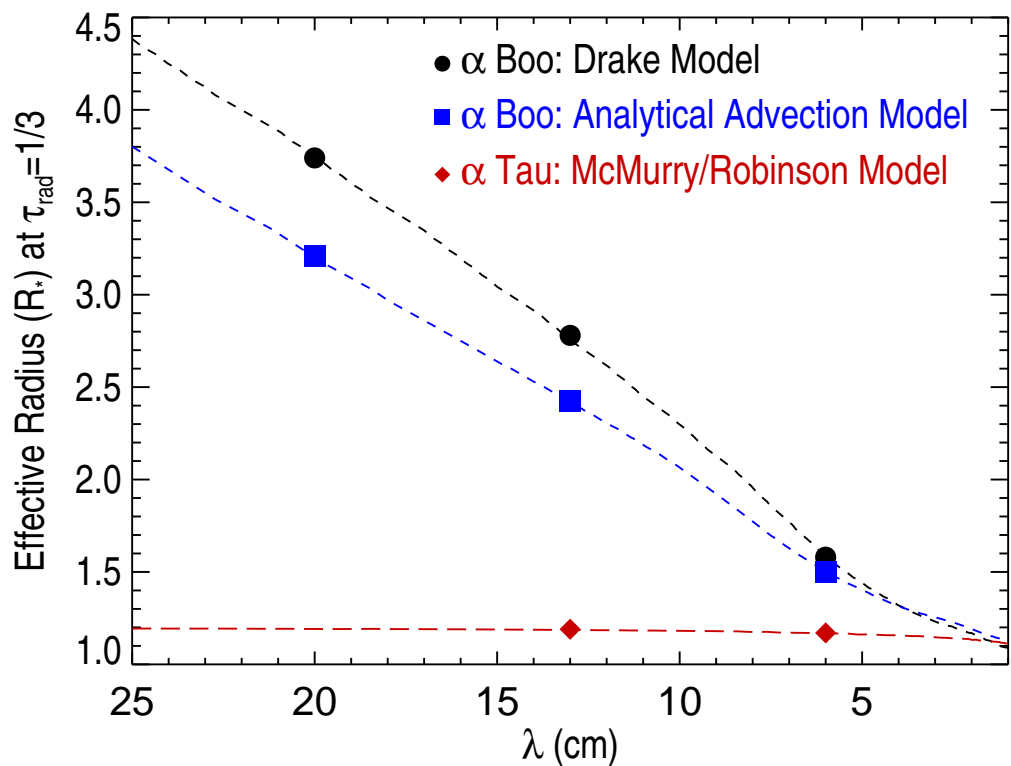


Figure 6.7: Predicted effective radius (dashed lines) as a function of wavelength derived from the existing atmospheric models of α Boo and α Tau. Also plotted is the predicted effective radius derived from our analytical advection model for α Boo (discussed in Section 6.6). Points corresponding to our long wavelength VLA measurements are also shown. At the same radio wavelengths the lower mass loss rate of α Tau's outflow results in a smaller effective radius than that for α Boo.

To investigate this matter further, we estimate the effective radius of the radio emitting region as a function of wavelength based on the Drake model for α Boo and the hybrid McMurry and Robinson et al. model for α Tau. We follow

6.6 Analytical Advection Model for α Boo's Wind

the approach used by [Cassinelli & Hartmann \(1977\)](#) and assume that the radio emission at each wavelength is characterized by emission from a radial optical depth $\tau_{\text{rad}} \sim 1/3$. This is a modification of the Eddington-Barbier relation for an extended atmosphere where emission from smaller optical depths has added weight. Since the radio free-free opacity increases at longer wavelengths the optical depth along a line of sight into the stellar outflow also increases at longer wavelengths. This implies that the effective radius (i.e., the radius where $\tau_\lambda = \tau_{\text{rad}}$) will increase with longer wavelengths and will be greater for outflows with higher densities of ionized material as $\tau_\lambda(r) \propto \lambda^{2.1} \int n_{\text{ion}}(r)n_e(r)dr$.

The larger mass loss rate of α Boo in comparison to α Tau means that the latter has a substantially smaller effective radius at longer wavelengths, as seen in Figure 6.7. At 6, 13, and 20 cm the effective radius of α Boo at $\tau_{\text{rad}} = 1/3$ is predicted to be 1.6, 2.8, and 3.7 R_\star but is only $\sim 1.2 R_\star$ at 6 and 13 cm for α Tau. [Robinson et al. \(1998\)](#) predict that α Tau's wind reaches $\sim 80\%$ of its terminal velocity by $3 R_\star$, but even our longest-wavelength observations are highly unlikely to sample the wind outside the lower velocity layers closer to the star. For α Boo however, [Drake \(1985\)](#) predicts that the wind has reached its terminal velocity by $\sim 2 R_\star$ so based on this model our longest-wavelength measurements are of the region where the wind has reached a steady terminal velocity. From Figure 6.6, this implies that the n_e coefficient is $p = 2$ and thus the T_e coefficient is $n = 1.65$. Pure adiabatic spherical expansion cooling with no heat source has $n = 1.33$ so additional cooling routes must be operating, possibly due to line cooling. Finally, the wind ionization balance may not have become *frozen-in* in the region of α Boo's wind where the radio emission emanates from. If this is true, then the excess slope of the spectral index could be due to a combination of both cooling and changing ionization fraction. In this scenario the temperature coefficient n , would be smaller than our derived value because Equation 6.10 assumes a constant ionization fraction.

6.6 Analytical Advection Model for α Boo's Wind

A failure of the Drake model for α Boo is that it overestimates the long wavelength VLA radio flux densities which sample the outer atmosphere, as clearly shown

6.6 Analytical Advection Model for α Boo's Wind

in Figure 6.2. If these wavelengths are indeed sampling the wind at its terminal velocity then one reason for this overestimation is that the wind is cooling closer in than predicted by the existing model, which assumes a constant temperature of 8,000 K out to $\sim 20 R_\star$. The main mechanism for such cooling would be adiabatic expansion (O'Gorman & Harper, 2011) and would cause lower electron densities than those predicted by the existing model due to larger recombination rates. In the next two sections we derive the fraction of ionized hydrogen in a stellar outflow with a temperature gradient based on the work of Glassgold & Huggins (1986), and use this method to insert a temperature gradient into the outer atmosphere of the Drake model to see if such an atmosphere could better reproduce the new long wavelength VLA flux densities.

6.6.1 H II recombination in a stellar outflow

The time dependent non-static rate/statistical equations can be written as

$$\frac{\partial n_i}{\partial t} + \nabla \cdot (n_i v) = \sum_{i \neq j}^n n_j P_{ji} - n_i \sum_{i \neq j}^n P_{ij} \quad (6.11)$$

where v is the flow velocity, $n_{i,j}$ are the population densities of the energy levels i, j which are functions of radial distance r , and $P_{ij} = C_{ij} + R_{ij}$ are the total transition probabilities (s^{-1}) from energy levels $i \rightarrow j$. C_{ij} are the total collision rates (electrons, protons, and ions), and R_{ij} are the problematic radiative rates. In 1-D spherical geometry

$$\nabla \cdot \mathbf{A} = \frac{1}{r^2} \frac{d}{dr} (r^2 A), \quad (6.12)$$

where \mathbf{A} is some vector quantity and equals $n_i v$ in our case. Thus, for a steady flow the rate equations become

$$\frac{1}{r^2} \frac{d}{dr} (r^2 v n_{\text{tot}} \frac{n_i}{n_{\text{tot}}}) = \sum_{i \neq j}^n n_j P_{ji} - n_i \sum_{i \neq j}^n P_{ij} \quad (6.13)$$

where n_{tot} is the total hydrogen number density (i.e. $n_{\text{tot}} = n_{\text{HI}} + n_{\text{HII}}$). We note that $r^2 v n_{\text{tot}}$ is some constant of the flow defined by the mass continuity equation,

6.6 Analytical Advection Model for α Boo's Wind

and if we define the relative populations as $x_i = n_i/n_{\text{tot}}$ we get

$$v \frac{d}{dr}(x_i) = \sum_{i \neq j}^n x_j P_{ji} - x_i \sum_{i \neq j}^n P_{ij}. \quad (6.14)$$

To simplify Equation 6.14 further, we follow the approach of Glassgold & Huggins (1986) and assume:

1. A constant velocity mass outflow, i.e., $n_{\text{tot}} = C/r^2$ where C is a constant proportional to the ratio of the mass loss rate divided by the terminal velocity.
2. All hydrogen ionization processes cease beyond some distance r_1 (i.e. $P_{ij} = 0$). The ionization of hydrogen in the chromosphere and wind is a two stage process: the $n = 2$ level is excited by electron collisions and Lyman-alpha scattering, followed by photoionization by the optically thin Balmer continuum. When the temperature begins to decrease in the wind the collisional excitation rate and thus ionization rate decrease rapidly.
3. Only radiative recombination of hydrogen is considered [i.e. $R_{ji} = \alpha_{\text{rr}}(T_e)n_e$ where α_{rr} is the total radiative recombination coefficient].
4. A fixed ion contribution from metals with a low first ionization potential, $x_{\text{ion}} = n_{\text{ion}}/n_{\text{tot}}$, as these are easily ionized in the outflow. The total electron density is then $n_e = n_{\text{tot}}x_{\text{HII}} + n_{\text{tot}}x_{\text{ion}}$ where $x_{\text{HII}} = n_{\text{HII}}/(n_{\text{HI}} + n_{\text{HII}})$.

Using these assumptions Equation 6.14 becomes

$$\frac{dx_{\text{HII}}}{dr} = \frac{\alpha_{\text{rr}}C}{vr^2} (x_{\text{HII}}^2 + x_{\text{ion}}x_{\text{HII}}) \quad (6.15)$$

which can be rearranged and integrated between r_1 and r to give

$$\int_{x_{\text{HII}(r_1)}}^{x_{\text{HII}(r)}} \frac{dx_{\text{HII}}}{x_{\text{HII}}(x_{\text{HII}} + x_{\text{ion}})} = \int_{r_1}^r \frac{\alpha_{\text{rr}}C}{vr^2} dr. \quad (6.16)$$

The ionization fraction beyond r_1 is then given by

$$x_{\text{HII}}(r) = \frac{x_{\text{HII}}(r_1)x_{\text{ion}}e^{-I(r)}}{x_{\text{ion}} + x_{\text{HII}}(r_1)[1 - e^{-I(r)}]} \quad (6.17)$$

where

$$I(r) = \int_{r_1}^r \frac{x_{\text{ion}}\alpha_{\text{rr}}C}{vr^2} dr \quad (6.18)$$

6.6 Analytical Advection Model for α Boo's Wind

If we further assume a constant velocity, $T_e \propto r^{-n}$, and $\alpha_{rr} \propto T_e^{-\beta}$ giving $\alpha_{rr} \propto r^{-n\beta}$, then

$$x_{\text{HII}}(r) = \frac{x_{\text{HII}}(r_1)x_{\text{ion}}e^{-I(r)}}{x_{\text{ion}} + x_{\text{HII}}(r_1)(1 - e^{-I(r)})} \quad (6.19)$$

where

$$I(r) = w \left[1 - \left(\frac{r_1}{r} \right)^{1-n\beta} \right] \quad (6.20)$$

and

$$w = \frac{x_{\text{ion}}\alpha_{rr}(r_1)C}{vr_1(1 - n\beta)}. \quad (6.21)$$

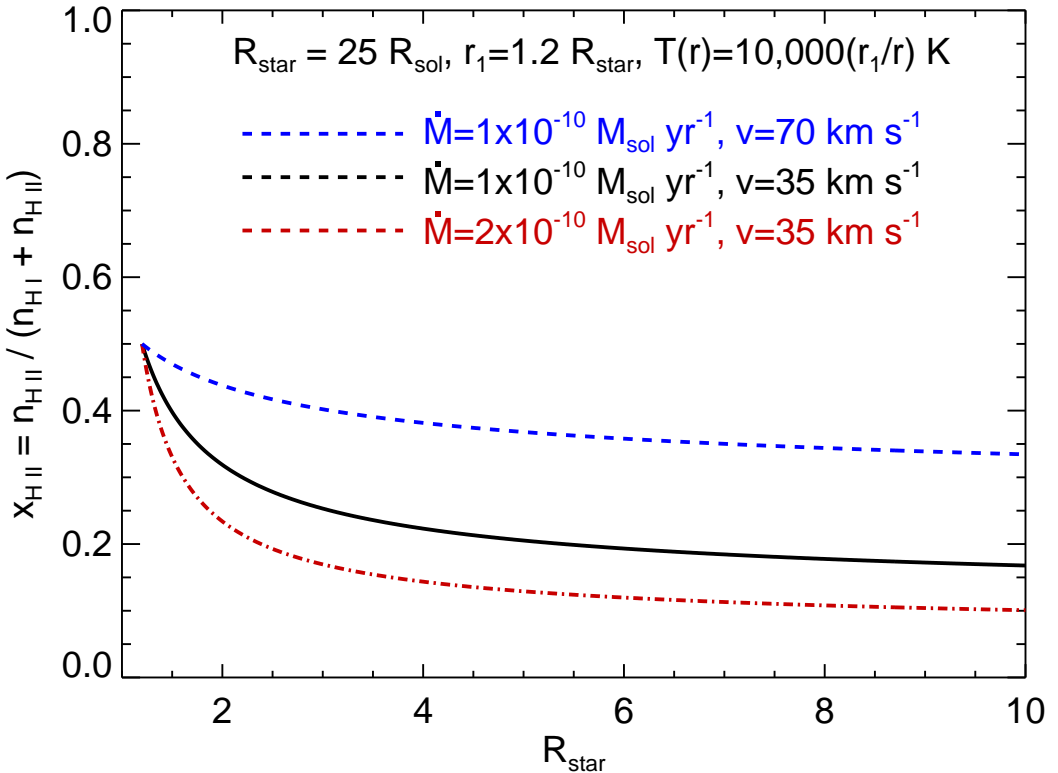


Figure 6.8: Illustration of how the ionization fraction *freezes-in* in a stellar wind for a hypothetical $25 R_{\star}$ star. The stars outflow has a maximum temperature of 10,000 K at $1.2 R_{\star}$ which then falls off linearly with distance. Blue dashed line: $\dot{M} = 1 \times 10^{-10} M_{\odot} \text{ yr}^{-1}$ and $v = 70 \text{ km s}^{-1}$. Black smooth line: $\dot{M} = 1 \times 10^{-10} M_{\odot} \text{ yr}^{-1}$ and $v = 35 \text{ km s}^{-1}$. Red dot-dashed line: $\dot{M} = 2 \times 10^{-10} M_{\odot} \text{ yr}^{-1}$ and $v = 35 \text{ km s}^{-1}$.

6.6 Analytical Advection Model for α Boo's Wind

As w is just a constant, $I(r)$ approaches a constant value for large r . This means that $x_{\text{HII}}(r)$ also approaches a constant value for large r , and the ionization fraction gets *frozen-in*. This is a universal property of all stellar winds. It occurs when the recombination timescale of the ions in the wind $\tau_{\text{rec}} = (\alpha_{\text{rec}} n_e)^{-1}$, becomes larger than the wind expansion timescale, $\tau_{\text{exp}} = |\rho(d\rho/dt)^{-1}| \simeq 0.5r/v$. Figure 6.5 shows that the ionization fraction in the outflow of a *typical* red giant *freezes-in* to higher values for winds with higher velocities and lower mass loss rates.

6.6.2 Application to α Boo's Wind

To investigate the possibility that α Boo's wind may be undergoing more rapid cooling closer in to the star than originally predicted by the Drake Model, we adjust one of the existing models [referred to as 'Model A' in [Drake \(1985\)](#)] to include a temperature power-law falloff of the form

$$T_e(r) = T_e(r_1) \left(\frac{r_1}{r}\right)^n, \quad (6.22)$$

at some distance r_1 from the star. We set the temperature coefficient to the value obtained from our new VLA data which was derived assuming a constant velocity flow, i.e. $n = 1.65$ (see Figure 6.6). We introduce the distance r_1 as the outer limit to ionization processes; at $r > r_1$, the ionization fraction is only determined by recombination. To calculate the new electron densities in the wind regime where this temperature falloff occurs, we use Equations 6.19, 6.20, and 6.21 to calculate the hydrogen ionization fraction, $x_{\text{HII}} = n_{\text{HII}}/n_{\text{H}}$. We assume a fixed ion contribution from metals with a low first ionization potential of $x_{\text{ion}} = 1 \times 10^{-4}$. So, knowing that the total hydrogen density does not change, the electron density at any point in the wind post r_1 can be found by the following formula

$$n_e(r) = n_{\text{tot}}(r)[x_{\text{HII}}(r) + 1 \times 10^{-4}]. \quad (6.23)$$

Using the same wind terminal velocity as that used in 'Model A' (i.e. 35 km s⁻¹) and the mass loss rate defined in Table ??, we find the constant proportional to the ratio of the mass loss rate divided by the terminal velocity to be $C = 1.7 \times 10^{32}$ cm⁻¹ for α Boo. To calculate the temperature dependent radiative

6.6 Analytical Advection Model for α Boo's Wind

recombination coefficient α_{rr} and its power law coefficient β used in Equation 6.21, we consider only radiative recombination of hydrogen and exclude captures to the n=1 level. Spitzer (1978) has tabulated values for the variation of this recombination coefficient with temperature and it is often referred to as α_B in the literature when captures to the n=1 level are excluded. To find the power law form of α_B we found the best fit to the tabulated data between the expected range of temperatures in the outflow of α Boo. This approach is shown in Figure 6.9, where β was found to be 0.77 by fitting a power law to values of α_B between 1,000 and 16,000 K. For completeness, we also show in Figure 6.9 the slight variation in β if a wider range of temperatures is used and also if captures to the n=1 level are included. It can then be easily shown that the ionization fraction beyond r_1

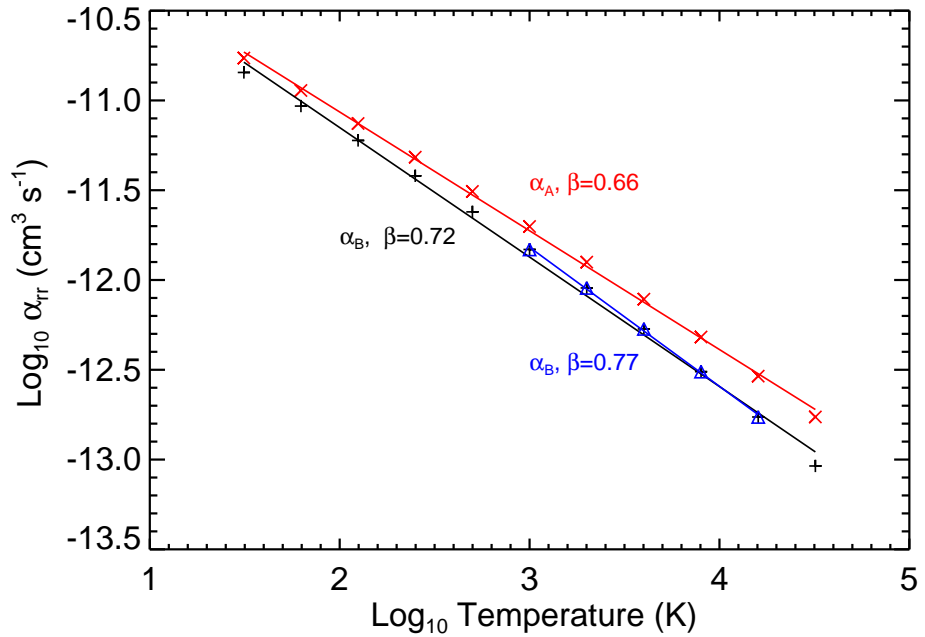


Figure 6.9: The temperature dependent recombination rates for hydrogen. The variation of the recombination rate excluding captures to the n=1 level α_B , with temperature is derived for the tabulated temperatures in Spitzer (1978) (black) and for the more realistic temperatures existing in α Boo's outflow (blue). We also show the how the recombination coefficient varies with temperature if captures to the n=1 level are included (red).

6.7 Constraining α Tau's Molsphere

is given by

$$x_{\text{HII}}(r) = \frac{x_{\text{HII}}(r_1)x_{\text{ion}}e^{-I(r)}}{x_{\text{ion}} + x_{\text{HII}}(r_1)[1 - e^{-I(r)}]} \quad (6.24)$$

where

$$I(r) = \frac{4.7 \times 10^9}{r_1} \left[\left(\frac{r_1}{r} \right)^{-0.27} - 1 \right], \text{ and } r \geq r_1. \quad (6.25)$$

We then adjusted the value of r_1 to obtain the best fit to our long wavelength observations and found this happened when $r_1 = 2.3 R_\star$. To get this best fit, the existing atmospheric model needed to be adjusted so that it now has a narrower and slightly larger temperature plateau of $T_e = 10,000$ K between 1.2 and $2.3 R_\star$, and a temperature profile and a density profile governed by Equation 6.22 and Equation 6.24 beyond $r_1 = 2.3 R_\star$, respectively. This gives much better agreement with our new long wavelength VLA data as shown in Figure 6.2. This new *hybrid* atmospheric model which is plotted along with the original Drake model in Figure 6.10, still has the original ionization fraction of $x_{\text{HII}} \approx 0.5$ inside $2.3 R_\star$ but now contains an initial rapid decrease in x_{HII} beyond $2.3 R_\star$ which then *freezes-in* to a constant value of ~ 0.04 beyond $\sim 10 R_\star$.

Encouraging as it is that such a simple analytical model can reproduce values close to the observed radio fluxes at long wavelengths, it must be stressed that this *hybrid* model is just a first order approximation. It assumes that the excess slope from the radio spectrum is a result of rapid cooling only. It still does not reproduce the radio fluxes at wavelengths shorter than ~ 3 cm and therefore a new atmospheric model is still required that can reproduce all of the observed flux densities. To do so, the non-trivial task of simultaneously solving the radiative transfer equation and non-LTE atomic level populations which include advection will be required.

6.7 Constraining α Tau's Molsphere

Recently, Ohnaka (2013) has detected a layer of CO in the outer atmosphere of α Tau (i.e. a so-called MOLsphere) which extends out to $\sim 2.5 R_\star$, has a temperature of 1500 ± 200 K, and a CO column density of $\sim 1 \times 10^{20} \text{ cm}^{-2}$. They were unable to constrain the geometrical thickness ΔL , of the MOLsphere from

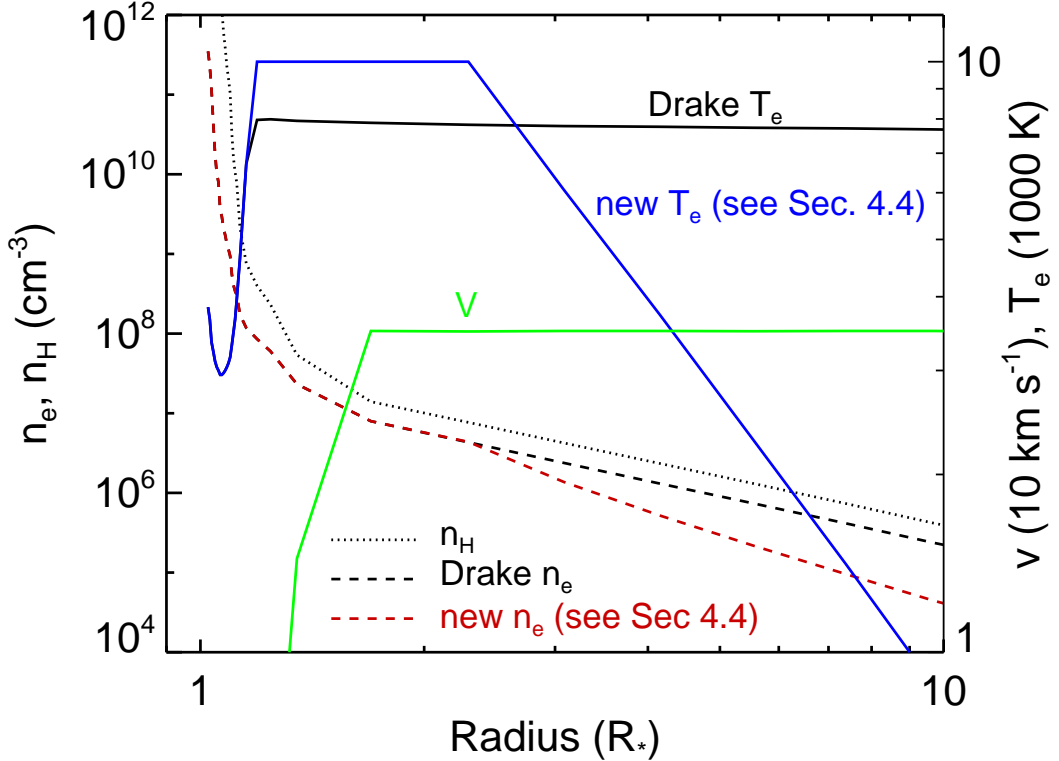


Figure 6.10: Existing atmospheric model for α Boo (Drake, 1985, ‘model A’) along with the same model which undergoes rapid wind cooling beyond $\sim 2.3 R_\star$. The original Drake Model’s have a temperature plateau of $\sim 8,000$ K between 1.2 and $\sim 20 R_\star$ (solid black line), reach a terminal velocity of $35 - 40 \text{ km s}^{-1}$ within $2 R_\star$ (solid green line), and have a wind which is 50% ionized (dashed and dotted black lines).

the data however, and arbitrarily set it to $0.1 R_\star$. We now try and constrain the thickness of this MOLsphere from our VLA data.

At VLA wavelengths, the opacity corrected for stimulated emission is

$$\kappa_\nu = \frac{0.212 n_e n_{ion} Z_{ion}^2}{T_e^{1.35} \nu^{2.1}} \text{ cm}^{-1} \quad (6.26)$$

and the optical depth of a shell of width ΔL is

$$\tau_\nu = \kappa_\nu \Delta L. \quad (6.27)$$

To calculate the electron density within the MOLsphere we have conservatively

assumed that the electrons only come from singly ionized metals and have an abundance of $n_{\text{ion}} = 1 \times 10^{-5} n_{\text{tot}}$, where n_{tot} is the total hydrogen number density whose value is constant throughout the MOLsphere. We estimate the CO number density by dividing the CO column density by the geometrical thickness of the shell and assume the CO filling factor to be unity. If the MOLsphere extends from the stars surface out to the derived distance of $2.5 R_{\star}$, then $\Delta L = 1.5$ and $n_{\text{co}} = 2.2 \times 10^7 \text{ cm}^{-3}$. This equates to a total hydrogen number density of $n_{\text{tot}} = 1.2 \times 10^{11} \text{ cm}^{-3}$ (Ohnaka, 2013) giving an abundance ratio of $n_{\text{co}}/n_{\text{tot}} = 3.3 \times 10^{-4}$. We can then use Equations 6.26 and 6.27 to show that such a MOLsphere would be optically thin at all VLA wavelengths that we observed the star with. If on the other hand, the MOLsphere has only a geometric width of $\Delta L = 0.1 R_{\star}$ then assuming the same abundances we get $n_{\text{H}} = 1.76 \times 10^{12} \text{ cm}^{-3}$, and the MOLsphere would be optically thick at 3.5, 6, and 9.5 cm (i.e. X, C, and S-band). Focusing on our high S/N C-band measurement, it can be shown that such a MOLsphere would have an optical depth of $\tau_{6 \text{ cm}} = 4.6$ and would produce a corresponding flux density of 0.06 mJy (assuming an optically thick disk) which is considerably lower than our measurement of 0.15 mJy. The disagreement in values between our radio data and the predicted flux for an optically thick disk could mean that the MOLsphere is optically thin at long VLA wavelengths and that the radio emission emanates from the more ionized material closer to the star. It can also be shown that the MOLsphere becomes optically thin at C-band (i.e. $\tau_{6 \text{ cm}} < 1$) for $\Delta L > 0.45 R_{\star}$. In the next section we argue that the radio emission from α Tau even at long VLA wavelengths comes from a region closer in to the star where the wind is undergoing rapid acceleration, which suggests that the MOLsphere either has a geometrical width $> 0.45 R_{\star}$ or has a filling factor less than unity.

6.8 Ionized Mass Loss Rates

The free-free radio emission from the atmospheres of red giants is only sensitive to the ionized component of the outflow. Non-coronal and hybrid atmosphere red giants have only partially ionized atmospheres and so we are only ever capable of finding a lower limit on the mass loss rate from their thermal continuum radio emission. Nevertheless, it is a sufficiently worthwhile goal and can test the validity

6.8 Ionized Mass Loss Rates

of existing values obtained from optically thick emission lines in the UV or optical regime. For a partially ionized outflow such as that expected from α Boo and α Tau, the ionized mass loss rate can be estimated from the radio emission assuming a constant velocity, constant temperature, and constant ionization fraction and can be written as

$$\dot{M}_{\text{ion}} \simeq 5.58 \times 10^{-14} \left(\frac{v_{\infty}}{\text{km s}^{-1}} \right) \left(\frac{D}{\text{pc}} \right) \left(\frac{F_{\nu}}{\text{mJy}} \right)^{0.75} \left(\frac{\lambda}{\text{cm}} \right)^{0.45} \left(\frac{T_e}{10^4 \text{K}} \right)^{0.1} \dot{M}_{\odot} \text{ yr}^{-1} \quad (6.28)$$

where D is the distance and v_{∞} is the wind terminal velocity defined previously in Table 3.1. Using this expression, the ionized mass loss rates were derived for each of the long wavelength measurements for both stars and are listed in Table 6.3. These values are based on the assumption of a $T_e = 10^4$ K wind for both stars.

Table 6.3: Ionized mass loss rates for α Boo and α Tau.

Star	Wavelength (cm)	$\dot{M}_{\text{ion}} (M_{\odot} \text{ yr}^{-1})$
α Boo	6.0	5.9×10^{-11}
	9.5	5.5×10^{-11}
	10.0	5.1×10^{-11}
	20.0	4.3×10^{-11}
α Tau	6.0	$\leq 8.2 \times 10^{-11}$
	9.5	$\leq 5.3 \times 10^{-11}$

We have discussed in the previous sections that for α Boo, these long wavelengths sample the outer atmosphere of the star where the wind is close to or has reached its terminal velocity and is beginning to cool due to gas expansion. In this case, these \dot{M}_{ion} values would be lower than those given in Table 6.3 as the electron temperature is probably lower than 10,000 K. However, as \dot{M}_{ion} is only weakly dependent on T_e this makes only a small difference and amounts to about a 7% increase in the ionized mass loss if the temperature is actually lower by 50%. If the ionization balance is frozen-in in the regions of the outflow where these long wavelengths sample, then the derived \dot{M}_{ion} should be the same for these wavelengths. The decrease in \dot{M}_{ion} with longer wavelengths is very small as

6.8 Ionized Mass Loss Rates

seen in Table 6.3 and may be a hint that the ionization fraction may be close to frozen-in at these wavelengths. If we were to assume that the total stellar mass loss rate derived by Drake (1985) is correct, then a comparison with our longest wavelength value for the ionized mass loss rate suggests an ionization fraction of ~ 0.2 in the outer wind of α Boo. Deriving the exact ionized mass loss rate for α Tau is more difficult because as we have argued in the previous sections, the longest wavelengths are still sampling the acceleration zone, and thus the velocity in the region where the long wavelength radio emission emanates from will be less than 30 km s^{-1} . In Table 6.3 the values are derived assuming the radio emission emanates from the outer atmosphere where the wind has reached its terminal velocity (i.e., 30 km s^{-1}) and so are just upper limits.

A

List of Abbreviations

Table A.1: List of Abbreviations

Abbreviation	Meaning
BIMA	Berkeley Illinois Maryland Association
CARMA	Combined Array for Research in Millimeter-wave Astronomy
CSE	Circumstellar Envelope
DDT	Director's Discretionary Time
e-MERLIN	e-Multi-Element Radio Linked Interferometer Network
FOV	Field of View
GREAT	German Receiver for Astronomy at Terahertz Frequencies
HPBW	Half Power Beamwidth
HST	Hubble Space Telescope
IOTA	Infrared Optical Telescope Array
IR	Infrared
IRAM	Institut de Radioastronomie Millimétrique
IUE	International Ultraviolet Explorer
LSR	Local Standard of Rest
MEM	Maximum Entropy Method
OVRO	Owens Valley Radio Observatory
RFI	Radio Frequency Interference
S/N	signal-to-noise
SOFIA	Stratospheric Observatory for Infrared Astronomy
SMA	Submillimeter Array
UV	Ultraviolet
VLA	Karl G. Jansky Very Large Array
VLBA	Very Long Baseline Array
VLT	Very Large Telescope

References

- AIRAPETIAN, V., CARPENTER, K.G. & OFMAN, L. (2010). Winds from Luminous Late-type Stars. II. Broadband Frequency Distribution of Alfvén Waves. *Astrophysical Journal*, **723**, 1210–1218. (Cited on page [125](#).)
- ALTENHOFF, W.J., HUCHTMEIER, W.K., SCHMIDT, J., SCHRAML, J.B. & STUMPFF, P. (1986). Radio continuum observations of comet Halley. *Astronomy & Astrophysics*, **164**, 227–230. (Cited on page [122](#).)
- ALTENHOFF, W.J., THUM, C. & WENDKER, H.J. (1994). Radio emission from stars: A survey at 250 GHz. *Astronomy & Astrophysics*, **281**, 161–183. (Cited on pages [98](#) and [122](#).)
- AURIÈRE, M., DONATI, J.F., KONSTANTINOVA-ANTOVA, R., PERRIN, G., PETIT, P. & ROUDIER, T. (2010). The magnetic field of Betelgeuse: a local dynamo from giant convection cells? *Astronomy & Astrophysics*, **516**, L2. (Cited on page [30](#).)
- AYRES, T.R. (1996). Thermal bifurcation as a driver of stellar surface inhomogeneities (review). In K.G. Strassmeier & J.L. Linsky, eds., *Stellar Surface Structure*, vol. 176 of *IAU Symposium*, 371. (Cited on page [128](#).)
- AYRES, T.R. & LINSKY, J.L. (1975). Stellar model chromospheres. III - Arcturus /K2 III/. *Astrophysical Journal*, **200**, 660–674. (Cited on pages [42](#) and [125](#).)
- AYRES, T.R., BROWN, A. & HARPER, G.M. (2003). Buried Alive in the Coronal Graveyard. *Astrophysical Journal*, **598**, 610–625. (Cited on pages [43](#) and [45](#).)
- BAADE, R., KIRSCH, T., REIMERS, D., TOUSSAINT, F., BENNETT, P.D., BROWN, A. & HARPER, G.M. (1996). The Wind Outflow of zeta Aurigae: A Model Revision Using Hubble Space Telescope Spectra. *Astrophysical Journal*, **466**, 979. (Cited on page [40](#).)
- BEASLEY, A.J., STEWART, R.T. & CARTER, B.D. (1992). Non-thermal radio emission from post-main-sequence stars. *Monthly Notices of the Royal Astronomical Society*, **254**, 1–6. (Cited on page [121](#).)
- BECKLIN, E.E. & GEHRZ, R.D. (2009). SOFIA: Stratospheric Observatory for Infrared Astronomy. In D. C. Lis, J. E. Vaillancourt, P. F. Goldsmith, T. A. Bell, N. Z. Scoville, & J. Zmuidzinas, ed., *Submillimeter Astrophysics and Technology: a Symposium Honoring Thomas G. Phillips*, vol. 417 of *Astronomical Society of the Pacific Conference Series*, 101. (Cited on page [98](#).)

REFERENCES

- BEDECARRAX, I., PETIT, P., AURIÈRE, M., GRUNHUT, J., WADE, G., CHIAVASSA, A., DONATI, J.F., KONSTANTINOVA-ANTOVA, R. & PERRIN, G. (2013). Long-term spectropolarimetric monitoring of the cool supergiant betelgeuse. In *EAS Publications Series*, vol. 60 of *EAS Publications Series*, 161–165. (Cited on page [29](#).)
- BERIO, P., MERLE, T., THÉVENIN, F., BONNEAU, D., MOURARD, D., CHESNEAU, O., DELLA, O., LIGI, R., NARDETTO, N., PERRAUT, K., PICHON, B., STEE, P., TALLON-BOSC, I., CLAUSSE, J.M., SPANG, A., MCALISTER, H., TEN BRUMMELAAR, T., STURMANN, J., STURMANN, L., TURNER, N., FARRINGTON, C. & GOLDFINGER, P.J. (2011). Chromosphere of K giant stars. Geometrical extent and spatial structure detection. *Astronomy & Astrophysics*, **535**, A59. (Cited on page [40](#).)
- BERNAT, A.P., HALL, D.N.B., HINKLE, K.H. & RIDGWAY, S.T. (1979). Observations of CO circumstellar absorption in the 4.6 micron spectrum of Alpha Orionis. *Astrophysical Journal Letters*, **233**, L135–L139. (Cited on pages [30](#), [78](#), [79](#), [90](#), [101](#) and [102](#).)
- BLUNDELL, R. (2007). The Submillimeter Array. In *IEEE MTT-S International Microwave Symposium Digest*, 1857–1860. (Cited on page [98](#).)
- BOCK, D.C.J. (2006). CARMA: Combined Array for Research in Millimeter-Wave Astronomy. In D.C. Backer, J.M. Moran & J.L. Turner, eds., *Revealing the Molecular Universe: One Antenna is Never Enough*, vol. 356 of *Astronomical Society of the Pacific Conference Series*, 17. (Cited on pages [33](#) and [34](#).)
- BOOKBINDER, J.A., STENCEL, R.E., DRAKE, S.A., SIMON, T., LINSKY, J.L. & FLORKOWSKI, D. (1987). VLA Observations of Rapid 6 cm Flux Variations in α Ori. In J. L. Linsky & R. E. Stencel, ed., *Cool Stars, Stellar Systems and the Sun*, vol. 291 of *Lecture Notes in Physics*, Berlin Springer Verlag, 337. (Cited on pages [97](#) and [110](#).)
- BOOTHROYD, A.I. & SACKMANN, I.J. (1999). The CNO Isotopes: Deep Circulation in Red Giants and First and Second Dredge-up. *Astrophysical Journal*, **510**, 232–250. (Cited on page [78](#).)
- BOTTLINGER, C.F. (1911). Die Bahn des spektroskopischen Doppelsternes α Orionis. *Astronomische Nachrichten*, **187**, 33. (Cited on page [81](#).)
- BRACEWELL, R.N. (2000). *The Fourier Transform and Its Applications*. Columbus, OH: McGraw Hill, 3rd edn. (Cited on page [95](#).)
- BROWN, K.I.T. (2007). Long-Term Spectroscopic and Precise Radial Velocity Monitoring of Arcturus. *Publications of the Astronomical Society of the Pacific*, **119**, 237–237. (Cited on page [41](#).)
- BROWN, K.I.T., GRAY, D.F. & BALIUNAS, S.L. (2008). Long-Term Spectroscopic Monitoring of Arcturus. *Astrophysical Journal*, **679**, 1531–1540. (Cited on page [43](#).)
- BUSCHER, D.F., BALDWIN, J.E., WARNER, P.J. & HANIFF, C.A. (1990). Detection of a bright feature on the surface of Betelgeuse. *Monthly Notices of the Royal Astronomical Society*, **245**, 7P–11P. (Cited on page [114](#).)

REFERENCES

- CARLSSON, M. (1986). A computer program for solving multi-level non-LTE radiative transfer-problems in moving or static atmospheres. *Uppsala Astronomical Observatory Reports*, **33**. (Cited on page [127](#).)
- CARPENTER, K.G. & ROBINSON, R.D. (1996). HST Studies of Carbon and K-M Giant/Superiant Stars. In P. Benvenuti, F.D. Macchetto & E.J. Schreier, eds., *Science with the Hubble Space Telescope - II*, 418. (Cited on page [44](#).)
- CARPENTER, K.G. & ROBINSON, R.D. (1997). GHRS Observations of Cool, Low-Gravity Stars. III. Plasma Flows and Turbulence in the Outer Atmosphere of alpha Orionis (M2 Iab). *Astrophysical Journal*, **479**, 970–+. (Cited on pages [96](#) and [109](#).)
- CARPENTER, K.G., ROBINSON, R.D., HARPER, G.M., BENNETT, P.D., BROWN, A. & MULLAN, D.J. (1999). GHRS Observations of Cool, Low-Gravity Stars. V. The Outer Atmosphere and Wind of the Nearby K Supergiant lambda Velorum. *Astrophysical Journal*, **521**, 382–406. (Cited on page [40](#).)
- CASSINELLI, J.P. & HARTMANN, L. (1977). The effect of winds and coronae of hot stars on the infrared and radio continua. *Astrophysical Journal*, **212**, 488–493. (Cited on page [135](#).)
- CHAPMAN, R.D. (1981). The 1979-1980 eclipse of Zeta Aurigae. I - The circumstellar envelope. *Astrophysical Journal*, **248**, 1043–1052. (Cited on page [40](#).)
- CHARBONNEAU, P. & MACGREGOR, K.B. (1995). Stellar Winds with Non-WKB Alfvén Waves. II. Wind Models for Cool, Evolved Stars. *Astrophysical Journal*, **454**, 901. (Cited on page [129](#).)
- CHARBONNEL, C. (1995). A Consistent Explanation for 12C/ 13C, 7Li and 3He Anomalies in Red Giant Stars. *Astrophysical Journal Letters*, **453**, L41. (Cited on page [78](#).)
- CHIAVASSA, A., HAUBOIS, X., YOUNG, J.S., PLEZ, B., JOSSELIN, E., PERRIN, G. & FREYTAG, B. (2010). Radiative hydrodynamics simulations of red supergiant stars. II. Simulations of convection on Betelgeuse match interferometric observations. *Astronomy & Astrophysics*, **515**, A12. (Cited on page [32](#).)
- COHEN, M., CARBON, D.F., WELCH, W.J., LIM, T., SCHULZ, B., McMURRY, A.D., FORSTER, J.R. & GOORVITCH, D. (2005). Far-Infrared and Millimeter Continuum Studies of K Giants: α Bootis and α Tauri. *Astronomical Journal*, **129**, 2836–2848. (Cited on page [122](#).)
- CORNWELL, T., BRAUN, R. & BRIGGS, D.S. (1999). Deconvolution. In G.B. Taylor, C.L. Carilli & R.A. Perley, eds., *Synthesis Imaging in Radio Astronomy II*, vol. 180 of *Astronomical Society of the Pacific Conference Series*, 151. (Cited on page [26](#).)
- CORNWELL, T.J. (2008). Multiscale CLEAN Deconvolution of Radio Synthesis Images. *IEEE Journal of Selected Topics in Signal Processing*, **2**, 793–801. (Cited on page [72](#).)
- CROWLEY, C., ESPEY, B.R. & MCCANDLISS, S.R. (2008). EG And: Far Ultraviolet Spectroscopic Explorer and Hubble Space Telescope STIS Monitoring of an Eclipsing Symbiotic Binary. *Astrophysical Journal*, **675**, 711–722. (Cited on page [40](#).)

REFERENCES

- DANCHI, W.C., BESTER, M., DEGIACOMI, C.G., GREENHILL, L.J. & TOWNES, C.H. (1994). Characteristics of dust shells around 13 late-type stars. *Astronomical Journal*, **107**, 1469–1513. (Cited on page [77](#).)
- DE GRAAUW, T., HELMICH, F.P., PHILLIPS, T.G., STUTZKI, J., CAUX, E., WHYBORN, N.D., DIELEMAN, P., ROELFSEMA, P.R., AARTS, H., ASSENDORP, R., BACHILLER, R., BAECHTOLD, W., BARCIA, A., BEINTEMA, D.A., BELITSKY, V., BENZ, A.O., BIEBER, R., BOOGERT, A., BORYS, C., BUMBLE, B., CAÏS, P., CARIS, M., CERULLI-IRELLI, P., CHATTOPADHYAY, G., CHEREDNICHENKO, S., CIECHANOWICZ, M., COEUR-JOLY, O., COMITO, C., CROS, A., DE JONGE, A., DE LANGE, G., DELFORGES, B., DELORME, Y., DEN BOGGENDE, T., DESBAT, J.M., DIEZ-GONZÁLEZ, C., DI GIORGIO, A.M., DUBBELDAM, L., EDWARDS, K., EGGENS, M., ERICKSON, N., EVERE, J., FICH, M., FINN, T., FRANKE, B., GAIER, T., GAL, C., GAO, J.R., GALLEG, J.D., GAUFFRE, S., GILL, J.J., GLENZ, S., GOLSTEIN, H., GOLOOZE, H., GUNSING, T., GÜSTEN, R., HARTOGH, P., HATCH, W.A., HIGGINS, R., HONINGH, E.C., HUISMAN, R., JACKSON, B.D., JACOBS, H., JACOBS, K., JARCHOW, C., JAVADI, H., JELLEMA, W., JUSTEN, M., KARPOV, A., KASEMANN, C., KAWAMURA, J., KEIZER, G., KESTER, D., KLAAPWIJK, T.M., KLEIN, T., KOLLBERG, E., KOOI, J., KOOIMAN, P.P., KOPF, B., KRAUSE, M., KRIEG, J.M., KRAMER, C., KRUIZENGA, B., KUHN, T., LAUWEN, W., LAI, R., LARSSON, B., LEDUC, H.G., LEINZ, C., LIN, R.H., LISEAU, R., LIU, G.S., LOOSE, A., LÓPEZ-FERNANDEZ, I., LORD, S., LUINGE, W., MARSTON, A., MARTÍN-PINTADO, J., MAESTRINI, A., MAIWALD, F.W., MCCOEY, C., MEHDI, I., MEGEJ, A., MELCHIOR, M., MEINSMA, L., MERKEL, H., MICHALSKA, M., MONSTEIN, C., MORATSCHKE, D., MORRIS, P., MULLER, H., MURPHY, J.A., NABER, A., NATALE, E., NOWOSIELSKI, W., NUZZOLO, F., OLBERG, M., OLBRICH, M., ORFEI, R., ORLEANSKI, P., OSSENKOPF, V., PEACOCK, T., PEARSON, J.C., PERON, I., PHILLIP-MAY, S., PIAZZO, L., PLANESAS, P., RATAJ, M., RAVERA, L., RISACHER, C., SALEZ, M., SAMOSKA, L.A., SARACENO, P., SCHIEDER, R., SCHLECHT, E., SCHLÖDER, F., SCHMÜLLING, F., SCHULTZ, M., SCHUSTER, K., SIEBERTZ, O., SMIT, H., SZCZERBA, R., SHIPMAN, R., STEINMETZ, E., STERN, J.A., STOKROOS, M., TEIPEN, R., TEYSSIER, D., TILS, T., TRAPPE, N., VAN BAAREN, C., VAN LEEUWEN, B.J., VAN DE STADT, H., VISSER, H., WILDEMAN, K.J., WAFELBAKKER, C.K., WARD, J.S., WESSELUS, P., WILD, W., WULFF, S., WUNSCH, H.J., TIELENS, X., ZAAL, P., ZIRATH, H., ZMUDZINAS, J. & ZWART, F. (2010). The Herschel-Heterodyne Instrument for the Far-Infrared (HIFI). *Astronomy & Astrophysics*, **518**, L6. (Cited on page [99](#).)
- DECIN, L., VANDENBUSSCHE, B., WAELKENS, C., DECIN, G., ERIKSSON, K., GUSTAFSSON, B., PLEZ, B. & SAUVAL, A.J. (2003). ISO-SWS calibration and the accurate modelling of cool-star atmospheres. IV. G9 to M2 stars. *Astronomy & Astrophysics*, **400**, 709–727. (Cited on pages [42](#) and [44](#).)
- DECIN, L., COX, N.L.J., ROYER, P., VAN MARLE, A.J., VANDENBUSSCHE, B., LADJAL, D., KERSCHBAUM, F., OTTENSAMER, R., BARLOW, M.J., BLOMMAERT, J.A.D.L., GOMEZ, H.L., GROENEWEGEN, M.A.T., LIM, T., SWINYARD, B.M., WAELKENS, C. & TIELENS, A.G.G.M. (2012). The enigmatic nature of the circumstellar envelope and bow shock surrounding Betelgeuse as revealed by Herschel. I. Evidence of clumps, multiple arcs, and a linear bar-like structure. *Astronomy & Astrophysics*, **548**, A113. (Cited on page [32](#).)
- DEHAES, S., BAUWENS, E., DECIN, L., ERIKSSON, K., RASKIN, G., BUTLER, B., DOWELL, C.D., ALI, B. & BLOMMAERT, J.A.D.L. (2011). Structure of the outer layers of cool standard stars. *Astronomy & Astrophysics*, **533**, A107. (Cited on pages [121](#) and [122](#).)

REFERENCES

- DI BENEDETTO, G.P. (1993). Empirical effective temperatures and angular diameters of stars cooler than the sun. *Astronomy & Astrophysics*, **270**, 315–334. (Cited on pages [41](#) and [42](#).)
- DRAKE, S. & LINSKY, J. (1986). Radio continuum emission from winds, chromospheres, and coronae of cool giants and supergiants. *Astronomical Journal*, **91**, 602–620. (Cited on pages [121](#), [122](#), [131](#) and [132](#).)
- DRAKE, S.A. (1985). Modeling lines formed in the expanding chromospheres of red giants. In J.E. Beckman & L. Crivellari, eds., *Progress in stellar spectral line formation theory; Proceedings of the Advanced Research Workshop, Trieste, Italy, September 4-7, 1984 (A86-37976 17-90)*. Dordrecht, D. Reidel Publishing Co., 1985, p. 351-357., 351–357. (Cited on pages [42](#), [43](#), [123](#), [125](#), [126](#), [135](#), [139](#), [142](#) and [145](#).)
- DRAKE, S.A. & LINSKY, J.L. (1983a). First detection of winds in red giants by microwave continuum techniques. *Astrophysical Journal Letters*, **274**, L77–L81. (Cited on pages [120](#) and [121](#).)
- DRAKE, S.A. & LINSKY, J.L. (1983b). The formation of emission lines in the expanding chromospheres of luminous cool stars. I - The importance of atmospheric extension and partial redistribution effects. *Astrophysical Journal*, **273**, 299–308. (Cited on page [125](#).)
- DRAKE, S.A., BOOKBINDER, J.A., FLORKOWSKI, D.R., LINSKY, J.L., SIMON, T. & STENCEL, R.E. (1992). Four Years of Monitoring a Orionis with the VLA: Where have all the Flares Gone? In M. S. Giampapa & J. A. Bookbinder, ed., *Cool Stars, Stellar Systems, and the Sun*, vol. 26 of *Astronomical Society of the Pacific Conference Series*, 455. (Cited on pages [97](#) and [110](#).)
- DUPREE, A.K., BALIUNAS, S.L., HARTMANN, L., GUINAN, E.F. & SONNEBORN, G. (1990). Alpha ORI - Evidence for pulsation. In C. Cacciari & G. Clementini, eds., *Confrontation Between Stellar Pulsation and Evolution*, vol. 11 of *Astronomical Society of the Pacific Conference Series*, 468–471. (Cited on page [80](#).)
- DUPREE, A.K., LOBEL, A., YOUNG, P.R., AKE, T.B., LINSKY, J.L. & REDFIELD, S. (2005). A Far-Ultraviolet Spectroscopic Survey of Luminous Cool Stars. *Astrophysical Journal*, **622**, 629–652. (Cited on page [45](#).)
- DZIEMBOWSKI, W.A., GOUGH, D.O., HOODEK, G. & SIENKIEWICZ, R. (2001). Oscillations of α UMa and other red giants. *Monthly Notices of the Royal Astronomical Society*, **328**, 601–610. (Cited on page [41](#).)
- EATON, J.A. (2008). A Model for the Chromosphere/Wind of 31 Cygni and Its Implications for Single Stars. *Astronomical Journal*, **136**, 1964–1979. (Cited on page [40](#).)
- EGGEN, O.J. (1971). The Arcturus Group. *Publications of the Astronomical Society of the Pacific*, **83**, 271. (Cited on page [41](#).)
- EGGEN, O.J. (1996). Star Streams and Galactic Structure. *Astronomical Journal*, **112**, 1595. (Cited on page [41](#).)

REFERENCES

- EGGLETON, P.P., DEARBORN, D.S.P. & LATTANZIO, J.C. (2007). Compulsory Deep Mixing of ^3He and CNO Isotopes on the First Giant Branch. In R.J. Stancliffe, G. Houdek, R.G. Martin & C.A. Tout, eds., *Unsolved Problems in Stellar Physics: A Conference in Honor of Douglas Gough*, vol. 948 of *American Institute of Physics Conference Series*, 27–34. (Cited on page 78.)
- FAMAЕY, B., JORISSEN, A., LURI, X., MAYOR, M., UDRY, S., DEJONGHE, H. & TURON, C. (2005). Local kinematics of K and M giants from CORAVEL/Hipparcos/Tycho-2 data. Revisiting the concept of superclusters. *Astronomy & Astrophysics*, **430**, 165–186. (Cited on page 85.)
- GILLILAND, R.L. & DUPREE, A.K. (1996). First Image of the Surface of a Star with the Hubble Space Telescope. *Astrophysical Journal Letters*, **463**, L29. (Cited on pages 31 and 103.)
- GLASSGOLD, A.E. & HUGGINS, P.J. (1986). The ionization structure of the circumstellar envelope of Alpha Orionis. *Astrophysical Journal*, **306**, 605–617. (Cited on pages 136 and 137.)
- GOLDBERG, L. (1984). The variability of alpha Orionis. *Publications of the Astronomical Society of the Pacific*, **96**, 366–371. (Cited on pages 81 and 96.)
- GOLDBERG, L., RAMSEY, L., TESTERMAN, L. & CARBON, D. (1975). High-resolution profiles of sodium and potassium lines in alpha Orionis. *Astrophysical Journal*, **199**, 427–431. (Cited on page 79.)
- GRAY, D.F. (2008). Mass Motions in the Photosphere of Betelgeuse. *Astronomical Journal*, **135**, 1450–1458. (Cited on page 114.)
- GRAY, R.O., CORBALLY, C.J., GARRISON, R.F., MCFADDEN, M.T., BUBAR, E.J., McGAHEE, C.E., O'DONOOGHUE, A.A. & KNOX, E.R. (2006). Contributions to the Nearby Stars (NStars) Project: Spectroscopy of Stars Earlier than M0 within 40 pc-The Southern Sample. *Astronomical Journal*, **132**, 161–170. (Cited on pages 42 and 126.)
- GRIFFIN, R.E.M. (1996). Arcturus and human evolution. *The Observatory*, **116**, 404–405. (Cited on page 41.)
- GUESTEN, R., HARTOGH, P., HUEBERS, H.W., GRAF, U.U., JACOBS, K., ROESER, H.P., SCHAEFER, F., SCHIEDER, R.T., STARK, R., STUTZKI, J., VAN DER WAL, P. & WUNSCH, A. (2000). GREAT: the first-generation German heterodyne receiver for SOFIA. In R. K. Melugin & H.-P. Röser, ed., *Society of Photo-Optical Instrumentation Engineers (SPIE) Conference Series*, vol. 4014, 23–30. (Cited on page 98.)
- HAMAKER, J.P., BREGMAN, J.D. & SAULT, R.J. (1996). Understanding radio polarimetry. I. Mathematical foundations. *Astronomy & Astrophysics Supplemental*, **117**, 137–147. (Cited on page 64.)
- HARPER, G.M. (1994). A Computer Program for Solving Multilevel Non-Lte Radiative Transfer Problems in Spherical Geometry in Moving or Static Atmospheres. *Monthly Notices of the Royal Astronomical Society*, **268**, 894. (Cited on page 125.)

REFERENCES

- HARPER, G.M. (2010). Betelgeuse: A Case Study of an Inhomogeneous Extended Atmosphere. In C. Leitherer, P.D. Bennett, P.W. Morris & J.T. Van Loon, eds., *Hot and Cool: Bridging Gaps in Massive Star Evolution*, vol. 425 of *Astronomical Society of the Pacific Conference Series*, 152. (Cited on page 32.)
- HARPER, G.M., BROWN, A. & LIM, J. (2001). A Spatially Resolved, Semiempirical Model for the Extended Atmosphere of α Orionis (M2 Iab). *Astrophysical Journal*, **551**, 1073–1098. (Cited on pages 29, 30, 31, 77, 104, 106, 107, 108 and 111.)
- HARPER, G.M., BROWN, A., BENNETT, P.D., BAADE, R., WALDER, R. & HUMMEL, C.A. (2005). VLA Observations of ζ Aurigae: Confirmation of the Slow Acceleration Wind Density Structure. *Astronomical Journal*, **129**, 1018–1034. (Cited on page 40.)
- HARPER, G.M., BROWN, A. & GUINAN, E.F. (2008). A New VLA-Hipparcos Distance to Betelgeuse and its Implications. *Astronomical Journal*, **135**, 1430–1440. (Cited on pages xiii, 29, 30, 81, 85, 105 and 109.)
- HARPER, G.M., RICHTER, M.J., RYDE, N., BROWN, A., BROWN, J., GREATHOUSE, T.K. & STRONG, S. (2009). Texes Observations of M Supergiants: Dynamics and Thermodynamics of Wind Acceleration. *Astrophysical Journal*, **701**, 1464–1483. (Cited on page 31.)
- HARPER, G.M., O'RIAIN, N. & AYRES, T.R. (2013). Chromospheric thermal continuum millimetre emission from non-dusty K and M red giants. *Monthly Notices of the Royal Astronomical Society*, **428**, 2064–2073. (Cited on pages 40 and 121.)
- HARRIS, M.J. & LAMBERT, D.L. (1984). Oxygen isotopes in the atmospheres of Betelgeuse and Antares. *Astrophysical Journal*, **281**, 739–745. (Cited on pages 30 and 78.)
- HARTMANN, L. & AVRETT, E.H. (1984). On the extended chromosphere of Alpha Orionis. *Astrophysical Journal*, **284**, 238–249. (Cited on pages 31 and 103.)
- HARTMANN, L. & MACGREGOR, K.B. (1980). Momentum and energy deposition in late-type stellar atmospheres and winds. *Astrophysical Journal*, **242**, 260–282. (Cited on page 133.)
- HARTMANN, L., AVRETT, E. & EDWARDS, S. (1982). Wave-driven winds from cool stars. II - Models for T Tauri stars. *Astrophysical Journal*, **261**, 279–292. (Cited on page 133.)
- HATZES, A.P. & COCHRAN, W.D. (1993). Long-period radial velocity variations in three K giants. *Astrophysical Journal*, **413**, 339–348. (Cited on pages 41, 42 and 44.)
- HATZES, A.P. & COCHRAN, W.D. (1998). On the nature of the radial velocity variability of Aldebaran - A search for spectral line bisector variations. *Monthly Notices of the Royal Astronomical Society*, **293**, 469. (Cited on page 44.)
- HAUBOIS, X., PERRIN, G., LACOUR, S., VERHOELST, T., MEIMON, S., MUGNIER, L., THIÉBAUT, E., BERGER, J.P., RIDGWAY, S.T., MONNIER, J.D., MILLAN-GABET, R. & TRAUB, W. (2009). Imaging the spotty surface of $\text{[ASTROBJ]}\beta\text{Betelgeuse}\text{[ASTROBJ]}$ in the H band. *Astronomy & Astrophysics*, **508**, 923–932. (Cited on page 32.)
- HINKLE, K.H., LAMBERT, D.L. & SNELL, R.L. (1976). The C-12/C-13 ratio in stellar atmospheres. VI - Five luminous cool stars. *Astrophysical Journal*, **210**, 684–693. (Cited on page 78.)

REFERENCES

- HÖGBOM, J.A. (1974). Aperture Synthesis with a Non-Regular Distribution of Interferometer Baselines. *Astronomy & Astrophysics Supplemental*, **15**, 417. (Cited on page [26](#).)
- HOLZER, T.E., FLA, T. & LEER, E. (1983). Alfvén waves in stellar winds. *Astrophysical Journal*, **275**, 808–835. (Cited on pages [128](#) and [133](#).)
- HOOGWERF, R., DE BRUIJNE, J.H.J. & DE ZEEUW, P.T. (2000). The Origin of Runaway Stars. *Astrophysical Journal Letters*, **544**, L133–L136. (Cited on page [29](#).)
- HUGGINS, P.J. (1987). CO in the circumstellar envelope of Alpha Orionis. *Astrophysical Journal*, **313**, 400–407. (Cited on pages [79](#), [83](#), [84](#) and [90](#).)
- HUGGINS, P.J., BACHILLER, R., COX, P. & FORVEILLE, T. (1994). Neutral carbon in the circumstellar envelope of alpha Orionis. *Astrophysical Journal Letters*, **424**, L127–L130. (Cited on pages [79](#), [80](#), [88](#) and [90](#).)
- HUMMER, D.G. (1988). A fast and accurate method for evaluating the nonrelativistic free-free Gaunt factor for hydrogenic ions. *Astrophysical Journal*, **327**, 477–484. (Cited on page [125](#).)
- JACKSON, N. (2008). Principles of Interferometry. In F. Bacciotti, L. Testi & E. Whelan, eds., *Jets from Young Stars II*, vol. 742 of *Lecture Notes in Physics*, Berlin Springer Verlag, 193. (Cited on pages [14](#) and [16](#).)
- JATENCO-PEREIRA, V. & OPHÉR, R. (1989). Effect of diverging magnetic fields on mass loss in late-type giant stars. *Astronomy & Astrophysics*, **209**, 327–336. (Cited on page [133](#).)
- JOHNSON, H.R. (1973). Cooling effect of CO in stellar atmospheres. *Astrophysical Journal*, **180**, 81–89. (Cited on page [127](#).)
- JOSSELIN, E. & PLEZ, B. (2007). Atmospheric dynamics and the mass loss process in red supergiant stars. *Astronomy & Astrophysics*, **469**, 671–680. (Cited on page [114](#).)
- KALER, J.B., IBEN, I., JR. & BECKER, S.A. (1978). On the enhancement of helium and nitrogen in planetary nebulae. *Astrophysical Journal Letters*, **224**, L63–L66. (Cited on page [78](#).)
- KALLINGER, T., WEISS, W.W., BARBAN, C., BAUDIN, F., CAMERON, C., CARRIER, F., DE RIDDER, J., GOUPIL, M.J., GRUBERBAUER, M., HATZES, A., HEKKER, S., SAMADI, R. & DELEUIL, M. (2010). Oscillating red giants in the CoRoT exofield: asteroseismic mass and radius determination. *Astronomy & Astrophysics*, **509**, A77. (Cited on pages [41](#) and [42](#).)
- KAMIŃSKI, T., GOTTLIEB, C.A., SCHMIDT, M.R., PATEL, N.A., YOUNG, K.H., MENTEN, K.M., BRÜNKEN, S., MÜLLER, H.S.P., WINTERS, J.M. & McCARTHY, M.C. (2013). Dust-forming molecules in VY Canis Majoris (and Betelgeuse). In *EAS Publications Series*, vol. 60 of *EAS Publications Series*, 191–198. (Cited on page [32](#).)
- KELCH, W.L., CHANG, S.H., FURENLID, I., LINSKY, J.L., BASRI, G.S., CHIU, H.Y. & MARAN, S.P. (1978). Stellar model chromospheres. VII - Capella /G5 III +/, Pollux /K0 III/, and Aldebaran /K5 III/. *Astrophysical Journal*, **220**, 962–979. (Cited on pages [44](#) and [45](#).)

REFERENCES

- KERVELLA, P., VERHOELST, T., RIDGWAY, S.T., PERRIN, G., LACOUR, S., CAMI, J. & HAUBOIS, X. (2009). The close circumstellar environment of Betelgeuse. Adaptive optics spectro-imaging in the near-IR with VLT/NACO. *Astronomy & Astrophysics*, **504**, 115–125. (Cited on page [32](#).)
- KERVELLA, P., PERRIN, G., CHIAVASSA, A., RIDGWAY, S.T., CAMI, J., HAUBOIS, X. & VERHOELST, T. (2011). The close circumstellar environment of Betelgeuse. II. Diffraction-limited spectro-imaging from 7.76 to 19.50 μm with VLT/VISIR. *Astronomy & Astrophysics*, **531**, A117. (Cited on pages [32](#) and [95](#).)
- KNAPP, G.R. & MORRIS, M. (1985). Mass loss from evolved stars. III - Mass loss rates for fifty stars from CO $J = 1-0$ observations. *Astrophysical Journal*, **292**, 640–669. (Cited on page [79](#).)
- KNAPP, G.R., PHILLIPS, T.G. & HUGGINS, P.J. (1980). Detection of CO Emission at 1.3-MILLIMETERS from the Betelgeuse Circumstellar Shell. *Astrophysical Journal Letters*, **242**, L25+. (Cited on pages [79](#), [84](#) and [90](#).)
- KRAUS, J.D., TIURI, M., RAISANEN, A.V. & CARR, T.D. (1986). *Radio astronomy receivers*. (Cited on page [5](#).)
- KROGULEC, M. (1988). Alfvén wave driven wind - Models of Alpha Boo atmosphere. *Acta Astronomica*, **38**, 107–126. (Cited on page [128](#).)
- KROGULEC, M. (1989). Alfvén wave driven wind. II - Models of cool giant and supergiant stars. *Acta Astronomica*, **39**, 51–67. (Cited on page [128](#).)
- LACOUR, S., MEIMON, S., THIÉBAUT, E., PERRIN, G., VERHOELST, T., PEDRETTI, E., SCHULLER, P.A., MUGNIER, L., MONNIER, J., BERGER, J.P., HAUBOIS, X., PONCELET, A., LE BESNERAIS, G., ERIKSSON, K., MILLAN-GABET, R., RAGLAND, S., LACASSE, M. & TRAUB, W. (2008). The limb-darkened Arcturus: imaging with the IOTA/IONIC interferometer. *Astronomy & Astrophysics*, **485**, 561–570. (Cited on page [41](#).)
- LAMB, S.A., IBEN, I., JR. & HOWARD, W.M. (1976). On the evolution of massive stars through the core carbon-burning phase. *Astrophysical Journal*, **207**, 209–232. (Cited on page [77](#).)
- LAMBERT, D.L. & VANDEN BOUT, P.A. (1978). Constraints on the properties of circumstellar shells from observations of thermal CO and SiO millimeter line emission. *Astrophysical Journal*, **221**, 854–860. (Cited on page [99](#).)
- LAMBERT, D.L., DEARBORN, D.S. & SNEDEN, C. (1974). The C-12/C-13 ratio in stellar atmospheres. II - CN and CO in alpha Orionis. *Astrophysical Journal*, **193**, 621–630. (Cited on page [78](#).)
- LAMBERT, D.L., BROWN, J.A., HINKLE, K.H. & JOHNSON, H.R. (1984). Carbon, nitrogen, and oxygen abundances in Betelgeuse. *Astrophysical Journal*, **284**, 223–237. (Cited on pages [30](#) and [77](#).)
- LAMERS, H.J.G.L.M., CERRUTI-SOLA, M. & PERINOTTO, M. (1987). The 'SEI' method for accurate and efficient calculations of line profiles in spherically symmetric stellar winds. *Astrophysical Journal*, **314**, 726–738. (Cited on page [127](#).)

REFERENCES

- LEBZELTER, T., HEITER, U., ABIA, C., ERIKSSON, K., IRELAND, M., NEILSON, H., NOWOTNY, W., MALDONADO, J., MERLE, T., PETERSON, R., PLEZ, B., SHORT, C.I., WAHLGREN, G.M., WORLEY, C., ARINGER, B., BLADH, S., DE LAVERNY, P., GOSWAMI, A., MORA, A., NORRIS, R.P., RECIO-BLANCO, A., SCHOLZ, M., THÉVENIN, F., TSUJI, T., KORDOPATIS, G., MONTESINOS, B. & WING, R.F. (2012). Comparative modelling of the spectra of cool giants. *Astronomy & Astrophysics*, **547**, A108. (Cited on page [42](#).)
- LEVESQUE, E.M., MASSEY, P., OLSEN, K.A.G., PLEZ, B., JOSSELIN, E., MAEDER, A. & MEYNET, G. (2005). The Effective Temperature Scale of Galactic Red Supergiants: Cool, but Not As Cool As We Thought. *Astrophysical Journal*, **628**, 973–985. (Cited on pages [30](#) and [105](#).)
- LIM, J., CARILLI, C.L., WHITE, S.M., BEASLEY, A.J. & MARSON, R.G. (1998). Large convection cells as the source of Betelgeuse's extended atmosphere. *Nature*, **392**, 575–577. (Cited on pages [30](#), [31](#), [55](#), [96](#), [103](#), [104](#), [106](#) and [110](#).)
- LINSKY, J.L. & HAISCH, B.M. (1979). Outer atmospheres of cool stars. I - The sharp division into solar-type and non-solar-type stars. *Astrophysical Journal Letters*, **229**, L27–L32. (Cited on pages [43](#) and [44](#).)
- MASSAROTTI, A., LATHAM, D.W., STEFANIK, R.P. & FOGL, J. (2008). Rotational and Radial Velocities for a Sample of 761 HIPPARCOS Giants and the Role of Binarity. *Astronomical Journal*, **135**, 209–231. (Cited on page [42](#).)
- MCMULLIN, J.P., WATERS, B., SCHIEBEL, D., YOUNG, W. & GOLAP, K. (2007). CASA Architecture and Applications. In R.A. Shaw, F. Hill & D.J. Bell, eds., *Astronomical Data Analysis Software and Systems XVI*, vol. 376 of *Astronomical Society of the Pacific Conference Series*, 127. (Cited on page [59](#).)
- MCMURRY, A.D. (1999). The outer atmosphere of Tau - I. A new chromospheric model. *Monthly Notices of the Royal Astronomical Society*, **302**, 37–47. (Cited on pages [42](#), [126](#) and [127](#).)
- MERLINE, W.J. (1999). Precise Velocity Observation of K-Giants: Evidence for Solar-Like Oscillations in Arcturus. In J.B. Hearnshaw & C.D. Scarfe, eds., *IAU Colloq. 170: Precise Stellar Radial Velocities*, vol. 185 of *Astronomical Society of the Pacific Conference Series*, 187. (Cited on page [41](#).)
- MEYNET, G. & MAEDER, A. (2003). Stellar evolution with rotation. X. Wolf-Rayet star populations at solar metallicity. *Astronomy & Astrophysics*, **404**, 975–990. (Cited on pages [29](#), [30](#) and [85](#).)
- MICHELSON, A.A. (1890). *Phil. Mag.*, **30**, 1–21. (Cited on page [20](#).)
- MHALAS, D. (1978). *Stellar atmospheres /2nd edition/*. (Cited on page [125](#).)
- MUXLOW, T.W.B. (2003). e-MERLIN - a Real-Time VLBI Array. In Y.C. Minh, ed., *New technologies in VLBI*, vol. 306 of *Astronomical Society of the Pacific Conference Series*, 245. (Cited on page [103](#).)
- NAVARRO, J.F., HELMI, A. & FREEMAN, K.C. (2004). The Extragalactic Origin of the Arcturus Group. *Astrophysical Journal Letters*, **601**, L43–L46. (Cited on page [41](#).)

REFERENCES

- NEWELL, R.T. & HJELLMING, R.M. (1982). Radio emission from the extended chromosphere of Alpha Orionis. *Astrophysical Journal Letters*, **263**, L85–L87. (Cited on pages [31](#), [103](#), [110](#) and [111](#).)
- O'GORMAN, E. & HARPER, G.M. (2011). What is Heating Arcturus' Wind? In C. Johns-Krull, M.K. Browning & A.A. West, eds., *16th Cambridge Workshop on Cool Stars, Stellar Systems, and the Sun*, vol. 448 of *Astronomical Society of the Pacific Conference Series*, 691. (Cited on page [136](#).)
- O'GORMAN, E., HARPER, G.M., BROWN, J.M., BROWN, A., REDFIELD, S., RICHTER, M.J. & REQUENA-TORRES, M.A. (2012). CARMA CO($J = 2 - 1$) Observations of the Circumstellar Envelope of Betelgeuse. *Astronomical Journal*, **144**, 36. (Cited on pages [58](#) and [76](#).)
- O'GORMAN, E., HARPER, G.M., BROWN, A., DRAKE, S. & RICHARDS, A.M.S. (2013). Multi-wavelength Radio Continuum Emission Studies of Dust-free Red Giants. *Astronomical Journal*, **144**, 36. (Cited on pages [58](#) and [115](#).)
- OHNAKA, K. (2013). Spatially resolved, high-spectral resolution observation of the K giant Aldebaran in the CO first overtone lines with VLTI/AMBER. *Astronomy & Astrophysics*, **553**, A3. (Cited on pages [141](#) and [143](#).)
- OLNON, F.M. (1975). Thermal bremsstrahlung radiospectra for inhomogeneous objects, with an application to MWC 349. *Astronomy & Astrophysics*, **39**, 217–223. (Cited on pages [127](#) and [129](#).)
- PANAGIA, N. & FELLI, M. (1975). The spectrum of the free-free radiation from extended envelopes. *Astronomy & Astrophysics*, **39**, 1–5. (Cited on pages [127](#) and [129](#).)
- PAVLENKO, Y.V., JONES, H.R.A. & LONGMORE, A.J. (2003). Carbon abundances and $^{12}\text{C}/^{13}\text{C}$ from globular cluster giants. *Monthly Notices of the Royal Astronomical Society*, **345**, 311–324. (Cited on page [78](#).)
- PERLEY, R.A. & BUTLER, B.J. (2013). An Accurate Flux Density Scale from 1 to 50 GHz. *Astrophysical Journal Supplemental Series*, **204**, 19. (Cited on pages [66](#) and [117](#).)
- PERRIN, G., RIDGWAY, S.T., COUDÉ DU FORESTO, V., MENNESSON, B., TRAUB, W.A. & LACASSE, M.G. (2004). Interferometric observations of the supergiant stars α Orionis and α Herculis with FLUOR at IOTA. *Astronomy & Astrophysics*, **418**, 675–685. (Cited on page [30](#).)
- PERRIN, G., VERHOELST, T., RIDGWAY, S.T., CAMI, J., NGUYEN, Q.N., CHESNEAU, O., LOPEZ, B., LEINERT, C. & RICHICHI, A. (2007). The molecular and dusty composition of Betelgeuse's inner circumstellar environment. *Astronomy & Astrophysics*, **474**, 599–608. (Cited on page [32](#).)
- PERRYMAN, M.A.C., LINDEGREN, L., KOVALEVSKY, J., HOEG, E., BASTIAN, U., BERNACCA, P.L., CRÉZÉ, M., DONATI, F., GRENON, M., GREWING, M., VAN LEEUWEN, F., VAN DER MAREL, H., MIGNARD, F., MURRAY, C.A., LE POOLE, R.S., SCHRIJVER, H., TURON, C., ARENOU, F., FROESCHLÉ, M. & PETERSEN, C.S. (1997). The HIPPARCOS Catalogue. *Astronomy & Astrophysics*, **323**, L49–L52. (Cited on pages [30](#), [41](#) and [42](#).)

REFERENCES

- PILBRATT, G.L., RIEDINGER, J.R., PASSVOGEL, T., CRONE, G., DOYLE, D., GAGEUR, U., HERAS, A.M., JEWELL, C., METCALFE, L., OTT, S. & SCHMIDT, M. (2010). Herschel Space Observatory. An ESA facility for far-infrared and submillimetre astronomy. *Astronomy & Astrophysics*, **518**, L1. (Cited on page [99](#).)
- PLEZ, B. & LAMBERT, D.L. (2002). The outer atmosphere of the M-type supergiant alpha Orionis: K I 7699 Åemission. *Astronomy & Astrophysics*, **386**, 1009–1018. (Cited on pages [95](#) and [102](#).)
- PROTHERO, D. & BUELL, C. (2007). *Evolution: what the fossils say and why it matters*. Columbia University Press. (Cited on page [1](#).)
- RAMÍREZ, I. & ALLENDE PRIETO, C. (2011). Fundamental Parameters and Chemical Composition of Arcturus. *Astrophysical Journal*, **743**, 135. (Cited on pages [41](#) and [42](#).)
- RAMÍREZ, S.V., SELLGREN, K., CARR, J.S., BALACHANDRAN, S.C., BLUM, R., TERNDRUP, D.M. & STEED, A. (2000). Stellar Iron Abundances at the Galactic Center. *Astrophysical Journal*, **537**, 205–220. (Cited on page [30](#).)
- RETTER, A., BEDDING, T.R., BUZASI, D.L., KJELDSEN, H. & KISS, L.L. (2003). Oscillations in Arcturus from WIRE Photometry. *Astrophysical Journal Letters*, **591**, L151–L154. (Cited on page [41](#).)
- RICH, J.W., DE BLOK, W.J.G., CORNWELL, T.J., BRINKS, E., WALTER, F., BAGETAKOS, I. & KENNICUTT, R.C., JR. (2008). Multi-Scale CLEAN: A Comparison of its Performance Against Classical CLEAN on Galaxies Using THINGS. *Astronomical Journal*, **136**, 2897–2920. (Cited on pages [73](#) and [75](#).)
- RICHARDS, A.M.S., DAVIS, R.J., DECIN, L., ETOKA, S., HARPER, G.M., LIM, J.J., GARINGTON, S.T., GRAY, M.D., McDONALD, I., O'GORMAN, E. & WITTKOWSKI, M. (2013). e-MERLIN resolves Betelgeuse at λ 5 cm: hotspots at 5 R. *Monthly Notices of the Royal Astronomical Society*, **432**, L61. (Cited on pages [55](#), [76](#), [103](#), [105](#), [106](#), [110](#) and [111](#).)
- RICHICHI, A. & ROCCATAGLIATA, V. (2005). Aldebaran's angular diameter: How well do we know it? *Astronomy & Astrophysics*, **433**, 305–312. (Cited on page [42](#).)
- ROBINSON, R.D., CARPENTER, K.G. & BROWN, A. (1998). Goddard High-Resolution Spectrograph Observations of Cool Low-Gravity Stars. IV. A Comparison of the K5 III Stars alpha Tauri and gamma Draconis. *Astrophysical Journal*, **503**, 396. (Cited on pages [42](#), [44](#), [126](#), [127](#) and [135](#).)
- RODGERS, B. & GLASSGOLD, A.E. (1991). The temperature of the circumstellar envelope of Alpha Orionis. *Astrophysical Journal*, **382**, 606–616. (Cited on page [30](#).)
- RYDE, N., LAMBERT, D.L., RICHTER, M.J. & LACY, J.H. (2002). Detection of Water Vapor in the Photosphere of Arcturus. *Astrophysical Journal*, **580**, 447–458. (Cited on page [43](#).)
- SAGAN, C. (1997). *The Demon-Haunted World: Science as a Candle in the Dark*. Ballantine Books. (Cited on page [1](#).)
- SAHA, S.K. (2011). *Aperture Synthesis*. (Cited on page [105](#).)

REFERENCES

- SANFORD, R.F. (1933). No. 464. The variation in the radial velocity of alpha Orionis from 1923 to 1931. *Contributions from the Mount Wilson Observatory / Carnegie Institution of Washington*, **464**, 1–10. (Cited on pages [80](#) and [81](#).)
- SAULT, R.J., TEUBEN, P.J. & WRIGHT, M.C.H. (1995). A Retrospective View of MIRIAD. In R.A. Shaw, H.E. Payne & J.J.E. Hayes, eds., *Astronomical Data Analysis Software and Systems IV*, vol. 77 of *Astronomical Society of the Pacific Conference Series*, 433. (Cited on page [59](#).)
- SCHWARZ, U.J. (1978). Mathematical-statistical Description of the Iterative Beam Removing Technique (Method CLEAN). *Astronomy & Astrophysics*, **65**, 345. (Cited on page [26](#).)
- SCHWARZSCHILD, M. (1975). On the scale of photospheric convection in red giants and supergiants. *Astrophysical Journal*, **195**, 137–144. (Cited on pages [29](#) and [114](#).)
- SEAQUIST, E.R. & TAYLOR, A.R. (1987). A detailed analysis of the radio emission from the symbiotic star RX Puppis. *Astrophysical Journal*, **312**, 813–821. (Cited on page [129](#).)
- SENNHAUSER, C. & BERDYUGINA, S.V. (2011). First detection of a weak magnetic field on the giant Arcturus: remnants of a solar dynamo? *Astronomy & Astrophysics*, **529**, A100. (Cited on pages [42](#) and [43](#).)
- SKINNER, C.J., DOUGHERTY, S.M., MEIXNER, M., BODE, M.F., DAVIS, R.J., DRAKE, S.A., ARENS, J.F. & JERNIGAN, J.G. (1997). Circumstellar environments - V. The asymmetric chromosphere and dust shell of alpha Orionis. *Monthly Notices of the Royal Astronomical Society*, **288**, 295–306. (Cited on pages [32](#) and [103](#).)
- SLEE, O.B., STEWART, R.T., BUNTON, J.D., BEASLEY, A.J., CARTER, B.D. & NELSON, G.J. (1989). A microwave survey of southern red giants. *Monthly Notices of the Royal Astronomical Society*, **239**, 913–922. (Cited on page [121](#).)
- SMITH, M.A., PATTEN, B.M. & GOLDBERG, L. (1989). Radial-velocity variations in Alpha Ori, Alpha Sco, and Alpha HER. *Astronomical Journal*, **98**, 2233–2248. (Cited on page [80](#).)
- SMITH, N., HINKLE, K.H. & RYDE, N. (2009). Red Supergiants as Potential Type IIn Supernova Progenitors: Spatially Resolved 4.6 μ m CO Emission Around VY CMa and Betelgeuse. *Astronomical Journal*, **137**, 3558–3573. (Cited on page [95](#).)
- SODERHJELM, S. & MIGNARD, F. (1998). Arcturus as a double star. *The Observatory*, **118**, 365–366. (Cited on page [41](#).)
- SPENCER JONES, H. (1928). The radial velocity variations of a Orionis and a Scorpis. *Monthly Notices of the Royal Astronomical Society*, **88**, 660. (Cited on pages [80](#) and [81](#).)
- SPINRAD, H. & VARDYA, M.S. (1966). Approximate Abundances of the Light Elements from the Molecular Spectra of M and S Stars. *Astrophysical Journal*, **146**, 399. (Cited on page [77](#).)
- SPITZER, L. (1978). *Physical processes in the interstellar medium*. New York Wiley-Interscience, 1978. 333 p. (Cited on page [140](#).)
- STEBBINS, J. & HUFFER, C.M. (1931). Photo-electric studies of five variable stars. *Publications of the Washburn Observatory*, **15**, 178–213. (Cited on page [80](#).)

REFERENCES

- STOTHERS, R. & LEUNG, K.C. (1971). Luminosities, masses and periodicities of massive red supergiants. *Astronomy & Astrophysics*, **10**, 290–300. (Cited on pages [80](#) and [114](#).)
- TATEBE, K., CHANDLER, A.A., WISHNOW, E.H., HALE, D.D.S. & TOWNES, C.H. (2007). The Nonspherical Shape of Betelgeuse in the Mid-Infrared. *Astrophysical Journal Letters*, **670**, L21–L24. (Cited on page [32](#).)
- TAYLOR, G.B., CARILLI, C.L. & PERLEY, R.A., eds. (1999). *Synthesis Imaging in Radio Astronomy II*, vol. 180 of *Astronomical Society of the Pacific Conference Series*. (Cited on pages [9](#), [10](#) and [117](#).)
- TSUJI, T. (1979). A probe of optically thin dust shells around late-type stars. *Publications of the Astronomical Society of Japan*, **31**, 43–60. (Cited on page [79](#).)
- TSUJI, T. (2000). Water on the Early M Supergiant Stars α Orionis and μ Cephei. *Astrophysical Journal*, **538**, 801–807. (Cited on page [32](#).)
- TSUJI, T. (2008). Cool luminous stars: the hybrid nature of their infrared spectra. *Astronomy & Astrophysics*, **489**, 1271–1289. (Cited on page [44](#).)
- TSUJI, T. (2009). The K giant star Arcturus: the hybrid nature of its infrared spectrum. *Astronomy & Astrophysics*, **504**, 543–559. (Cited on page [43](#).)
- TURNER, N.H., TEN BRUMMELAAR, T.A. & MASON, B.D. (1999). Adaptive Optics Observations of Arcturus using the Mount Wilson 100 Inch Telescope. *Publications of the Astronomical Society of the Pacific*, **111**, 556–558. (Cited on page [41](#).)
- TUTHILL, P.G., HANIFF, C.A. & BALDWIN, J.E. (1997). Hotspots on late-type supergiants. *Monthly Notices of the Royal Astronomical Society*, **285**, 529–539. (Cited on page [114](#).)
- URITENBROEK, H., DUPREE, A.K. & GILLILAND, R.L. (1998). Spatially Resolved Hubble Space Telescope Spectra of the Chromosphere of alpha Orionis. *Astronomical Journal*, **116**, 2501–2512. (Cited on pages [29](#) and [30](#).)
- VAN CITTERT, P.H. (1934). Die Wahrscheinliche Schwingungsverteilung in Einer von Einer Lichtquelle Direkt Oder Mittels Einer Linse Beleuchteten Ebene. *Physica*, **1**, 201–210. (Cited on page [21](#).)
- VAN LEEUWEN, F. (2007). Validation of the new Hipparcos reduction. *Astronomy & Astrophysics*, **474**, 653–664. (Cited on pages [30](#) and [42](#).)
- VERHOELST, T., DECIN, L., VAN MALDEREN, R., HONY, S., CAMI, J., ERIKSSON, K., PERRIN, G., DEROO, P., VANDENBUSSCHE, B. & WATERS, L.B.F.M. (2006). Amorphous alumina in the extended atmosphere of α Orionis. *Astronomy & Astrophysics*, **447**, 311–324. (Cited on page [32](#).)
- VIDOTTO, A.A., FALCETA-GONÇALVES, D. & JATENCO-PEREIRA, V. (2006). A Self-Consistent Determination of the Temperature Profile and The Magnetic Field Geometry in Winds of Late-Type Stars. *Space Science Reviews*, **122**, 181–188. (Cited on page [133](#).)
- VÖGLER, A. & SCHÜSSLER, M. (2007). A solar surface dynamo. *Astronomy & Astrophysics*, **465**, L43–L46. (Cited on page [29](#).)

REFERENCES

- WEI, L., WOODY, D., TEUBEN, P., LA VIGNE, M. & VOGEL, S. (2008). Bandpass Calibration for CARMA. In *CARMA Memorandum Series*, vol. 45 of *BIMA memos*. (Cited on page [35](#).)
- WEYMANN, R. (1962). Physical Conditions in the Circumstellar Envelope of α Orionis. *Astrophysical Journal*, **136**, 844–+. (Cited on pages [79](#) and [81](#).)
- WHITE, S.M. (2009). Single Dish Aperture Efficiency Measurements at CARMA. In *CARMA Memorandum Series*, vol. 49 of *CARMA Memorandum Series*. (Cited on page [65](#).)
- WIEDEMANN, G., AYRES, T.R., JENNINGS, D.E. & SAAR, S.H. (1994). Carbon Monoxide Fundamental Bands in Late-Type Stars. III. Chromosphere or CO-mosphere? *Astrophysical Journal*, **423**, 806. (Cited on pages [43](#), [45](#) and [128](#).)
- WILLIAMS, M.E.K., FREEMAN, K.C., HELMI, A. & RAVE COLLABORATION (2009). The Arcturus Moving Group: Its Place in the Galaxy. In J. Andersen, Nordströara, B. m & J. Bland-Hawthorn, eds., *IAU Symposium*, vol. 254 of *IAU Symposium*, 139–144. (Cited on page [41](#).)
- WILSON, R.W., BALDWIN, J.E., BUSCHER, D.F. & WARNER, P.J. (1992). High-resolution imaging of Betelgeuse and Mira. *Monthly Notices of the Royal Astronomical Society*, **257**, 369–376. (Cited on page [114](#).)
- WOITKE, P. (2006). Too little radiation pressure on dust in the winds of oxygen-rich AGB stars. *Astronomy & Astrophysics*, **460**, L9–L12. (Cited on page [32](#).)
- WOOD, B.E., HARPER, G.M., MÜLLER, H.R., HEERIKHUISEN, J. & ZANK, G.P. (2007). The Wind-ISM Interaction of α Tauri. *Astrophysical Journal*, **655**, 946–957. (Cited on pages [45](#), [122](#), [125](#) and [132](#).)
- WRIGHT, A.E. & BARLOW, M.J. (1975). The radio and infrared spectrum of early-type stars undergoing mass loss. *Monthly Notices of the Royal Astronomical Society*, **170**, 41–51. (Cited on pages [127](#) and [129](#).)
- WRIGHT, K.O. (1970). The Zeta Aurigae stars. *Vistas in Astronomy*, **12**, 147–182. (Cited on page [40](#).)
- WRIGHT, M.C.H. (1999). Image Fidelity. In *BIMA memo 73: Image Fidelity*, vol. 73 of *BIMA memos*. (Cited on page [33](#).)